Carbon nanotubes: Vibrational and electronic properties

vorgelegt von
Diplom-Physikerin
Stephanie Reich
aus Berlin

von der Fakultät II - Mathematik und Naturwissenschaften
der Technischen Universität Berlin
zur Erlangung des akademischen Grades

Doktor der Naturwissenschaften
- Dr. rer. nat. -

genehmigte Dissertation

Promotionsausschuss:

Vorsitzender: Prof. Dr. P. Zimmermann
Berichter: Prof. Dr. C. Thomsen
Berichter: Prof. Dr. P. Ordejón

Tag der wissenschaftlichen Aussprache: 18. Dezember 2001

Berlin 2002
D83

Zusammenfassung

In dieser Arbeit untersuche ich Phononen und die elektronische Bandstruktur von Kohlenstoffnanotubes. Die beiden Problemkreise sind durch die Ramanspektroskopie, meine experimentelle Methode, eng verzahnt. Durch die Vielzahl von optischen Übergängen bei unterschiedlichem Durchmesser oder Chiralität sind Ramanspektren von Kohlenstoffnanotubes über den ganzen sichtbaren Bereich von resonanter Streuung hervorgerufen. Sie haben dadurch ein ungewöhnlich intensives Ramansignal, es ist sogar möglich, das Ramanspektrum eines einzelnen Tubes mit kommerziellen Spektrometern zu messen. Dieser erfreulichen experimentellen Tatsache standen gerade wegen der Resonanzeffekte Schwierigkeiten bei der Interpretation der Spektren gegenüber, die wegen der Resonanzeffekte nicht zu verstehen waren. Die gängige, nicht resonante Theorie der Ramanstreuung sagte zwar Phononen im Frequenzbereich der experimentellen Spektren voraus, versagte aber bei genauerem Hinsehen. Experimentell waren es vor allem die folgenden Punkte, die mich an der etablierten Interpretation zweifeln ließen:

- Die Auswahlregeln der Ramanspektren, die ich mit Hilfe von linearem und zirkularem Licht an ungeordneten Proben bestimmt habe (Kapitel 3.), zeigten, dass lediglich voll symmetrische A_1 Phononen und auch diese nur in paralleler Polarisation entlang der Nanotubeachse zur Streuung beitragen. Die Standardinterpretation hingegen stützte sich auf Moden verschiedener Symmetrie.
- Die identische Frequenzveränderung der hochenergetischen Phononen unter hydrostatischem Druck ließ sich nicht mit der Vorstellung von longitudinalen und transversalen Phononen verbinden (Kapitel 4.).
- Die Frequenz der Ramanmoden in Kohlenstoffnanotubes änderte sich mit der Wellenlänge des anregenden Lasers (Kapitel 6.). Dieses ungewöhnliche Verhalten versuchte ich zunächst mit leicht unterschiedlichen Phononenfrequenzen in verschiedenen Nanotubes zu erklären, was aber zu Widersprüchen führte.

Zusammengenommen schien es mir notwendig nach einer neuen Interpretation der Ramanspektren von Nanotubes zu suchen. Die neue Idee basiert auf doppelresonanter Ramanstreuung, wie wir sie auch für Graphit gefunden haben. Sie ist nicht nur in der Lage, die Form der Ramanspektren ohne weitere Annahmen korrekt vorherzusagen, sie löst auch die oben angeführten Probleme. Insbesondere erklärt sie vollständig die Abhängigkeit der Ramanmoden von der Anregungsenergie.

Während meiner Untersuchungen stieß ich immer wieder auf Fragestellungen, die sich mit experimentellen Methoden nicht oder nur schwierig beantworten ließen. So hatte ich mir etwa überlegt, dass der Schlüssel für ein Verständnis der Hochdruckexperimente in den Phononeneigenvektoren von chiralen Tubes liegt oder der für die Auswahlregeln in einer stark anisotropen Absorption. Ein Großteil dieser Arbeit befasst sich deshalb mit *ab initio* Berechnungen von Nanotubes. Die berechneten Eigenvektoren zeigen, dass tatsächlich Schwingungen in chiralen Nanotubes nicht mehr entlang

der Achse oder entlang des Umfanges erfolgen, sondern eine beliebige Auslenkungsrichtung in Bezug auf die Achse haben (Kapitel 4.). Die *ab initio* Rechnungen zur optischen Absorption bestätigten meine Vorstellung von den optischen Eigenschaften, zeigten mir aber auch, dass sich die elektronische Bandstruktur von Kohlenstoffnanotubes stark von der vom Graphit abgeleiteten unterscheidet. Ich habe daraufhin ein Reihe von Nanotubes berechnet und ihre elektronische Bandstruktur genauer untersucht (Kapitel 5.). So reduziert etwa die Krümmung der Graphitwand im allgemeinen die Bandlücke in halbleitenden Nanotubes. Sie wirkt sich aber auch auf die für Ramanstreuung wichtigen optischen Übergänge aus, die zum Teil um 0.1 eV zu kleineren Energien verschoben werden. Die Bündelung der Tubes zu einer hexagonal geordneten Struktur wie sie experimentell meist vorliegt, verschiebt die elektronischen Übergänge weiter zu kleineren Energien. Darüber fhinaus entsteht durch die Wechselwirkung zwischen den einzelnen Nanotubes auch eine elektronische Dispersion senkrecht zur Achse, ein Punkt der in der Interpretation experimenteller Ergebnisse bisher vernachlässigt wurde.

List of publications

1. Electronic band structures of isolated and bundled carbon nanotubes.
   S. Reich, C. Thomsen, and P. Ordejón
   Phys. Rev. B (in print 2002).

2. Phonon dispersion of carbon nanotubes.
   J. Maultzsch, S. Reich, C. Thomsen, E. Dobardžić, I. Milosešević, and M. Damnjanović. Solid State Commun. (in print 2002).

3. *Ab initio* determination of the phonon deformation potentials of graphene.
   C. Thomsen, S. Reich, and P. Ordejón
   Phys. Rev. B **65**, 073403 (2002).

4. Eigenvectors of chiral nanotubes.
   S. Reich, C. Thomsen, and P. Ordejón
   Phys. Rev. B **64**, 195 416 (2001).

5. Chirality selective Raman scattering of the D-mode in carbon nanotubes.
   J. Maultzsch, S. Reich, and C. Thomsen
   Phys. Rev. B **64**, 121 407(R) (2001).

6. The dependence on excitation energy of the D-mode in graphite and carbon nanotubes.
   C. Thomsen, S. Reich, and J. Maultzsch
   In *Electronic Properties of Novel Materials-Progress in Molecular Nanostructures*, edited by H. Kuzmany, J. Fink, M. Mehring, and S. Roth, IWEPS Kirchberg (2001).

7. Structural and vibrational properties of single walled nanotubes under hydrostatic pressure.
   S. Reich, C. Thomsen, and P. Ordejón
   In *Electronic Properties of Novel Materials-Progress in Molecular Nanostructures*, edited by H. Kuzmany, J. Fink, M. Mehring, and S. Roth, IWEPS Kirchberg (2001).

8. The pressure dependence of the high-energy Raman modes in empty and filled multiwalled carbon nanotubes.
   C. Thomsen and S. Reich.
   phys. stat. sol. (b), **225**, R9, (2001).

9. Intensities of the Raman-active modes in single and multiwall nanotubes.
   S. Reich, C. Thomsen, G. S. Duesberg, and S. Roth
   Phys. Rev. B **63**, R41401 (2001).

10. Resonant Raman scattering in GaAs induced by an embedded InAs monolayer.
    J. Maultzsch, S. Reich, A. R. Goñi, and C. Thomsen
    Phys. Rev. B **63**, 033306 (2001).

11. Double resonant Raman scattering in graphite.
    C. Thomsen and S. Reich
    Phys. Rev. Lett. **85**, 5214 (2000).

12. Comment on "Polarized Raman study of aligned multiwalled carbon nanotubes".
    S. Reich and C. Thomsen
    Phys. Rev. Lett. **85**, 3544 (2000).

13. Resonant Raman scattering in an InAs/GaAs monolayer structure.
    J. Maultzsch, S. Reich, A. R. Goñi, and C. Thomsen.
    In *Proc. 25th ICPS, Osaka*, N. Miura and T. Ando, editors, page 697, Berlin, Springer (2001).

14. Tensor invariants in resonant Raman scattering on carbon nanotubes.
    S. Reich and C. Thomsen.
    In *Proc. 25th ICPS, Osaka*, N. Miura and T. Ando, editors, page 1649, Berlin, Springer (2001).

15. Chirality dependence of the density-of-states singularities in carbon nanotubes.
    S. Reich and C. Thomsen
    Phys. Rev. B **62**, 4273 (2000).

16. Different temperature renormalizations for heavy and light-hole states of monolayer-thick heterostructures.
    A. R. Goñi, A. Cantarero, H. Scheel, S. Reich, C. Thomsen, P. V. Santos, F. Heinrichsdorff, and D. Bimberg
    Solid State Commun. **116**, 121 (2000).

17. Resonant Raman scattering on carbon nanotubes.
    C. Thomsen, P. M. Rafailov, H. Jantoljak, and S. Reich
    phys. stat. sol. (b) **220** 561 (2000).

18. Shear strain in carbon nanotubes under hydrostatic pressure.
    S. Reich, H. Jantoljak, and C. Thomsen
    Phys. Rev. B **61**, R13 389 (2000).

19. Lattice dynamics of hexagonal and cubic InN: Raman-scattering experiments and calculations.
    G. Kaczmarczyk, A. Kaschner, S. Reich, A. Hoffmann, C. Thomsen, D. J. As, A. P. Lima, D. Schikora, K. Lischka, R. Averbeck, and H. Riechert
    Appl. Phys. Lett. **76**, 2122 (2000).

20. Intramolecular interaction in carbon nanotube ropes.
C. Thomsen, S. Reich, A. R. Goñi, H. Jantoljak, P. Rafailov, I. Loa, K. Syassen, C. Journet, and P. Bernier.
phys. stat. sol. (b) **215**, 435 (1999).

21. Raman scattering by optical phonons in a highly strained InAs/GaAs monolayer.
S. Reich, A. R. Goñi, C. Thomsen, F. Heinrichsdorff, A. Krost, and D. Bimberg
phys. stat. sol. (b) **215**, 419 (1999).

22. Symmetry of the high-energy modes in carbon nanotubes.
C. Thomsen, S. Reich, P. M. Rafailov, and H. Jantoljak
phys. stat. sol. (b) **214** R15 (1999).

23. Raman spectrocopy on single and multi-walled nanotubes under pressure.
C. Thomsen, S. Reich, H. Jantoljak, I. Loa, K. Syassen, M. Burghard, G. S. Duesberg, and S. Roth.
Appl. Phys. A **69** 309 (1999).

Manuscripts under review

24. Elastic properties of carbon nanotubes under hydrostatic pressure.
S. Reich, C. Thomsen, and P. Ordejón
submitted to Phys. Rev. B (11/2001).

25. Raman scattering in carbon nanotubes revisited.
J. Maultzsch, S. Reich, and C. Thomsen
submitted to Phys. Rev. Lett. (10/2001).

Contents

Chapter 1

Introduction

Carbon nanotubes were discovered almost 10 years ago. The first report by Iijima[1] was on the multiwall form, coaxial carbon cylinders with a few tens of nanometers in outer diameter. Two years later single walled nanotubes were reported.[2,3] They are typically between 1 and 1.5 nm in diameter, but several microns in length. After a slow start in the mid 90's the field suddenly exploded two years ago. A first application – displays made out of field emitting multiwall tubes – is planned to be comercially available during the next years.[4] Other proposed applications include, e.g., nanotubes in intergrated circuits, nanotube actuators, or nanotubes for hydrogen storage.[5–9] From a physics point of view they are probably the best realized example of a one-dimensional system. Around the nanotube's circumference the wave vector is quantized, whereas k can take continous values along the axis. The abundance of new phenomena found in single-walled nanotubes comes not only from the confinement *per se*, but also from the multiple ways to contruct a tube. The best known example for a sudden change in the nanotube properties with their particular structure is their electronic dispersion. Depending on the direction of the confinement direction with respect to graphite nanotubes are metallic or semiconducting. The band structure can even be further manipulated, e.g., by introducing defects into a tube.[10]

When I started to work on nanotubes I was fascinated by the apparent contradiction between two models we developed to explain the pressure dependence of the nanotube Raman spectra: On the one hand, we studied the elastic properties of the tubes within macroscopic elasticity theory.[11] On the other hand, I tried to work out the phonon eigenvectors with group projector techniques and found that they strongly vary with the microscopic structure of a tube.[12] I was particularly interested in the high-energy part of the Raman spectrum between 1500 and 1600 cm^{-1} where the confined graphene optical modes give rise to a peculiarly shaped group of peaks. My idea at this point was to study the Raman spectrum to find out more

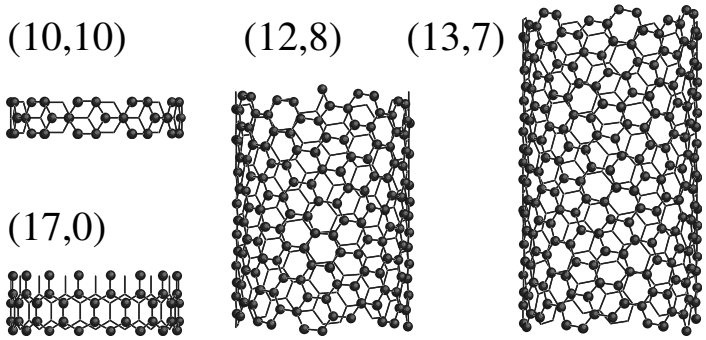

Figure 1.1: Unit cells of an armchair (10,10), a zig-zag (17,0), and the chiral (12,8) and (13,7) tubes. The diameters of the four tubes are between 13.3 and 13.8 Å.

about carbon nanotubes. The first step was to explain the origin of the high-energy modes. Interestingly, this turned out to be the difficult part; only recently we proposed a model, which I believe finally solves the problem.[13] For some time, however, I only found out what the peaks are not. For example, the two most dominant peaks are not LO and TO-like vibrations split by confinement and curvature as we thought in the beginning.[14] Most of the difficulties were due to the strong resonances in nanotubes which dominate the Raman signal. The scattering cross section is so large that it is even possible to obtain a Raman spectrum on single tube in dilute samples.[15,16] At this point – thinking about resonant scattering in general – also the so-called *D* mode in graphite and nanotubes came into the picture.[17] This disorder-activated Raman peak was long known to depend on the energy of the exciting laser.[18] We showed that this unusual dependence is naturally explained by a double resonant Raman process.[19–21] Double resonant scattering is, in fact, the origin of the entire Raman spectrum in single walled carbon nanotubes.[13] Before discussing all these points in detail I want to give a short introduction to Raman scattering on nanotubes and to the state of the research as it was two years ago.

1.1. Raman scattering on nanotubes

Single walled nanotubes can be regarded as long and narrow cylinders made out of a single graphene sheet. To specify the structure of an ideal infinitely long tube three quantities have be known: the diameter, the translational periodicity along the z axis, and the way in which the graphene hexagons are placed on the cylinder wall. All three quantities, however, are determined by the chiral vector $\boldsymbol{c} = n_1\boldsymbol{a_1} + n_2\boldsymbol{a_2}$, the vector around the tube circumference in terms of the unit cell vectors of graphene $\boldsymbol{a_1}$ and $\boldsymbol{a_2}$. Thus, the common way to refer to a particular tube is to give the tuple (n_1, n_2). Fig. 1.1 shows the unit cells of four different nanotubes with diameters $d \approx 13.5$ Å. The (10,10) and the (17,0) tube to the left are examples of the achiral (n,n) armchair and $(n,0)$ zig-zag tubes. In achiral nanotubes the carbon-carbon

bonds point around the circumference or along the z axis. In chiral nanotubes like the (12,8) and the (13,7) tube in Fig. 1.1 the translational periodicity and the unit cell is much larger than in achiral tubes. Despite the many atoms in the unit cell single walled carbon nanotubes are – in some sense – simple from a structural point of view. They are single orbit systems, i.e., a tube can be constructed from a single carbon atom by the symmetry operations, and thus perfect for the application of group theory.[22] The symmetries of nanotubes I discuss in Chapter 2.

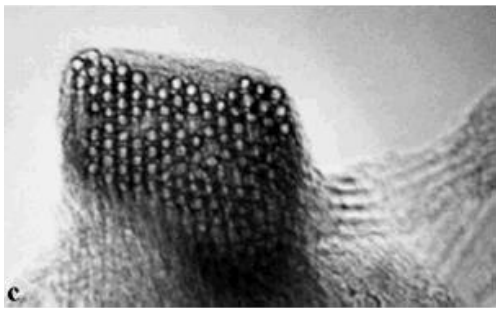

Figure 1.2: High resolution TEM picture of a bundle of single walled nanotubes. The hexagonal packing is nicely seen in the edge-on picture. Taken from Ref. 23.

Single walled nanotubes produced by laser ablation or the arc-discharge technique have a narrow Gaussian distribution of diameters $d = |\boldsymbol{c}|/\pi$ with mean diameters $d_0 \approx 1.2 - 1.5\,\text{nm}$ and $\sigma \approx 0.1 - 0.2\,\text{nm}$.[23] The chiralities, i.e., the angle Θ between $\boldsymbol{c}$ and $\boldsymbol{a_1}$, are in contrast evenly distributed ranging from zig-zag tubes $\Theta = 0°$ to armchair tubes $\Theta = 30°$.[24] Another well known structure which single walled tubes show are the hexagonal-packed bundles they form during the growth process. Fig. 1.2 shows a TEM picture of such a bundle. The wall to wall distance between two tubes is in the same range as the interlayer distance in graphite 3.41 Å.

Multiwall nanotubes have similar lengths as single walled tubes, but much larger diameters. Their inner and out diameters are around 5 and 100 nm, respectively, corresponding to ≈ 30 coaxial tubes. Confinement effects are expected to be less dominant than in single walled tubes, because of the large circumference. Many of the properties of multiwall tubes are already quite close to graphite.

The first Raman spectra of carbon nanotubes were published 1993 by H. Hiura and coworkers.[25] This very first spectrum looked exactly like graphite with a single peak $\approx 1580\,\text{cm}^{-1}$. J. M. Holden *et al.*[26] for the first time reported the group of broad Raman peaks just below $1600\,\text{cm}^{-1}$, which is typical for single walled nanotubes. They obtained their result by subtracting the spectra of catalysts free and Co-catalyzed nanotubes; the latter process was known to produce not only multiwall tubes and amorphous carbon, but single walled tubes as well.[3,26] A tentative assignment of all Raman modes to calculated frequencies was made by Rao *et al.*[27] Partly, this assignment is still considered to be correct. The high-energy part of the spectrum, however, is not explained by a simple correspondence between a Γ point eigenfrequency and an observed experimentally peak. In Fig. 1.3 I show a Raman spectrum of single walled nanotubes taken on a present day sample. The first order spectrum has three

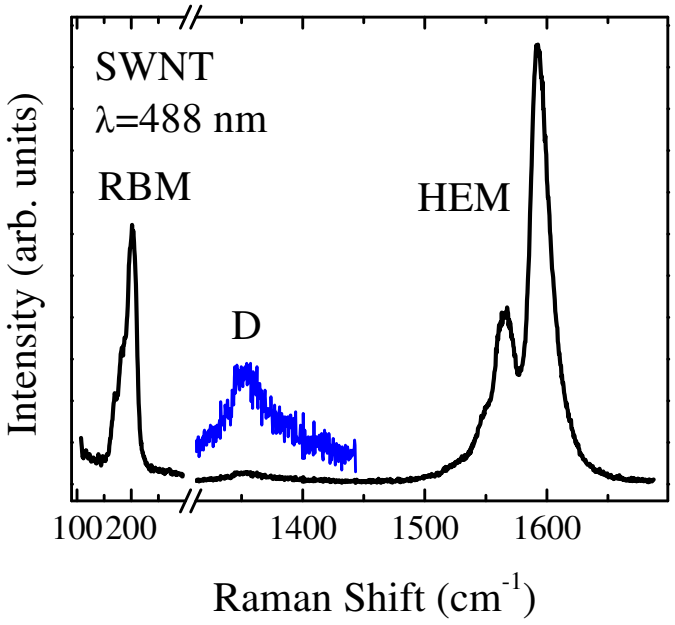

Figure 1.3: Raman spectrum of single walled nanotubes excited with 488 nm. The spectrum is typical for semiconducting nanotubes.

distinct features, the radial breathing mode around 200 cm^{-1}, the *D* mode, a disorder induced Raman peak, and the high-energy modes between 1500 and 1600 cm^{-1}.

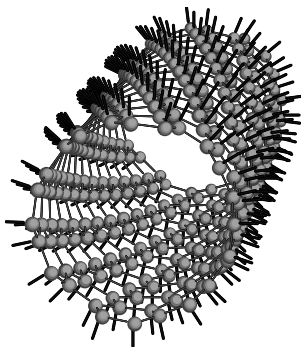

Figure 1.4: Radial breathing mode of an (8,4) nanotube with a diameter of $d = 8$ Å.

In the radial breathing mode all carbon atoms move in phase in the radial direction creating a breathing like vibration of the entire tube, see Fig. 1.4. The force needed for a radial deformation of a nanotube increases as the diameter and hence the circumference decreases. The expected dependence of the radial-breathing mode frequency on diameter $\omega_{\mathrm{RBM}} = C/d$ was used to measure the diameters of single walled nanotubes.[27,28] Although this simple approach is still used to some extent, it was found to be insufficient for a precise determination of the diameter because of additional van-der-Waals forces in nanotube bundles and resonance effects.[29–31] In high-pressure experiments Venkateswaran *et al.*[29] and our group[30] found that the normalized pressure dependence of the radial breathing mode was ≈ 16 times larger than the normalized shift of the high-energy modes. The striking difference in the pressure slopes can only be explained by the additional van-der-Waals forces between the tubes in a bundle. Since the van-der-Waals forces are much weaker than the intertube interaction, the tube-tube distance and thus the frequency of the radial breathing modes changes more rapidly under pressure than the diameter and the length of the tube itself.[30] In turn, the van-der-Waals force constants also contribute to the radial breathing mode frequency at ambient pressure. The total frequency is given by the diameter dependent part plus a (to first approximation constant) upshift by the tube-tube interaction. The exact

magnitude of this upshift is not known yet. The values obtained by pressure experiments and calculations range from 5 to almost 30 %.[29–33]

The second reason why the low-energy Raman spectrum yields only a rough estimate of the diameter is resonant scattering. Milnera *et al.*[31] thoroughly studied the Raman spectrum of the radial breathing mode as a function of the excitation energy between 1.44 and 2.71 eV; selected spectra are reproduced in Fig. 1.5. It can be nicely seen how the spectrum changes when excited with different laser energies. The diameters obtained from the two lowest traces by the $1/d$ dependence differ by $\approx 13\,\%$. The dependence of the scattering frequency on excitation energy points to selective resonances with different tubes and/or different scattering wave vectors. I discuss this point in detail in connection with the D mode in graphite and nanotubes (Chapter 6.). The electronic energy bands of single walled nanotubes depend in a first approximation only on the diameter,[34,35] whereas the chirality is important for the higher order corrections.[36,37] A measured resonant spectrum is given by a convolution of the electronic and vibrational properties of the nanotubes. Milnera *et al.*[31] modeled their spectra assuming a homogeneous distribution of chiralities and found good agreement with the measured spectra in Fig. 1.5.

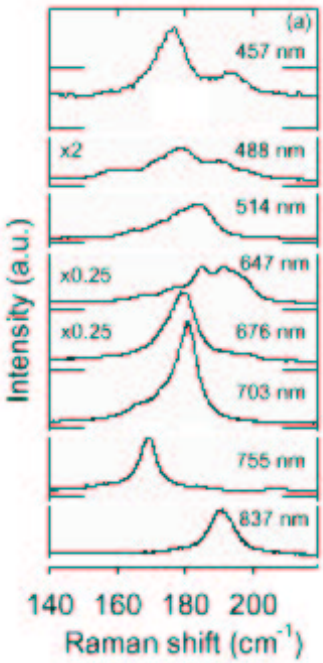

Figure 1.5: Raman spectrum in the low energy range measured with different excitation wavelengths. Modified figure from Ref. 31.

Of course, it is possible to qualitatively compare the diameters in, e.g., two samples grown at different temperatures, by Raman scattering.[28,38] Values for the mean diameter or even for (n_1, n_2) as recently claimed by Jorio *et al.*,[16] however, must be treated with care. The results depend much on the parameters chosen for the diameter dependence of the radial-breathing mode frequency $\omega_{\mathrm{RBM}} = C/d$ and assumed the electronic band structure. In Chapter 5. I study the electronic band structure for isolated and bundled nanotubes by first principles methods. In particular, I show that the simple tight-binding approximation is not precise enough for an assignment of (n_1, n_2) values.

The D mode at $1350\,\mathrm{cm}^{-1}$ in Fig. 1.3 has been known in graphite for 30 years.[17] It does not orginate from a Γ point Raman active vibration. Tuinstra *et al.*[17] showed that the D mode peak is induced by disorder. They measured different graphite samples and found that the intensity of this mode increases linearly with decreasing crystallite size. In a further

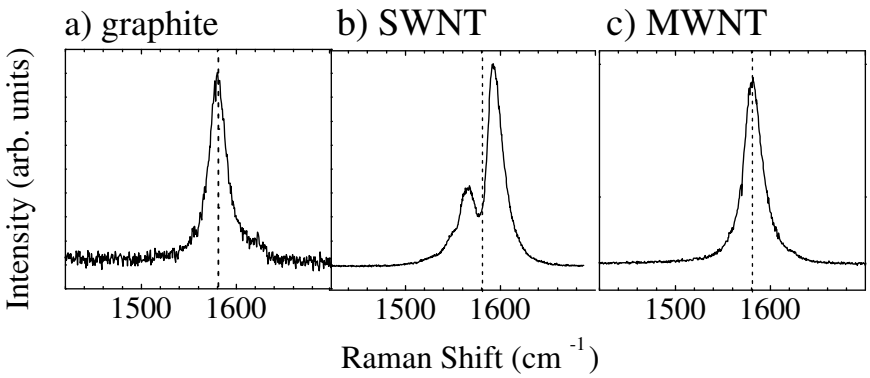

Figure 1.6: High-energy Raman spectra of a) graphite, b) single walled, and c) multiwall nanotubes. The dashed vertical line is at 1582 cm^{-1}, the E_{2g} phonon energy in graphite. Note that at 1582 cm^{-1} (dashed line) single walled nanotubes have a local minimum in the Raman intensity.

investigation Vidano *et al.*[18] studied the graphite Raman spectrum as a function of excitation energy. Their measurements revealed a Raman puzzle, which remained unsolved for almost 20 years: The frequency of the *D* mode shifted with the energy of the exciting laser. A similar shift as in graphite is found in multiwall and single walled nanotubes as well.[39,40] Recently, we showed that this dependence is due to a double resonant Raman process, which selects a particular wave vector for a given excitation energy. Since the phonon band is dispersive, the change in wave vector fulfilling the double resonant condition results in a shifting phonon energy as observed experimentally.[19]

The high-energy part of the Raman spectrum in Fig. 1.3 is, like the radial breathing mode, specific to single walled nanotubes. It consists of 3 to 4 close by peaks when the excitation energy is in the green or blue energy range. These peaks are broad – e.g., the dominant features at 1593 and 1570 cm^{-1} have a half width at full maximum of 16 and 30 cm^{-1} – and do not have a Lorentzian line shape. The high-energy Raman spectrum varies only slightly with tube diameter.[38,41] In Fig. 1.6 I compare the high-energy spectrum of a) graphite, b) single walled, and c) multiwall tubes. Graphite has a single Raman active mode at 1582 cm^{-1}. The scattering phonon is of E_{2g} symmetry with an in-plane optical eigenvector, i.e., the two carbon atoms in the hexagonal unit cell move out of phase within the graphite planes. Similar vibrations also give rise to the high-energy spectra in nanotubes, but additionally the confinement around the circumference and the curvature of the graphene sheet must be taken into account.

The wave vectors k_θ in the circumferential direction are quantized because of the finite length of the circumference. The wavelength of any quasiparticle must be equal to $\pi d/m$, where m is an integer. When $m = 0$, i.e., an infinite wavelength, the nanotube eigenvector corresponds to the eigenvector of graphene at the Γ point. If $m = 0$ phonon eigenvectors transform as

the fully symmetric representation and they are Raman active. The two other Γ point Raman active representations of nanotubes are E_1 and E_2 corresponding to $m = 1$ and 2, respectively. Thus, in a simple "only confinement" picture the nanotube Raman spectrum can be obtained in the following way:* Find the optical frequencies in graphene at $k = 0, 2/d$, and $1/d$ in the direction of the reciprocal chiral vector. These are the high-energy Raman modes in nanotubes. This easy approach obviously fails to explain the details of the experimental spectra. As can be seen in Fig. 1.6 the Raman spectrum of single walled nanotubes has a minimum at the graphite frequency [compare the dashed lines in a) and b)] and the dominant peak is at higher frequency. Within zone folding A_1 modes always have the same frequency as the Γ mode in graphene. The only mode predicted to be significantly above $1580\,\mathrm{cm}^{-1}$ is the E_2 mode, because of the overbending in the graphene phonon dispersion. This would mean that E_2 phonons yield the highest Raman intensity and that scattering by A_1 modes is negligible in nanotubes. Both findings are not only uncommon in Raman scattering on other materials, they also contradict the experimental findings on nanotubes, see Chapter 3..

Including the effect of curvature in the calculation of the phonon frequencies is less straightforward than including confinement. Two hand-waving explanations predict opposite shifts of the graphene frequency when the sheet is rolled up, and, moreover, the experimental findings are contradictory as well. Experimentally, a softening of the second order spectrum was observed by Thomsen.[40] Since the second order spectrum reflects the phonon density of states, he concluded that the curvature shifts the phonon frequencies to lower energies. However, as already pointed out, the first order spectrum is at slightly higher frequencies in nanotubes than in graphite. When a graphene sheet is rolled up to form a nanotube the pure sp^2 bonding of graphite is distorted and the bonds become partially sp^3 hybridized. Diamond as an example of a material with only sp^3 bonding, has the lowest optical phonon frequency of all carbon materials. Therefore, a down-shift of the phonon energy is expected. On the other hand, the carbon bonds are shorter on a curved wall than on a flat sheet; the angles vary correspondingly. This distortion is similar to a small compressive strain, which should yield a blue-shift of the vibrational frequencies.

Resonant scattering as described for the radial-breathing and the *D* mode is important in the high-energy range as well. The spectrum shown in Fig. 1.3 was excited with a laser wavelength $\lambda_L = 488\,\mathrm{nm}$ and is considered to be typical for semiconducting nanotubes. The spectral shape in the high-energy range varies strongly at different laser energies.[42–44] In Fig. 1.7 I show Raman spectra recorded with three different excitation energies, which were obtained by Rafailov *et al.*[44] The two lowest traces with $\lambda_L = 488\,\mathrm{nm}$ on two different samples

*This is basically the approach used by Rao *et al.*[27] in the first assignment of the Raman active modes.

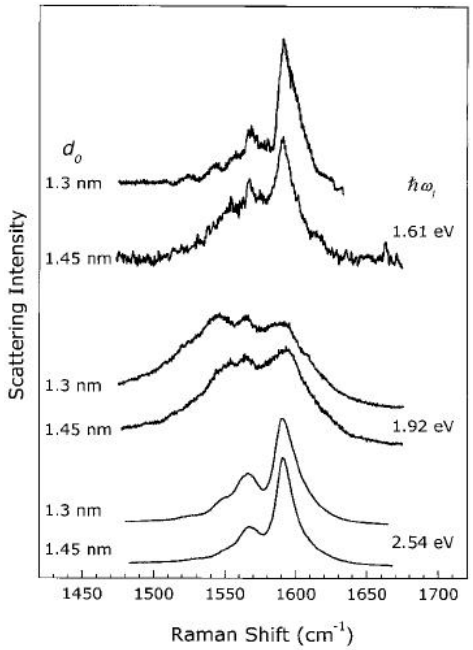

Figure 1.7: Raman spectra in the high-energy range excited with three different laser energies and on two samples with a mean diameter $d_0 = 1.3$ and 1.45 nm, respectively. Taken from Ref. 44.

are very similar to the high-energy Raman spectra shown above. For red excitation additional peaks appear on the low-energy side of the spectrum. In the infrared (1.61 eV) the shape of the blue spectrum is more or less recovered. It was first pointed out by Kasuya *et al.*[42] that this dependence of the high-energy spectrum on excitation energy can be explained by the different electronic structure of metallic and semiconducting nanotubes. The first singularities in the joint density of states are in the red for metallic tubes, but in the infrared and near UV in semiconducting tubes.[34,35] A detailed investigation of the Raman intensities in nanotubes normalized to a CaF_2 reference signal was later published by Rafailov *et al.*[44] They showed that indeed the metallic resonance in the red is accompanied by a loss of resonant enhancement for semiconducting tubes as expected from the joint density of states.

1.2. Summary

In this introduction to Raman scattering on nanotubes I discussed the three features in the first order spectra, the radial-breathing mode, the disorder induced *D* mode, and the high-energy modes in metallic and semiconducting tubes. For each of these distinct parts of the Raman spectrum the term "resonant scattering" turned up sooner or later. Resonant scattering is more difficult to describe theoretically than non-resonant scattering, because not only the vibrational modes, but also the details of the electronic states, the selection rules for optical absorption, and the electron-phonon coupling between particular electronic and vibrational states must be considered. This work tries to approach these problems from different viewpoints and with a number of techniques ranging from Raman scattering to *ab initio* calculations.

All selection rules are consequences of symmetry. Chapter 2. is therefore devoted to the symmetry properties of single-walled carbon nanotubes. The concept of line groups for one-dimensional systems is introduced. As an example for the application of group theory I show how to obtain phonon eigenvectors in achiral nanotubes by projection techniques. In the last

section I discuss the electronic states and their representations, which were obtained within the tight-binding approximation by M. Damnjanović and I. Milošević using the modified group projector technique.[45] An important question for the interpretation and understanding of Raman spectra is the symmetry of the observed phonon modes. In Chapter 3. I explain how to measure Raman tensor invariants on unoriented samples using linearly and circularly polarized light. Experimentally I found that even the symmetry of the scattered light is dominated by resonances and optical absorption, which somehow frustrates the use of the Raman tensors to learn more about the phonons – in particular the phonon eigenvectors – involved in the scattering process. Another experimental method, however, allows to study the high-energy eigenvectors, namely, Raman scattering under high pressure. I show in Chapter 4. that circumferential and axial eigenmodes are distinguished by their expected pressure slopes, because of the highly anisotropic nature of carbon nanotubes. The apparent discrepancies between the theoretical prediction and the experimental observations motivated me to calculate the phonon eigenvectors of chiral nanotubes by first principles methods. The results of the calculations, which were done with the *ab initio* code SIESTA developed by P. Ordejón and coworkers,[46,47] are presented in the last section of Chapter 4. An introduction to the SIESTA method and a description of the various calculations performed in this work are collected in Appendix I.. To obtain a better understanding of the electronic band structure, in particular, the effects of the nanotube curvature and the bundling of the tubes, I performed first principles band structure calculations for a series of chiral and achiral nanotubes. The results are presented in Chapter 5. where I also study the validity of the frequently used zone-folding approximation of the graphene π orbitals for finding the electronic states in single walled carbon nanotubes. Finally, Chapter 6. comes back more explicitly to resonances. The unusual frequency shift of the disorder mode in graphite and nanotubes I show to be due to double resonant Raman scattering. I disuss our recent suggestions that the entire Raman spectrum of carbon nanotubes is in fact caused by a double resonant process and present first calculations and measurements to support our idea.

Chapter 2

Symmetry

When discussing symmetry in crystals and group theory solid state physicists are usually familiar with two concepts: point groups of molecules and space groups of infinite three-dimensional crystals and their isogonal point groups. Low-dimensional systems are often described within the same concepts. Either only some high-symmetry points and their point groups are considered or a three-dimensional crystal is constructed and space groups are used. Applying the first idea is of course possible for carbon nanotubes as well. It bears the risk of missing additional symmetry operations besides the translational periodicity (as in fact happened for carbon nanotubes) and reduces the power of group theory. The second way out – constructing a crystal – is impossible for carbon nanotubes without reducing the symmetry of the single tube. The good news is that groups for low-dimensional systems exist, and many of their properties have been tabulated in a number of papers.[48–52] These groups are the diperiodic groups for two-dimensional structures and line groups for one-dimensional systems like carbon nanotubes. The properties of these groups were studied at the University of Belgrade for more than three decades, currently in the group of M. Damnjanović. They recently also worked out the modified group projectors, a method to apply projector techniques to infinite groups.

After introducing the structure of carbon nanotubes in more detail in Section 2.1. I describe their line-group symmetries in Secion 2.2. The rest of this chapter investigates the application of group theory to study physical properties of nanotubes. I find the phonon eigenmodes of achiral nanotubes by a graphical and the modified group projector technique in Section 2.4.2. and 2.5.1. In the last section I present the electronic dispersion of nanotubes in a symmetry-adapted tight-binding approximation.

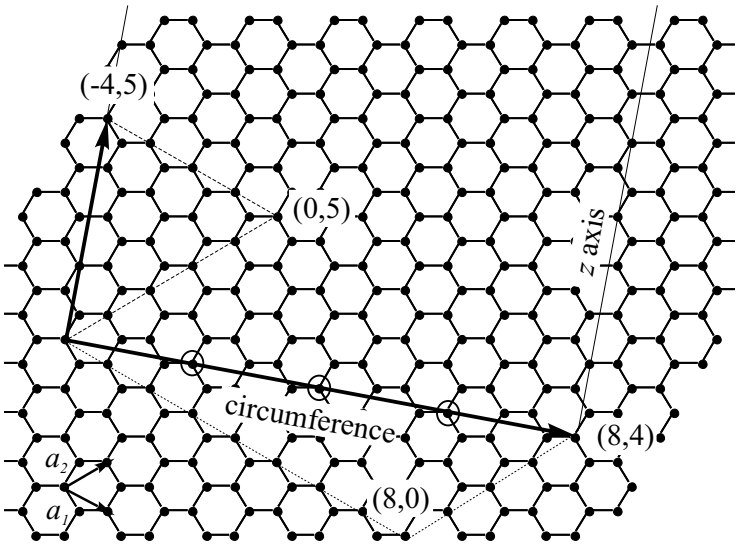

Figure 2.1: Graphene hexagonal lattice and the construction of an (8,4) nanotube. The two vectors $\boldsymbol{a_1}$ and $\boldsymbol{a_2}$ form the unit cell of graphene. The circumference of the tube is specified by $\boldsymbol{c} = 8\boldsymbol{a_1} + 4\boldsymbol{a_2}$, the tube axis is perpendicular to $\boldsymbol{c}$. The smallest lattice vector along the z axis is the translation periodicity of the tube, in this case $\boldsymbol{a} = -4\boldsymbol{a_1} + 5\boldsymbol{a_2}$. The three circles highlight the primitive translations in graphene which correspond to a C_4 symmetry operation of the tube (see next section).

2.1. Structure of carbon nanotubes

In the introduction I mentioned that a single-walled nanotube is uniquely determined by the tuple (n_1, n_2) specifying the chiral vector $\boldsymbol{c}$. In this section I summarize the structural properties in terms of the two integers n_1 and n_2. Extensive reviews can be found in some books on carbon nanotubes, e.g., Ref. 53.

The hexagonal graphene unit cell is spanned by the two vectors $\boldsymbol{a_1}$ and $\boldsymbol{a_2}$. They form an angle of 60° and their length is $|\boldsymbol{a_1}| = |\boldsymbol{a_2}| = a_0 = 2.461$ Å, see Fig. 2.1. Graphene has two atoms in the unit cell located at the origin and at $\frac{1}{3}(\boldsymbol{a_1} + \boldsymbol{a_2})$. To obtain a (n_1, n_2) nanotube first a long and narrow rectangle is cut from the graphene sheet. The direction and length of the narrower side is given by the vector $\boldsymbol{c} = n_1 \cdot \boldsymbol{a_1} + n_2 \cdot \boldsymbol{a_2}$. This sheet is then rolled up to a cylinder so that $\boldsymbol{c}$ becomes the circumference of the tube. The direction of the nanotube axis is naturally perpendicular to $\boldsymbol{c}$. In Fig. 2.1 I illustrate how to find the circumferential and axial direction for an (8,4) nanotube. First $\boldsymbol{c}$ is constructed (thin broken lines) and then the axial direction perpendicular to $\boldsymbol{c}$ (thin full lines). The translational periodicity along z is the smallest possible lattice vector along the z axis; for the (8,4) tube the translation period $\boldsymbol{a} = -4\boldsymbol{a_1} + 5\boldsymbol{a_2}$, see Fig. 2.1. The two conditions for constructing a tube also yield an analytic expression for $\boldsymbol{a}$

$$\boldsymbol{a} = -\frac{2n_2 + n_1}{n\mathcal{R}}\boldsymbol{a_1} + \frac{2n_1 + n_2}{n\mathcal{R}}\boldsymbol{a_2}, \tag{2.1}$$

and

$$a = |\boldsymbol{a}| = \frac{\sqrt{3\,(n_1^2 + n_2^2 + n_1 n_2)}}{n\mathcal{R}} a_0 \tag{2.2}$$

Tube			Radius	Translation Period
	n	N	r	a
(n_1,n_2)	GCD(n_1,n_2)	$n_1^2+n_2^2+n_1n_2$	$a_0\sqrt{N}/2\pi$	$\sqrt{3N}a_0/n\mathcal{R}$
(n,n)	n	$3n^2$	$\sqrt{3}a_0\,n/2\pi$	a_0
$(n,0)$	n	n^2	$a_0\,n/2\pi$	$\sqrt{3}a_0$
		Chiral angle		Helical angle
	$q=n_C/2$	Θ	w	ϕ
(n_1,n_2)	$2N/n\mathcal{R}$	$\arccos\left[(n_1+n_2/2)/\sqrt{N}\right]$	see Eq. (2.6)	$\arccos[w/\sqrt{w^2+3/\mathcal{R}}]$
(n,n)	$2n$	30°	1	30°
$(n,0)$	$2n$	0°	1	60°

Table 2.1: Structural parameters and symmetry properties of chiral, achiral, and zig-zag nanotubes. The symbols are explained in the text; this list is meant as a quick reference only.

where n is the greatest common divisor of n_1 and n_2, $\mathcal{R}=3$ if $(n_1-n_2)/3n$ is integer and $\mathcal{R}=1$ otherwise. The number of graphene cells in the nanotube unit cell q follows from the total cell area

$$S_t = a\cdot d = \boldsymbol{a}\times\boldsymbol{c} = \frac{\sqrt{3}}{2}\cdot\frac{2\,(n_1^2+n_2^2+n_1\,n_2)}{n\mathcal{R}}\,a_0^2$$

divided by the area of the graphene cell $S_g=\frac{\sqrt{3}}{2}\cdot a_0^2$; d is the diameter of the nanotube. The number of carbon atoms in the nanotube unit cell is finally given by

$$n_c = 2\,q = 4\,\frac{n_1^2+n_2^2+n_1\,n_2}{n\mathcal{R}}. \tag{2.3}$$

Since a depends inversely on n and $\mathcal{R}$ the translation periodicity and thus the number of carbon atoms varies strongly for tubes with similar diameter. For example, the number of atoms in the unit cells for the tubes shown on page 6 in Fig. 1.1 range from 40 for the (10,10) to 412 for the (13,7) tube. A (13,8) nanotube – indistinguishable from the (13,7) at first sight – has 1348 atoms in the unit cell, because both n and $\mathcal{R}=1$ in this example. In Table 2.1 I compiled a list of the structural parameters of carbon nanotubes; the other quantities listed in the Table will be introduced throughout this chapter.

2.2. Symmetry of carbon nanotubes

Symmetry belongs to the properties of single walled nanotubes which strongly depend on the particular choice of (n_1,n_2). In fact, every chiral nanotube belongs to a different line group. Only an (n,n) armchair and an $(n,0)$ zig-zag tube with the same n have the same symmetry. Another interesting result is that although achiral tubes have mirror planes not present in chiral tubes and thus appear more symmetric, they are in fact of lower symmetry, i.e., the

number of symmetry operations is smaller because of the small order of the principal screw axis. Symmetries of carbon and other nanotubes were studied extensively by Damnjanović *et al.*[22,45,54,55] In the following I will introduce the reader to the fundamental concepts and the meaning of their results. Those interested in the exact derivations are referred to the original work.

Line groups describe the symmetries of systems with a translational periodicity in only one direction. Along the periodic axis, the z axis, the system is considered to be infinite. A line group symmetry operation must transform a point $\tilde{z}$ on this axis either into itself or into another point z' at the axis separated from $\tilde{z}$ by ba, where a is the primitive translation and b an integer. Therefore, only the following symmetry operations (and their combinations) are compatible with one-dimensionality: (i) pure translations along z, (ii) rotations C_n around the z axis by any angle $2\pi/n$, (iii) rotations around an axis perpendicular to z by 180°, C_2' or U, (iv) reflections at a plane either containing the z axis, σ_v, or perpendicular to it, σ_h, and (v) the inversion, I. The infinitely many line groups $\boldsymbol{L}$ are products $\boldsymbol{L} = \boldsymbol{ZP}$, where $\boldsymbol{P}$ is a point group containing only the operations (ii) - (v). $\boldsymbol{Z}$ is the group of generalized translations, i.e., screw axis, pure translations, and glide planes.

To find the line group of carbon nanotubes Damnjanović *et al.*[22] looked for the graphene space group operations which are preserved when the graphene sheet is cut and rolled up to form a nanotube. It turns out that pure translations in graphene transform into pure rotations or screw operations in nanotubes. To give an example, consider the chiral vector $\boldsymbol{c} = n_1\boldsymbol{a_1} + n_2\boldsymbol{a_2} = n\cdot(\tilde{n}_1\boldsymbol{a_1} + \tilde{n}_2\boldsymbol{a_2}) = n\cdot\boldsymbol{c'}$, where n is the greatest common divisor of n_1 and n_2. Obviously, translations by $\boldsymbol{c'}$ leave the graphene lattice invariant, because $\boldsymbol{c'}$ is a graphene lattice vector, see Fig. 2.1 where $\boldsymbol{c'}$ is indicated by the circles around the atoms. When the sheet is rolled up to a tube $\boldsymbol{c'}$ becomes the nth section of the circumference and the translations by $\boldsymbol{c'}$ a rotation by $2\pi/n$ around the z axis. Single walled nanotubes thus have n pure rotations in their line groups denoted by $C_n^s = (C_n)^s$ $(s = 0, 1, \ldots, n-1)$. In a similar way the other primitive translations of graphene become the screw axis $\boldsymbol{T}_q^w$ of the nanotubes. The other graphene symmetry operations which need to be considered for nanotubes are rotations by 180° around an axis perpendicular to the sheet and reflections. As shown in Fig. 2.2 chiral and achiral nanotubes have C_2' or U axes. For the two achiral tubes shown at the right this symmetry is immediately seen in the Figure; the U axis in the chiral tube can be verified by rotating this page by 180°. The U' axis located between two carbon atoms is related to U by the screw symmetry of the tube. Achiral nanotubes also have a number of mirror and glide planes, some of them are shown in Fig 2.2. Chiral nanotubes never have mirror planes. A

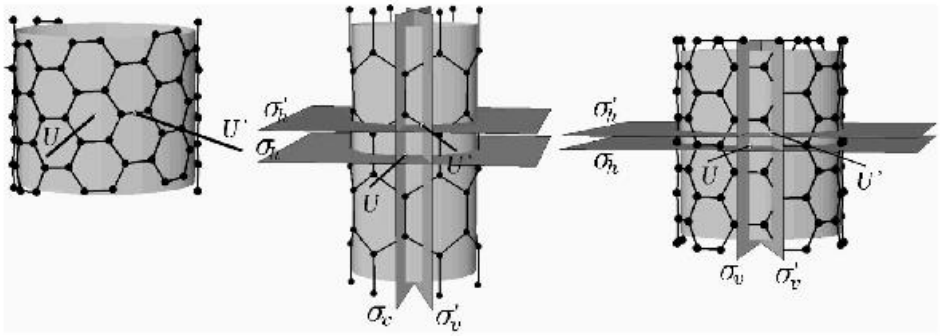

Figure 2.2: Symmetries of chiral and achiral nanotubes – horizontal rotational axes and mirror and glide planes. Left: Chiral (8,6) nanotube with the line group $\boldsymbol{T}^{12}_{148}\boldsymbol{D}_2$; one of the U and U' axes are shown. Middle and right: zig-zag (6,0) and armchair (6,6) nanotube belonging to the same $\boldsymbol{T}^{1}_{12}\boldsymbol{D}_{6h}$ line group. Additionally to the horizontal rotational axes, achiral tubes have also σ_h and σ_v mirror planes, the glide plane $\sigma_{v'}$, and the rotoreflection plane $\sigma_{h'}$. Taken from Ref. 22.

reflection which transforms the graphene hexagon into itself necessarily mixes the z and the two other axes and thus cannot be a line group symmetry operation.

The full symmetry group of a carbon nanotube is the product of the point group $\boldsymbol{P} = \boldsymbol{D}_n$ (chiral) and $\boldsymbol{D}_{nh}$ (achiral) and the axial group $\boldsymbol{Z} = \boldsymbol{T}^w_q$; q was already defined in Eq. (2.3) as the number of graphene unit cells in the unit cell of the tube, w will be given below. Note that all nanotubes have nonsymmorphic line groups, the isogonal point group is larger than $\boldsymbol{P}$. To summarize, the line groups and isogonal point groups of achiral tubes are

$$\boldsymbol{L}_{\mathcal{AZ}} = \boldsymbol{T}^1_{2n}\boldsymbol{D}_{nh} = \boldsymbol{L}2n_n/mcm \qquad \text{isogonal point group:} \quad \boldsymbol{D}_{2nh} \tag{2.4}$$

and of chiral tubes

$$\boldsymbol{L}_{\mathcal{C}} = \boldsymbol{T}^w_q\boldsymbol{D}_n = \boldsymbol{L}q_p22 \qquad \text{isogonal point group:} \quad \boldsymbol{D}_q \tag{2.5}$$

with the parameters

$$w = \frac{q}{n}\mathrm{Fr}\left[\frac{n}{q\mathcal{R}}\left(3-2\frac{n_1-n_2}{n_1}\right)+\frac{n}{n_1}\left(\frac{n_1-n_2}{n}\right)^{\varphi(n_1/n)-1}\right] \tag{2.6}$$

and

$$p = q\mathrm{Fr}\left\{\frac{n\mathcal{R}}{q\cdot(2n_1+n_2)}\left[q\cdot\left(\frac{2n_2+n_1}{n\mathcal{R}}\right)^{\varphi(2n_1+n_2/n\mathcal{R})-1} - n_2\right]\right\}, \tag{2.7}$$

where Fr[] is the fractional part of a rational number and $\varphi(m)$ the Euler function. I included the international notation, although I will not use it in this work, for a better reference to the Tables of Kronecker Products in Ref. 52 and 51.* The generating element for the groups

*Care must be taken when working with those Tables, because the symbols n, m, q, and p in the references have completely different meanings.

given in Eq. (2.4) and (2.5) are the screw generator $(C_q^w|\frac{na}{q})$, C_n, U, and, for achiral tubes only, σ_x (one of the σ_v mirror planes). Every other symmetry operation can be expressed as a combination of the generating elements, e.g., the horizontal mirror plane in achiral tubes is obtained by $\sigma_h = U\sigma_x$. $(C_q^w|\frac{an}{q})$ denotes a rotation by $2\pi w/q$ followed by the fractional translation an/q in the z direction. On the unwrapped sheet this corresponds to the primitive graphene translation $\frac{w}{q}\boldsymbol{c} + \frac{n}{q}\boldsymbol{a}$.

When acting on a particular carbon atom with an element of the line group the atom is either left invariant or transformed to another position in the nanotube. Two important questions for the application of group theory are (i) which operations leave the atom invariant – they are known as stabilizers or the site symmetry of the atom – and (ii) how many different starting atoms do I need to obtain the whole nanotube by the symmetry operations? Let us first turn to the second question. We already saw that the primitive translations of graphene correspond to the screw axis, simple rotations around z, and primitive translations in the tube. Therefore, the number of starting atoms needed – referred to as distinct sites or orbitals – can at most be 2, the number of atoms in the graphene unit cell. These two atoms, however, are mapped onto each other by the U operation. Carbon nanotubes are thus single orbit systems; the entire nanotube is obtained from a single atom by repeated application of $(C_q^w|\frac{na}{q})$, C_n, and U. Following Damnjanović *et al.*[22] I define the position of the first atom $\boldsymbol{r}_{000} = \frac{1}{3}(\boldsymbol{a_1} + \boldsymbol{a_2})$. By convention the x axis is chosen to coincide with the U axis. In cylindrical coordinates $\boldsymbol{r}_{000}(r_0, \Phi_0, z_0)$ is given by (see Table 2.1)

$$\boldsymbol{r}_{000} = (r, 2\pi\frac{n_1+n_2}{2N}, \frac{n_1-n_2}{2\sqrt{6N}a_0}), \tag{2.8}$$

where $N = nq\mathcal{R} = n_1^2 + n_1n_2 + n_2^2$, see Table 2.1. An element of $\boldsymbol{T}_q^w\boldsymbol{D}_n$ (the group generated by the screw axis, pure rotations, and the horizontal rotation) gives the new atomic position

$$\begin{aligned} \boldsymbol{r}_{tsu} &= (C_q^{wt}C_n^sU^u|t\frac{na}{q})\boldsymbol{r}_{000} \\ &= \left[r, (-1)^u\Phi_0 + 2\pi\left(\frac{wt}{q} + \frac{s}{n}\right), (-1)^uz_0 + \frac{tn}{q}a\right] \end{aligned} \tag{2.9}$$

where $u = 0, 1$, $s = 0, 1, \ldots, n-1$, and $t = 0, \pm1, \pm2, \ldots$. By inspection of Eq. (2.9) it is easily seen that not only the entire tube is generated by the symmetry elements as explained above, but that, likewise, *any* element of $\boldsymbol{T}_q^w\boldsymbol{D}_n$ maps the starting atom at $\boldsymbol{r}_{000}$ to *another* at $\boldsymbol{r}_{tsu}$, i.e., none of the operations leaves the atom invariant. For chiral tubes $\boldsymbol{T}_q^w\boldsymbol{D}_n$ is already the full line group symmetry. The problem of the stabilizers in chiral tube is thus trivially answered: Chiral tubes have only the trivial stabilizer, the identity operation E. To find the answer for achiral tubes we must look at the additional symmetry operations, which are introduced by

the σ_x generator. Looking at Fig. 2.2 it is seen that σ_h in armchair tubes and one of the vertical mirror planes $\sigma_v = C_n\sigma_x$ in zig-zag tubes transform a given atom into itself. The site symmetry of a carbon atom in armchair and zig-zag tubes is C_{1h}.

2.3. Digression: Notations

Group theory is a field with a wide variety of notations, e.g., for the symmetry operations and the irreducible representations. In the last section I assumed that the reader is familiar with the Schönflies and the Koster-Seitz symbols for symmetry operations. Both notations are quite popular for space groups; explanations and conversions can be found in a number of textbooks.[56–59] For the irreducible representations I will use two different notations in this work: the molecular notation and the notation used in the papers on line groups. Both have their benefits and their shortcomings. The molecular notation can again be found in any textbook on group theory, I will therefore use it as the reference in this section. The line group notation is very clear in the sense that it uses the full set of quantum numbers to denote an irreducible representation. Moreover, it is not restricted to the Γ point of the Brillouin zone as the molecular point group notation naturally is. I briefly introduce the line group notation in this section and give a conversion table for the two notations at $k = 0$.

The isogonal point groups of chiral and achiral nanotubes belong to the dihedral groups and the order of the principal rotation axis q is always even, see Table 2.1. In the molecular or Mulliken notation non-degenerate irreducible representations are labeled by the character A or B and doubly degenerate by E. The symbols A and B distinguish between the character of the q fold rotation being $+1$ and -1, respectively. The subscripts 1 and 2 for the non-degenerate representations reflect the characters $+1$ and -1 of the U or C_2' axis. The degenerate E representations have subscripts running from $m = 1, 2, \ldots, (q/2-1)$, which are derived from the character of the C_q rotation $\chi^{E_m}(C_q) = 2\cos(m \cdot 2\pi/n)$. Finally, all symbols carry the additional subscript g or u for even or odd parity under inversion in the point groups of achiral nanotubes. Table 2.2 is a character table of the D_{qh} molecular point group for q even corresponding to achiral nanotubes; the character table for chiral nanotubes is obtained by omitting the symmetry operations involving the inversion and dropping the g and u subscripts for the representations.

The line group notation also uses the symbols A and B for non-degenerate representations, but A and B now stand for even (character $+1$) and odd (character -1) parity under the vertical reflection σ_x. I first explain the notation used for the Γ point of the Brillouin zone or $k = 0$. The other irreducible representations follow more or less the same idea. The general

D_{qh}	E	$2C_q$	$2C_q^2$	…	$C_q^n = C_2$	$\frac{q}{2}C_2' = U$	$\frac{q}{2}C_2'' = U'$	I	$2IC_q$	$2IC_q^2$	…	$IC_2 = \sigma_h$	$\frac{q}{2}\sigma_v$	$\frac{q}{2}\sigma_{v'}$
A_{1g}	1	1	1	…	1	1	1	1	1	1	…	1	1	1
A_{1u}	1	1	1	…	1	1	1	−1	−1	−1	…	−1	−1	−1
A_{2g}	1	1	1	…	1	−1	−1	1	1	1	…	1	−1	−1
A_{2u}	1	1	1	…	1	−1	−1	−1	−1	−1	…	−1	1	1
B_{1g}	1	−1	1	…	$(-1)^n$	1	−1	1	−1	1	…	$(-1)^n$	1	−1
B_{1u}	1	−1	1	…	$(-1)^n$	1	−1	−1	1	−1	…	$-(-1)^n$	−1	1
B_{2g}	1	−1	1	…	$(-1)^n$	−1	1	1	−1	1	…	$(-1)^n$	−1	1
B_{2u}	1	−1	1	…	$(-1)^n$	−1	1	−1	1	−1	…	$-(-1)^n$	1	−1
E_{1g}	2	$2\cos\alpha$	$2\cos 2\alpha$	…	−2	0	0	2	$2\cos\alpha$	$2\cos 2\alpha$	…	−2	0	0
E_{1u}	2	$2\cos\alpha$	$2\cos 2\alpha$	…	−2	0	0	−2	$-2\cos\alpha$	$-2\cos 2\alpha$	…	2	0	0
E_{2g}	2	$2\cos 2\alpha$	$2\cos 4\alpha$	…	2	0	0	2	$2\cos 2\alpha$	$2\cos 4\alpha$	…	2	0	0
E_{2u}	2	$2\cos 2\alpha$	$2\cos 4\alpha$	…	2	0	0	−2	$-2\cos 2\alpha$	$-2\cos 4\alpha$	…	−2	0	0
…	…	…	…	…	…	…	…	…	…	…	…	…	…	…
$E_{(n-1)g}$	2	$2\cos(n-1)\alpha$	$2\cos 2(n-1)\alpha$	…	$2\cos(n-1)\pi$	0	0	2	$2\cos(n-1)\alpha$	$2\cos 2(n-1)\alpha$	…	$2\cos(n-1)\pi$	0	0
$E_{(n-1)u}$	2	$2\cos(n-1)\alpha$	$2\cos 2(n-1)\alpha$	…	$2\cos(n-1)\pi$	0	0	−2	$-2\cos(n-1)\alpha$	$-2\cos 2(n-1)\alpha$	…	$-2\cos(n-1)\pi$	0	0

Table 2.2: Character table of the D_{qh} point groups with even q; $\alpha = 2\pi/q$, $n = q/2$. To obtain the table for D_q omit I and all following symmetry operations.

	$(C_{2n}^{2r}\|t)$	$(C_{2n}^{2r+1}\|\frac{1}{2}+t)$	$(\sigma_v C_{2n}^{2r}\|t)$	$(\sigma_v C_{2n}^{2r+1}\|\frac{1}{2}+t)$	$(\sigma_h C_{2n}^{2r}\|-t)$	$(\sigma_h C_{2n}^{2r+1}\|-\frac{1}{2}-t)$	$(\sigma_h\sigma_v C_{2n}^{2r}\|-t)$	$(\sigma_h\sigma_v C_{2n}^{2r+1}\|-\frac{1}{2}-t)$
			$(\sigma_x C_{2n}^{2r}\|t)$	$(\sigma_{v'} C_{2n}^{2r}\|\frac{1}{2}+t)$	$(\sigma_x U C_{2n}^{2r}\|-t)$	$(\sigma_x U' C_{2n}^{2r}\|-\frac{1}{2}-t)$	$(UC_{2n}^{2r}\|-t)$	$(U' C_{2n}^{2r}\|-\frac{1}{2}-t)$
${}_0A_0^{\pm}$	1	1	1	1	±1	±1	±1	±1
${}_0B_0^{\pm}$	1	1	−1	−1	±1	±1	∓1	∓1
${}_0A_n^{\pm}$	1	−1	1	−1	±1	∓1	±1	∓1
${}_0B_n^{\pm}$	1	−1	−1	1	±1	∓1	∓1	±1
${}_0E_m^{\pm}$	$2\cos 2rm\alpha$	$2\cos(2r+1)m\alpha$	0	0	$\pm 2\cos 2rm\alpha$	$\pm 2\cos(2r+1)m\alpha$	0	0
${}_kE_{A_0}$	$2\cos kt$	$2\cos k(\frac{1}{2}+t)$	$2\cos kt$	$2\cos k(\frac{1}{2}+t)$	0	0	0	0
${}_kE_{B_0}$	$2\cos kt$	$2\cos k(\frac{1}{2}+t)$	$-2\cos kt$	$-2\cos k(\frac{1}{2}+t)$	0	0	0	0
${}_kE_{A_n}$	$2\cos kt$	$-2\cos k(\frac{1}{2}+t)$	$2\cos kt$	$-2\cos k(\frac{1}{2}+t)$	0	0	0	0
${}_kE_{B_n}$	$2\cos kt$	$-2\cos k(\frac{1}{2}+t)$	$-2\cos kt$	$2\cos k(\frac{1}{2}+t)$	0	0	0	0
${}_\pi E_{A_0}^{A_2}$	$2(-1)^t$	0	$2(-1)^t$	0	0	0	0	0
${}_\pi E_{B_0}^{B_2}$	$2(-1)^t$	0	$-2(-1)^t$	0	0	0	0	0
${}_kG_m$	$4\cos kt\,\cos 2rm\alpha$	$4\cos k(\frac{1}{2}+t)$ $\times\cos(2r+1)m\alpha$	0	0	0	0	0	0
${}_\pi G_j^{n-j}$	$(-1)^t 4\cos 2jr\alpha$	0	0	0	0	0	0	0
and for n even								
${}_\pi E_{q/2}^{\pm}$	$2(-1)^{r+t}$	0	0	0	0	0	$\pm 2(-1)^{r+t}$	0

Table 2.3: Character table for the $\boldsymbol{T}_{2q}^{w}\boldsymbol{D}_{nh}$ line groups. The characters for the chiral line groups can be found in Ref. 49; they can also be obtained from essentially the same patterns as observed by a close inspection of this table. Note that the inversion $I = \sigma_h C_2$. The ± superscript in the line group notation does not correspond to the g/u subscript in the molecular notation. Here $\alpha = 2\pi/2n$, $t = 0, \pm 1, \pm 2, \ldots$, $m = 1, 2, \ldots, (n-1)$, $r = 0, 1, \ldots, n-1$, and $k \in (0, \pi)$.

A_0^+	A_0^-	B_0^+	B_0^-	A_q^+	A_q^-	B_q^+	B_q^-	E_m^+	E_m^-
A_{1g}	A_{2u}	A_{2g}	A_{1u}	B_{1g} [1]	B_{2u} [1]	B_{2g} [1]	B_{1u} [1]	E_{mg} [3]	E_{mu} [3]
				B_{2u} [2]	B_{1g} [2]	B_{1u} [2]	B_{2g} [2]	E_{mu} [4]	E_{mg} [4]

[1] n even [2] n odd [3] m even [4] m odd

Table 2.4: Correspondence between the line group notation for $k = 0$ and the molecular notation. Note that the exact relation between g and u and the horizontal mirror parity (denoted as the superscript in the line group notation) depends on the quantum number m being even or odd. The correspondence for chiral nanotubes is obtained by omitting the $\pm$ superscript in the line group notation and the g/u subscript in the molecular notation.

labeling of the representations at the Γ point is

$$k{=}0\rightarrow \quad {}_0S_m^{\pm} \quad \begin{matrix} \leftarrow \sigma_h \text{ parity} \\ \leftarrow m \text{ quantum number} \end{matrix}, \tag{2.10}$$

where m is the absolute value of the quantum number of the z component of the angular momentum and S stands for A, B, or E. The character for the rotation around the z axis and the screw axis is given by $2\cos m\beta$, where β is the rotation angle. For $m = 0, n$ the representations are non-degenerate, all other m have doubly degenerate E representations. The two degenerate eigenstates are $+m$ and $-m$. The σ_h parity is not to be confused with even and odd transformation under inversion. The inversion is given by $\sigma_h C_2$ and an even parity under σ_h corresponds to g or u in the molecular notation depending on m being even or odd, respectively. Non-degenerate representations exist only at the Γ point of the Brillouin zone. At wave vectors $k \neq 0, \pi$ the representations are fourfold or doubly degenerate in achiral nanotubes, which is indicated by the symbols G and E, respectively. Chiral nanotubes have only doubly degenerate representations. The fourfold degenerate representations ${}_kG_m$ are labeled in the same way as given above except that σ_h is no longer a symmetry operation and the superscript is omitted. For the E representations the subscripts denote the irreducible representation which is obtained for $k \rightarrow 0$, e.g., ${}_kE_{A_0}$.

The character table of achiral line groups is given in Table 2.3. For the chiral line groups it can be obtained by omitting the symmetry operations of achiral tubes not present in chiral nanotubes or looked up in Ref. 49. Finally, Table 2.4 gives the correspondence between the molecular and line group notation at the Γ point.

Although the line group notation might seem unfamiliar at first sight, it has the huge benefit of using the full set of quantum numbers for the labeling of the irreducible representation, which is particularly handsome when dealing with selection rules. For example, consider the selection rules for Raman scattering in (xx) configuration, i.e., the incoming and scattered light are polarized parallel to the nanotubes axis. The selection rules for optical absorption in x polarization are $\Delta m = \pm 1$ and $\sigma_h = +1$. The total change by the absorption and emission

of a photon is thus $\Delta m_{\text{tot}} = 0, +2, -2$ and the total σ_h parity is left invariant (+1). Since both m and σ_h must be conserved in the whole Raman process and the initial and final electronic states are the same, the only phonon symmetries contributing to (xx) scattering are ${}_0A_0^+ = A_{1g}$ and ${}_0E_2^+ = E_{2g}$.* This argumentation gives a better physical understanding and is much simpler to perform than the reduction of the corresponding Kronecker product.

2.4. Phonon symmetries and eigenvectors

In the preceding sections I introduced the line and point group symmetries of carbon nanotubes. Every quasiparticle like electrons or phonons in nanotubes must belong to one irreducible representation of those groups. Irreducible representations specify the rules under which the eigenvector of a quasiparticle transforms under the symmetry operations. On the other hand, the irreducible representations fully determine selection rules. If, e.g., the Raman selection rules are measured experimentally, a first assignment of the observed Raman modes to the theoretically expected phonon modes is possible. This assignment, however, is not unique in most systems, because several phonons might belong to the same irreducible representation. The vibrational modes are symmetry adapted bases of an irreducible representation and the eigenvectors and eigenstates of the dynamical matrix. Nevertheless, I show in this section that symmetry adapted displacements together with some general assumption on the strength of the force constants give insight into the phonon frequencies and eigenvectors expected in single walled nanotubes. The symmetry approach works particularly well for achiral tubes, because of their mirror planes. We will see in Chapter 4. that the phonons calculated by first principles methods agree very well with the predictions made by symmetry. Before saying anything about selection rules, Raman scattering, or phonon eigenvectors we must, however, find the possible phonon symmetries in carbon nanotubes.

2.4.1. The dynamical representation

The representation of all vibrations is the so-called dynamical representation, which is best visualized as all atoms in the unit cell carrying a displacement vector. The phonon symmetries are found by decomposing the dynamical representation into its irreducible representations. There are multiple ways to do this. The most elegant – the site group analysis – uses induced representations and obtains the phonon symmetries (and partly, also the eigenvectors) from the full line or space group of the system and the stabilizer or site symmetry of

*The conservation of the angular momentum quantum number is not strictly correct, since m is only a good quantum number if Umklapp processes are omitted.

the atoms. The benefit of this method is that is has to be carried out only once, tabelized, and then can be looked up for a specific system. Exhaustive tables for space groups and an introduction to the method can be found in the papers by Rousseau *et al.*[60] and Fateley *et al.*,[61] for line groups they were published by Milošević and Damnjanović.[62] The conceptionally easiest method, on the other hand, is to directly set up the dynamical representation from the atomic and vector representation and to reduce it by hand (factor group analysis). I will demonstrate this method by the example of a (10,10) armchair tube. In general, this method for finding the phonon symmetries must be carried out for the specific system under consideration.

As already mentioned the dynamical representation can be understood as the atoms in the unit cell with a vector attached to every atom. To find the characters of this representation we must look at the transformation properties of the atoms in the unit cell and the vector representation. Every atom which is left invariant by a symmetry operation contributes $+1$ to the character of the atomic representation, which then has to be multiplied by the transformation properties of the attached displacement vector. In other words, the dynamical representation Γ_{DR} is the direct product of the atomic and the vector representation $\Gamma_{\mathrm{DR}} = \Gamma_{\mathrm{a}} \otimes \Gamma_{\mathrm{vec}}$. In armchair tubes the only operations transforming an atom into itself are the identity E and the horizontal mirror plane σ_h. All 40 atoms in the unit cell are invariant under both operations yielding a character of 40 for E and σ_h in (10,10) armchair tubes; the other characters are zero. The characters of the vector representation are given by

$$\chi_{\mathrm{vec}} = \pm 1 \pm 2\cos\beta, \tag{2.11}$$

where β is the rotation angle and $+$ and $-$ hold for proper and improper rotations, respectively. Since the dynamical representation is the product of the atomic and the vector representation, we only need the character of the identity $\chi_{\mathrm{vec}}(E) = 3$ and the horizontal mirror plane $\chi_{\mathrm{vec}}(\sigma_h) = 1$. By multiplying the character of both representations we finally obtain $\chi_{\mathrm{DR}}(E) = 120$, which is equal to the number of the normal modes $3n_c$, and $\chi_{\mathrm{DR}}(\sigma_h) = 40$; the other characters are zero. We thus obtained the characters of the dynamical representation. The next and final step for finding the normal modes of the (10,10) nanotube is to reduce this representation into irreducible representations of the point group D_{20h}.

A representation can be decomposed into the sum of its irreducible representations by the following formula

$$f_\alpha = \frac{1}{g}\sum_G \chi^{(\alpha)}(G)^\star \chi^{(\Gamma_{\mathrm{DG}})}(G), \tag{2.12}$$

where f_α is the frequency number, the times the irreducible representation α appears, g is the order of the symmetry group, its number of symmetry elements; the sum is over all

	Phonon symmetries at the Γ point	m
(n,n)	$2(A_0^+ \oplus B_0^+ \oplus A_n^+ \oplus B_n^+) \oplus A_0^- \oplus B_0^- \oplus A_n^- \oplus B_n^- \oplus \sum_m (4E_m^+ \oplus 2E_m^-)$	$[1,n-1]$
$(n,0)$	$2(A_0^+ \oplus A_0^- \oplus A_n^+ \oplus A_n^-) \oplus B_0^+ \oplus B_0^- \oplus B_n^+ \oplus B_n^- \oplus \sum_m 3(E_m^+ \oplus E_m^-)$	$[1,n-1]$
(n_1,n_2)	$3(A_0^+ \oplus A_0^- \oplus A_{q/2}^+ \oplus A_{q/2}^-) \oplus \sum_m 6E_m$	$[1,q/2-1]$

Table 2.5: Phonon symmetries of single walled nanotubes at the Γ point. The subscript for $k=0$ was omitted for clarity. The last column specifies the range of m in the sums of the doubly degenerate representations.

symmetry operations G. The proof of Eq. (2.12) can be found in any group theory textbook, e.g., Ref. 56, 58. For the A_{1g} representation, for example, Eq. (2.12) reads

$$f_{A_{1g}} = \frac{1}{80}(1\cdot 120 + 1\cdot 40) = 2. \tag{2.13}$$

A (10,10) armchair tube has two vibrational modes of A_{1g} symmetry. The frequency numbers of the other representations are easily found with the help of Table 2.2. The total decomposition for a (10,10) armchair tube at the Γ point is

$$\begin{aligned}\Gamma_{\mathrm{DC}}^{(10,10)} =& 2A_{1g} \oplus A_{1u} \oplus 2A_{2g} \oplus A_{2u} \oplus 2B_{1g} \oplus B_{1u} \oplus 2B_{2g} \oplus B_{2u} \oplus 2E_{1g} \oplus 4E_{1u} \\ & \oplus 4E_{2g} \oplus 2E_{2u} \oplus 2E_{3g} \oplus 4E_{3u} \oplus 4E_{4g} \oplus 2E_{4u} \oplus \ldots \oplus 2E_{9g} \oplus 4E_{9u} \\ =& 2({}_0A_0^+ \oplus {}_0B_0^+ \oplus {}_0A_{10}^+ \oplus {}_0B_{10}^+) \\ & \oplus {}_0A_0^- \oplus {}_0B_0^- \oplus {}_0A_{10}^- \oplus {}_0B_{10}^- \oplus \sum\nolimits_{m=1,9}(4\,{}_0E_m^+ \oplus 2\,{}_0E_m^-).\end{aligned} \tag{2.14}$$

This result can be generalized for armchair, zig-zag, and chiral nanotubes. I list he phonon symmetries at the Γ point in these three types of tubes in Table 2.5 in the line group notation. The phonons at other k points can be found in the paper by Damnjanović *et al.*[22]

The Raman Γ_{R} and infrared active Γ_{ir} vibrations transform according to the representation of the second rank tensor and the vector representation, respectively.[50]

$$\Gamma_{\mathrm{R}} = [\Gamma_{\mathrm{vec}} \otimes \Gamma_{\mathrm{vec}}] \quad = {}_0A_0^+ \oplus {}_0E_1^- \oplus {}_0E_2^+ \quad (\oplus {}_0B_0^+) \quad = A_{1g} \oplus E_{1g} \oplus E_{2g} \quad (\oplus A_{2g}) \tag{2.15}$$

$$\Gamma_{\mathrm{ir}} = \Gamma_{\mathrm{vec}} \quad = {}_0A_0^- \oplus {}_0E_1^+ \quad = A_{2u} \oplus E_{1u}. \tag{2.16}$$

The irreducible representation A_{2g} given in paranthesis in Eq. (2.15) is totally antisymmetric. It can only contribute to resonant Raman scattering and is usually not expected to have strong intensities in Raman experiments. In the introduction, however, I showed that resonances play a dominant role in Raman scattering on carbon nanotubes. Therefore, we cannot exclude antisymmetric contributions to the scattered light as in non-resonant Raman experiments. In Chapter 3. I discuss the selection rules for Raman scattering in more detail and show how to obtain the contributions of the four representations in Eq. (2.15) experimentally.

2.4.2. Projection operators I: Arrow drawing

Projection operators in group theory solve the problem: How do I find a function transforming as a particular irreducible representation? I used the term function in a general sense; in the case of phonons it stands for the displacement pattern of the eigenvectors.

Consider an arbitrary function F. This function can, in general, be expanded into several irreducible representations $F = \sum_\alpha \sum_n c_\alpha^n \zeta_\alpha^n$, where α labels the irreducible representations, c_α^n are the coefficients of the expansion, and the ζ_α^n are functions transforming according to the representation α. A projection operator defined by

$$P_{l(n)}^{(\beta)} = \frac{d_\beta}{g} \sum_G D_{ln}^{(\beta)}(G)^* G \tag{2.17}$$

applied to F picks out the symmetry adapted function $\zeta_l^{(\beta)}$. In Eq. (2.17) d_β is the degeneracy of the irreducible representation β, g the order of the symmetry group, G are the symmetry operations, and $D_{ln}^{(\beta)}$ is the lnth element of the representation matrix $D^{(\beta)}$.

As a simple example how to work with projection operators I take a vector (x,y,z) in the D_{4h} point group. In the last section we found that the vector representation is the sum $A_{2u} \oplus E_{1u}$. I look for the part of the vector transforming according to A_{2u}. A projection onto non-degenerate representations is particularly easy, because the representation matrix $D^{(\beta)}$ is equal to the characters of the representation. The full projection according to Eq. (2.17) and Table 2.2 reads

$$\begin{aligned} P^{(A_{2u})}(x,y,z) &= \tfrac{1}{16} \quad (E + C_4 + C_4^{-1} + C_2 - C_{21}' - C_{22}' - C_{21}'' - C_{22}'' - I - \ldots)(x,y,z) \\ &= \tfrac{1}{16} \quad [(x,y,z) + (y,-x,z) + (-y,x,z) + (-x,-y,z) - (x,-y,-z) - \\ &\qquad (-x,y,-z) - (y,x,-z) - (-y,-x,-z) - (-x,-y,-z)\ldots] \\ &= \tfrac{2}{16} \quad (0,0,8z) = (0,0,z). \end{aligned}$$

The z component of a vector transforms as the A_{2u} representation in the D_{4h} point group. The result is easily checked with the character table and the known transformation properties of z. To summarize, to project a function F onto a non-degenerate representation first transform F by the symmetry operations of the group, then multiply the result by the character of the symmetry operation, and finally sum over the transformed functions.

The projection to degenerate representations is more involved. Here one needs a matrix representation to set up the projection operator. The construction of a matrix representation is usually done with the standard symmetry adapted basis, which for E_{1u} in the D_{4h} point group is (x,y). The transformation properties of this standard basis straightforwardly yield

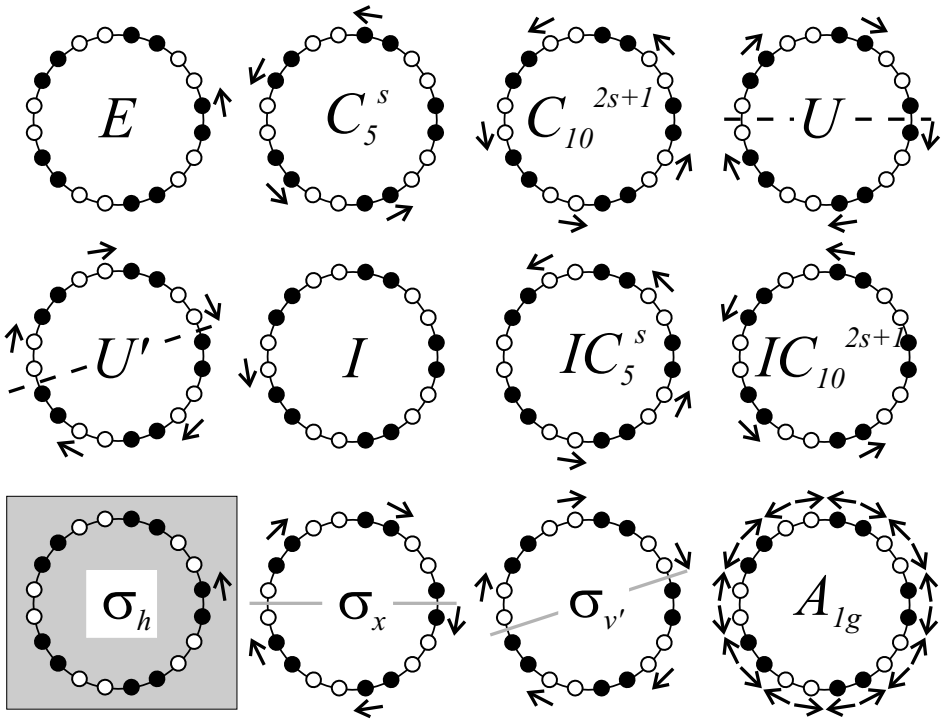

Figure 2.3: Projection to the circumferential A_{1g} displacement pattern in a (5,5) nanotube. The displacement vector of the starting atom (E symmetry operation) is successively transformed into vectors at the all the other atoms in the unit cell. To project onto the fully symmetric representation the newly obtained displacement vector is multiplied by 1, the character of A_{1g} for all symmetry operations.

a possible matrix representation, which is two-dimensional for E_{1u}. The extension of the simple vector example from the last paragraph is trivial, since the standard basis is contained in the vector representation.

To find the symmetry adapted displacement pattern a graphical version of the projection operators is particularly handy. In Fig. 2.3 I depict the unit cell of a (5,5) nanotube, where the z axis is pointing at the reader. The full and open circles represent the atoms in the two graphene sublattices, i.e., their z components are different. The atomic displacements are indicated by the arrows next to the atoms. The function F is now a circumferential displacement at the atom located at $\boldsymbol{r}_{000}$. I want to project this displacement onto the A_{1g} representation, which yields one possible phonon mode belonging to the fully symmetric representation. The sequences of pictures (excluding the last at the right lower corner) shows how the displacement vector transforms under the symmetry operations of the nanotube. In, e.g., the second picture (C_5^s) the nanotube is rotated by $s2\pi/n$ around the z axis, and the starting atom with the attached displacement vector is transformed into another black atom. The displacement vector is multiplied by $+1$ to project onto the fully symmetric representation. Note that every atom is reached twice. E.g., the starting atom is transformed

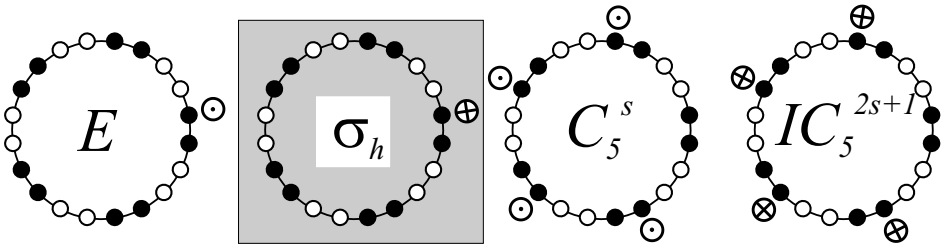

Figure 2.4: Projection of an axial A_{1g} displacement pattern. Only four selected symmetry operations are depicted. The two different symmetry operation reaching a particular atom yield opposite displacements which add up to zero. Axial modes never belong to the A_{1g} representation in armchair nanotubes.

into itself by σ_h (lower left corner); likewise C_5^s and $IC_{10}^{(2s+1)}$ yield the same atoms. The fully symmetric circumferential displacement pattern I obtain by summing over all pictures and multiplying by $1/40$. The result is shown in the last picture in the right hand lower corner. One atom is located at every atomic position; the displacement vectors are normalized. I projected an A_{1g} circumferential mode, where the atoms of the two graphene sublattices are vibrating out-of-phase. On the unwrapped nanotube this displacement corresponds to one of the doubly degenerate high-energy E_{2g} vibrations at the Γ point of graphene. The graphene frequency is around $1580\,\mathrm{cm}^{-1}$; a similar frequency is expected for the nanotube circumferential A_{1g} displacement.

Up to now the results of the projection might seem trivial; rolling up the E_{2g}-like displaced carbon sheet leads the same type of mode in a nanotube. But let us repeat the A_{1g} projection with an axial displacement. In Fig. 2.4 I show four selected symmetry operations of the (5,5) armchair tube from an axial displacement of the first atom, see E operation. The two pairs E, σ_h and $C_5^s, IC_{10}^{(2s+1)}$ yield the same transformed atoms. The horizontal mirror reflects the axial displacement into its negative, which is then multiplied by $+1$ for the A_{1g} projection. When summing over the symmetry operations the axial E and σ_h displacement cancel; the same result is obtained for all other symmetry operations that project onto the same atom, e.g., the C_5 and IC_{10}^7 pair. An axial phonon eigenvector is, therefore, never of A_{1g} symmetry in armchair carbon nanotubes. The axial high-energy mode corresponding to the circumferential eigenvector in Fig. 2.3, is of A_{1u} symmetry and hence not Raman active.

As a last example I project a circumferential displacement with the help of the $P_{1(1)}^{(E_{2g})}$ operator. I demonstrate only the E, C_5^s, and $\sigma_{x\bullet}$ symmetry operations to explain projection operators to degenerate representations. According to Eq. (2.17) I first need a possible set of transformation matrices for E_{2g}; the standard basis of E_{2g} is (x^2-y^2, xy). The matrix

representation of the identity for E_{2g} and any other two-dimensional representation is

$$D(E)^{E_{2g}} = \begin{pmatrix} 1 & 0 \\ 0 & 1 \end{pmatrix}. \tag{2.18}$$

To operate with $P_{1(1)}$ (I dropped the superscript for the representation) I first transform the atom with the displacement atom and then multiply the result by the element in the first row and first column of the matrix (2.18), i.e., by $+1$. The projection with the E operation is shown in the first picture in Fig. 2.5. The representation matrix for C_5^s is found with the help of the symmetry adapted basis (x^2-y^2, xy), the transformation properties of (x,y) under rotation, and the properties of the trigonometric functions. (x^2-y^2, xy) transforms as (x,y) under the rotation of the doubled angle

$$D(C_5^s)^{E_{2g}} = \begin{pmatrix} \cos(2s\cdot 2\pi/5) & \sin(2s\cdot 2\pi/5) \\ -\sin(2s\cdot 2\pi/5) & \cos(2s\cdot 2\pi/5) \end{pmatrix}. \tag{2.19}$$

This is a general rule; any basis of E_m transforms under the principal rotation by α as (x,y) rotated by $m\alpha$ around the z axis. The symmetry operation C_5 transforms the starting atom plus its displacement vector into the atom rotated by 72° around z. The transformed displacement vector is then multiplied by $\cos 144^\circ \approx -0.81$. This is shown in the second picture of Fig. 2.5 for $C_5^{\pm}$ and $C_5^{2\pm}$. Finally, the matrix representation of σ_{x1} is

$$D(\sigma_{x1})^{E_{2g}} = \begin{pmatrix} 1 & 0 \\ 0 & -1 \end{pmatrix}, \tag{2.20}$$

since $\sigma_{x1}(x^2-y^2) = x^2-(-y)^2 = (x^2-y^2)$ and $\sigma_{x1}(xy) = -(xy)$. The matrices of the other $\sigma_{x\bullet}$ reflections can be set up from σ_{x1} followed by C_5^s. The displacement pattern after applying $P_{1(1)}(\sigma_{x\bullet})$ is shown in the third picture in Fig. 2.5. The atomic displacement obtained by the full projection is shown in the last picture of the figure. The circumferential mode has four nodes around the circumference and corresponds to a graphene high-energy mode away from the Γ point of the graphene Brillouin zone.

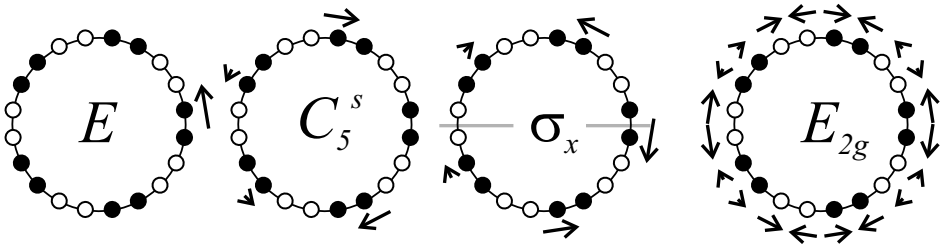

Figure 2.5: Projection of an E_{2g} circumferential displacement pattern in a (5,5) nanotube. Only the E, C_5^s, and the σ_h symmetry operations are shown. The projection operator used in this figure is $P_{1(1)}^{(E_{2g})}$. The other projection operators applied to a circumferential displacement yield either the mode degenerate to the one shown or an in-phase displacement of the two graphene sublattices.

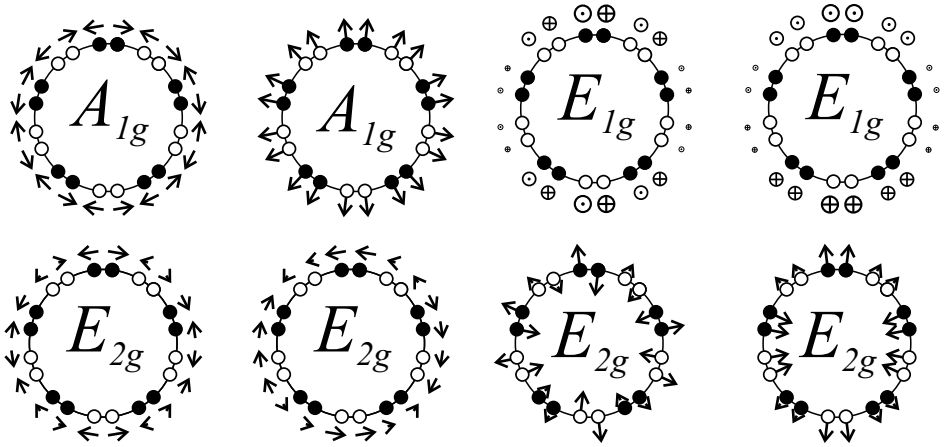

Figure 2.6: Projection of all Raman active displacement patterns in armchair nanotubes. Although group theory allows the mixing of displacements belonging to the same representation, a mixing of the different axial and circumferential displacements is unlikely because of the different force constants.

What displacement patterns do the other possible projection operators of E_{2g} yield, e.g., $P^{E_{2g}}_{1(2)}$ multiplying by the element in the first row and second column after operating with a symmetry transformation? Using $P_{1(2)}$ one finds the mode degenerate to the one in Fig. 2.5. The degenerate eigenmode is obtained from a given eigenvector by a 90° rotation of the displacement pattern around the tube. If C_4 is not a symmetry operation of the nanotube the displacement vectors must be extended to the new atomic positions. The resulting eigenvector has its nodes where the atoms are fully displaced in Fig. 2.5 and *vice versa*. The pair of projection operators $P_{2(2)}$ and $P_{2(1)}$ project onto another degenerate E_{2g} mode, namely, an in-phase displacement of the two graphene sublattices.

2.4.3. Symmetry adapted phonon eigenvectors

In Fig. 2.6 I show all circumferential, radial, and axial displacement patterns which are non-vanishing for the projections onto the Raman active representations A_{1g}, E_{1g}, and E_{2g} in armchair nanotubes. Clearly, axial eigenvectors are singled out; axial modes always belong to the E_{1g} representation in armchair tubes. This is due to the non-trivial σ_h stabilizer. Displacements within the mirror plane (circumferential and radial) must always transform as $+1$ under the horizontal reflection. This is conform with A_{1g} and E_{2g} symmetry, where a possible representation matrix is the identity matrix. In contrast, axial displacements transform as -1 under σ_h, which is only fulfilled by the E_{1g} Raman active representation. Non-degenerate representations have a constant displacement magnitude. The E_m representations have eigenvectors with $2m$ nodes around the circumference; the in-phase and out-of-phase combination of the two graphene sublattices belong to the same representation in armchair tubes.

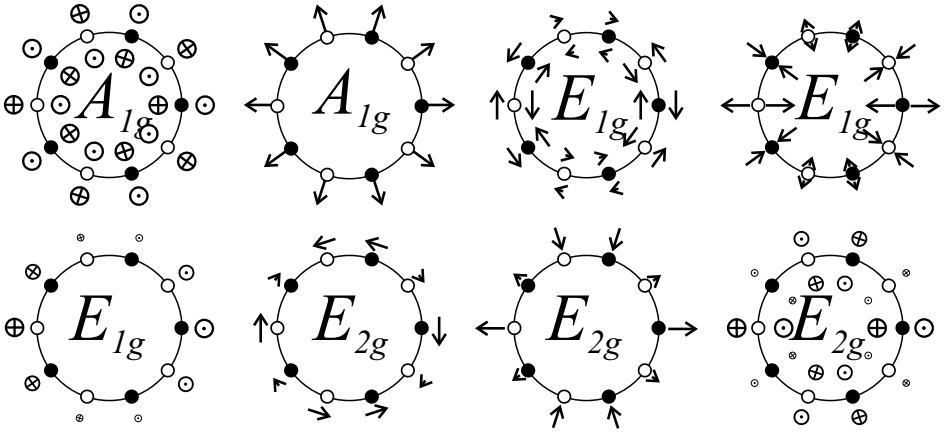

Figure 2.7: Projection of all Raman active displacement patterns in zig-zag nanotubes. Every circle corresponds to two atoms located on top of each other at different z positions. If the two atoms representated by the same circle are displaced in the same direction only one displacement arrow is shown for both.

The stabilizer in zig-zag nanotubes is the vertical reflection σ_x. The totally symmetric phonons therefore show displacements within this mirror plane, i.e., an axial high-energy vibration and the radial breathing mode. The ordering of the E_1 and E_2 symmetry modes is more complicated in zig-zag than in armchair tubes, because both plus and minus parity are possible for σ_x, see Eq. (2.20). Nevertheless, if we concentrate on the high-energy displacement patterns in Fig. 2.7 we find that the direction of the tangential displacement in zig-zag tubes is opposite to the displacement in armchair tubes. For example, the E_{1g} high-energy mode is axial in armchair but circumferential in zig-zag tubes. I summarized the displacement patterns for the high-energy modes in achiral nanotubes in Table 2.6

By symmetry the displacement patterns in armchair and zig-zag tubes belonging to the same irreducible representation can mix to form the "true" phonon eigenvector. However, a mixing of the high-energy eigenvectors shown in Fig. 2.6 and 2.7 with either in-phase displacement patterns or radial modes can safely be excluded, because of the frequencies expected for these vibrations. The frequencies of the three high-energy modes are around $1600\,\mathrm{cm}^{-1}$ similar to the graphene optical frequency. The phonon displacement with the next highest energy is the out-of-phase radial displacement around $800\,\mathrm{cm}^{-1}$ (E_{2g} and E_{1g} representation in armchair and zig-zag tubes, respectively). All other Raman active vibrations are even lower in energy. For the other displacement patterns of same symmetry the differences are not as drastic. In

	A_{1g}	E_{1g}	E_{2g}
(n,n)	circumferential	axial	circumferential
$(n,0)$	axial	circumferential	axial

Table 2.6: Displacement direction of the high-energy tangential modes in armchair and zig-zag nanotubes.

most cases, however, a relative energy splitting of 50% is predicted by zone folding. I thus expect the atomic displacements in armchair and zig-zag tubes to point either along the z axis, the circumference, or into the radial direction.

In the projection of the phonon eigenvectors the non-trivial stabilizers in armchair and zig-zag tubes played a crucial role. In particular, the transformation of a displacement pattern under reflection allowed me to distinguish the two displacement directions tangential to the nanotube wall. In chiral tubes there are no mirror planes. The atomic stabilizer is only the identity operation; the other symmetry transformations do not leave an atom invariant. Projection operators in chiral tubes yield only very general results. The fully symmetric displacements must be in-phase for the radial, but out-of-phase for the two tangential A_1 modes, because of the horizontal U axes. The E_m representations have $2m$ nodes around the circumference and both the in-phase and out-of-phase combination of the radial and the two tangential displacement directions. This yields a total of 6 modes for E_1 and E_2, respectively. Axial and circumferential eigenvectors of similar frequency now belong to the same symmetry. The phonon eigenvectors cannot be deduced from symmetry and some general assumptions on the strength of the force constants alone. The expected mixing of the two tangential displacements is verified by the first-principles calculations, which I present in Chaper 4.

2.5. Symmetry adapted electronic band structure

First work on the electronic states in carbon nanotubes concentrated on the electronic density of states in a zone-folding approximation. The starting point of these analyses was the tight-binding expression for the π orbitals of a graphene sheet, which was then modified to account for the confinement around the nanotubes circumference.[34,63,64] I introduce and discuss this approach in Chapter 5. in connection with the electronic band structure of isolated and bundled nanotubes. An early work by White and coworkers[65] and later on the studies by Damnjanović *et al.*,[45] however, used a different approach to solve the tight-binding problem for nanotubes. Instead of simplifying the problem by making reference to the graphene sheet they used the high symmetry of carbon nanotubes. With a modified group projectors technique, Damnjanović *et al.*[45,66] reduced the tight-binding Hamiltonian of the whole nanotube to a Hamiltonian for a single carbon atom, which was solved analytically. I give the analytic solution in Section 2.5.2. after an introduction to modified group projectors in the next paragraph and the following section.

Group projectors are particularly powerful for single walled carbon nanotubes because of the single orbit character of this system. In the last section I showed how the classical projectors help in finding the symmetry adapted eigenvectors for $k = 0$. The restriction to the Γ point of the Brillouin zone was necessary to work with the isogonal point group instead of the line group of nanotubes. Line and space groups are infinite and the projection operator in Eq. (2.17) sums over infinite elements. Even the restricted sum over the elements of the point group may be quite large; setting up the matrices for the degenerate representations is a tedious procedure. Modified group projectors circumvent these problems by the following ideas:

1. The projection on any irreducible representation is reduced to the projection onto the fully symmetric representation. This projection is particularly simple, because all representation matrices are equal to 1. Of course, one has to pay for a simpler projection operator, in this case by having to enlarge the Hilbert space. When dealing with a projection operator we want to find in a Hilbert space $\mathcal{H}$ the functions $|\,\mu\,\rangle$ transforming according to the irreducible representation μ. To work with the modified projector the original Hilbert space $\mathcal{H}$ is multiplied by $\mathcal{H}^{\mu^*}$. The functions $|\,\mu\,\rangle \otimes |\,\mu^*\,\rangle$, which are invariant under any symmetry operation (fixed point), reside in the product space $\mathcal{H} \otimes \mathcal{H}^{\mu^*}$.

2. What is the advantage in looking for the fixed points in the larger space than for the functions transforming as μ in the original space? Consider a group which is a product of a number of generators, i.e., a product of cyclic groups. In Section 2.2. I mentioned that the line groups of single walled nanotubes have only three or four generators. In fact, every line or space group is such a product. Let us further assume that we already found the fixed point $|x\rangle$ for all generators $\gamma_1, \gamma_2, \ldots, \gamma_n$. Then any product or power of the γ_i will have the same fixed point. To find the fixed point of the whole symmetry group in the increased auxiliary Hilbert space it is sufficient to look for the common fixed point of the generating elements. Instead of summing over all symmetry operations like for classical projection operators we need to solve only the eigenproblem with the eigenvalue 1 for the generating elements.

3. The last simplification is obtained when induced representations are used. The carbon atoms in nanotubes had their own symmetry – the stabilizer, a subgroup of the full nanotube line group. The total space of any physical problem is then spanned by the so-called interior spaces attached to the atoms. The interior space is given by the physical problem we want to study, e.g., for phonons the interior space is the three-dimensional

vector space. To construct the whole nanotube we need to give only the position of a single atom and the line group symmetry. Likewise, the total space is completely determined by the interior space of this atom. If the symmetry adapted basis or even the eigenvectors of a Hamiltonian are known for the representing atom, the basis or the eigenvector is easily found for the whole tube using symmetry operations. Note that the concept of induced representations also works for infinite representations like plane waves.

Modified group projectors allow the implementation of symmetry into computer programs. First the problem of finding the eigenvalues and eigenfunctions of a Hamiltonian is restricted to the interior space of the orbit representative. An auxiliary Hamilton operator is constructed for the space $\mathcal{H}^{\mu^*}$ and the functions $|\mu\rangle$ are required both to yield fixed points in the increased Hilbert space and to be eigenvectors of the auxiliary Hamilton operator. Finally, the induced representation in the original total Hilbert space is constructed. Modified group projectors are, in general, not intended to be used by hand like the graphical version I presented in the last section. Nevertheless, I sketch in the following how to find the E_{1g} eigenvectors of an armchair nanotube by the modified group projectors. This is meant to give a rough idea how those projectors actually work.

2.5.1. Projection operators II: Modified group projectors

In this section I again find the E_{1g} phonon eigenvectors of armchair tubes, but with the help of the modified group projectors. In Fig. 2.8 I show schematically the six projection steps,

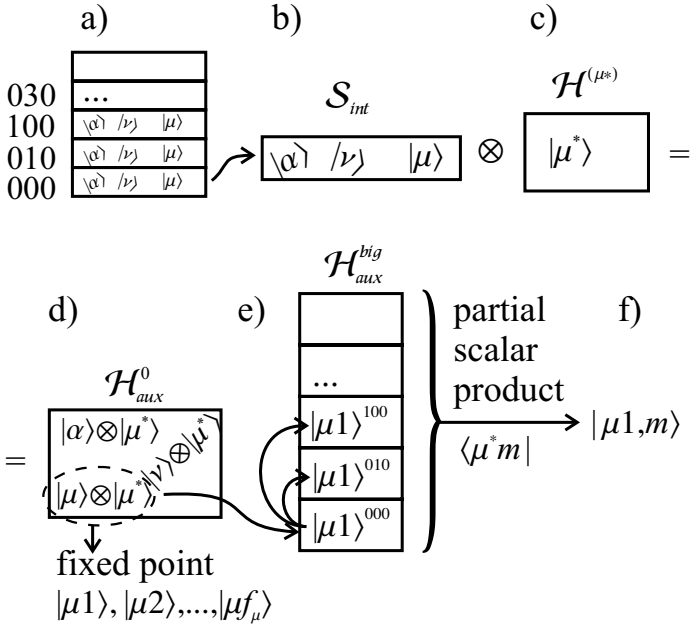

Figure 2.8: The modified group projector technique: a) The total space is divided into interior spaces of the atoms b) The interior $\mathcal{S}_{\text{int}}$ is spanned by $|\alpha\rangle^0, |\nu\rangle^0, |\mu\rangle^0, \ldots$ c) To construct the fixed point in the auxiliary space the functions in $\mathcal{S}_{\text{int}}$ are multiplied by $|\mu^*\rangle$. d) The auxiliary space $\mathcal{H}^0_{\text{aux}}$ of the representing atom contains the fixed points $|\mu 1\rangle^0, |\mu 2\rangle^0, \ldots, |\mu f_\mu\rangle^0$ e) A fixed point $|\mu t_\mu\rangle$ of the total auxiliary space $\mathcal{H}^{\text{big}}_{\text{aux}}$ is induced with the operators switching between the interior space. f) The symmetry adapted basis $|\mu t_\mu, m\rangle$ is the partial scalar product $\langle\mu^* m|\mu t_\mu\rangle$.

which I first describe in general and then apply to my example. Fig. 2.8a) depicts the total space $\mathcal{H}$ of the physical problem. The Hilbert space is divided into an infinite number of interior spaces (rectangles) each belonging to a different atom in the nanotube (or any other system). The interior space $\mathcal{S}_{\text{int}}$ of the representing atom is singled out in Fig. 2.8b). Since nanotubes are single orbit systems one interior space represents the total space. For, e.g., phonon eigenvectors the interior is a three-dimensional vector space. $\mathcal{S}_{\text{int}}$ is spanned by the functions $|\alpha\rangle^0, |\nu\rangle^0, |\mu\rangle^0 \ldots$ transforming as the irreducible representations $\alpha, \nu, \mu \ldots$ of the nanotube symmetry group. With the modified group projector I want to find the functions $|\mu\rangle$ transforming as μ. I first construct the auxiliary space $\mathcal{H}^0_{\text{aux}} = \mathcal{S}_{\text{int}} \otimes \mathcal{H}^{(\mu*)}$ with the functions $|\alpha\rangle^0 \otimes |\mu^*\rangle, |\nu\rangle^0 \otimes |\mu^*\rangle, |\mu\rangle^0 \otimes |\mu^*\rangle, \ldots$ as shown in Fig. 2.8c) and d). Only $|\mu\rangle \otimes |\mu^*\rangle$ is left invariant under any symmetry operation of the group. The generally reducible representation in $\mathcal{H}^0_{\text{aux}}$ constructed from the representation D_δ in the interior space is

$$\gamma^\mu(\boldsymbol{S}) = D_\delta(\boldsymbol{S}) \otimes D^{(\mu*)}(\boldsymbol{G} \downarrow \boldsymbol{S}) \tag{2.21}$$

for the example of achiral nanotubes and the vector representation

$$\gamma^\mu(C_{1h}) = D_{\text{vec}}(C_{1h}) \otimes D^{(\mu*)}(\boldsymbol{G} \downarrow C_{1h}). \tag{2.22}$$

$\boldsymbol{S}$ is the stabilizer of the atoms equal to $C_{1h} = \{E, \sigma\}$ in armchair or zig-zag nanotubes. The symbol $(\boldsymbol{G} \downarrow \boldsymbol{S})$ denotes that the full symmetry group $\boldsymbol{G}$ is restricted to $\boldsymbol{S}$, i.e., only those symmetry operations belonging to $\boldsymbol{S}$ are considered. The trace of $\gamma^\mu(\boldsymbol{S})$ is equal to the frequency number f_μ, the number of times the irreducible representation μ appears in the reducible representation D_δ. The eigenvectors of $\gamma^\mu(\boldsymbol{S})$ to the eigenvalue 1 are the fixed points $|\mu 1\rangle^0, |\mu 2\rangle^0, \ldots, |\mu f_\mu\rangle^0$ we are looking for.

The fixed points $|\mu t_\mu\rangle^0$ of the interior auxiliary space $\mathcal{H}^0_{\text{aux}}$ of the representing atom 0 are now expanded to the total auxiliary space $\mathcal{H}^{\text{big}}_{\text{aux}}$. A fixed point $|\mu t_\mu\rangle$ in $\mathcal{H}^{\text{big}}_{\text{aux}}$ is obtained with the transformation operator $|\mu t_\mu\rangle = B^\mu |\mu t_\mu\rangle^0$, where

$$B^\mu = \frac{1}{\sqrt{Z}} \sum_t E^t_0 \otimes \beta^\mu_t = \frac{1}{\sqrt{Z}} \sum_t E^t_0 \otimes I_\delta \otimes D^{(\mu*)}(\mathcal{Z}_t). \tag{2.23}$$

The sum in Eq. (2.23) is over all elements of the transversal. The transversal is the group of symmetry operations $\mathcal{Z}_t$ transforming the atoms of the same orbit into each other; Z is the order of the transversal. The operator $E^t_0 \otimes \beta^\mu_t$ transforms the fixed point $|\mu t_\mu\rangle$ of the representing atom into the fixed point $|\mu t_\mu\rangle^t$ of another atom t. E^t_0 literally switches between the atoms; it is a matrix with the $0t$'th element equal to 1, all other are zero. $\beta^\mu_t = I_\delta \otimes D^{(\mu*)}(\mathcal{Z}_t)$ takes care of the symmetry in the auxiliary Hilbert space. The identity matrix I_δ

of the interior space is used only to enlarge the dimension. The sum over the fixed point in all interior spaces t is the fixed point in the total auxiliary space $\mathcal{H}_{\text{aux}}^{\text{big}}$. The action of B^{μ} is shown in Fig. 2.8e). Finally, in Fig. 2.8f) the symmetry adapted basis in the original Hilbert space $\mathcal{H}$ is extracted with the help of the partial scalar product

$$\langle \mu^* m | \mu\, t_\mu \rangle = \langle \mu^* m | (|\, \mu\, t_\mu n \rangle \otimes |\, \mu^* m \rangle) = |\, \mu\, t_\mu m \rangle. \tag{2.24}$$

The vectors $|\, \mu\, t_\mu m \rangle$ in the total Hilbert space $\mathcal{H}$ is the m'th component of the t_μ'th eigenvector transforming according to the irreducible representation μ.

After discussing the modified group projectors in a general way I now apply the method to the problem of finding the phonon eigenvectors transforming as E_{1g} in a (5,5) armchair nanotube. As already mentioned the interior space for this physical problem is the three-dimensional vector space, the reducible representation is the vector representation, and the stabilizer in armchair nanotubes is C_{1h}. With the standard basis of E_{1g} (xz, yz) Eq. (2.21) reads

$$\begin{aligned}
\gamma^{E_{1g}}(C_{1h}) &= D_{vec}(C_{1h}) \otimes D^{(E_{1g})}(G \downarrow C_{1h}) && (2.25)\\
&= \frac{1}{2}\Bigg[\underbrace{\begin{pmatrix} 1 & & \\ & 1 & \\ & & 1 \end{pmatrix}}_{D_{vec}(E)} \otimes \underbrace{\begin{pmatrix} 1 & \\ & 1 \end{pmatrix}}_{D_{E_{1g}}(E)} + \underbrace{\begin{pmatrix} 1 & & \\ & 1 & \\ & & -1 \end{pmatrix}}_{D_{vec}(\sigma_h)} \otimes \underbrace{\begin{pmatrix} -1 & \\ & -1 \end{pmatrix}}_{D_{E_{1g}}(\sigma_h)} \Bigg] \\
&= \frac{1}{2} \begin{pmatrix} 0 & & & & & \\ & 0 & & & & \\ & & 0 & & & \\ & & & 0 & & \\ & & & & 2 & \\ & & & & & 2 \end{pmatrix} && (2.26)
\end{aligned}$$

The trace $Tr[\gamma^{E_{1g}}(C_{1h})] = 2$, i.e., two phonons in armchair tubes are of E_{1g} symmetry as already obtained in Section 2.4.1. The two eigenvectors $(0,0,0,0,1,0)$ and $(0,0,0,0,0,1)$ are the fixed points in the auxiliary space $\mathcal{H}_{\text{aux}}^{0}$. In the following I consider only the first fixed point for simplicity; its vector can be expressed as

$$|\, E_{1g} 1 \rangle^0 = \begin{pmatrix} 0 \\ 0 \\ 1 \end{pmatrix} \otimes \begin{pmatrix} 1 \\ 0 \end{pmatrix} + \begin{pmatrix} 0 \\ 0 \\ 0 \end{pmatrix} \otimes \begin{pmatrix} 0 \\ 1 \end{pmatrix} = z_0 \otimes \begin{pmatrix} 1 \\ 0 \end{pmatrix}, \tag{2.27}$$

where z_0 stands for the z displacement component of the representing atom. The two vectors $(1,0)$ and $(0,1)$ are a basis of E_{1g} in the nanotube's symmetry group. Note that we already found that E_{1g} modes are always axial in armchair nanotubes. Only the z component in the interior space of the representing atom transforms as E_{1g}. Since no line group symmetry

operation transforms the principal axis in the x or y axis, the eigenvector for the whole tube will be axially as well. I did not specify the particular armchair nanotube up to now. The finding of only axial E_{1g} eigenvectors is therefore valid for any armchair nanotube.

With the fixed point in the interior space of the representing atom I have to induce the fixed point in the total auxiliary space $\mathcal{H}_{\mathrm{aux}}^{\mathrm{big}}$. The transversal for armchair nanotubes is $\boldsymbol{T}_q^w \boldsymbol{D}_n = \boldsymbol{T}_{2n}\boldsymbol{D}_n$. To apply the transformation operator $B^{E_{1g}}$ to the first fixed point $|E_{1g}1\rangle^0$ I need an E_{1g} matrix representation for the generators of the transversal and its combinations

$$C_n = \begin{pmatrix} \cos 2\pi/n & \sin 2\pi/n \\ -\sin 2\pi/n & \cos 2\pi/n \end{pmatrix} \quad (C_{2n}|\tfrac{a}{2}) \overset{k=0}{=} \begin{pmatrix} \cos \pi/n & \sin \pi/n \\ -\sin \pi/n & \cos \pi/n \end{pmatrix} \quad U = \begin{pmatrix} -1 & 0 \\ 0 & 1 \end{pmatrix}$$

$$(C_n^s C_{2n}^l U^u | l\tfrac{a}{2}) \overset{k=0}{=} \begin{bmatrix} (-1)^u \cos \pi \frac{2s+l}{n} & \sin \pi \frac{2s+l}{n} \\ -(-1)^u \sin \pi \frac{2s+l}{n} & \cos \pi \frac{2s+l}{n} \end{bmatrix}. \tag{2.28}$$

In Eq. (2.27) I separated the eigenvector $|E_{1g}1\rangle^0$ into a sum of two direct products. Therefore we can skip the identity representation I_δ appearing in β_t^μ in Eq. (2.23)

$$\begin{aligned} |E_{1g}1\rangle = \big[&E_0^{000} \otimes \beta_{000}^{E_{1g}} + E_0^{010} \otimes \beta_{010}^{E_{1g}} + E_0^{100} \otimes \beta_{100}^{E_{1g}} + E_0^{030} \otimes \beta_{030}^{E_{1g}} + E_0^{200} \otimes \beta_{200}^{E_{1g}} + \\ &+ E_0^{050} \otimes \beta_{050}^{E_{1g}} + \cdots + E_0^{001} \otimes \beta_{001}^{E_{1g}} + E_0^{101} \otimes \beta_{101}^{E_{1g}} \ldots \big] \big[z_0 \otimes \left(\begin{smallmatrix} 1 \\ 0 \end{smallmatrix}\right)\big] \end{aligned}$$

with $(A \otimes B)(A' \otimes B') = (AA') \otimes (BB')$ and $\mathrm{c}\, l = \cos(l \cdot 2\pi/n)$, $\mathrm{s}\, l = \sin(l \cdot 2\pi/n)$

$$\begin{aligned} = z_{000} \otimes \left(\begin{smallmatrix} 1 \\ 0 \end{smallmatrix}\right) + z_{010} \otimes \left(\begin{smallmatrix} \mathrm{c}\,1 \\ -\mathrm{s}\,1 \end{smallmatrix}\right) + z_{100} \otimes \left(\begin{smallmatrix} \mathrm{c}\,2 \\ -\mathrm{s}\,2 \end{smallmatrix}\right) + z_{030} \otimes \left(\begin{smallmatrix} \mathrm{c}\,3 \\ -\mathrm{s}\,3 \end{smallmatrix}\right) + z_{200} \otimes \left(\begin{smallmatrix} \mathrm{c}\,4 \\ -\mathrm{s}\,4 \end{smallmatrix}\right) \\ + z_{050} \otimes \left(\begin{smallmatrix} \mathrm{c}\,5 \\ -\mathrm{s}\,5 \end{smallmatrix}\right) + \cdots + (-z_{001}) \otimes \left(\begin{smallmatrix} -1 \\ 0 \end{smallmatrix}\right) + (-z_{101}) \otimes \left(\begin{smallmatrix} -\mathrm{c}\,1 \\ \mathrm{s}\,1 \end{smallmatrix}\right) \ldots \end{aligned} \tag{2.29}$$

The interior coordinate system is transformed together with the atoms. Therefore the z component of the displacement changes sign under the U operation, which I indicated by the minus sign at z for the symmetry operations in Eq. (2.29) containing U (the last two). The vector in Eq. (2.29) is the fixed point in the total auxiliary Hilbert space $\mathcal{H}_{\mathrm{aux}}^{\mathrm{big}}$. To finally find the phonon eigenvectors $|\mu 1m\rangle = |E_{1g}1,1\rangle$ and $|E_{1g}1,2\rangle$ transforming as E_{1g} I take the partial scalar product and obtain

$$\begin{aligned} |E_{1g}1,1\rangle &= \langle E_{1g}^* 1 | E_{1g}1\rangle = z_{000} + \mathrm{c}\,1 \cdot z_{010} + \\ &\quad + \mathrm{c}\,2 \cdot z_{100} + \mathrm{c}\,3 \cdot z_{030} + \mathrm{c}\,4 \cdot z_{200} + \mathrm{c}\,5 \cdot z_{050} + \ldots z_{001} + \mathrm{c}\,1 \cdot z_{101} \ldots \\ |E_{1g}1,2\rangle &= \langle E_{1g}^* 2 | E_{1g}1\rangle = -\mathrm{s}\,1 \cdot z_{010} - \mathrm{s}\,2 \cdot z_{100} - \\ &\quad - \mathrm{s}\,3 \cdot z_{030} - \mathrm{s}\,4 \cdot z_{200} - \mathrm{s}\,5 \cdot z_{050} + \cdots + \mathrm{s}\,1 \cdot z_{101} \ldots \end{aligned} \tag{2.30}$$

Fig. 2.9 shows the two phonon eigenvectors $|E_{1g}1,1\rangle$ (left) and $|E_{1g}1,2\rangle$ (right), which are degenerate. The displacement pattern to the left can already be found on page 31 in the

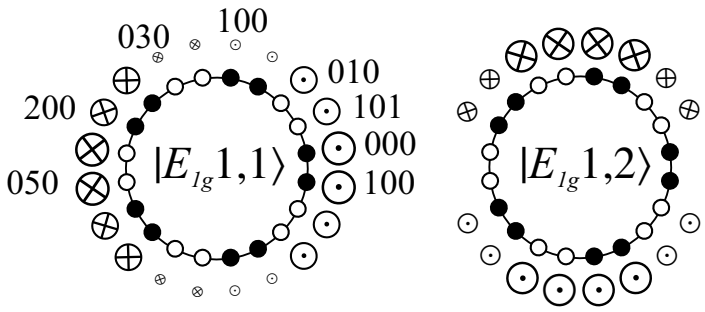

Figure 2.9: Degenerate E_{1g} phonon eigenvectors in armchair nanotubes obtained with the modified group projector technique. For the transformation explicitly written in Eq. (2.30) the atoms were labeled correspondingly in the left hand tube.

upper right corner of Fig. 2.6, where the same eigenvector was projected with the help of the graphical projectors. It is a mode with two nodes around the circumference and an in-phase displacement of the two graphene sublattices. In an isolated, finite molecule these eigenvectors are a rotation around the x and y axis. The projection of the second fixed point of $\gamma^{E1g}(C_{1h})$ yields the two degenerate high-energy modes of E_{1g} symmetry. Similarly, the other results of Section 2.4.2. can also be obtained with the modified group projector technique. In chiral nanotubes group projectors *per se* are not suited for finding the eigenvectors, because of the trivial stabilizer in this tubes. After introducing the technique in this section I now turn to the projection of the electronic states in carbon nanotubes.

2.5.2. Tight-binding electronic dispersion

Solving the Hamiltonian for the electronic states in carbon nanotubes within the tight-binding or any other approximation is quite involved, because of the many atoms in the unit cell. Throughout this chapter, however, we saw how much the vibrational properties of nanotubes are simplified by their symmetry. Essentially the same methods can be applied to the electronic states as well. Modified group projectors also help in solving an Hamiltonian. Instead of projecting to the eigenvalue $+1$ as for finding the symmetry adapted displacement pattern, the functions are additionally required to be the eigenvectors of an auxiliary Hamilton operator $H_\mu = H \otimes I_\mu$, where I_μ is the identity representation in $\mathcal{H}^{(\mu *)}$. As described in the previous section the auxiliary operator is then restricted to the interior space of the representing atom, its eigenvalues yield the electronic dispersion, and its eigenfunctions induce the irreducible representations for the whole nanotube.

The tight-binding Hamiltonian assumes only nearest neighbor interaction with the same carbon-carbon interaction energy γ_0 for the three neighbors. The latter assumptions neglects the curvature of the graphene sheet; the extension to different γ_0 is given in Ref. 45. Moreover, only the π orbitals of graphene are considered as I dicuss in Chapter 5. The auxiliary

Hamiltonian in the interior space of the representing atom is

$$H_{\mu}^{\downarrow} = \gamma_0 \sum_{i=0}^{3} D^{(\mu*)^{\dagger}}(\mathcal{Z}_i), \tag{2.31}$$

where i runs over the nearest neighbors of the representing atom. With the symmetry adapted basis $|k,m,\Pi\rangle$, where Π stands for the parities and is only defined at high-symmetry points of the Brillouin zone, the Hamiltonian in Eq. (2.31) is straightforwardly solved for tubes of any chirality.

$$\varepsilon_m(k_z) = \pm\gamma_0\sqrt{\textstyle\sum_{i=1}^{3}(1+\cos\psi_i)} \qquad \text{(chiral tubes} \quad 2.32\text{a)}$$

with

$$\psi_1 = -ka\frac{n_2}{q} + 2\pi m\frac{2n_1+n_2}{qn\mathcal{R}}, \quad \psi_2 = ka\frac{n_1}{q} + 2\pi m\frac{n_1+2n_2}{qn\mathcal{R}}, \text{ and } \quad \psi_3 = \psi_2 - \psi_1 \tag{2.32b}$$

$$\varepsilon_m(k_z) = \pm\gamma_0\sqrt{1+4\cos\frac{ka}{2}\cos\frac{m\pi}{n}+4\cos^2\frac{ka}{2}} \qquad \text{(armchair tubes} \quad 2.32\text{c)}$$

$$\varepsilon_m(k_z) = \pm\gamma_0\sqrt{1+4\cos\frac{ka}{2}\cos\frac{m\pi}{n}+4\cos^2\frac{m\pi}{n}} \qquad \text{(zig-zag tubes} \quad 2.32\text{d)}$$

Note that the two limiting cases of armchair and zig-zag tubes are contained in the expression for chiral in tubes in Eq. (2.32) by setting, e.g., for armchair tubes $n_1 = n_2 = n$. Most of the electronic states belong to the doubly degenerate E irreducible representation in chiral nanotubes. At $k = 0, \pi$ and some selected m also the non-degenerate representations appear, but their energies are far beyond the visible and will not be considered here. In armchair and zig-zag tubes the electronic states at the Γ point are doubly degenerate as well except for $m = 0, n$. For $k \neq 0, \pi$ the electronic bands are, in general, four-fold degenerate in achiral nanotubes. For a compilation of the electronic symmetries in achiral and chiral nanotubes see Table 2 in Ref. 45.

As two examples of the electronic band structure of achiral nanotubes I show in Fig. 2.10 the bands of a metallic (11,11) and a semiconducting (19,0) nanotube. The plots were obtained from Eq. (2.32) with $\gamma_0 = 2.75\,\text{eV}$. The bands lying closest to the Fermi level are labeled by their irreducible representation at the Γ point. The vanishing gradients of the electronic bands at $k = 0$ and around $2\pi/3$ in the armchair and $k = 0$ in the zig-zag tubes, which yield the singularities in the density of states, are nicely seen. In armchair nanotubes of reasonable size the singularities for transitions in the visible are well separated in energy and are associated with different k vectors. The situation is different in the zig-zag tubes, with Γ as the only critical point in this energy range. In general, both in chiral and achiral tubes the k vectors of

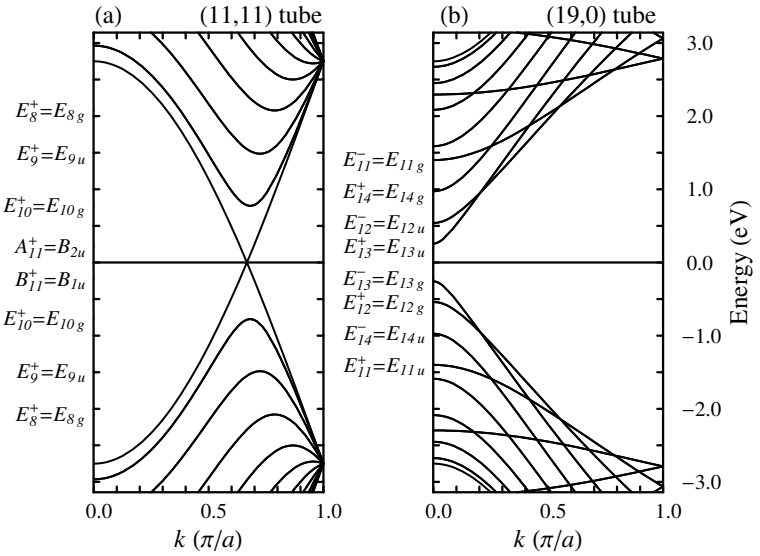

Figure 2.10: Bandstructure of an $(11,11)$ armchair and an $(19,0)$ zig-zag nanotubes. The two bands crossing at the Fermi level in the armchair tubes are of E_{11}^B and E_{11}^A symmetry, the superscripts specify the B_{11}^+ and A_{11}^+ representation at the Γ point, respectively; the other armchair bands belong to the G_m representation. The labels at the left axis name the irreducible representation at the Γ point for the first singularities, which are between $2\pi/3a < k_s < \pi/a$ in the armchair and at $k = 0$ in the zig-zag tubes.

vanishing slope are determined by the parameter $\mathcal{R} = 3$ for tubes with $(n_1 - n_2)/3n$ integer and $\mathcal{R} = 1$ otherwise, see Section 2.1.[55] If $\mathcal{R} = 3$ as in all armchair and most metallic chiral nanotubes the singularities associated with visible optical transitions arise from k vectors between 2/3 and the boundary of the nanotube Brillouin zone. In contrast, all semiconducting chiral tubes, all zig-zag tubes, and some metallic chiral nanotubes as, e.g., the (12,6) tube, belong to the class with $\mathcal{R} = 1$. Then only Γ and X are critical points with a large electronic density of states. This interesting difference in the electronic band structure will play a major role in defect induced Raman scattering, which I discuss in connection with the D mode in carbon nanotubes and graphite in Chapter 6.. We will see there that only tubes with $\mathcal{R} = 3$ are expected to show a double resonant Raman process leading to the experimental observation of this mode. I discuss the symmetries of the electronic bands in more detail in connection with the Raman selection rules in the next chapter. Here I only stress that optical transitions between the two bands crossing at the Fermi level are forbidden by selection rules for any polarization of the light.

The band structure is more complicated in chiral nanotubes as exemplified in Fig. 2.11a) for a metallic $(15,6)$ and 2.11b) for a semiconducting $(12,8)$ tube. The (15,6) tube belongs again to the class $\mathcal{R} = 3$ and correspondingly the valence and conduction band cross at $k_F \approx 2\pi/3$ in the homogeneous tight-binding approximation. The crossing of the two bands is, however, forbidden by symmetry; the bands show a level anticrossing and develop a small singularity at the Fermi energy if the curvature is included in the calculation.[55] Many of the differences in the band structure of achiral and chiral nanotubes arise because of the absence of mirror planes and the much smaller Brillouin zone in chiral nanotubes. The missing reflection symmetries split the four-fold degenerate bands in achiral nanotubes to

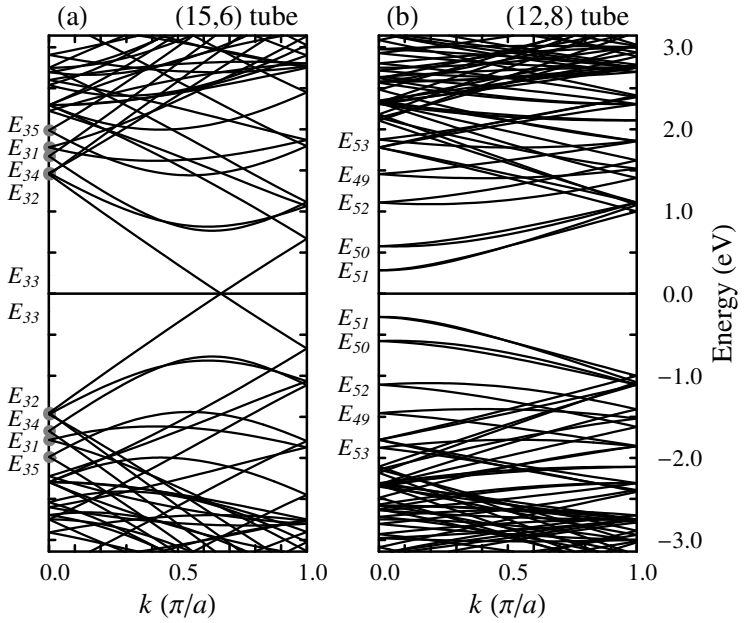

Figure 2.11: Bandstructure of a (15,6) metallic ($d = 1.47\,\mathrm{nm}$) and a (12,8) semiconducting ($d = 1.37\,\mathrm{nm}$) chiral tube. In the metallic tube the bands cross at $k = 2\pi/3a$, because $\mathcal{R} = 3$. The energy of the bands corresponding to the first four singularities in (a) are marked by gray dots; the symmetries in (a) for $E > 0$ refer to the downbending band, *vice versa* for $E < 0$.

two doubly degenerate E bands. This is nicely seen in Fig. 2.11, in particular around the $2\pi/3$ singularities in the metallic and the Γ point in the semiconducting tubes. The splitting of the metallic singularities was already predicted from the zone-folding approximation when the higher-order terms of the graphene tight-binding structure are included.[36] The effect of the larger translational periodicity in chiral nanotubes can also be observed in the figure. I selected here two chiral examples with a large greatest common divisor n – otherwise the band structure plot would be almost black on this scale. The periodicity along the nanotube axis is 3.6 times larger in the (15,6) than in the (11,11) tube; correspondingly the Brillouin zone is smaller by the same factor. When following, e.g., the E_{32} band in Fig. 2.11a) across the two zone boundaries it becomes apparent that an electronic dispersion similar to the G_{10} in Fig. 2.10a) is obtained by unfolding the dispersion to an extended zone scheme.

2.6. Summary

The high-symmetry of single walled carbon nanotubes greatly helps in studying and predicting their physical properties. In this chapter I introduced line groups to describe the symmetries of one-dimensional systems. Except for $(n,0)$ zig-zag and (n,n) armchair nanotubes with the same n every nanotube belongs to a symmetry group of its own. The isogonal point groups of carbon nanotubes are given by q, the number of graphene cells in the unit cell of the nanotubes, namely, $D_{qh} = D_{2nh}$ for achiral and D_q for chiral tubes. After discussing the symmetry properties of carbon nanotubes I found the phonon displacement patterns and the electronic bands of single walled nanotubes using two different projector techniques.

The graphical version of the projection operators is particularly helpful when looking for the phonon eigenvectors of a system. Using this "arrow drawing" technique I showed that the atomic displacement for vibrations in achiral tubes is fixed by their mirror symmetries. The large difference between the tangential and radial force constants, moreover, results in exclusively radial, circumferential, or axial phonon eigenvectors. Chiral nanotubes do not have such mirror planes in their symmetry groups and, even more importantly, their stabilizer is only the trivial identity operation. Their phonon modes are not given by symmetry, but need to be calculated as the eigenvalues of the dynamical matrix. I expected the high-energy modes to be of mixed circumferential and axial character; a topic which is further investigated with high-pressure experiment and *ab initio* calculations in Chapter 4.

The modified group projectors is a projector technique developed only recently by Damnjanović *et al.*[45,66] Problems of the classical projectors arising from infinite symmetry groups or infinite-dimensional representations are solved by this method. The modified group projectors together with a homogeneous tight-binding approximation yield a simple expression for the electronic bands of carbon nanotubes. I presented the electronic dispersion of two achiral and chiral nanotubes and pointed out the fundamental differences and similarities in their electronic dispersion. The most prominent features in the electronic dispersion are the points of vanishing slope, which give rise to the typical singularities in the one-dimensional density of states. These points are at $k = 0$ in semiconducting, zig-zag, and some metallic chiral nanotubes, and around $2/3$ of the Brillouin zone in armchair and most metallic chiral tubes. This peculiar difference is important for the defect induced double-resonant Raman process, which will be discussed in Chapter 6.

Chapter 3

Raman Scattering and Tensor Invariants

When a new material is discovered – or a long-known material suddenly turns out to be of great physical interest – Raman spectroscopy is usually among the first experimental techniques used for characterization. Raman spectra can be recorded on small and poor samples, but provide deep insight into the physical properties as well as the material quality. During the last decade Raman spectrometers got rather cheap and easy to handle, in particular, the single-grating spectrometers working with a notch filter. Papers concentrating on preparation methods very often contain figures with a Raman spectrum comparing them with known spectra of the same material. On the other hand, the Raman process yields information not only on the vibrational properties. To name only a few examples, resonant scattering is deeply influenced by the electronic states of a system, phase transitions are nicely studied by recording the Raman spectra, and experiments under external pressure allow us to understand the elastic properties as well. Probably the most important question when trying to interpret the Raman spectrum of a new material is the experimentally observed symmetry of the modes. If a single crystal is at hand, the exact structure of the material is known, and the Raman process is essentially non-resonant, determining the mode symmetry is straightforward, although it may still be involved experimentally. If either of these conditions fail, however, a more detailed analysis has to be performed. I show in this chapter how the symmetry of the Raman scattered light can be measured on unoriented samples. The strongly anisotropic Raman tensor I found experimentally on nanotubes points to a scattering process which is dominated by the electronic and optical properties.

The chapter starts with a very brief introduction to the Raman effect in Section 3.1. concentrating on the selection rules and the Raman tensors for the nanotube symmetry group. How to deduce the phonon symmetry from unoriented crystals is explained in Section 3.2. In Section 3.3. I discuss my experimental setup, which was also used for the excitation en-

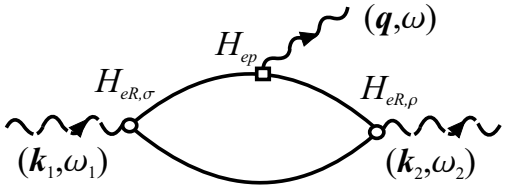

Figure 3.1: Feynman diagram of a first-order Raman process. An incoming photon with frequency ω_1 and wave vector $\boldsymbol{k}_1$ excites an electron-hole pair. The electron is then scattered inelastically emitting a phonon with frequency ω and wave vector $\boldsymbol{q}$. The electron-hole pair recombines under the emission of the scattered photon $(\boldsymbol{k}_2, \omega_2)$. Modified figure from Ref. 67.

ergy dependent measurements in Chapter 6. The results for the tensor invariants and the symmetry of the Raman scattered light in single and multiwall nanotubes are presented in Section 3.4. Additionally, I discuss *ab initio* calculations of the optical absorption spectra and the symmetry properties of the *D* mode in graphite.

3.1. Selection rules

First order Raman scattering is a three step process as shown in Fig. 3.1. The absorption of an incoming photon with a frequency ω_1 creates an electron-hole pair, which then scatters inelastically under the emission of a phonon with frequency ω, and finally recombines and emits the scattered photon ω_2.[67,68] In this work I concentrate on resonant scattering and may thus neglect all other possible time orders of the Raman process. I have to include, however, the details of the electron-photon and the electron-phonon coupling. Let the polarization of the incoming (outgoing) light be σ (ρ) and the Hamiltonian for electron-radiation interaction $H_{eR,\sigma}$ ($H_{eR,\rho}$). The electron-phonon coupling is described by H_{ep}. The matrix element $K_{2f,10}$ of the process in Fig. 3.1 is then[69]

$$K_{2f,10} = \sum_{a,b} \frac{\langle \omega_2, f, i | H_{eR,\rho} | 0, f, b \rangle \langle 0, f, b | H_{ep} | 0, 0, a \rangle \langle 0, 0, a | H_{eR,\sigma} | \omega_1, 0, i \rangle}{(E_1 - E^e_{ai} - i\gamma)(E_1 - \bar{h}\omega - E^e_{bi} - i\gamma)}, \tag{3.1}$$

where $|\omega_1, 0, i\rangle$ denotes the state with an incoming photon of energy $E_1 = \bar{h}\omega_1$, the ground state 0 of the phonon (no phonon excited), and the ground electronic state i; the other states are labeled accordingly. The initial and the final electronic states are assumed to be the same; the sum is over all possible intermediate electronic states a and b. The final phononic state is denoted by f. The E^e_{ai} are the energy difference between the electronic states a and i; the lifetime of the excited states γ was taken to be the same.[67,69]

Right now, I am only interested in selection rules, i.e., I am asking whether the matrix element in Eq. (3.1) is zero or not. The quickest way to work out the selection rules for Raman scattering in carbon nanotubes is to use the conservation of the quasi-angular momentum

Scattering geometry	Phonon symmetries	
	line group notation	molecular notation
(z,z)	${}_0A_0^+$	A_{1g}
(x,z), (z,x), (y,z), (z,y)	${}_0E_1^-$	E_{1g}
(x,x), (y,y)	${}_0A_0^+$, ${}_0E_2^+$	A_{1g}, E_{2g}
(x,y), (y,x)	${}_0B_0^+$, ${}_0E_2^+$	A_{2g}, E_{2g}

Table 3.1: Phonon symmetries conserving the angular momentum quantum number and the σ_h parity in the Raman configurations. In chiral tubes σ_h is not a symmetry operation; the superscript $\pm$ and the subscript g are omitted.

m and the parity σ_h (the latter only for achiral tubes). If I treat m as a conserved quantum number I implicitly assume that no Umklapp processes occur in the Raman transition.[51] An extension to more general transitions, in particular in defect induced scattering, will be done in Chapter 6.[21] The Raman tensors found by the more general treatment are, however, essentially the same as those I give below. The eigenstates in Eq. (3.1) are composed of an electronic, a vibronic, and a photonic part. The quantum numbers are conserved for the total eigenstate. Since the initial and final electronic state is the same – I exclude vibro-electronic coupling[70,71] – $\Delta m = 0$ and $\sigma_h = +1$ for the electronic part. A z polarized optical transition conserves the angular momentum $\Delta m = 0$ and changes the mirror parity $\sigma_h = -1$; for transitions polarized perpendicular to the tube axis $\Delta m = \pm 1$ and $\sigma_h = +1$.[50] The change in angular momentum and parity induced by the absorption and emission of a photon must be compensated by the phonon. For z polarized incoming and outgoing light – (zz) configuration – the angular momentum and the parity are fully conserved by the photons. Therefore, only $A_0^+ = A_{1g}$ phonons are allowed in this scattering configuration. In (xz) or (zx) scattering geometry $\Delta m_{\text{photon}} = \pm 1$ and $\sigma_{h,\text{photon}} = -1$ giving rise to $E_1^- = E_{1g}$ phonon scattering. The selection rules are summarized in Table 3.1 for all possible scattering configurations.

How do the Raman tensors of the modes given in Table 3.1 look? Again, this question can be answered by group projector techniques. Nevertheless, an inspection of the table together with symmetry arguments is sufficient to find the general form of the Raman tensors. The A_{1g} representation appears only for parallel polarizations, hence all non-diagonal elements of its Raman tensor are zero. Various symmetry operations transform the xx and the yy components into each other in nanotubes. To obtain an A_{1g} representation these two entries of the tensor must be the same. The zz component, on the other hand, is linearly independent, because all line group symmetry operations preserve the z axis. I thus obtained $diag[a,a,b]$, i.e., a purely diagonal matrix with $\alpha_{xx} = \alpha_{yy} = a$ and $\alpha_{zz} = b$, see Table 3.2, as a general A_{1g} tensor of single walled nanotubes. E_{1g} can only have xz, zx, yz, zy non-zero elements. Again xz and yz transform into each other under the symmetry operations of the tubes and are not

independent, whereas xz and zx are decoupled. Similarly, the other Raman tensors can be found. I list them in Table 3.2. With a single crystal of carbon nanotubes, aligned not only along the z axis, but in the plane perpendicular to z as well, the phonon symmetries and the relative values of the tensor elements in Table 3.2 could be measured using the well-known relation for the intensity in (e_s, e_i) configuration $I \sim |e_s \Re e_i|$, where $\Re$ is the Raman tensor. At present nanotube single crystals are not available. Samples with a partial alignment along the z axis or dilute nanotube samples on different substrates have been reported recently and used for Raman experiments.[15,72–75] The symmetries of the Raman scattered light can also be studied on unoriented samples by measuring the Raman tensor invariants,[76,77] which is the topic of the next section.

3.2. Tensor invariants

As I discussed at the end of the last section determining the symmetry of the Raman scattered light on a single crystal is straightforward from an experimental point of view. The interpretation of the results, however, may still be difficult under resonant conditions or with an unknown crystal structure. But how is the situation if the sample is completely unoriented? At first sight this may seem to preclude any symmetry determination, which, of course, is not correct. It is still possible to find the invariants of the Raman tensor by using different scattering configurations. Invariants are those combinations of the tensor elements which are left invariant under rotation.[78,79] I will show below that these tensor invariants can be understood from the decomposition of the Raman tensor into irreducible tensors instead of the representations of the crystal point group. First I demonstrate with a simple example how to find the Raman intensities in the lab frame by integrating over all orientations of the scattering elements.

Let us assume that I have a phonon with a diagonal Raman tensor with three elements $a_1 \neq a_2 \neq a_3$. Further, the scattering configuration in my lab frame is (ZZ). To find the Raman

A_{1g}	A_{2g}	E_{1g}	E_{1g}	E_{2g}	E_{2g}
$\begin{pmatrix} a & 0 & 0 \\ 0 & a & 0 \\ 0 & 0 & b \end{pmatrix}$	$\begin{pmatrix} 0 & e & 0 \\ -e & 0 & 0 \\ 0 & 0 & 0 \end{pmatrix}$	$\begin{pmatrix} 0 & 0 & c \\ 0 & 0 & 0 \\ d & 0 & 0 \end{pmatrix}$	$\begin{pmatrix} 0 & 0 & 0 \\ 0 & 0 & -c \\ 0 & -d & 0 \end{pmatrix}$	$\begin{pmatrix} 0 & f & 0 \\ f & 0 & 0 \\ 0 & 0 & 0 \end{pmatrix}$	$\begin{pmatrix} -f & 0 & 0 \\ 0 & f & 0 \\ 0 & 0 & 0 \end{pmatrix}$

Table 3.2: Raman tensors of the phonons in carbon nanotubes. They are valid for the D_q and D_{qh} point groups with $q > 3$, which refers to all realistic tubes.

intensity I have to integrate and average over all orientations of the crystal. Using Euler's angles[80,81]

$$I_{ZZ} = \frac{1}{8\pi^2}\int_0^{\pi}\int_0^{2\pi}\int_0^{2\pi} |e_i \cdot \Re \cdot e_s|^2 \, d\psi \, d\varphi \sin\theta \, d\theta \tag{3.2}$$

$$= \frac{1}{8\pi^2}\int_0^{\pi}\int_0^{2\pi}\int_0^{2\pi} \langle \begin{pmatrix} \sin\varphi\sin\theta \\ \cos\varphi\sin\theta \\ \cos\theta \end{pmatrix} \begin{pmatrix} a_1 & & \\ & a_2 & \\ & & a_3 \end{pmatrix} \begin{pmatrix} \sin\varphi\sin\theta \\ \cos\varphi\sin\theta \\ \cos\theta \end{pmatrix} \rangle^2 \, d\psi \, d\varphi \sin\theta \, d\theta \tag{3.3}$$

integrating and rearanging yields

$$I_{ZZ} = \frac{45\bar{\alpha}^2 + 4\,\gamma_s'^2}{45} \tag{3.4}$$

$$\text{with} \quad \bar{\alpha} = \tfrac{1}{3}(a_1 + a_2 + a_3) \tag{3.5}$$

$$\gamma_s'^2 = \tfrac{1}{2}\left[(a_1 - a_2)^2 + (a_2 - a_3)^2 + (a_3 - a_1)^2\right]. \tag{3.6}$$

The result in Eq. (3.4) holds for all parallel polarizations of the incoming and outgoing linearly polarized light and for every Raman tensor except that $\gamma_s'^2$ then has a more general form (see below). For perpendicular linear polarization, e.g., I_{XZ}, the integration yields $I_{XZ} = 3\,\gamma_s'^2/45$. Now it becomes obvious that the symmetry can partially also be deduced from experiments on unoriented crystals. For example, if the three elements of the Raman tensor are the same (as for cubic point groups), Raman scattering is forbidden in crossed linear polarization, and in parallel linear polarization we find $I_{ZZ} = a^2$. On the other hand, a fully uniaxial Raman tensor ($a_1 = a_2 = 0, a_3 = b$) results in $I_{XZ}/I_{ZZ} = 1/3$.

In Appendix II. I show how to generalize the results of the preceding paragraph for arbitrary Raman tensors. The intensity on unoriented crystals follows directly from the transformation of a tensor under rotation. A second rank tensor can be decomposed with respect to the rotation group into a scalar (tensor of rank zero), an antisymmetric matrix (rank one), and a symmetric traceless matrix (rank two). These irreducible components have well defined quantum numbers and transformation properties under rotation. The matrix element for a fixed orientation is obtained from the Wigner-Eckart theorem; the integration over all crystal orientations is determined by the tensor invariants. Different authors use slightly different invariants in Raman scattering. Following Nestor and Spiro[82] I define the isotropic invariant

$$\bar{\alpha} = \tfrac{1}{3}(\alpha_{xx} + \alpha_{yy} + \alpha_{zz}), \tag{3.7}$$

the antisymmetric anisotropy

$$\gamma_{as}^2 = \tfrac{3}{4}\left[(\alpha_{xy} - \alpha_{yx})^2 + (\alpha_{xz} - \alpha_{zx})^2 + (\alpha_{yz} - \alpha_{zy})^2\right], \tag{3.8}$$

and the symmetric anisotropy

$$\gamma_s^2 = \tfrac{1}{2}[(\alpha_{xx}-\alpha_{yy})^2+(\alpha_{yy}-\alpha_{zz})^2+(\alpha_{zz}-\alpha_{xx})^2]+\tfrac{3}{4}[(\alpha_{xy}+\alpha_{yx})^2 +(\alpha_{xz}+\alpha_{zx})^2+(\alpha_{yz}+\alpha_{zy})^2], \tag{3.9}$$

where α_{ij} $(i,j=x,y,z)$ are the elements of the Raman matrix as given in Table 3.2 for carbon nanotubes.

The scattering intensity on an unoriented sample in any scattering configuration can be expressed by a linear combination of the tensor invariants, see Appendix II. For linear parallel $(\|)$ and perpendicular $(\perp)$ polarization of the incoming and scattered light the intensities are given by (apart from a constant factor; Table II.2)

$$I_{\|} = 45\bar{\alpha}^2+4\,\gamma_s^2 \tag{3.10}$$

$$I_{\perp} = 3\,\gamma_s^2+5\,\gamma_{as}^2, \tag{3.11}$$

which is the generalized result of Eq. (3.4). The quotient $I_\perp/I_\|$ is known as the depolarization ratio ρ. Under non-resonant conditions the antisymmetric invariant $\gamma_{as}^2=0$. Measuring the intensity under parallel and crossed polarization is then sufficient to find the tensor invariants. Under resonances antisymmetric scattering does not necessarily vanish. We need at least one more independent measurement to find the tensor invariants. Using circular instead of linear polarization the intensities in backscattering configuration are

$$I_{\circlearrowleft\circlearrowleft} = 6\,\gamma_s^2 \tag{3.12}$$

$$I_{\circlearrowleft\circlearrowright} = 45\bar{\alpha}^2+\gamma_s^2+5\,\gamma_{as}^2, \tag{3.13}$$

where $I_{\circlearrowleft\circlearrowleft}$ is the intensity for corotating and $I_{\circlearrowleft\circlearrowright}$ for contrarotating incoming and outgoing light, $I_{\circlearrowleft\circlearrowleft}/I_{\circlearrowleft\circlearrowright}$ is the reversal coefficient P. Solving the system of four equations Eq. (3.10)-(3.13) with respect to the tensor invariants we obtain as one possible solution[82]

$$45\,\bar{\alpha}^2 = I_{\|}-\tfrac{2}{3}I_{\circlearrowleft\circlearrowleft}, \tag{3.14}$$

$$5\,\gamma_{as}^2 = I_{\perp}-\tfrac{1}{2}I_{\circlearrowleft\circlearrowleft}, \tag{3.15}$$

$$6\,\gamma_s^2 = I_{\circlearrowleft\circlearrowleft}. \tag{3.16}$$

With the last quantity $I_{\circlearrowleft\circlearrowright}$ we can measure the experimental error. The experimentally obtained tensor invariants are only accepted as significantly different from zero if they are larger than $\Delta I = |(I_\|+I_\perp)-(I_{\circlearrowleft\circlearrowleft}+I_{\circlearrowleft\circlearrowright})|$.

Before I turn to the description of the experimental setup for measuring the tensor invariants and the results for carbon nanotubes, I want to discuss in general the conclusions which can be drawn from experiments on unoriented samples. The only symmetry which has a non-vanishing isotropic part $\bar{\alpha}$ is the fully symmetric representation in any point or space group. Thus, phonons of A_1 symmetry are readily distinguished from the other species. Of particular interest is the observation of antisymmetric contributions to the Raman intensity, i.e., $\gamma_{as}^2 \neq 0$. If only the antisymmetric component is present the Raman peak originates from a phonon transforming as the totally antisymmetric representation, in the point group of nanotubes this is A_2 (see Table 3.2). Totally antisymmetric scattering is rather rarely observed experimentally; more frequent is an antisymmetric contribution to a degenerate mode.[82–84] The only possible modes in nanotubes showing mixed symmetric and antisymmetric scattering are E_1 modes. For example, a strong incoming resonance with an optical transition which is allowed in z polarization, but forbidden in x or y polarization yields in the matrix representation of the E_1 Raman tensor $c \neq d$ in Table 3.2. Such antisymmetric contributions where reported by Rao *et al.*[74,85,86] for multiwall nanotubes. Degenerate modes have a symmetric anisotropy γ_s^2 different from zero, but $\bar{\alpha}^2 = 0$. A large ratio $\bar{\alpha}^2/\gamma_s^2$ can serve as an indicator for scattering by E_1 and E_2 symmetry modes in carbon nanotubes.

3.3. Experiments

The light scattered by a material consists of an elastically scattered part – Raleigh scattering – and an inelastically scattered part – Raman scattering. The cross section for Raleigh scattering exceeds the one for Raman scattering by several orders of magnitude. Moreover, the difference in energy between the Raman signal and the incoming light is on the order of 10^{-2}. The experimental setup must, therefore, be optimized to detect weak signals in the vicinity of the intense Raleigh peak. A standard Raman experiment nowadays uses lasers for excitation. A triple-grating spectrometer or a single-grating system with a notch filter suppresses the elastically scattered light and disperses the Raman spectrum. The spectrum is recorded with multichannel detectors like charge-coupled-device (CCD) cameras.

In the present work scattering was excited by Ar^+ or Kr^+ laser lines or an HeNe laser. The excitation density was kept below 100 W/cm^2 to avoid heating of the strongly absorbing nanotubes material. The two spectrometers used for the measurements and the detailed setup I describe in the following.

Triple-grating DILOR XY800

The setup is shown schematically in Fig. 3.2. The laser light first passes a small prism monochromator to remove the plasma lines of the laser. It is then focused onto the sample with a commercial photo objective ($f = 35\,\mathrm{mm}$) or a achromat-meniscus lens ($f = 60\,\mathrm{mm}$). The scattered light is collected in backscattering geometry. The first two gratings of the spectrometer are used to suppress the elastically scattered light. They are arranged in subtractive mode – placed "back to back" – and thus act as a narrow band pass filter of variable wavelength. The light is dispersed by the last grating (1800 mm^{-1}) and collected by a charge-coupled-device detector. In the green and blue energy range a liquid nitrogen cooled back-thinned CCD was used, in the red a Peltier cooled CCD without back thinning. The resolution achieved with a 200 μm entrance slit is between $1.5\,\mathrm{cm}^{-1}$ at 647 nm and $3\,\mathrm{cm}^{-1}$ at 488 nm, which is much smaller than the width of the Raman peaks observed in carbon nanotubes. The specific strengths of this spectrometer for experiments on nanotubes are its flexibility, i.e., it is not restricted to particular excitation energies, and for the observation of the radial breathing mode at $\approx 200\,\mathrm{cm}^{-1}$ the narrow width of the filtering by the first two gratings.

Single-grating DILOR LABRAM

The Labram is a compact micro Raman spectrometer depicted in Fig. 3.3. The plasma lines are removed by an interference filter before the notch filter reflects the laser beam into an optical microscope. An 100x objective was used to focus the light onto the sample and collect the backscattered radiation. The scattered light again reaches the notch filter, where the light

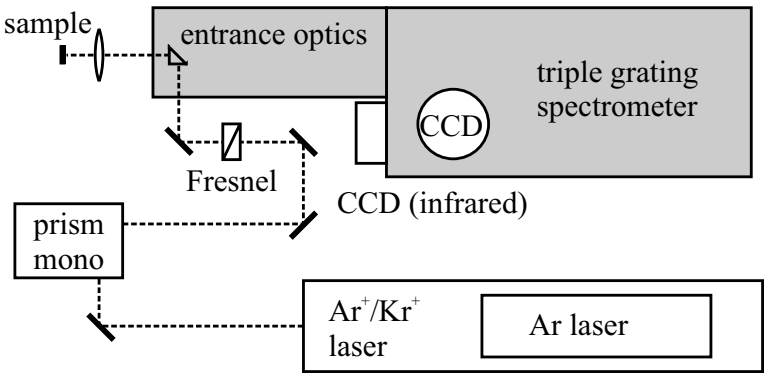

Figure 3.2: Experimental setup for the Raman measurements with the DILOR XY800. The plasma lines of the Ar^+/Kr^+ or Ar laser are removed by the prism monochromator. After passing a Fresnel rhomb the light is reflected and focused onto the sample. The backscattered light is analyzed with a triple-grating spectrometer and collected by a CCD.

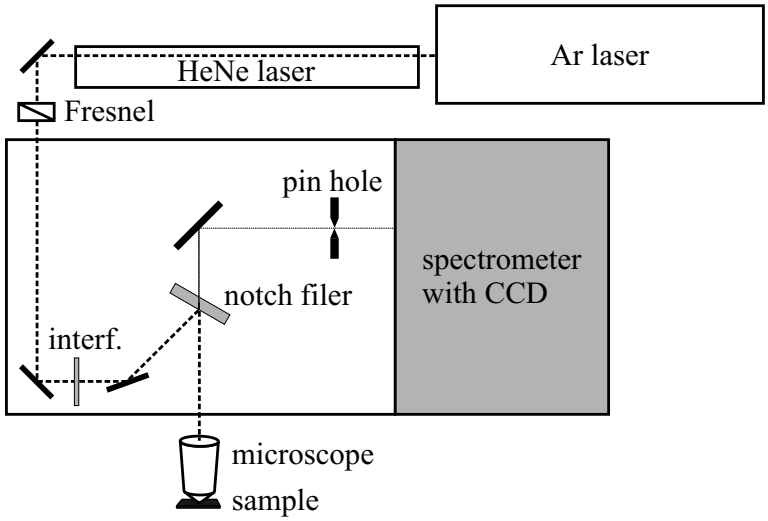

Figure 3.3: Experimental setup for Raman measurements with the DILOR LABRAM. The entrance optics of the Labram spectrometer are shown schematically. An interference filter (interf.) rejects the plasma lines of the HeNe or Ar laser. The laser is reflected by the notch filter and focused with a microscope objective onto the sample. The Raman scattered light passes the notch filter, is focused onto the entrance slit of a single-grating spectrometer. The spectrometer is equipped with a Peltier cooled CCD.

within a bandwidth of $\approx 3\,\mathrm{nm}$ of the laser line is reflected, whereas the other wavelengths pass the notch filter. To further suppress stray light and to increase the spatial resolution a pin hole with a diameter $d = 200\,\mu\mathrm{m}$ is placed into an intermediate focus. Finally the scattered light is focused onto the entrance slits of a single grating spectrometer ($1200\,\mathrm{mm}^{-1}$) and collected with a Peltier cooled CCD. By the construction of the entrance optics the Labram is restricted to excitation wavelengths for which an interference and notch filter combination is available; I used the 632 nm HeNe line and the 514 and 488 nm Ar line for excitation.

Single grating spectrometers became increasingly popular because they are easy to handle and comparatively cheap. Another advantage is their high throughput allowing the observation of weak signals. On the other hand, the observation of Raman modes close to the laser line is usually not possible. I was only able to record the radial breathing mode of single walled nanotubes when working with red excitation and using two SuperNotch filters to suppress the Raleigh scattered light. For the green and blue laser line only a single SuperNotch and SuperNotchPlus filter was available, respectively. Moreover, the difference in wavelength between the incoming and outgoing light is $1.5-2$ times smaller for these excitation energies than for 632 nm; the light scattered by the radial breathing mode was within the band widths of the notch filter. The experimental resolution was around $3\,\mathrm{cm}^{-1}$ in the red and $5\mathrm{cm}^{-1}$ in the blue energy range.

3.3.1. Polarized measurements

The tensor invariants of the Raman scattered light are obtained from a linear combination of the intensities in linear and circular polarization as shown in Section 3.2.. To determine them experimentally I need to record the Raman intensities in parallel, perpendicular, corotating, and contrarotating polarization without changing the illumination level or removing any polarizing elements in the light path between the measurements.[76,77,82] The basic setup I used – a combination of two linear polarizing elements (a Fresnel rhomb and a polarization filter) and a $\lambda/4$ wave plate – is shown in Fig. 3.4. With the position of the polarizing elements as indicated in the figure a backscattering Raman spectrum under corotating polarization is recorded: The light coming from the laser is vertically polarized. After passing the Fresnel rhomb (90° position) the light is horizontally linear polarized. The angle between the principle axis of the $\lambda/4$ wave plate and the horizontal plane is 45°; the light is circularly polarized after passing the wave plate. It is then focused onto the sample and the scattered beam consists of a left and right hand circularly polarized part. Going back through the $\lambda/4$ wave plate the circular polarization is converted into linear polarization. The corotating part is polarized vertical and the contraroting part horizontal (the circular polarizations are specified in the lab frame). Only vertically polarized light can pass the analyzer and thus be recorded by the spectrometer and the CCD.

In the experiments the polarization direction of the analyzer was chosen according to the larger sensitivity of the spectrometer, which is horizontal in the blue and vertical in the red energy range. The intensities in the four different polarizations are then obtained by rotating the Fresnel rhomb and the $\lambda/4$ wave plate. Let us assume that the analyzer is vertical, the

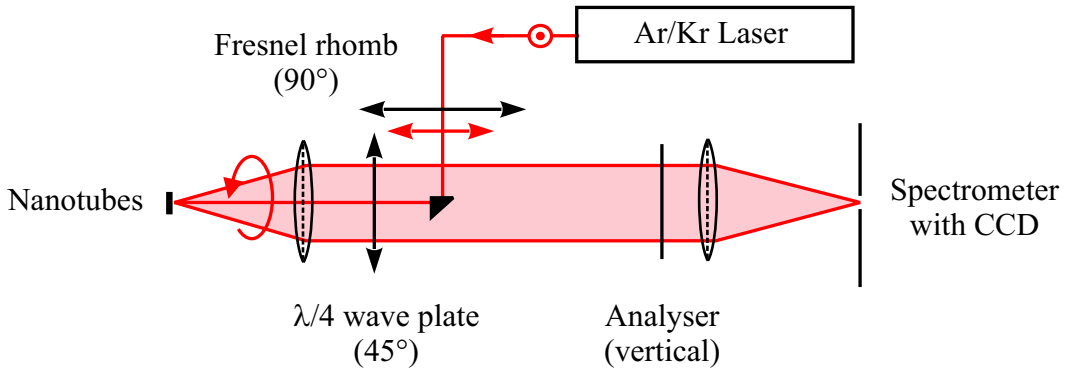

Figure 3.4: Setup for the measurements of the tensor invariants. The polarization direction of the incoming light is chosen by the Fresnel rhomb. The laser then passes a $\lambda/4$ zero-order wave plate and is focused onto the sample. The scattered light comes back through the $\lambda/4$ plate, is analyzed with a polarization filter, and focused onto the entrance slits of the spectrometer.

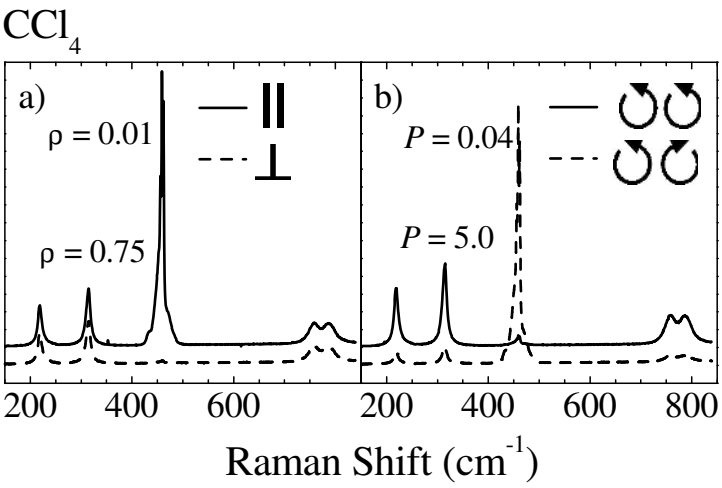

Figure 3.5: Raman spectra of CCl_4 a) under linear and b) circular polarization. Next to the fully symmetric mode at 460 cm^{-1} and the mode at 314 cm^{-1} the measured depolarization ratio ρ and reversal coefficient P are given.

Raman intensities are then given by

parallel	$I_{\parallel}$	Fresnel rhomb	0°	$\lambda/4$ wave plate 0°	analyzer vertical
perpendicular	$I_{\perp}$		90°	0°	vertical
corotating	$I_{\circlearrowleft\circlearrowleft}$		0°	45°	vertical
contrarotating	$I_{\circlearrowleft\circlearrowright}$		90°	45°	vertical

I used high-precision zero-order wave plates for 488 and 647 nm excitation wavelength; only a multi-order wave plate was available for 514 nm. The $\lambda/4$ wave plate was placed right before the focusing lenses or the microscope objective and aligned perpendicular to the laser beam. The angular positions of all polarizing elements I verified by looking at the minima and maxima in the intensity of the fully polarized laser light reflected at a metall surface and by measuring the known tensor invariants of CCl_4. Figure 3.5 shows the Raman spectra of CCl_4 in a) the two linear and b) the circular polarizations. In this molecule the fully symmetric mode is characterized by only the isotropic invariant $\bar{\alpha}^2$ being different from zero. For the A_{1g} peak at 460 cm^{-1} a depolarization ratio $\rho = 0$ and a reversal coefficient $P = 0$ are expected, which is in excellent agreement with the measured values given in Fig. 3.5. All other modes should show $\rho = 0.75$ and $P = 6$ ($\bar{\alpha}^2 = 0$, $\gamma_{as}^2 = 0$). Deviations from the theoretical value are usually found for the reversal coefficient, because the circular polarizations are much stronger affected by the non-ideal backscattering.[70,82] Whereas the theoretical depolarization ratio is the same regardless of the scattering geometry, the reversal coefficient, e.g., in forward scattering is the inverse of the backscattering value. In CCl_4 the measured P for the non-fully symmetric modes varies between 3.6 at 780 cm^{-1} and 5.3 at 220 cm^{-1}. A better (more robust) indicator for the symmetry of a Raman mode than the raw values of ρ and P are the ratios between the tensor invariants. In particular, the ratio between the symmetric anisotropy and the isotropic invariant $\gamma_s^2/\bar{\alpha}^2 = 0.4$ for the 460 cm^{-1} mode, but $\gamma_s^2/\bar{\alpha}^2$ is well above 100 for all other modes.

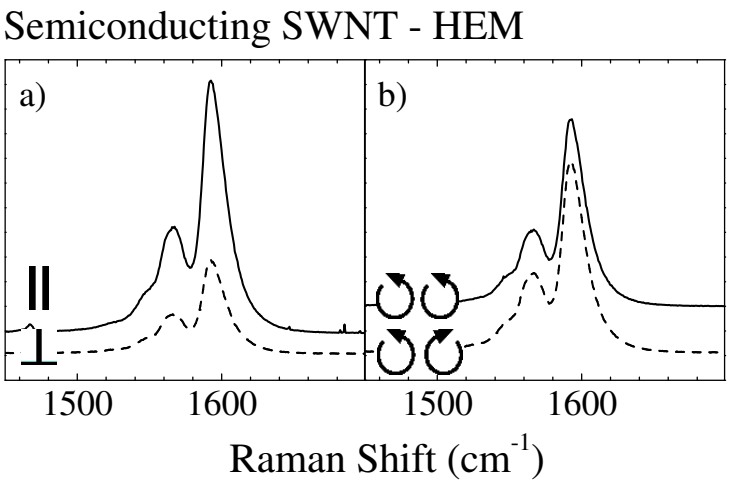

Figure 3.6: Raman tensor invariants of the high-energy modes in single walled nanotubes excited with 488 nm. a) Parallel and perpendicular linear polarization yielding $\rho = 0.35$ for all Raman peaks. b) Corotating and contrarotating polarization with $P = 1.01$.

3.4. Tensor invariants of carbon nanotubes

When I measured the tensor invariants on nanotubes I was expecting the spectral shape, in particular of the high-energy modes, to change in the different polarizations. A decomposition of the different weights in the polarized spectra would then have allowed me to partly identify the phonon symmetries contributing to the high-energy modes. Instead I found a uniform behavior of all phonon modes over the entire range of measured Raman frequencies.[76,77,85,87]

In Fig. 3.6 I show the measured high-energy Raman spectra of single walled carbon nanotubes excited with 488 nm; part a) displays the two linear and b) the circular polarizations. Only the overall intensity scales in the four polarized measurements. Moreover, the factors between the polarizations are almost the same as for the radial breathing mode around 200 cm^{-1} (Fig. 3.7) and the D mode at 1350 cm^{-1} for this excitation wavelength. The depolarization ratio is around $\rho \approx 0.34$ and the reversal coefficient $P \approx 1.01$ for all Raman

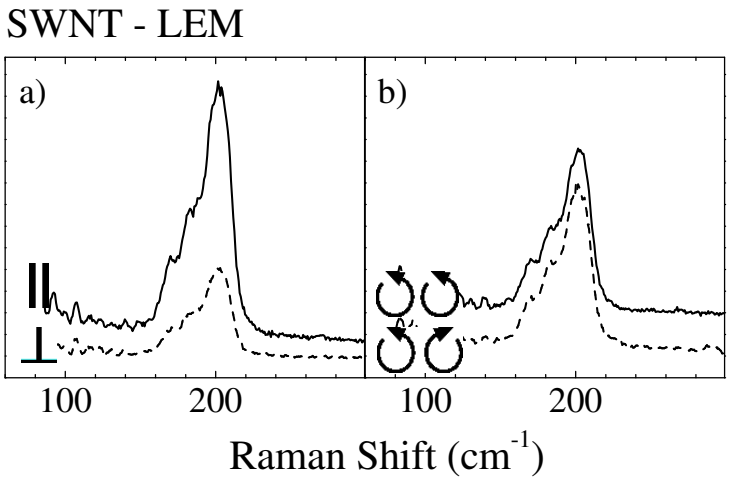

Figure 3.7: Raman tensor invariants of the radial breathing mode of single walled nanotubes excited with 488 nm. a) Parallel and perpendicular linear polarization yielding $\rho = 0.34$. b) Corotating and contrarotating polarization with $P = 1.01$.

modes. Changing the laser energy to 647 nm only slightly affects these values ($\rho = 0.36$ and $P = 1.20$), but again the ratios are the same in the entire Raman spectrum. The high-energy mode in multiwall nanotubes, in contrast, has a depolarization ratio of $\rho = 0.45$ and $P = 1.64$, see Fig. 3.8. Table 3.3 lists the tensor invariants I obtained in single and multiwall nanotubes and graphite. The last column gives the ratio $\gamma_s^2/\bar{\alpha}^2$ which is indicative of the mode symmetry. For non-totally symmetric modes the ratio should be infinity, which agrees nicely with the high ratio found for the E_{2g} graphite high-energy mode. A purely diagonal Raman tensor, on the other hand, is characterized by $\gamma_s^2/\bar{\alpha}^2 = 0$. Obviously none of the single and multiwall Raman peaks belong to this category. Before further analyzing the symmetric and isotropic tensor invariants I briefly turn to the antisymmetric tensor component. I find γ_{as}^2 to be within experimental error for both multi and single walled nanotubes. This is in contrast to the measurements on aligned multiwall nanotubes by Rao *et al.*[74] who reported the Raman spectra in (xy,z) and (z,xy) to differ by a factor of 1.7.[85,86] The reason for the discrepancy is not fully resolved; however, determining selection rules by micro-Raman scattering as done by Rao *et al.*[74] is more difficult than by a macro-Raman setup, because of the large collecting angle of the microscope objective. Difficulties with the experimental setup indeed seem to be very likely in the reference, since it reports the depolarization ratio of graphite as $\rho = 1$ instead of the E_{2g} ratio of 0.75.[85,86]

Interpreting the other tensor invariants of Table 3.3 and extracting the scattering phonon symmetries requires further experimental input. From the vanishing antisymmetric component I know the A_2 contributions to be zero ($e = 0$ in Table 3.2) and the two independent E_1 elements to the same ($c = d$), but I still have four independent parameters if I do not, e.g., exclude a phonon symmetry explicitly. Additional information is found in a number of papers where the Raman intensity was measured on nanotubes aligned along the z axis.[15,72,73,75,88] Such measurements are not able to distinguish between A_1 and E_2 symmetry modes, but

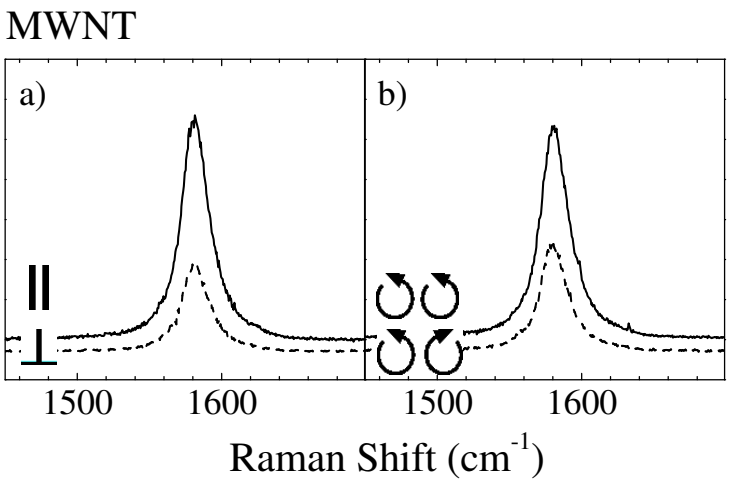

Figure 3.8: Raman tensor invariants of the high-energy modes in multiwall nanotubes excited with 488 nm. a) Parallel and perpendicular linear polarization yielding $\rho = 0.45$ for all Raman peaks. b) Corotating and contrarotating polarization with $P = 1.64$.

Frequency (cm^{-1})		$45\bar{\alpha}^2$	$6\gamma_s^2$	$5\gamma_{as}^2$	ΔI	$\gamma_s^2/\bar{\alpha}^2$
SWNT ($\lambda_{exc} = 488\,nm$)	1594	204	252	3	50	9.3
	1565	64	80	1.5	20	9.3
	1554	20	26	1.4	2	9.7
	1350	14	17	2	−3	8.8
SWNT ($\lambda_{exc} = 647\,nm$)	1580	50	68	−0.5	2	10.0
	1567	25	66	−0.4	7	10.9
SWNT ($\lambda_{exc} = 488\,nm$)	202	19	24	−0.3	3	9.6
	183	7.8	9.6	0.04	0.7	9.2
	167	3.6	5.0	0.1	0.8	10.3
MWNT	1581	2.5	5.8	0.8	0.5	17.2
graphite	1582 (E_{2g})	0.72	16.3	0.4	1	170
	1350	1.3	2.4	0.0	0.4	13.4

Table 3.3: Tensor invariants (arb. units) of the Raman modes in single walled and multiwall tubes and graphite. Quantities comparable to the experimental error ΔI can be considered zero. For single walled nanotubes $\lambda_{exc} = 488\,nm$ corresponds to the spectra shown n Fig. 3.6, while $\lambda_{exc} = 647\,nm$ is within the red resonance window. The error in the last column is 10 %.

combined with the tensor invariants the phonon symmetries can be uniquely identified. In Ref. 76 I decomposed the Raman signal into A_1, E_1, and E_2 components based on the first aligned measurements which were then published.[72,89] In single walled nanotubes I thereby found that at least 70 % of the total scattering intensity originates from the zz matrix element of the fully symmetric modes.[76,77] In the meantime, however, A. Rinzler and his group published Raman experiments on highly aligned nanotube fibers, which suggest an even higher zz contribution.[73,88] I therefore base the following discussion on their new results.

The ratio between the symmetric anisotropy and the isotropic tensor invariant in terms of the Raman matrix elements in Table 3.2 is given by [see Eq. (3.9)]

$$\frac{\gamma_s^2}{\bar{\alpha}^2} = \frac{9[(a-b)^2 + 6(c^2+f^2)]}{(2a+b)^2}. \tag{3.17}$$

In the Raman measurements on nanotube fibers Hwang *et al.*[88] reported the intensity in parallel polarization perpendicular to the tubes axis $I_{(xy,xy)}$ to be zero. Since the nanotube fibers are aligned with respect to the z axis but randomly oriented in the perpendicular plane the (xy,xy) intensity is $I_{(xy,xy)} = a^2 + f^2 = 0$. The $\gamma_s^2/\bar{\alpha}^2$ ratio in semiconducting tubes is ≈ 9. From Eq. (3.17) it is then immediately seen that the only non-zero Raman matrix element is $b = \alpha_{zz}$. For red excitation $\gamma_s^2/\bar{\alpha}^2$ is systematically a little higher, but not really significantly different. The entire Raman signal of single walled nanotubes thus comes from zz polarized totally symmetric $A_{1(g)}$ phonons. In multiwall nanotubes the $\gamma_s^2/\bar{\alpha}^2$ ratio is increasing to 17, which cannot be explained by zz scattering alone. Assuming nevertheless

that only A_1 phonons give rise to the measured spectra Eq. (3.17) yields $a = -0.10$ (b is normalized to unity, $c = f = 0$ for A_1 scattering), i.e., zz polarized A_1 symmetry scattering still dominates the Raman process. The only polarized measurements on aligned multiwall nanotubes are those by Rao *et al.*[74] They agree nicely that the by far strongest intensity is found in (z,z) polarization, but report similar intensities for parallel (xy,xy) and crossed (xy,z) polarization perpendicular to the tube axis. This implies that the assumption of only A_1 scattering is not fully justified. Including all Raman active symmetries in the analysis and using the intensities of Ref. 74 I obtained relative contributions of $\approx 20\,\%$ for E_1 and E_2 (still xx scattering is negligible).[76,77] An increase in the traceless scattering intensity in multiwall nanotubes is reasonable because of their large diameter. In the limit of $d \to \infty$ all scattering intensity is transferred to E_{2g}, the Raman active graphite high-energy mode.

In single walled nanotubes only zz polarized Raman scattering is observed experimentally, although two other representations are Raman active as well. Additionally surprising is that even the radial breathing mode does not show xx and yy contributions. In this mode all carbon atoms move in the radial direction; naively one would expect the in plane matrix element to be larger than the axial matrix element. This argumentation, however, is based solely on electron-phonon coupling and neglects the optical absorption in the Raman process. It is thus only valid far away from resonances, but resonances are the key in understanding Raman scattering on nanotubes. The optical absorption coefficient is highly anisotropic in single walled nanotubes explaining the dominant (zz) component.

3.4.1. Optical absorption in nanotubes

To obtain first insight into the optical transition probabilities of carbon nanotubes I discuss the symmetry imposed selection rules. As the example I use the (19,0) zig-zag tube; its band structure I showed in Fig. 2.10 on page 41. Optical transitions are allowed between electronic states with $\Delta m = 0, \pm 1$, in particular, $\Delta m = 0$ for z polarized transitions and $\Delta m = \pm 1$ for x and y polarizations. Additionally, the σ_h parity is conserved in achiral nanotubes with $\sigma_h = -1$ for z and $\sigma_h = +1$ for xy polarized photons. I labeled the electronic bands by their irreducible representations at the Γ point in Fig. 2.10b), which is the only critical point for transitions in the visible energy range in zig-zag tubes. The representations of the electronic wave functions immediately show that (i) z polarized transitions are allowed starting from any valence band to the conduction band of same m and (ii) only the two conduction and valence bands closest to the Fermi level contribute to x and y polarized absorption. Zig-zag tubes are thus almost transparent for visible light polarized perpendicular to the tube axis. In chiral nanotubes σ_h no longer is a symmetry operation. Nevertheless, for chiral tubes with

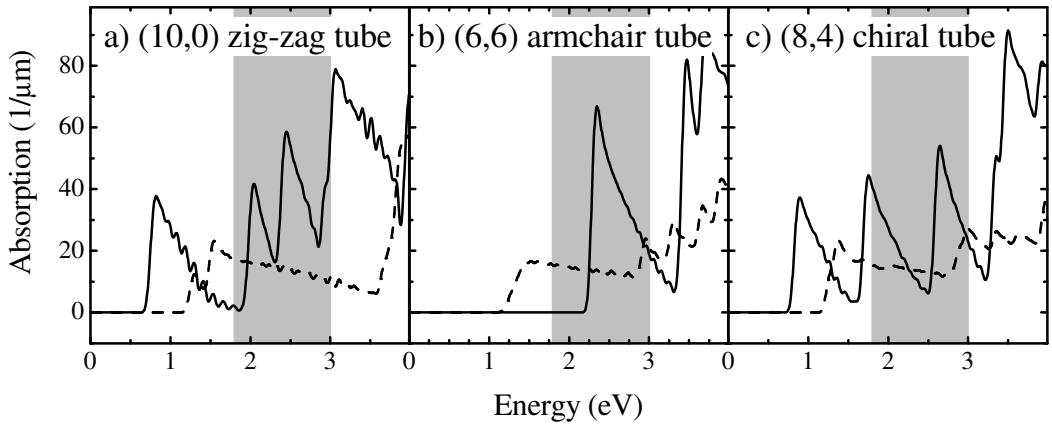

Figure 3.9: Optical absorption in a (10,0) zig-zag tube a), a (6,6) armchair tube b), and an (8,4) chiral tube c). Full lines are for light polarized along the tube z axis, broken lines for perpendicular polarization. The shaded area corresponds roughly to the visible energy range; the calculated transition energies are not to be compared directly to experiment (see Chapter 5. for discussion).

$\mathcal{R} = 1$, which have an electronic band structure similar to zig-zag tubes, I still expect the x and y transition matrix elements to be small, because of the stringent selection rule in the higher symmetry tubes. For armchair tubes [see Fig. 2.10a)] and chiral tubes with $\mathcal{R} = 3$ symmetry does not impose restrictions on the visible absorption besides the Δm selection rules. The singularities in the electronic density of states originate from the interior of the Brillouin zone – around $k_F = 2\pi/3a$ – where σ_h is not a symmetry operation. Hand wavingly, one might suggest that still z transitions are more likely than x or y polarized transitions, since a very small change in the chiral vector changes an $\mathcal{R} = 3$ tube into one with $\mathcal{R} = 1$. To study this question more profoundly I calculated the optical matrix elements in carbon nanotubes by first principles methods (see Appendix I. and Chapter 5. for a discussion of the *ab initio* method and band structure results).

In Fig. 3.9 I show the calculated absorption coefficient for a zig-zag, an armchair, and a chiral nanotube. Full lines denote z polarized transitions, broken lines x and y polarization. The calculated transition energies cannot be directly compared to experiment because of the small diameter of the calculated nanotubes, hybridization effects in small diameter tubes, and the error introduced by the local density approximation, see Chapter 5. To estimate the range of the visible within the *ab initio* calculation I used the approximation by Mintmire and White[34,35] and the normalized Raman measurements by Rafailov *et al.*[44] The energy region which correspond to the visible and near infrared ($\approx 1.5 - 2.5\,\mathrm{eV}$) in larger diameter nanotubes is shaded in gray in Fig. 3.9. In zig-zag tubes optical absorption was most restricted by symmetry. Comparing my *ab initio* results to the symmetry imposed selection rules thus nicely verifies the calculations. Indeed in Fig. 3.9a) and z polarization (full lines) I

find a series of square root like singularities, which are typical for the joint density of states and thus the absorption probability in one-dimensional systems. For x polarized light only the two lowest lying transitions contribute to the optical absorption as expected by symmetry arguments. That this is really an effect of the vanishing matrix elements and not of the energetic separation of the valence and conduction bands becomes apparent when looking at the electronic band structure of the (10,0) nanotube in Fig. 5.7 on page 94. Additionally, the *ab initio* calculations show that the matrix element for x polarized absorption even for the allowed transitions is smaller than in z polarization; the singularities in the absorption coefficient for x polarized light are twice smaller than those for z polarization. The optical absorption for a (6,6) armchair tube is shown in Fig. 3.9b). For z polarized light metallic tubes have only a single singularity for energies in the visible and below.[34,35] Moreover, the absorption in metallic nanotubes is high at energies where it is low in semiconducting nanotubes and *vice versa*, which is known as the metallic resonance window in Raman scattering for red excitation.[43,44] In x polarization only transitions to and from the bands crossing at the Fermi level yield a non-vanishing matrix element, see the onset of the step around 1.1 eV in Fig. 3.9b) (broken lines). Since the two crossing bands have a linear slope throughout most parts of the Brillouin zone the joint density of electronic states and hence the absorption coefficient has a step-like behavior in b) in contrast to the square root peaks in the (10,0) nanotube. The chiral (8,4) nanotube in Fig. 3.9c) somehow shows a "superposition" of the zig-zag and the armchair behavior for perpendicular polarization. At low energy ($\approx 1.5\,\mathrm{eV}$) it has two square root singularities in the absorption strength, which are not fully resolved by the calculations and apper as one peak. Above 3 eV a number of small peaks are seen as in the armchair tube. The calculated absorption spectrum for z polarization resembles those of the zig-zag tube, since both the (8,4) and the (10,0) tube are semiconducting.

Bulk nanotube samples always show a homogeneous contribution of chiralities. As a first approximation of the optical absorption in such a sample I consider the average of the three spectra in Fig. 3.9 for parallel and perpendicular polarization. When summing up part a) to c) z polarized absorption is by a factor of ≈ 4 stronger than x polarized absorption over the whole visible energy range (shaded area). Raman scattering involves both the absorption and emission of a photon. If I assume both transitions to be resonant or nearly resonant I obtain a factor of 16 between (zz) and (xy,xy) phonon scattering from the optical absorption strength alone. Although this difference is large, it is in fact not sufficient to explain the experimentally observed ratio between the two polarizations. On particularly well aligned nanotube fibers Hwang *et al.*[88] found a ratio of 1/127 between the Raman spectra recorded in parallel and perpendicular polarization with respect to the nanotube axis.[90] That the optical absorption for perpendicular polarization is additionally supressed by a screening of the external

potential was first suggest by Ajiki and Ando.[91,92] It was recently confirmed by polarized absorption experiments on nanotubes aligned in zeolite channels.[93] Nanotubes grown by this method are perfectly aligned within the channel and have a very small diameter $d \approx 4$ Å, i.e., only a very limited number of (n_1, n_2) nanotube can form within the channels. Li *et al.*[93] directly compared LDA band structure calculations to their measurements. Although electronic transitions were expected from the calculated band structure, the sample was almost transparent when the light was polarized perpendicular to the nanotubes axis. The large anisotropy in the optical absorption thus is the reason for the measured symmetry of the Raman scattered light and the dominant intensity in (zz) polarization. Nevertheless, it would be interesting to repeat such experiments for infrared excitation (≈ 1 eV), where the absorption probability is small for z polarized light.

3.4.2. Tensor invariants of the D mode

Before concluding this chapter I briefly comment on the tensor invariants I measured for the D mode in single walled nanotubes and graphite. The defect induced D band is coming from a double resonant Raman process, which is the topic of Chapter 6., and thus dominated by the electronic properties in both materials. In single walled nanotubes the D mode scattered light has the same symmetry as the other parts of the Raman spectrum, see Table 3.3. The ratio between the anisotropic and the isotropic tensor invariant $\gamma_s^2/\bar{\alpha}^2 \approx 9$, i.e., the Raman tensor is of the form $diag[0,0,b]$. In graphite the measured ratio of ≈ 13 is quite interesting. It is often assumed that this mode has an A_1 Raman tensor $diag[a,a,b]$. Under this assumption, however, $\gamma_s^2/\bar{\alpha}^2 = 13$ together with Eq. (3.17) yields $a \approx -1.5$ for b normalized to unity. This implies that the optical absorption in graphite – the first and last step in the double resonant Raman process – is almost isotropic for light polarized parallel and perpendicular to the c axis, which contradicts experiments and *ab initio* calculations.[94,95] In fact, in a single graphene sheet z polarized transitions are forbidden below 6 eV; for graphite I found in a first principles calculation a factor of 10 in the visible range and below. The much lower optical absorption for light polarized along c suggests a Raman tensor with only xx, yy, xy, and yx non-vanishing elements as a better starting point. The optical phonons giving rise to the D mode originate from the neighborhood of the K point in the graphite Brillouin zone, see Chapter 6.[19] To analyze the D mode Raman tensor I consider only phonons at the ΓK line as a first approximation. The doubly degenerate E_{2g} graphite optical mode splits into a LO branch with A_1 symmetry and a TO branch with B_1 symmetry along the high-symmetry ΓK direction. The LO A_1 representation is correlated with the $A_{1g} \oplus E_{2g}$ representation in the graphite point group (also with B_{1u} and E_{1u} which will not give an important contribution),

whereas the TO B_1 correspond to $A_{2g} \oplus E_{2g}$ and two odd representations. Since only the fully symmetric A_{1g} representation has a non-zero isotropic tensor invariant $\bar{\alpha}^2$ the D band comes from the LO graphite optical branch. Its Raman tensor has the general form

$$\Re(D) = \begin{pmatrix} a+f & f & \cdot \\ f & a-f & \cdot \\ \cdot & \cdot & \cdot \end{pmatrix}. \tag{3.18}$$

With $\gamma_s^2/\bar{\alpha}^2 = 13$ I find $a = 1$ and $f = \pm 0.56$. Note that the *xx*-*yy* isotropy is broken for the D mode, because the scattering occurs for phonons far away from the Γ point. It would be interesting to further confirm the Raman tensor I proposed in Eq. (3.18). Since the D band is not Raman active in single graphite crystals the only opportunity is to measure a sample which is only 2D unoriented, i.e., aligned along the c axis, but random within the *xy* plane. The ratio between the crossed and parallel polarization after 2D integration of $\Re(D)$ is $I_\perp/I_\parallel(\mathrm{2D}) = f^2/(a^2+f^2) = 0.25$. To best of my knowledge such measurements for the D mode were not performed so far; they were done, however, for its second order overtone, the D^* band. Nemanich and Solin[96] reported a ratio of 0.4 between the crossed and parallel polarized D^* band in highly oriented pyrolytic graphite. This value in particular confirms that the D mode does not have a fully symmetric Raman tensor for which a ratio of $I_\perp/I_\parallel(\mathrm{2D}) = 0$ follows for both the D and D^* mode.

3.5. Summary

In this chapter I studied the symmetry of the Raman scattered light in single and multiwall nanotubes and graphite. Partly the scattering phonon symmetries can be obtained on unoriented systems by finding the Raman tensor invariants from linearly and circularly polarized measurements. In single walled nanotubes only (zz) polarized scattering contributes to the Raman spectra, because of the highly anisotropic optical absorption coefficient in the tubes. In *ab initio* calculations of the optical matrix elements I found a factor of ≈ 4 between z polarized and x or y polarized incoming light, although the perpendicular absorption seems to be additionally suppressed in the experiment. Multiwall nanotubes have small $A_1(xx)$, E_1, and E_2 components in their Raman scattered light, but still $A_1(zz)$ dominates the experimental spectra ($70-90\,\%$). Lastly, I discussed the Raman tensor of the D mode in graphite and proposed an experiment to further clarify the exact symmetry of the disorder induced Raman band.

Chapter 4

Nanotubes Under Hydrostatic Pressure

Applying hydrostatic pressure to a material changes the volume and in anisotropic systems also the shape of the unit cell. Studying the crystal structure under pressure already gives valuable insight into the elastic properties of material. Pressure experiments are, however, not restricted to finding the elastic constants. Every property of a material depends on the shape and volume of the crystal unit cell and can be manipulated by an applied pressure.

In this chapter I show how high-pressure experiments help our general understanding of Raman scattering by the high-energy modes in carbon nanotubes. Section 4.1. gives an overview over the vibrational properties of carbon nanotubes under pressure. I develop in Section 4.2.1. an elastic continuum model of carbon nanotubes under pressure, which is in remarkably good agreement with more sophisticated calculations described later on. Because of the highly anisotropic structure of carbon nanotubes the pressure slope of a Raman peak is expected to depend on the direction of the atomic displacement with respect to the nanotube axis, which is in contrast with the experimentally observed uniform shift of all Raman modes. I discuss in Section 4.4. that this apparent discrepancy is resolved by the high-energy phonon eigenvectors. In chiral nanotubes the atomic displacement may point in arbitrary directions with respect to the tube's axis and even show an angular dependence of its direction around the circumference. The homogeneous chirality distribution found in carbon nanotubes samples then averages out the expected shear strain splitting under pressure.

4.1. Raman experiments under pressure

Raman studies under hydrostatic pressure were carried out many groups.[11,14,29,30,97–101] The work concentrated on the pressure dependence of semiconducting nanotubes; one report was published on metallic nanotubes (by our group).[99] As an example for the evolution of

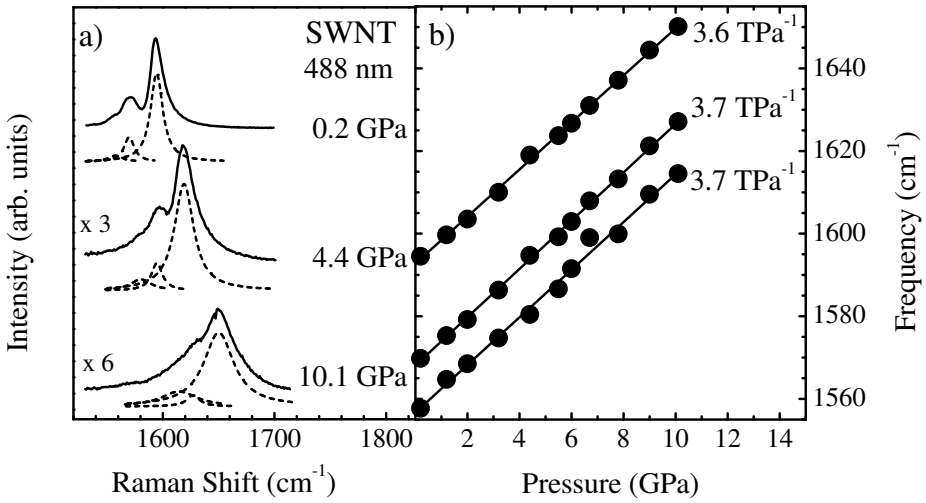

Figure 4.1: a) High-energy Raman spectra of semiconducting nanotubes under almost ambient and high pressure. b) Frequencies of the high-energy modes versus applied pressure. The normalized pressure slopes are the same for the three modes. Data from Reference 11.

the high-energy Raman modes under pressure I show in Fig. 4.1 the measurements by Thomsen *et al.*[11] The Raman spectrum shifts uniformly to higher frequencies under pressure. At the same time the modes are seen to broaden significantly and also to loose in intensity. The broadening and weakening of the signals under pressure are not fully understood yet. They have been attributed to phase transitions and also to a loss of resonance because of the change in the electronic band structure.[29,98,102] I will not discuss this behavior any further, instead I concentrate on the pressure dependence of the high-energy frequencies. In Fig. 4.1b) I plot the frequencies of the Raman peaks versus applied hydrostatic pressure. The normalized frequency shift $d\ln\omega/dp$ is the same for all high-energy modes. This seemingly ordinary result is in fact surprising for a highly anisotropic material like carbon nanotubes.[14,99] In uniaxial systems the different elastic properties along the principal axis and perpendicular to it are, in general, manifested in different phonon frequency shifts under pressure.

Table 4.1 lists the normalized pressure derivatives obtained by the various groups. Pressure slopes between 3.5 and 3.9 TPa^{-1} were reported in semiconducting nanotubes except in the work by Peters *et al.*[98] with the higher value of 4.5 TPa^{-1}. The differences between the references are due to varying mean values of the nanotubes diameter and – most likely also – to different fitting of the raw spectra. However, the slopes for the three high-energy modes reported on the same sample agree to within 3 %. Again Peters *et al.*[98] are the only who report a different slope for the third Raman peak, but in fact the Raman spectra taken in the diamond anvil cell (Fig. 5 of Ref. 98) hardly show the third peak at all. Also the scattering of the measured frequencies is much larger in this than in all other studies. For metallic nanotubes, unfortunately, only one Raman study under high pressures is available. In contrast

to the semiconducting tubes the three Raman modes have indeed different pressure slopes. The mode at 1592 cm^{-1} shows the same pressure dependence as the semiconducting peaks, whereas a total splitting of 15 % is found for the two other peaks. To obtain a more quantitative picture of the Raman frequency shifts I need to find the strain tensor in carbon nanotubes under hydrostatic pressure and then calculate the strain dependent frequencies with the help of the phonon-deformation potentials.

4.2. Elastic properties of carbon nanotubes

The relation between a macroscopic stress σ_{ij} applied to a material and the resulting microscopic deformation ε_{kl} is usually described with the help of the elastic constant tensor C_{ijkl} (repeated indices are to be summed over)[103]

$$\sigma_{ij} = C_{ijkl}\varepsilon_{kl}. \tag{4.1}$$

The symmetry of a crystal restricts the number of non-zero and linearly independent constants C_{ijkl}. For example in nanotubes obviously $C_{xxxx} = C_{yyyy}$, since the tubes are isotropic in the plane perpendicular to the z axis. The elastic constants can be measured by a variety of techniques like ultrasound experiments or direct measurements of the lattice constants under stress. Despite the large interest in the mechanical properties of carbon nanotubes, in particular as reinforcement materials,[104] successful measurements of the elasticity constants have not been reported up to now. Young's modulus E was investigated several times both theoretically and experimentally; it was found to be on the order of the graphite value.[105–107] For some selected tubes elastic constants were calculated with an empirical force constants

Reference	Normalized pressure dependence (TPa^{-1})		
Semiconducting tubes	1592 cm^{-1}	1570 cm^{-1}	1555 cm^{-1}
Venkateswaran *et al.*[29]	3.5	3.4	–
Thomsen *et al.*[11]	3.6	3.7	3.7
Peters *et al.*[98]	4.6	4.5	2.0
Teredesai *et al.*[97]	3.7	3.6	3.7
Venkateswaran *et al.*[101]	3.7	3.9	3.7
Metallic tubes	1592 cm^{-1}	1565 cm^{-1}	1544 cm^{-1}
Reich *et al.*[99]	3.8	4.1	3.5

Table 4.1: Logarithmic pressure derivatives of the high energy modes reported in the literature. The ambient pressure frequencies in the headings of the columns differ somewhat in the references; the number represents a label rather than an absolute frequency. The data of Venkateswaran *et al.*[29] were fitted by a straight line instead of the quadratic fit performed by the authors. Likewise, the two slopes by Peters *et al.*[98] were replaced by a single straight line.

model by Lu.[108,109] Here I chose another way for finding the elastic response of nanotubes under pressure. I approximate a nanotube by a hollow cylinder with closed ends and a finite wall thickness made out of graphene. In addition to yielding the deformation of a nanotube under pressure this model provides nice insight into the problem whether the different elastic properties of graphite and carbon nanotubes follow plainly from the geometry of the tube or some additional enforcement, e.g., by rehybridization.

4.2.1. Continuum model

The starting point of the continuum mechanical description is the equilibrium condition[110,111]

$$\frac{\partial \sigma_{ij}}{\partial x_k} = 0, \tag{4.2}$$

where x_k are the normal coordinates. The generalized Hooke's law in an isotropic medium is given by

$$\sigma_{ik} = \frac{E}{1-\nu}\Big(\frac{\nu}{1-2\nu}\varepsilon_{ll}\delta_{ik} + \varepsilon_{ik}\Big) \tag{4.3a}$$

or – the inverse relationship –

$$\varepsilon_{ik} = \frac{1}{E}\big[(1+\nu)\,\sigma_{ik} - \nu\,\sigma_{jj}\delta_{ik}\big], \tag{4.3b}$$

where E is again Young's modulus and ν Poisson's ratio. The strain ε_{ik} is defined by the displacement vector $\boldsymbol{u}$ describing the shift of a point in the deformed material

$$\varepsilon_{ik} = \varepsilon_{ki} = \frac{1}{2}\Big(\frac{\partial u_i}{\partial x_k} + \frac{\partial u_k}{\partial x_i}\Big). \tag{4.4}$$

Inserting Hooke's law (4.3) into Eq. (4.2) the fundamental equation of continuums mechanics can be derived[110]

$$(1-2\,\nu)\,\Delta\boldsymbol{u} + \operatorname{grad}\operatorname{div}\boldsymbol{u} = 2(1-\nu)\operatorname{grad}\operatorname{div}\boldsymbol{u} - (1-2\,\nu)\operatorname{rot}\operatorname{rot}\boldsymbol{u} = 0. \tag{4.5}$$

Since the rotation of $\boldsymbol{u}$ vanishes in our problem, Eq. (4.5) is further simplified, to yield, in cylindrical coordinates,

$$\operatorname{div}\boldsymbol{u} = \frac{1}{r}\frac{\partial(r\,u_r)}{\partial r} + \frac{1}{r}\frac{\partial u_\theta}{\partial \theta} + \frac{\partial u_z}{\partial z} = \text{const.} \tag{4.6}$$

Fig. 4.2 shows the continuum approximation of a single or multiwalled nanotube. The tube is modeled as a finite hollow graphene cylinder of length l with closed caps and inner and outer radius R_i and R_o, respectively. At $z = 0$ the displacement $u_z = 0$ and increases continuously

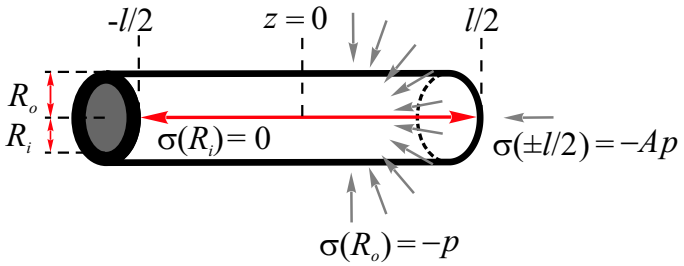

Figure 4.2: Continuum mechanical model of a nanotube - a closed cylinder of length l with inner radius R_i and outer radius R_o. The boundary conditions under hydrostatic pressure are indicated in the figure; A is the ratio between the cap area and the area supported by the cylinder walls $A = R_o^2/(R_i^2 - R_o^2)$.

in both directions $\varepsilon_{zz} = \partial u_z/\partial z = \text{const}$. The circumferential displacement u_θ is independent of θ, since our problem is rotationally symmetric, i.e., $\partial u_\theta/\partial\theta = 0$. Finally, according to Eq. (4.6) $1/r \cdot \partial(r u_r)/\partial r$ is again constant. The strains ε_{ii} in cylindrical coordinates are therefore given by[11]

$$\varepsilon_{rr} = \frac{\partial u_r}{\partial r} = a - \frac{b}{r^2}, \quad \varepsilon_{\theta\theta} = \frac{1}{r}\frac{\partial u_\theta}{\partial\theta} + \frac{u_r}{r} = a + \frac{b}{r^2}, \quad \text{and} \quad \varepsilon_{zz} = \frac{\partial u_z}{\partial z} = \text{const.} \tag{4.7}$$

The constants a, b, and ε_{zz} are determined by the boundary conditions for σ under hydrostatic pressure. I assume that the pressure media cannot enter the nanotube $\sigma_{rr}(R_i) = 0$ and $\sigma_{rr}(R_o) = -p$, where p is the applied pressure. Along the z direction the pressure transmits a force $-p \cdot \pi R_o^2$ to the caps of the tube. The area supported by the wall is $\pi(R_o^2 - R_i^2)$ and hence $\sigma_{zz} = -R_o^2/(R_o^2 - R_i^2) \cdot p = -Ap$. Inserting the boundary conditions into Eq. (4.3a) I obtain the constants in Eq. (4.7)

$$a = \varepsilon_{zz} = -(1-2\nu)\frac{pA}{E} \qquad b = -(1+\nu)\frac{pAR_i}{E}. \tag{4.8}$$

Reinserting the intergration constants into Eq. (4.7) finally yields the strain tensor in a nanotube under external hydrostatic pressure p

$$\varepsilon_{rr} = -\frac{Ap}{E}\left[(1-2\nu) - (1+\nu)\frac{R_i^2}{r^2}\right] \qquad \varepsilon_{\theta\theta} = -\frac{Ap}{E}\left[(1-2\nu) + (1+\nu)\frac{R_i^2}{r^2}\right]$$
$$\varepsilon_{zz} = -\frac{Ap}{E}(1-2\nu). \tag{4.9}$$

The mixed strain components $\varepsilon_{ij}, (i \neq j)$, vanish. The strain tensor in a nanotube under pressure is thus given by two elastic constants E and ν and the cylinder geometry.

Before substituting typical values into Eq. (4.9) I briefly discuss the general implications of the strain tensor found by the continuum approximation. The change in the tube length or the translational periodicity along the z axis is described by ε_{zz}, while $\varepsilon_{\theta\theta}$ is the radial or circumferential deformation. Both components are always negative for positive pressure. Moreover, the circumferential deformation is always larger than the axial deformation

$$\frac{\varepsilon_{\theta\theta}}{\varepsilon_{zz}} = 1 + \frac{1+\nu}{1-2\nu}\frac{R_i^2}{r^2} > 1, \tag{4.10}$$

as expected for an anisotropic system. Note that the differences are plainly a consequence of the cylindrical geometry; I assumed the nanotubes wall to be isotropic. The change in the wall thickness, ε_{rr}, can be positive or negative. In particular, it depends on r when going across the wall and at the inner radius $\varepsilon_{rr}(R_i) > 0$. For isolated single walled nanotubes a varying wall thickness is unlikely, since they consists only of one graphene sheet. This unphysical result is omitted by choosing $r_0 = \sqrt{(1+\nu)/(1-2\nu)}R_i$, i.e., $\varepsilon_{rr}(r_0) = 0$. However, as long as reasonable values for r are considered, e.g., another natural choice is the mean value of R_i and R_o, ε_{rr} and $\varepsilon_{\theta\theta}$ do not depend very much on r in single walled nanotubes.

The strain components which are responsible for the experimentally observed frequency shift of the high-energy Raman modes are the circumferential and tangential strain components. As I discussed in Chapter 2. the high-energy vibrations are parallel to the nanotube's wall. Hence ε_{rr} is negligible both for single and multiwall nanotubes. Consider now unwrapping the tube to a rectangle; the strain along the narrower, circumferential direction is then $\varepsilon_{\theta\theta}$ and the longer side is deformed according to ε_{zz}. With typical values for the radii and the elastic constants of single walled nanotubes ($R_i = 5.2\,\text{Å}$, $R_o = 8.6\,\text{Å}$, $E = 1\,\text{TPa}^{-1}$, and $\nu = 0.14$)[11,106] I find $\varepsilon_{\theta\theta}(p) = -2.04\,\text{TPa}^{-1}p$ and $\varepsilon_{zz}(p) = -1.07\,\text{TPa}^{-1}p$. Within the elastic continuum model the ratio between the circumferential and the axial strain is 1.9. From this two-dimensional strain pattern the change in phonon frequency follows from a linear expansion of the dynamical equation in the presence of strain. Before deriving the phonon slopes under pressure I compare the results of the elastic continuum model to other calculations of the elastic properties of carbon nanotubes.

4.2.2. *Ab initio*, tight-binding, and force-constants calculation

Two general approaches may be considered for theoretically finding the elastic properties of a material. Either the lattice constants under stress are calculated by directly incorporating the applied stress tensor into the calculation or the elastic constants are found from the second derivatives of the energy in a strained unit cell. The former approach was used in my *ab initio* calculation as well as by Venkateswaran *et al.*[29] in tight-binding molecular dynamics; the latter by Lu[108,109] in his force constants calculation.

In the *ab initio* calculations I considered three small diameter nanotubes, an armchair (6,6), a zig-zag (10,0), and a chiral (8,4) nanotube. Details on the computational scheme and the parameters are given in Appendix I.. The equilibrium lattice constant and the atomic positions were first obtained under ambient pressure by a conjugate gradient minimization. Then

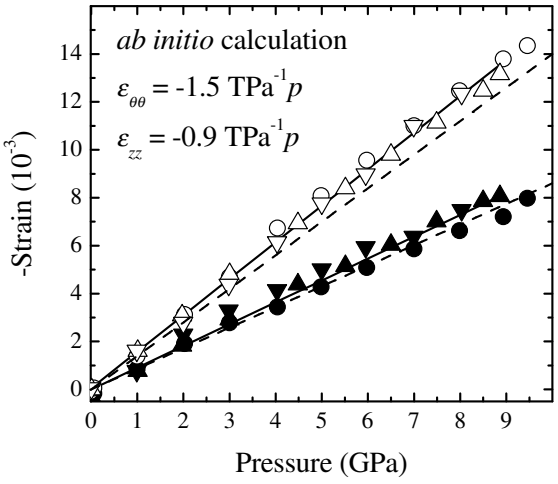

Figure 4.3: *Ab initio* calculation of the axial (closed symbols) and circumferential (open symbols) strain in single walled nanotubes bundles. Circles refer to an (8,4), up triangles to a (6,6), and down triangles to a (10,0) nanotube. The full lines show a least square fit of the strain components in the three tubes; the broken lines are for the continuum approximation [see Eq. (4.9), $r = 4.05$ Å].

I relaxed the geometry under the constraint of an hydrostatic stress tensor for several high-pressure points. The circumferential $\varepsilon_{\theta\theta} = [r(p) - r_a]/r_a$ and axial strain $\varepsilon_{zz} = [a(p) - a_a]/a_a$ are shown in Fig. 4.3; $r(p)$ and $a(p)$ are the stress dependent radius and translational periodicity, r_a and a_a are the ambient pressure values. As in the continuum approximation the circumferential strain is larger than the strain along the nanotube axis. Moreover, the strain components are found to a very good approximation to be independent of the chiralities of the nanotubes, a parameter which is completely neglected within the continuum approximation. The calculated pressure slopes of the radial and axial strain are $\varepsilon_{\theta\theta} = -1.5\,\mathrm{TPa}^{-1}p$ and $\varepsilon_{zz} = -0.9\,\mathrm{TPa}^{-1}p$ (full lines in Fig. 4.3). This is in excellent agreement with the elasticity model for $r = 4.05$ Å as can be seen in Fig. 4.3, where the strains obtained from Eq. (4.9) $\varepsilon_{\theta\theta} = -1.42\,\mathrm{TPa}^{-1}p$ and $\varepsilon_{zz} = -0.86\,\mathrm{TPa}^{-1}p$ are shown by the broken lines. The similarity between the elastic continuum model and the first principle calculations is quite remarkable. The continuum mechanical approximation works well even in the limit of a single atomic layer. A similar good agreement was found in two-dimensional semiconductors, see Ref. 112.

Two other studies of the elastic properties of armchair tubes were reported in the literature. Lu[109] calculated the elastic constants C_{ijkl} from force constants fitted to reproduce the phonon dispersion in nanotubes. From the elastic constants for a two-layer (10,10) tube in Ref. 109 the strain components are obtained with Eq. (4.1); they are given in Table 4.2. The strains in both directions are somewhat smaller than within the continuum model. The splitting between the axial and circumferential strain is predicted to be 3.5. Venkateswaran *et al.*[29] performed molecular dynamics simulations of (9,9) single tubes and bundles of tubes under pressure. The normalized axial and circumferential strain they reported in the bundle is shown in Fig. 4.4. The compressibility along the axis is similar to the continuum

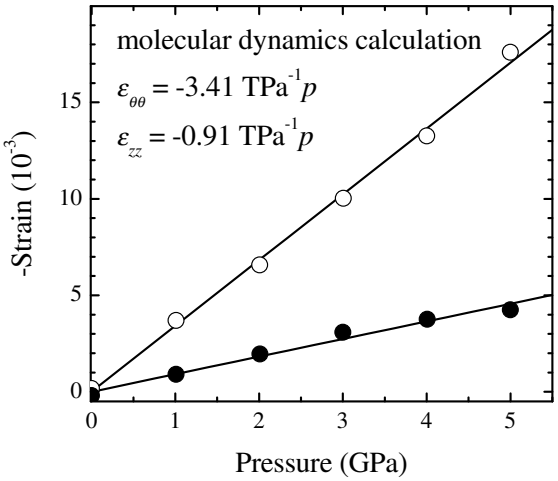

Figure 4.4: Molecular dynamics simulation of the axial (closed circles) and the circumferential (open circles) strain under hydrostatic pressure. The data points are taken from Fig. 4 of Ref. 29. The circumferential deformation shown here corresponds to the average of the two radii under pressure reported by Venkateswaran *et al.*[29]

value, whereas the circumferential strain was found to be much larger than in the continuum approximation.

Despite some differences in the absolute values of the predicted strains all four calculation agree in the following fundamental points: Under hydrostatic pressure the circumferential strain is by a factor of 2-4 larger than the axial strain. The linear compressibility along the nanotubes axis is similar to graphite ($-0.8\,\mathrm{TPa}^{-1}p$).

4.3. Phonon frequencies in strained crystals

From a known strain tensor the phonon frequency shifts follow from the dynamical equation modified to include terms linear in strain *via* the phonon-deformation potentials.[114–117] The phonon deformation potential relating the volume change of the unit cell with the frequency shift under pressure is called the Grüneisen parameter. Neither the Grüneisen parameter nor any other deformation potential are known for carbon nanotubes. Nevertheless, I show in the

	r(Å)	$d\varepsilon_{\theta\theta}/dp\,(\mathrm{TPa}^{-1})$	$d\varepsilon_{zz}/dp\,(\mathrm{TPa}^{-1})$	$\varepsilon_{\theta\theta}/\varepsilon_{zz}$
Continuum model	6.9	-2.04	-1.07	1.9
Elastic constants[109]	6.8	-1.74	-0.49	3.5
Molecular dynamics[29]	6.1	-3.41	-0.91	3.7
Continuum model	4.05	-1.42	-0.86	1.6
Ab initio	4.05	-1.5	-0.9	1.7
graphite[113]		-0.8	-0.8	

Table 4.2: Axial and circumferential strain under hydrostatic pressure in the four approximations discussed in this chapter. The first three rows are for radii typical for single walled nanotubes. The next two rows demonstrate the excellent agreement between the elastic continuum model and *ab initio* calculations. The experimental value for graphite is listed for comparison.

following how to derive the vibrational frequencies in nanotubes under pressure by making reference to the rolled up graphene sheet.

The basic idea of the approach is depicted in Fig. 4.5. The figure shows schematically a (6,6) and an (8,4) tube under exaggerated hydrostatic pressure (corresponding to $\approx 100\,\mathrm{GPa}$). Because of the larger strain in the radial than in the axial direction, hydrostatic pressure changes not only the area of the graphene hexagons but also distorts their shape. The sixfold hexagonal symmetry is broken under pressure, which splits the doubly degenerate E_{2g} graphene optical modes into a higher and lower frequency component vibrating parallel and perpendicular to the higher strain direction, respectively. For the nanotubes this corresponds to a stronger pressure dependence for a phonon eigenvector where the atomic displacement is along the circumferential direction than for an axial vibration.

For a quantitative analysis I unwrap the tube to a narrow graphene rectangle. The strain in the graphene sheet due to $\varepsilon_{\theta\theta}$ and ε_{zz} reads (after transformation to the principle axis of graphene)[99]

$$\varepsilon = \begin{pmatrix} \varepsilon_{\theta\theta}\cos^2\Theta + \varepsilon_{zz}\sin^2\Theta & \frac{1}{2}\sin(2\Theta)(\varepsilon_{zz}-\varepsilon_{\theta\theta}) \\ \frac{1}{2}\sin(2\Theta)(\varepsilon_{zz}-\varepsilon_{\theta\theta}) & \varepsilon_{\theta\theta}\sin^2\Theta + \varepsilon_{zz}\cos^2\Theta \end{pmatrix} \tag{4.11}$$

separated into the hydrostatic and non-hydrostatic components

$$= \frac{1}{2}(\varepsilon_{\theta\theta}+\varepsilon_{zz})\begin{pmatrix} 1 & 0 \\ 0 & 1 \end{pmatrix} + \frac{1}{2}(\varepsilon_{\theta\theta}-\varepsilon_{zz})\begin{pmatrix} \cos 2\Theta & \sin 2\Theta \\ \sin 2\Theta & -\cos 2\Theta \end{pmatrix}; \tag{4.12}$$

where Θ is the chiral angle. Obviously, the deformation of the graphene elementary cell given in Eq. (4.11) is not purely hydrostatic for any chirality.

To find the phonon frequencies in the strained graphene cell I expand the dynamical equation to terms linear in strain[114,117]

$$-m\ddot{v}_i = m\omega_0^2 v_i + \sum_{klm} K^{(1)}_{ikml}\varepsilon_{lm}v_k; \tag{4.13}$$

where $\boldsymbol{v}$ is the atomic displacement, m the reduced mass of the atoms, and ω_0 the strain free frequency. The second summand describes the change in phonon frequency due to the strain;

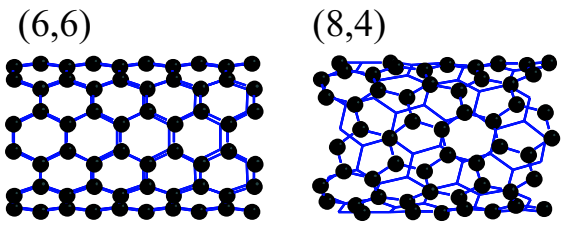

Figure 4.5: Schematic picture of the distortion of a (6,6) and an (8,4) nanotube under hydrostatic pressure, i.e., $\varepsilon_{\theta\theta} = 2\varepsilon_{zz}$. The strain is fully symmetric in the point groups of the tubes, but not for the graphene hexagon. The hexagon area as well as its shape are altered by applying pressure to a nanotubes.

$K_{ikml} = \partial K_{ik}/\partial \varepsilon_{kl}$ is the change in the spring constants of the strained crystal. The symmetric tensor $K^{(1)}$ has only three nonzero components because of the hexagonal symmetry of the graphene sheet, namely,[103]

$$\begin{aligned} K_{1111} = K_{2222} &= m \cdot \tilde{K}_{11} \\ K_{1122} &= m \cdot \tilde{K}_{12} \\ K_{1212} &= m \cdot \frac{1}{2}(\tilde{K}_{11} - \tilde{K}_{12}) . \end{aligned} \tag{4.14}$$

From the dynamical equation (4.13) I obtain an secular equation with the help of the $K^{(1)}$ tensor components in Eq. (4.14) and the strain in the graphene sheet (4.11)[114,117]

$$\frac{1}{2} \begin{vmatrix} (\tilde{K}_{11}+\tilde{K}_{12})(\varepsilon_{\theta\theta}+\varepsilon_{zz})+ & (\tilde{K}_{11}-\tilde{K}_{12})(\varepsilon_{\theta\theta}-\varepsilon_{zz})\sin 2\Theta \\ +(\tilde{K}_{11}-\tilde{K}_{12})(\varepsilon_{\theta\theta}-\varepsilon_{zz})\cos 2\Theta - 2\lambda & \\ (\tilde{K}_{11}-\tilde{K}_{12})(\varepsilon_{\theta\theta}-\varepsilon_{zz})\sin 2\Theta & (\tilde{K}_{11}+\tilde{K}_{12})(\varepsilon_{\theta\theta}+\varepsilon_{zz})- \\ & -(\tilde{K}_{11}-\tilde{K}_{12})(\varepsilon_{\theta\theta}-\varepsilon_{zz})\cos 2\Theta - 2\lambda \end{vmatrix} \equiv 0, \tag{4.15}$$

where $\lambda = \omega^2 - \omega_0^2$ is the difference between the squared strain dependent frequency ω and the frequency in the absence of strain ω_0. Diagonalizing Eq. (4.15) thus yields the relative shift of the phonon energy in the strained graphene sheet.[99]

$$\frac{\omega - \omega_0}{\omega_0} = \frac{\Delta\omega}{\omega_0} \approx \frac{\lambda}{2\omega_0^2} = \frac{(\tilde{K}_{11}+\tilde{K}_{12})}{4\,\omega_0^2}(\varepsilon_{\theta\theta}+\varepsilon_{zz}) \pm \frac{1}{2}\,\frac{(\tilde{K}_{11}-\tilde{K}_{12})}{2\,\omega_0^2}\,(\varepsilon_{\theta\theta}-\varepsilon_{zz}) . \tag{4.16}$$

In Eq. (4.16) two phonon deformation potentials relate the frequency shift with strain. The first deformation potential $(\tilde{K}_{11}+\tilde{K}_{12})/4\omega_0^2 = -\gamma$ is the Grüneisen parameter, which describes the frequency shift for an hydrostatic deformation of the graphene hexagon. The splitting of the modes under shear strain comes from the second term.

Interestingly, the frequency shift is independent of the chirality of nanotube, i.e., the way I cut and strained the graphene rectangle. A mode vibrating parallel to $\varepsilon_{\theta\theta}$, the high-strain direction, always shifts according to the plus solution of Eq. (4.16), whereas vibrations parallel to ε_{zz} have a frequency shift below the hydrostatic contribution. Between these two limiting cases the phonon modes show a dispersion similar to, e.g., the dispersion in wurzite crystals. The dependence of the phonon frequency on the displacement direction of the eigenvector in strained materials is discussed in two papers by Anastassakis.[118,119]

4.3.1. Pressure dependence of the phonons frequencies in nanotubes

The discussion of the last section was restricted to the unwrapped nanotube and the resulting nonhydrostatic deformation of graphene. I now roll up the sheet again bearing in mind the

phonon energies in Eq. (4.16). For armchair tubes – and achiral tubes in general – I found in Chapter 2. the complete set of phonon eigenvectors by group projection operators and some general assumptions on the strength of the force constants. The Raman active high-energy A_{1g} ($_0A_0^+$) and E_{2g} ($_0E_2^+$) phonons are vibrating along the circumference in armchair tubes, while the E_{1g} ($_0E_1^-$) mode has a purely axial eigenvector. The two circumferential vibrations are according to Eq. (4.16) expected to have a pressure derivative higher than the axial E_{1g} mode by $(\tilde{K}_{11}-\tilde{K}_{12})(\varepsilon_{zz}-\varepsilon_{\theta\theta})/2\omega_0^2$. In contrast, I presented in Section 4.1. Raman experiments where the pressure slope was the same for all high-energy peaks. Before discussing this apparent contradiction I briefly turn to metallic nanotubes, which indeed show the expected splitting in experiment.

In Fig. 4.6 I present the phonon frequencies of metallic nanotubes as a function of applied hydrostatic pressure. The insets show the Raman spectra at a low (0.34 GPa) and high-pressure (9.9 GPa) point. The intensity decrease, as in semiconducting nanotubes, is observed in metallic tubes as well. The analysis of the data is difficult due to the close proximity of the modes. Additionally, under pressure, the broadening of the peaks leads to a merging of the lines (see insets in Fig. 4.6). Nevertheless, when fitting the high-energy peak with three similarly sized Lorentzians or with a focus on the low and high-energy flanks for pressures up to 10 GPa, I find a splitting of 0.56 TPa^{-1} between the peaks at 1544 and 1565 cm^{-1} and a hydrostatic shift of 3.8 TPa^{-1}. The third peak, at 1592 cm^{-1}, which has been assigned to semiconducting tubes, has a pressure derivative of 3.8 TPa^{-1}.

For the comparison between the experiments and the theory developed in the last two sections I need to know the two phonon deformation potentials in Eq. (4.16). Table 4.3 lists a compilation of measured and calculated results in carbon based material. The shear de-

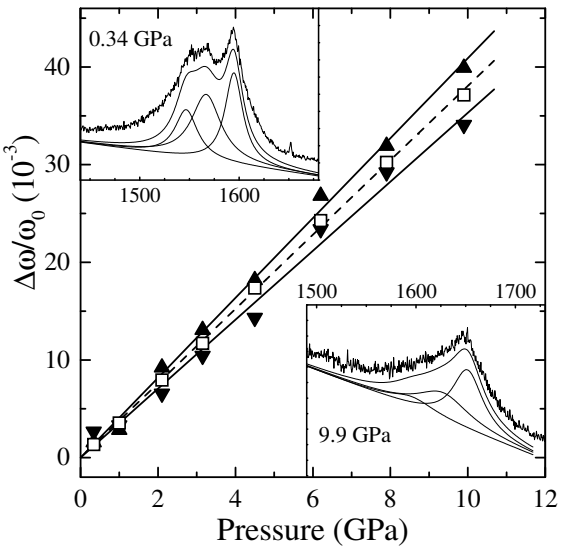

Figure 4.6: High-pressure Raman scattering on metallic nanotubes excited with an excitation energy 1.91 eV. The phonon energies were normalized to the value at ambient pressure. Up triangles refer to the mode at 1565 cm^{-1} at zero pressure, down triangles to the one at 1544 cm^{-1}, and the open squares to the 1592 cm^{-1} mode. The latter mode is usually assigned to semiconducting nanotubes at this excitation energy.[44] The insets show Raman spectra (Raman shift in cm^{-1}) at $p = 0.34$ and 9.9 GPa and the fit to the data.

	γ	$\frac{(\tilde{K}_{11}-\tilde{K}_{12})}{2\,\omega_0^2}$
nanotubes[33,76]	1.24	0.41
graphite	1.59[113]	0.66[120]
diamond (cubic)[121]	1.50	0.51

Table 4.3: Phonon deformation potentials for nanotubes (tight-binding calculation), graphite (experiment and *ab-initio* calculation), and diamond (experiment). The shear deformation potential in diamond is for an applied uniaxial stress along the (001) direction.

formation potentials of graphene or graphite are not accessible experimentally, because of graphite's brittleness when an uniaxial stress is applied along the basal plane. Using the circumferential and axial strain components obtained from elasticity theory and the elastic constant calculations by Lu[109] together with the phonon deformation potentials for graphene and nanotubes I find an hydrostatic component $\gamma\cdot(\varepsilon_{zz}+\varepsilon_{\theta\theta}) = -(3.8\pm1)\,\mathrm{TPa}^{-1}\,p$ and a shear strain splitting $(\tilde{K}_{11}-\tilde{K}_{12})(\varepsilon_{zz}-\varepsilon_{\theta\theta})/2\omega_0^2 = -(0.6\pm0.2)\,\mathrm{TPa}^{-1}\,p$. Both values are in very good agreement with the experimental values for metallic nanotubes. The large uncertainty is due to the uncertainties in the strain determination as well as in the phonon deformation potentials. Precise measurements of the elastic properties of carbon nanotubes are desirable to further clarify the high-pressure measurements.

The pressure dependence of the Raman peaks in metallic nanotubes is in general agreement with the idea of predominantly axial and circumferential high-energy Raman active vibrations. On the other hand, in semiconducting tubes only the hydrostatic part of the pressure shift was observed experimentally. The possible explanation for the absence of the shear strain splitting lies in the phonon eigenvectors of chiral nanotubes. In contrast to the higher-symmetry achiral tubes the phonon eigenvectors of chiral tubes are not fixed by symmetry because of the missing mirror planes, see Section 2.4. A distribution of displacement directions with respect to the circumference or the tube axis washes out the splitting introduced by the shear deformation in Eq. (4.16).[76,118] Only the hydrostatic component is then observed experimentally. To find out how the eigenvectors of chiral tubes actually look like I calculated the phonons of two selected chiral and two achiral nanotubes by first principles calculation.

4.4. Phonon eigenvectors of chiral tubes

The purpose for the *ab initio* calculations of the phonon eigenvectors in carbon nanotubes was to get a qualitative insight into the vibrational properties of chiral nanotubes. The large number of carbon atoms in the unit cell therefore restricted the possible nanotubes to examples with small diameters. Most other reports on *ab initio* calculations of nanotubes took the opposite approach, i.e., selecting diameters close to the one present in real samples, but

therefore had to stick to achiral tubes.[122–125] The higher achiral symmetry, however, often imposes a too severe restriction on the properties of chiral tubes as we will see in the following.

In the *ab initio* calculations I set up the dynamical matrix from the force constants obtained by successively displacing two carbon atoms and using the screw axis symmetry as described in detail in Appendix I.. Neither the mirror planes of achiral tubes nor the horizontal rotation axes of chiral tubes were used explicitly (see also Chapter 2.). The deviations from those symmetry operations in the eigenvectors measure the numerical accuracy of my calculations. The dynamical matrix was then diagonalized to yield the phonon frequencies and eigenvectors. In analyzing my results I concentrate on the eigenvectors and displacements, since the curvature effects in the calculated 8 Å diameter nanotubes strongly alter the force constants and phonon frequencies making them not suitable for a direct comparison to experiment.[12,14,126]

4.4.1. Eigenvectors in small nanotubes*

I first present the eigenvectors and frequencies of the two achiral nanotubes. The excellent agreement between my calculated and the symmetry imposed eigenvectors made me confident about the calculational procedure. Figure 4.7a) and Table 4.4 show the A_{1g}, E_{1g}, and E_{2g} eigenvectors and frequencies of the high-energy modes in (6,6) and b) in (10,0) nanotubes. All high-energy modes are found to be softened compared to graphene (1660 cm^{-1} in my calculations) in these fairly small tubes, which is in good agreement with previous *ab initio* calculations and experimental findings.[40,106] The softening appears to be a little overestimated for the A_1 circumferential mode, which is of A_{1u} symmetry in the (10,0) tube and at similar frequency (1550 cm^{-1}) as the A_{1g} mode in the (6,6) armchair tube. Note that the ordering of the frequencies is non-trivially changed in the calculated tubes as compared to simple zone folding. Both confinement and curvature effects are, however, much stronger

*This section and parts of the following section are taken from Ref. 12. I did the calculations and the analysis presented in the reference under supervision of Pablo Ordejón and Christian Thomsen who co authored the paper.

Table 4.4: Frequencies and angle α between the displacement and the circumferential direction for the Raman-active high-energy modes and the radial breathing mode in achiral nanotubes. The largest deviation (4°) from the symmetry imposed displacement was found for the E_{2g} mode of the zig-zag tube.

	(6,6)		(10,0)	
	ν (cm^{-1})	α (°)	ν (cm^{-1})	α (°)
RBM	285	0	289	2
A_{1g}	1545	0	1604	88
E_{1g}	1600	90	1606	2
E_{2g}	1629	0	1552	86

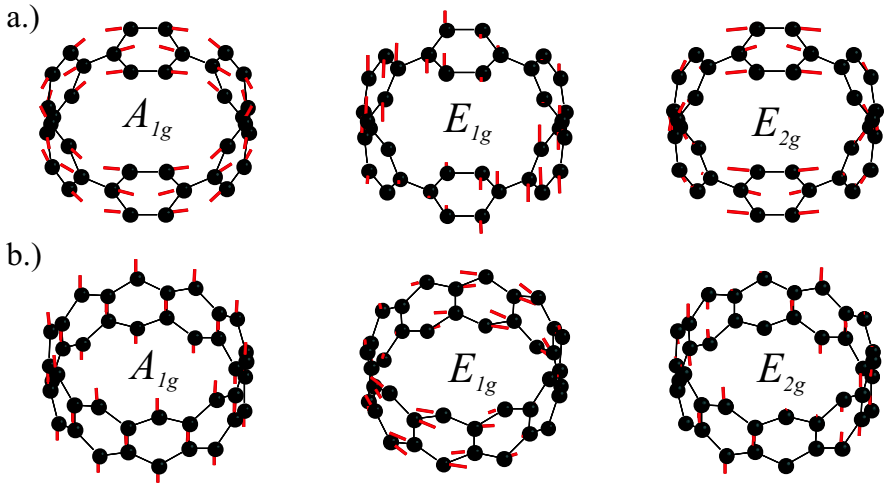

Figure 4.7: Raman active A_{1g}, E_{1g}, and E_{2g} high-energy modes a) of a (6,6) nanotubes and b) of a (10,0) nanotube.

in the calculated tubes than in real samples with a typical mean diameter ≈ 14 Å. In phonon calculations for achiral tubes of different diameter Dubay and Kresse found these effects to decrease rapidly with increasing diameter.[126] The calculated frequencies of the radial breathing mode in Table 4.4 are for achiral nanotube bundles. As can be seen in Fig. 4.7 the displacement patterns are in excellent agreement with the symmetry requirements. I found that the angle α between the atomic displacement and the circumference deviates by at most 5° from the circumferential $\alpha = 0^\circ$ or axial $\alpha = 90^\circ$ direction, showing the numerical accuracy of the calculation. I stress again that in the calculation of the force constants the mirror symmetries were not explicitly used.

In chiral nanotubes the atomic displacements are no longer, in general, along the cylindrical axes. In Fig. 4.8a.) I show an A_1 mode of an (8,4) tube and in b.) of a (9,3) tube. It can be seen that the displacement is along the circumference in the (8,4), but parallel to the bonds in the (9,3) nanotube. The smallest angle between the carbon-carbon bonds and the circumference in the (9,3) tube is $30^\circ - \theta = 16.1$, which coincides with the displacement direction as given

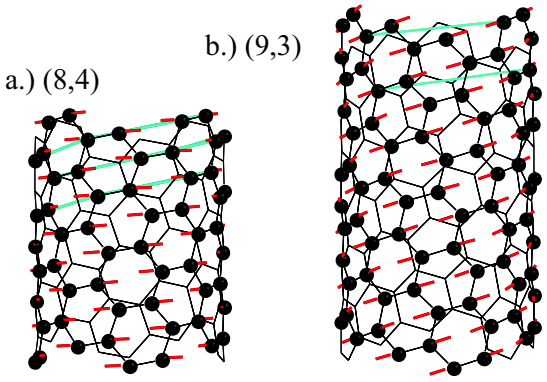

Figure 4.8: a) A_1 high-energy eigenvector of an (8,4) nanotube with a frequency of 1505 cm^{-1}. The atomic displacement is parallel to the circumference, i.e., $\alpha = 3^\circ$ is close to zero. b) A_1 high-energy eigenvector of a (9,3) tube (1627 cm^{-1}). The displacement is parallel to the carbon-carbon bonds. The direction of the helix in both tubes, which is obtained from the screw axis operation, is indicated by the gray lines.

Table 4.5: Frequencies and displacement directions for the high-energy and the radial breathing mode in chiral nanotubes. If the displacement direction was found not to be constant around the tube's circumference the mean value of α was given.

	(8,4)		(9,3)	
	ν (cm^{-1})	α (°)	ν (cm^{-1})	α (°)
RBM	275	1	292	1
A_1	1670	-87	1627	16
A_1	1505	3	1519	-74
E_1	1610	33	1620	38
E_1	1591	-59	1607	-51
E_2	1626	-6	1638	7
E_2	1554	85	1587	-84

in Table 4.5. In the (8,4) tube I also found vibrations along the bond direction, but they were of B_1 and B_2 symmetry and hence not optically active.

I now take a look at the degenerate modes in chiral tubes. In Fig. 4.9 I show an E_1 eigenvector of an (8,4) nanotube. I successively rotated the nanotube by 32° to show the reader how the eigenvector evolves when going around the nanotube. As expected the magnitude of the atomic displacement (the length of the ticks) is modulated by a $\sin\varphi$ function. Contrary to what is generally expected, however, the direction of the displacement varies as well. Whereas the tick on the highlighted atom is perpendicular to one of the carbon-carbon bonds in the first picture, i.e., $\alpha \approx 40°$, they are almost parallel to the bonds with $\alpha \approx 10°$ in last two pictures; Table 4.5 lists the mean value $\alpha = 33°$. For the E_2 eigenvector in the (8,4) tube no such variation is seen. The same sequence as in Fig. 4.9 is presented in Fig. 4.10 for the E_2 mode with a frequency of 1626 cm^{-1}. The atomic displacement is roughly parallel to the circumference in all four pictures.

The angular dependence of the direction of the eigenvectors becomes more obvious when plotting the atomic displacement along the z axis versus the circumferential displacement (Fig. 4.11). The first two diagrams at the top in Fig. 4.11 corresponds to the A_1 high-energy

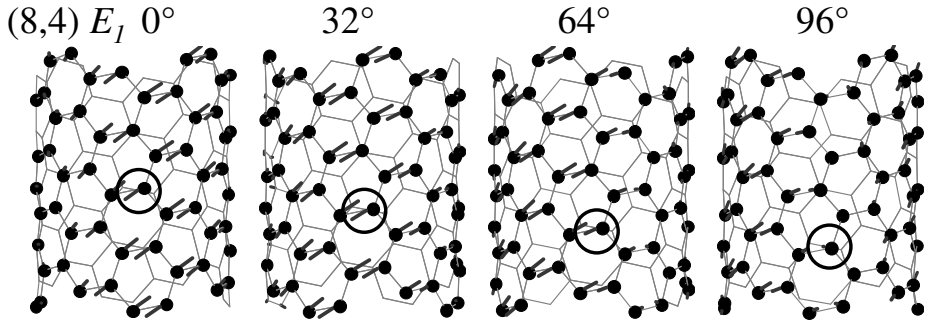

Figure 4.9: Doubly-degenerate E_1 eigenvector of an (8,4) tube with a frequency of 1610 cm^{-1}. The sequence shows the change in displacement when going around the tube in steps of 32°. The atoms which are highlighted by the small circles are connected by the screw symmetry of the tube.

modes in the (8,4) and (9,3) tube. For simplicity I considered only the displacement of the atoms belonging to the same graphene sublattice. Totally symmetric modes then show up as a single point in such a plot. The dashed lines point along the carbon-carbon bonds; the coincidence between the displacement and the bond direction in the (9,3) nanotube is obvious. A B symmetry mode (not shown) would be seen as two points in the $z-xy$ displacement diagram, because the character of the screw axis generator is -1.[45] Open ellipses describe E symmetry eigenvectors with a varying or "wobbling" displacement direction. The principal axis of the ellipse gives the average angle of the eigenmode, i.e., α. The open ellipse with $\alpha \approx 33^\circ$ of the (8,4) E_1 symmetry mode corresponds to the eigenvectors in Fig. 4.9. The degenerate eigenmode has the same ellipse. In general, the displacement of a degenerate eigenmode is obtained from a given eigenvector by a 90° rotation of the coordinate system around the z axis. The relationship between the axial and the circumferential displacement is thus the same for degenerate phonons. Two ellipses perpendicular two each other represent degenerate modes of the same symmetry but different frequencies. Correspondingly, the middle diagram of the (8,4) tube in Fig. 4.11 shows both the 1610 ($\alpha = 33^\circ$) and the 1591 cm^{-1} (-59°) E_1 eigenvector.

In the middle panel to the right I depict the displacement for the E_1 modes in the (9,3) nanotube. The xy and the z displacment are again of similar magnitude, i.e., $\alpha \approx 40^\circ$ and 50°, but they are now in phase and yield a constant direction of the atomic displacement around the tube. Two other examples of almost closed ellipses are the E_2 eigenmodes in both tubes (lowest panels in Fig. 4.11). Although the eigenvectors are in fact wobbling, the magnitude of the, e.g., the z displacement for the 1626 cm^{-1} E_2 (8,4) mode is very small. Therefore, the variation is not observable in the full eigenmode plot of Fig. 4.10.

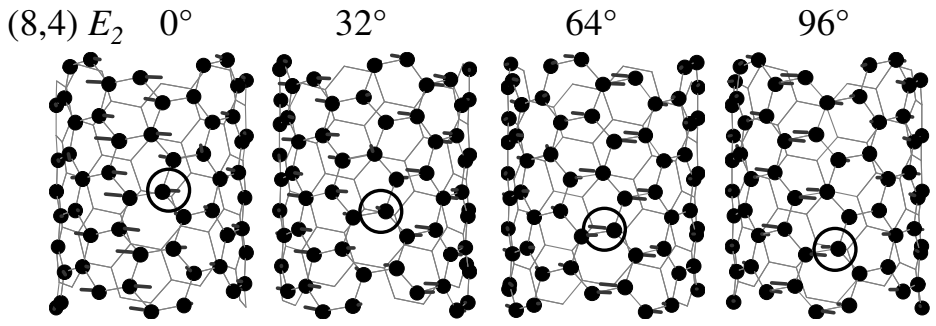

Figure 4.10: E_2 high-energy mode of an (8,4) nanotube with a calculated frequency of 1626 cm°. The atomic displacement is along the circumference and, in contrast to Fig. 4.9, no wobbling is evident. The modulation of the displacement magnitude by a $\sin 2\varphi$ around the circumference is nicely seen when following the highlighted atom.

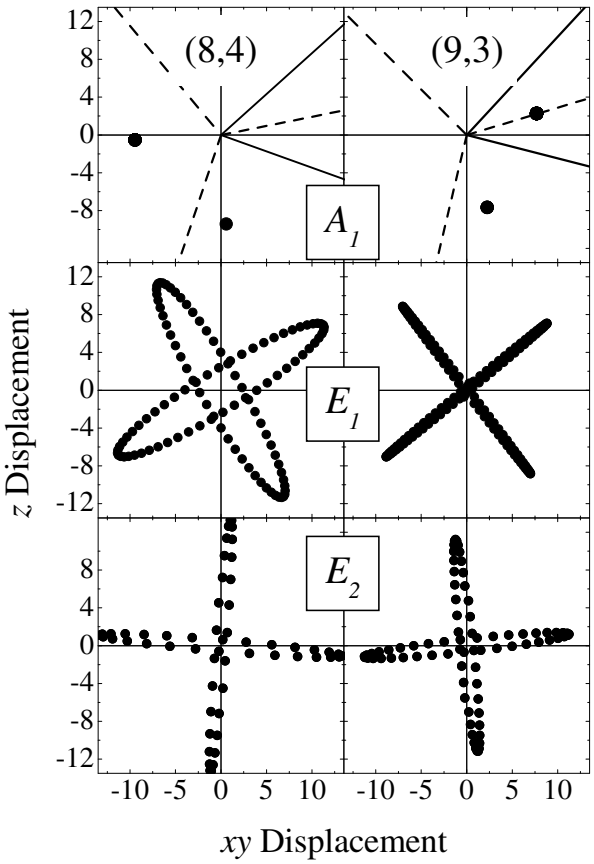

Figure 4.11: z component of the displacement versus the xy circumferential component. Top: A_1 high-energy eigenvectors of an (8,4) tube (left) and a (9,3) tube (right). The dashed lines point into the direction of the carbon-carbon bonds, the full lines are parallel to $\boldsymbol{a_1}$ and $\boldsymbol{a_2}$. Middle: E_1 eigenvectors of the two chiral nanotubes. The atomic displacement direction is strongly varying in the (8,4) nanotube resulting in an open displacement ellipses. In the (9,3) nanotube the z and circumferential component are similar in magnitude but with an almost vanishing phase difference. Bottom: E_2 eigenvectors of the chiral tubes. The small z or xy component result in a closed ellipse almost parallel to the circumference or the nanotube axis.

The symmetry of the phonon together with its displacement ellipse fully determine the phonon eigenvectors. The symmetry yields the $\sin m\varphi$ function of the axial and circumferential components, whereas the principle axes of the ellipses specify the relative magnitude and the phase shift between the two components.

In Section 2.4. I discussed that symmetry arguments are not able to predict the phonon eigenvectors of chiral nanotubes. The absence of mirror planes and the low-symmetry confinement wave vectors in chiral tubes affect their vibrational properties in a fundamental manner. In particular, a classification of the high-energy modes into LO and TO vibrations is not applicable to chiral nanotubes.

4.4.2. Diameter and pressure dependence of the eigenvectors

The crucial point for the wobbling and the mixed LO-TO character of the non-degenerate modes in chiral tubes is the splitting in the axial and circumferential force constants introduced by confinement and curvature. Naturally, the question arises how the modes and the eigenvectors, in particular, will evolve if these two effects are reduced as in tubes with larger diameter. To answer this question by first principles methods I needed to calculate a series of

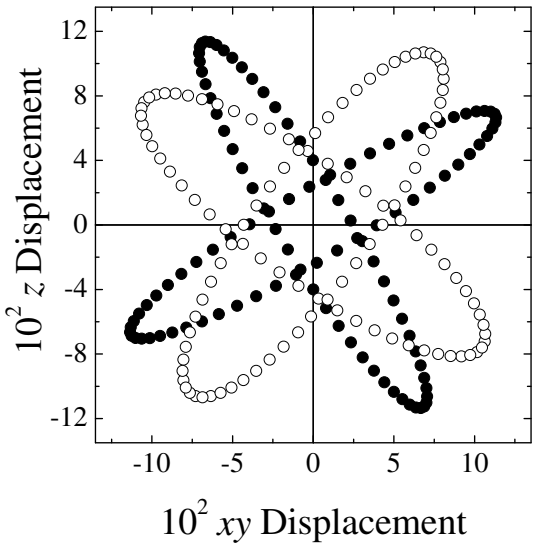

Figure 4.12: Phonon eigenvectors with an reduced splitting of the axial and circumferential force constants. The eigenvector calculated by first principles methods is shown by the full dots (same as shown in Fig. 4.11 in the (8,4) E_1 diagram). The open dots are the displacement ellipses for the E_1 high-energy eigenvectors after I slightly modified the force constants. The splitting of the two E_1 frequencies was reduced by 25 %.

chiral nanotubes with the same chiral angle. The next candidates for the (8,4) and (9,3) series are a (12,8) and (12,6), which are beyond our computational capability. Nevertheless, to obtain general insight into the eigenmode behavior with a reduced splitting, I slightly changed the *ab initio* force constants to make them more similar. The relative splitting between, e.g., the two E_1 high-energy phonons of the (8,4) tube was reduced by 25 %. In Fig. 4.12 I compare the old displacement ellipses (full dots) with the ellipses obtained from the modified force constants (open dots). It is nicely seen that the two eigenvectors look more degenerate, i.e., the ellipses are more open. In the limit of identical force constants both eigenvectors will degenerate to a circle. This limit corresponds to graphene, a tube with a infinite diameter, and the displacement direction can be chosen arbitrarily as required. The splitting of the force constants in real nanotubes will be less than in the small diameter nanotubes discussed here, but different from zero. The wobbling and the mixed LO-TO character of the high-energy phonons are thus even more dominant in real samples, because the wobbling is stronger for the modified force constants in Fig. 4.12 than for the *ab initio* calculated.

Interestingly, my artificial modification of the force constants resembles very much the effects expected for the eigenvectors under hydrostatic pressure: At ambient pressure the curvature of the tube's wall softens the force constants in the circumferential direction, whereas the axial force constants are not affected to first order approximation. Applying hydrostatic pressure to the nanotubes reduces the radius of the tube by a factor of ≈ 2 more than the axial direction as derived in Section 4.2. For the phonons this means that the circumferential force constants increase more rapidly than the axial force constants [see Eq. (4.16)]. Consequently, the curvature induced splitting of the forces reduces under pressure, i.e., a similar effect as introduced by hand in the previous paragraph. In Fig. 4.13 I show the displacement ellipses for the E_{1g} eigenvector in an (8,4) nanotube bundle calculated for pressures up to 8 GPa.

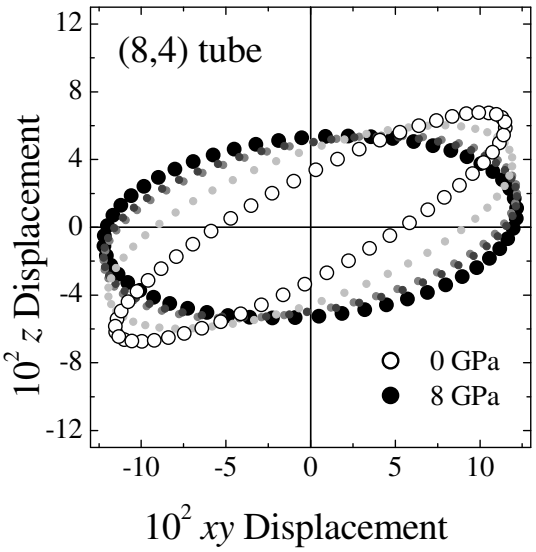

Figure 4.13: Pressure dependence of the E_{1g} high-energy eigenvector in the (8,4) nanotube. The white to black points show the displacement ellipse for increasing pressure from 0 to 8 GPa. Similar as observed for the manilupation of the force constants by hand, the "degeneracy" of the phonon eigenvector increases with pressure.

Indeed qualitatively the same behavior as in Fig. 4.12 is observed in Fig. 4.13 as well. The bad news is that the pressure dependence of the eigenvector itself makes the application of Eq. (4.16) for the phonon frequency shift under pressure difficult. In deriving the relation I implicitly assumed a constant direction of the atomic displacement in the strained crystal. A detailed analysis of the first principles calculation of the frequencies and eigenvectors will help in gaining a more fundamental understanding of the vibrational properties at ambient and high pressures.

4.5. Summary

In this chapter I discussed the elastic and vibrational properties of carbon nanotubes under high hydrostatic pressure and presented *ab initio* calculations of the phonon eigenvectors in chiral tubes. The phonon eigenvectors in chiral nanotubes are, in general, of mixed circumferential and axial character. This mixed character successfully explains the high-pressure experiments. On the other hand, it implies that interpreting the two most prominent peaks in the high-energy Raman spectrum of carbon nanotubes as being confined LO and TO vibrations is incorrect.

To describe the elastic response of nanotubes to pressure I developed a continuum model of carbon nanotubes within elasticity theory. The tube was approximated as a hollow cylinder made out of graphene with a finite wall thickness and closed end. The linear modulus in the circumferential or radial direction was found to be 2-3 times higher than in the axial direction, i.e., the deformation of the nanotubes unit cell under pressure is not fully hydrostatic. Instead a shear strain is present in the graphene hexagons. Because of this nonhydrostatic

strain component the E_{2g} graphene optical mode is expected to split; its frequency under pressure depends on the direction of the atomic displacement. For the nanotubes this implies different pressure slopes for axial and circumferential vibrations, whereas Raman experiments show uniform pressure dependencies of all high-energy modes. I proposed that the apparent contradiction is resolved by the phonon eigenvectors, which may be of mixed LO-TO character in chiral nanotubes.

To prove my idea I performed *ab initio* calculations of the phonons eigenvectors of two chiral nanotubes. The calculated atomic displacement of the nondegenerate modes in chiral tubes indeed pointed into various directions as I expected. Moreover, the degenerate E eigenvectors even showed a "wobbling" of the displacement direction when going around the circumference. This wobbling is seen as open ellipses in a plot of the z versus the circumferential displacement component; which is a way to uniquely specify a phonon eigenvector in nanotubes.

Chapter 5

Band Structure of Isolated and Bundled Nanotubes

The electronic structure of carbon nanotubes is characterized by a series of bands (sub- or minibands) arising from the confinement around the nanotube's circumference. The electronic properties are a focus in nanotube research because of their potential application, e.g., in transistors and integrated circuits. My attention was originally drawn to electronic structure calculations by the crucial role the optical absorption plays in resonant Raman scattering. The critical points in isolated nanotubes, which are at the Γ point, the Brillouin zone boundary, and sometimes also at $k_z \approx 2\pi/3$, give rise to the square-root like singularities in the density of states typical for one-dimensional systems.[34,35] These singularities were directly studied by scanning tunneling experiments[127–129] and also identified in Raman scattering on individual nanotubes.[130] When the experimental findings are compared to a theoretical band structure usually a zone-folding approach of graphene is pursued. This simple picture is frequently expanded to small tubes (diameter $d \lessapprox 10\,\text{Å}$) and to bundles of tubes, although Blase *et al.*[131] showed convincingly that rehybridization has a significant effect on the electronic states. Also ignored by this approach are intramolecular dispersions which are known to be quite large in solid C_{60} and graphite.[132,133]

In this chapter I study the electronic band structure of isolated and bundled nanotubes. Particular attention I pay to a comparison of first principles results to the simpler (but quicker) tight-binding and zone-folding pictures. In Section 5.1. I introduce zone-folding together with the graphene band structure and in Section 5.1.2. the widely used tight-binding approximation of the graphene π orbitals. The body of this chapter are *ab initio* calculations of different chiral and achiral nanotubes. The effects of hybridization by curvature and bundling

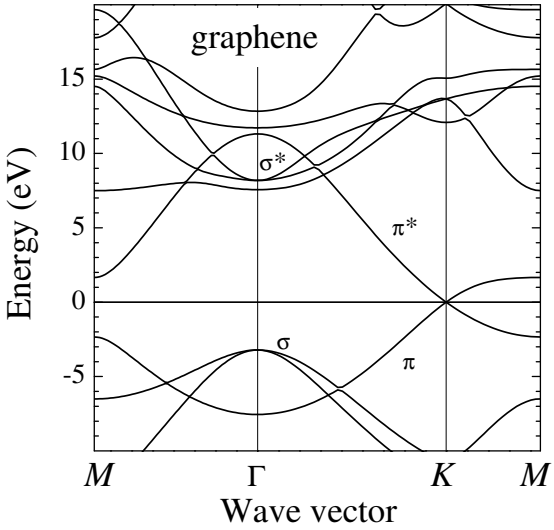

Figure 5.1: Electronic band structure of graphene calculated with SIESTA. The electronic bands cross at the *K* point of the graphene Brillouin zone. For the labeling of the special points in the Brillouin zone the same notation as in graphite was used. The irreducible domain in graphene thus corresponds to a cut in the Γ*KM* plane of the Brillouin zone shown in Fig. 5.2b).

of the tubes on the band structure will be considered in detail. In Section 3.3. I compare my theoretical results to STM and Raman measurements.*

5.1. Band structure of graphene

The electronic band structures of graphene and graphite were studied for decades both experimentally and theoretically.[63, 94, 133, 135–142] I first briefly discuss the band structure of these two materials before showing how to obtain the nanotube electronic dispersion by zone-folding of graphene.

Graphene is formed by a single sheet of carbon atoms placed onto a hexagonal lattice. It is one of the classical examples for covalent bonding in solid state physics. The σ and σ^* states lying within the carbon plane are formed by s, p_x, and p_y hybridization; the nonhybridized, p_z derived π and π^* states point perpendicular to the sheet. The band structure of graphene calculated with SIESTA is shown in Fig. 5.1. The valence and conduction band (π and π^*) touch at the *K* point of the Brillouin zone making the material a zero gap semiconductor. The σ valence and conduction bands, on the other hand, are strongly separated in energy; the smallest transition energy is well above 10 eV.

The *ABAB* stacking of graphene yields graphite, one of the natural carbon forms. The interlayer coupling is very weak in graphite, thus allowing a reliable comparison between theory and experiment for the single sheet as well. Since the number of carbon atoms in the unit cell is doubled in graphite when compared to graphene, the electronic bands are expected to split

*Section 5.2. to 5.4. are mainly taken from Ref. 134, which is currently under review for publication in Physical Review B. The calculations and analyses I did under supervision by my thesis advisors, Christian Thomsen and Pablo Ordejón, who co authored the paper.

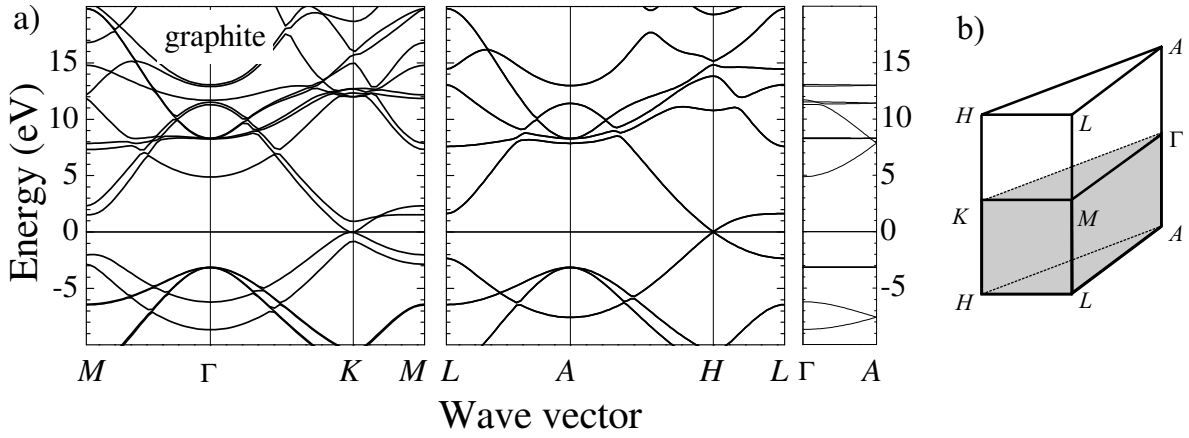

Figure 5.2: a) Electronic band structure of graphite in the Γ*KM* and the *AHL* plane. The panel to the right shows the interlayer dispersion from the Γ to the *A* point of the graphene Brillouin zone. The doubling of the carbon atoms splits the electronic bands of graphene in the Γ*KM* plane. Note the strong dispersion of the σ^* and π bands in the Γ*A* direction. b) Graphite Brillouin zone. The irreducible domain is shaded.

by the interlayer interaction. This behavior is nicely seen in the Γ*KM* plane in Fig. 5.2a). In the *AHL* directions, however, the splitting is forbidden by symmetry; the electronic bands shown in Fig. 5.2 are thus at least two-fold degenerate. An interesting consequence of the particularly large splitting of the σ^* ($\Delta E = 6.9\,\mathrm{eV}$) and the π (2.5 eV) states at the Γ point but their degeneracy at the *A* point is a strong interlayer dispersion of these two bands as can be seen in the right panel of Fig. 5.2a). In Table 5.1 I compare the calculated electronic energies of Fig. 5.2 to experimental values reported in the literature. The calculations of this work are in good agreement with previous theoretical papers;[133,142] the comparison to experiments is less satisfactory. In particular the energies of the lowest σ^* and the highest σ band deviate by $\approx 30-40\,\%$ from the measured values, which by Schabel and Martin[133] was attributed to an incomplete cancellation of the Hartree self-interaction in the local density approximation. On the other hand, the experimental values scatter considerably as well (up to 20 %); a compilation and discussion of different experiments can be found in Ref. 140.

5.1.1. Zone-folding

When the graphene sheet is cut and rolled to form a tube the wave vector around the circumference $\boldsymbol{k}_\perp$ is quantized by the boundary condition $c/\lambda = c \cdot k_\perp/2\pi = \text{integer}$ (c is the length of the chiral vector, see Chapter 2.). Along the z axis the wave vector $\boldsymbol{k}_z$ can still take continuous values. The allowed states in a nanotube thus correspond to parallel lines in the graphene Brillouin zone. To first approximation the electronic bands of a nanotube can be obtained by considering only the dispersion along those lines, which is known as the zone-folding or confinement approximation. This widely used approach in fact neglects the

	Conduction bands		Valence bands	
	Experiment (eV)	Calculation (eV)	Experiment (eV)	Calculation (eV)
π	12.2^a	11.5	-7.9^b	-6.2
		11.3	-8.9^b	-8.7
σ	3.6^c	4.9		
	7.4^b	8.2	-4.3^b	-3.1
	8.4^b	8.3		

[a] Willis *et al.*[143]
[b] Takahashi *et al.*[140]
[c] Fauster *et al.*[139]

Table 5.1: Electronic energies at the Γ point of graphite for some selected bands. The energies calculated in this work agree well with other *ab initio* calculations (not shown). The agreement between theory and experiment is found to be fairly good.

rolling up of the sheet. The nanotube is simply treated as a graphene rectangle. $\boldsymbol{k}_\perp$ and $\boldsymbol{k}_z$ are found from the chiral vector $\boldsymbol{c}$ and the translational period $\boldsymbol{a}$ [see. Eq. (2.1)]

$$\boldsymbol{k}_\perp = \frac{2n_1+n_2}{qn\mathcal{R}}\boldsymbol{k}_1 + \frac{2n_2+n_1}{qn\mathcal{R}}\boldsymbol{k}_2 \tag{5.1a}$$

$$\boldsymbol{k}_z = -\frac{n_2}{q}\boldsymbol{k}_1 + \frac{n_1}{q}\boldsymbol{k}_2, \tag{5.1b}$$

where n is the greatest common divisor of n_1 and n_2, $\mathcal{R}=3$ if $(n_1-n_2)/3n$ integer and $\mathcal{R}=1$ otherwise, and q is the number of graphene hexagons in the unit cell of the nanotube (see Section 2.1.). $\boldsymbol{k}_1$ and $\boldsymbol{k}_2$ are the reciprocal lattice vectors of graphene with $k_1=k_2=4\pi/\sqrt{3}a_0$, where a_0 is the lattice constant of graphene.

As an example I consider the Brillouin zone and the zone-folded bands of a (7,7) armchair tube. In armchair tubes the relation for the quantized vectors in Eq. (5.1a) simplifies to $\boldsymbol{k}_\perp = (\boldsymbol{k}_1+\boldsymbol{k}_2)/2n = (\boldsymbol{k}_1+\boldsymbol{k}_2)/14$. The quantization direction is the ΓM direction in armchair tubes. The graphene points in reciprocal space corresponding to the Γ point of the nanotube are given by $\boldsymbol{k}_\Gamma(m) = m\boldsymbol{k}_\perp$, where m is the z quantum number of the angular momentum with $-n=-q/2<m\leq q/2=n$ (see Chapter 2.). The band with $m=0$ thus always includes the Γ point of graphene; whereas $\boldsymbol{k}_\Gamma(n=7)=(\boldsymbol{k}_1+\boldsymbol{k}_2)/2$, i.e., the M point of the hexagonal Brillouin zone. The $\boldsymbol{k}_z$ vector of armchair tubes is given by $\boldsymbol{k}_z=(-\boldsymbol{k}_1+\boldsymbol{k}_2)/2$ pointing along the ΓKM line of the graphene Brillouin zone. The nanotubes zone boundary is located at $|-\boldsymbol{k}_1+\boldsymbol{k}_2|/4=\pi/a_0$. Since the K point of graphene is among the allowed nanotube k vectors, armchair nanotubes always show the crossing of the valence and conduction band typical for two-dimensional graphene, see Fig. 5.1. In Fig. 5.3a) I show the Brillouin zone of the (7,7) tube (white lines) on top of the graphene Brillouin zone. To emphasize the hexagonal symmetry the background is a contour plot of the graphene π^* or-

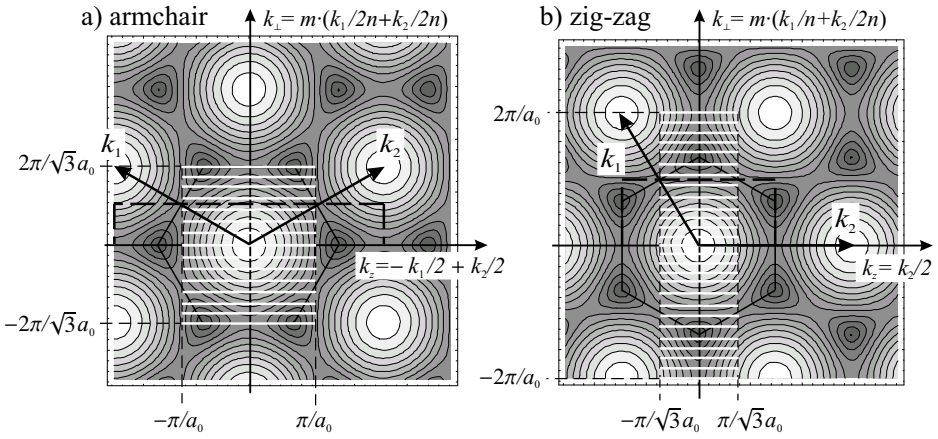

Figure 5.3: Brillouin zone of a) an (7,7) armchair and b) a (13,0) zig-zag tube. The background shows a contour plot of the electronic energies of the π^* orbitals of graphene to emphasize the hexagonal symmetry. $\boldsymbol{k}_1$ and $\boldsymbol{k}_2$ are the graphene reciprocal lattice vectors pointing along the ΓM direction. The white lines are the allowed k values in the nanotubes; the Γ point of the tubes corresponds to the states lying at $m\cdot\boldsymbol{k}_\perp$ [m takes integer values ranging from $(-n+1)\leq m\leq n$ in achiral nanotubes]. For larger armchair and zig-zag tubes the separation between the allowed lines becomes smaller, but the boundary of the tube's Brillouin zone remains the same as indicated in the figure. Note that the same Brillouin zone is obtained by restricting m to $(-n/2+1)\leq m\leq n/2$, but doubling the length of k_z [indicated by the dashed rectangle in a) and b)]. This corresponds to the so-called helical momenta $\tilde{m}$ and $\tilde{k}$; see Damnjanović *et al.*[45] for details.

bitals. In particular, this highlights the Umklapp rules for m and k when crossing the tube's zone boundary:[51,52] Following, e.g., the $m=0$ band beyond π/a_0 corresponds to changing m from 0 to 7 at the boundary and going back to the nanotube Γ point.

When instead of an armchair tube a zig-zag tube of similar diameter is considered the allowed lines are rotated by 30° around the Γ point and the Brillouin zone extension along k_z is reduced by $\sqrt{3}$. This is shown in Fig. 5.3b) for a (13,0) nanotube. Note that again the nanotube Γ point of the $m=n=13$ band coincides with the graphene M point. This is true in general even for chiral nanotubes. In chiral tubes the highest m quantum number is $m=q/2$. To find $\boldsymbol{k}_\Gamma(q/2)$ let me assume that I am dealing with an $\mathcal{R}=1$ nanotube. From Eq. (5.1) I obtain

$$\begin{aligned}\boldsymbol{k}_\Gamma(q/2) &= \frac{1}{n}\left(\frac{2n_1+n_2}{2}\boldsymbol{k}_1+\frac{2n_2+n_1}{2}\boldsymbol{k}_2\right)\\ &= \boldsymbol{G}+\frac{1}{n}\left(\frac{n_2}{2}\boldsymbol{k}_1+\frac{n_1}{2}\boldsymbol{k}_2\right),\end{aligned} \tag{5.2}$$

where $\boldsymbol{G}$ is a reciprocal lattice vector of graphene. The possible solution of Eq. (5.2) after subtracting reciprocal lattice vectors are $\boldsymbol{k}_1/2$, $\boldsymbol{k}_2/2$, and $(\boldsymbol{k}_1+\boldsymbol{k}_2)/2$. All three yield the M point of graphene. For the tube with $\mathcal{R}=3$ the same can be proven by using the condition $(n_1-n_2)/3n=$integer. When comparing the results of zone-folding and first principles

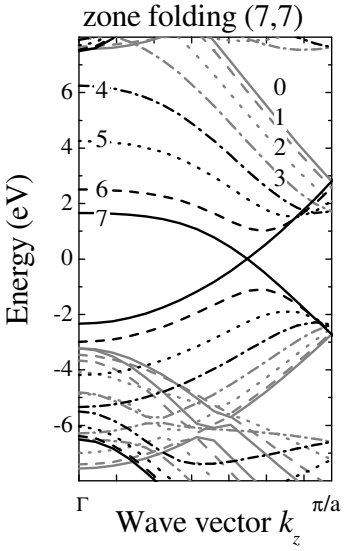

Figure 5.4: Electronic band structure of a (7,7) nanotube obtained within the zone-folding approximation. The underlying graphene electronic energies were calculated with SIESTA. The m quantum numbers of the π^* bands are indicated in the figure. Bands with the same m have the same style and color; black and gray lines of the same style were used for bands which are connected by the Umklapp rule and hence are degenerate at the corner of the Brillouin zone (see text for details).

calculations I will therefore use the electronic energies corresponding to the graphene M and Γ point to estimate the curvature effects on the electronic properties of nanotubes.

After having found the allowed k points in carbon nanotubes in terms of the chiral indices (n_1, n_2) and the reciprocal graphene lattice vectors zone-folding of the electronic bands is straightforward. In Fig. 5.4 I show the folded electronic dispersion of the (7,7) nanotube obtained from *ab initio* calculations of graphene. The folded π^* bands are labeled by their m quantum numbers. Similar calculations for other tubes I present in Section 5.2. in connection with first principles results.

5.1.2. Graphene π orbitals

The band structure of graphene around the Fermi level and for transition energies well above the optical range is determined by the π orbitals. The energetic separation of the bonding and antibonding σ bands is on the order of 10 eV. A common approximation for the low-energy electronic properties is hence a tight-binding Hamiltonian including only the carbon $2p_z$ states.[63] If, furthermore, the interaction is restricted to nearest neighbors only and the overlap of the p_z wave functions centered on different atoms is neglected a simple expression is found for the π bands in graphene[63]

$$E(\boldsymbol{k}) = \pm\gamma_0 w(\boldsymbol{k}) = \pm\gamma_0 \{3 + \cos\boldsymbol{k}\cdot\boldsymbol{a}_1 + 2\cos\boldsymbol{k}\cdot\boldsymbol{a}_2 + 2\cos\boldsymbol{k}\cdot(\boldsymbol{a}_1 - \boldsymbol{a}_2)\}^{1/2}, \qquad (5.3)$$

where γ_0 is the nearest neighbor interaction energy; the plus and minus sign hold for conduction and valence bands, respectively. Starting from Eq. (5.3) the electronic bands of carbon

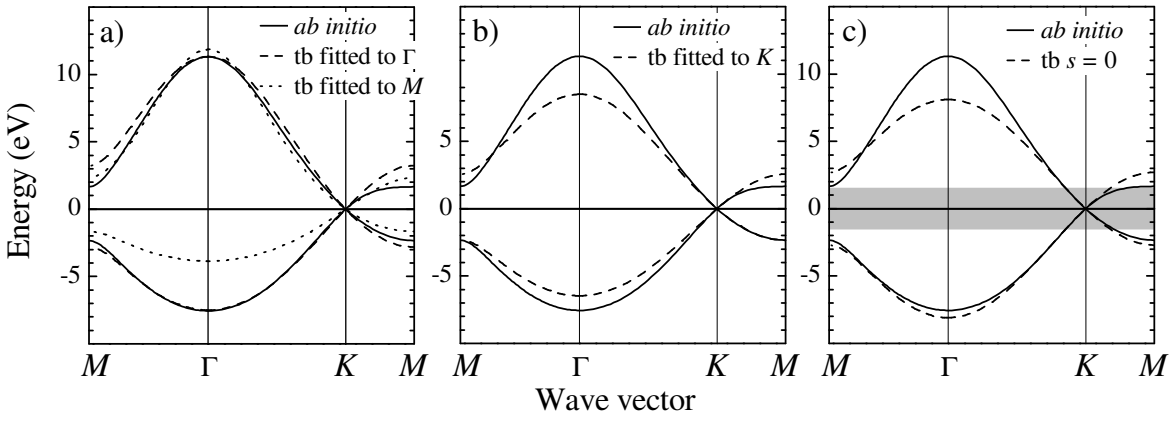

Figure 5.5: Comparison between the tight-binding approximation and *ab initio* calculations of graphene. The *ab initio* results are shown by the full lines in all three pictures. a) The dashed (dotted) lines are the tight-binding band structure obtained by fitting the *ab initio* Γ (M) point electronic energies. They correspond to $\gamma_0 = 3.01\,\mathrm{eV}$ and $s = 0.07$ ($\gamma_0 = 1.94\,\mathrm{eV}$, $s = 0.17$). b) Tight-binding band structure (dashed lines) obtained from fitting the linear dispersion around the Fermi level at the K point ($\gamma_0 = 2.45\,\mathrm{eV}$, $s = 0.04$). c) Tight-binding band structure (dashed lines) neglecting the nearest neighbor overlap. $\gamma_0 = 2.7\,\mathrm{eV}$ as used for the comparison to first principles results in the following sections. The area shaded in gray indicates the range of optical transition energies and below.

nanotubes can be found by zone-folding as described in the previous section. Many studies on the electronic and optical properties of nanotubes and graphite were based on this expression. For example, around the Fermi level Eq. (5.3) is to first order approximated by $E(\boldsymbol{k}) = \sqrt{3}a\,\gamma_0/2 \cdot |\boldsymbol{k} - \boldsymbol{k}_F|$. Its first derivative with respect to $\boldsymbol{k}_z$ yield the well-known universal density of states in carbon nanotubes as found by Mintmire and White[34,35]

$$\mathrm{DOS}(E) = \frac{2}{\sqrt{3}\,\gamma_0\,a} \cdot \frac{E}{\sqrt{E^2 - E_t^2}} \qquad \text{with} \qquad E_t = \frac{\gamma_0\,a}{\sqrt{3}\,d}|3t - n_1 + n_2|, \tag{5.4}$$

where t is integer. Since the universal density of states in Eq. (5.4) depends only on the diameter of the tubes, it is conveniently used to interpret experimental data obtained on bulk nanotube samples.[43,44,144] Higher order terms of the tight-binding electronic energies, however, introduce a dependence on the nanotube's chirality as well.[36,37]

The electronic energies in Eq. (5.3) are the same for the valence and conduction bands. Looking back at Fig. 5.1, it is apparent that the band structure of graphene is rather poorly approximated for $\boldsymbol{k}$ not being close to K. A slight improvement is obtained when the overlap between nearest neighbors is included, i.e., the asymmetry between bonding and antibonding states is taken into account. In terms of the function $w(\boldsymbol{k})$ defined in Eq. (5.3) the valence (E^-) and conduction (E^+) bands are then given by[37]

$$E^{\pm}(\boldsymbol{k}) = \pm\gamma_0\,w(\boldsymbol{k})/[1 \mp s\,w(\boldsymbol{k})], \tag{5.5}$$

where s is the nearest neighbor overlap. To test the quality of the nearest neighbor tight-binding description of the graphene π orbitals I fit the first principles results at high-symmetry points of the Brillouin zone with Eq. (5.5). In Fig. 5.5 I show the *ab initio* band structure of graphene (π orbitals only) in comparison to the tight-binding band structure. The dashed lines in Fig. 5.5 are for $\gamma_0 = 3.01\,\mathrm{eV}$ and $s = 0.07$, which I obtained from the Γ point electronic energies of the π and π^* in graphene (-7.55 and 11.31 eV). Between Γ and K the tight-binding approximation gives quite good results. Deviations result around the M point of the Brillouin zone. Note that the inclusion of the asymmetry Eq. (5.5) only scales the absolute energies. The separation of the conduction band from the Fermi level at the M is therefore larger than that of the valence band in the tight-binding energies in contrast to the first principles results. This does, however, not affect the transition energies. Using the M point electronic energies to find γ_0 and s does not give satisfactory results as can be seen by the dotted lines in Fig. 5.5a). Naturally, the best agreement in the optical energy range is obtained when fitting the electronic dispersion around the K point by straight lines, see dashed lines in Fig. 5.5b). The better agreement at low electronic energies results, however, in a large difference for the Γ point energies (2.81 for the conduction and $-1.08\,\mathrm{eV}$ for the valence band). Part c) in Fig. 5.5 shows the results for Eq. (5.3), i.e., neglecting the asymmetry of the bonding and anti-bonding states, and $\gamma_0 = 2.7\,\mathrm{eV}$, which is a typical value for nanotubes found in the literature. The overall agreement is similar to b).

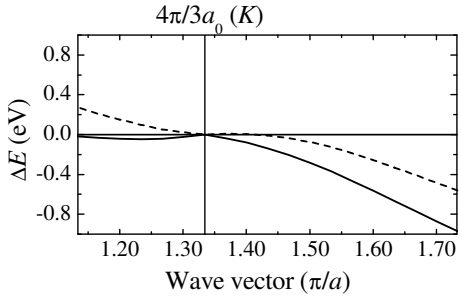

Figure 5.6: Difference between the tight-binding π orbitals and the first principles transition energies.

In general, the π orbital tight-binding approximation gives a reasonable description of the graphene electronic energies even if only nearest neighbor interaction is considered. The large advantage of the method is the resulting simple formula for the graphene band structure. Combined with zone-folding or the modified projection operators the electronic bands of carbon nanotubes are easily found within this approximation. Nevertheless, a good agreement for the graphene band structure to *ab initio* results is only achieved for a very limited range of electronic energies with a single value of γ_0. In Fig. 5.6 I show the difference between the optical transition energies obtained by first principles calculations and the π orbital tight-binding approach around the K point of the Brillouin zone. The k range correspond to transition energies below 3 eV [shaded area in Fig. 5.5c)]. The dashed line represents the tight-binding band structure of Fig. 5.5b), the full line the band structure in c). Even in this low energy range the transition energies differ by some 100 meV. Rolling up the sheet to a nanotube induces further deviations. We will see in the following that the rehybridization of the π

and σ states, which was first discussed by Blase *et al.*,[131] cannot simply be neglected in the description of the electronic energies in carbon nanotubes.

5.2. Isolated nanotubes

First principles studies of the electronic bands in ideal carbon nanotubes are surprisingly rare in the literature. Blase *et al.*[131] studied the rehybridization effects in small zig-zag nanotubes. They showed that the curvature of the nanotube wall strongly alters the band structure by mixing the π^* and σ^* graphene states. In contrast, Mintmire and White concluded from all-electron calculations of armchair tubes that the differences between first principles and tight-binding calculations are negligible for small enough energies.[145] I show in the following that rehybridization indeed differently affects tubes of different chirality; the effect is strongest in zig-zag tubes. I first discuss the band structure of a small armchair and zig-zag nanotube paying particular attention to rehybridization. The calculated band structure of two chiral nanotubes with a diameter $d \approx 8$ Å are presented in a separate subsection. Finally, the electronic dispersion in the optical range of a (19,0) tube is investigated. This tube has a diameter of 15 Å, which is typical for real nanotube samples.

5.2.1. Achiral nanotubes

In Fig. 5.7b) I show the band structure of an isolated (10,0) nanotube calculated with SIESTA. Figure 5.7a) contains the graphene electronic dispersion folded once along the ΓM direction and c) the tight-binding description including only the π orbitals. The dots in Fig. 5.7b) indicate the non-degenerate bands with quantum number $m = 0, n$. The Γ point ($k_z = 0$) of the nanotube for these bands corresponds to the Γ and M point of graphene as discussed in the previous section. If the curvature of the nanotube wall is neglected, the band structure of the zig-zag tube for the bands corresponding to $m = 0, n$ (that is the non-degenerate bands) would be the same as those of graphene along the $\Gamma - M$ direction [dotted bands in Fig. 5.7a) and b)]. Nanotube bands with other m's would also have their counterpart in the graphene band structure, but I will only analyze the comparison of the $m = 0, n$ bands for simplicity. Below the Fermi energy the (10,0) electronic dispersion agrees quite well with the confinement picture, in particular in the low energy region. Correspondingly, the tight-binding model, which is adjusted to reproduce the graphite electronic dispersion, gives an adequate description of the nanotube band structure below E_F. The conduction bands, however, are strongly affected by the rolling up of the graphene sheet. It was pointed out by Blase *et al.*[131] that the rehybridization in small nanotubes shifts the π^* and σ^* bands to lower and

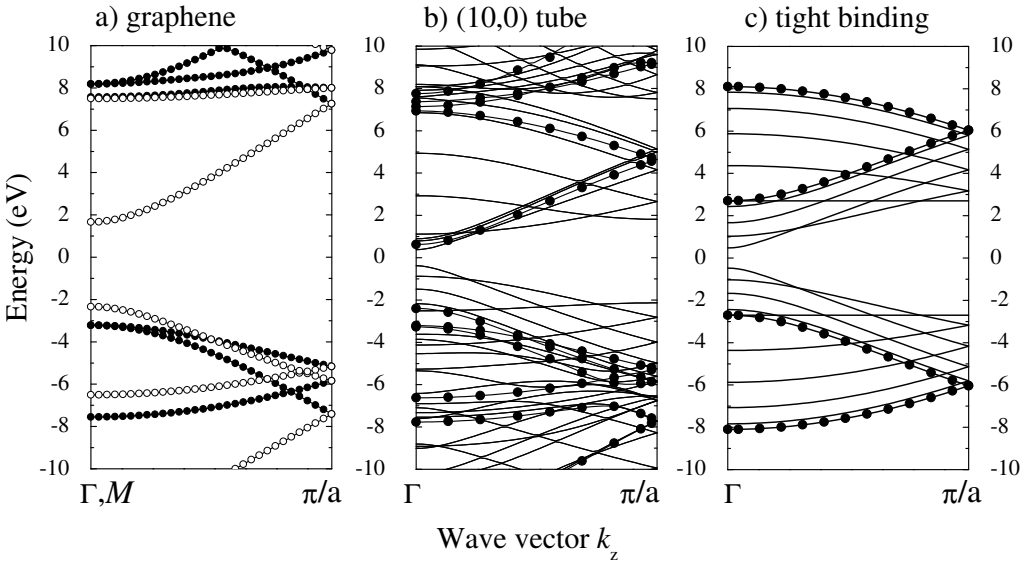

Figure 5.7: Band structure of a (10,0) isolated nanotube compared to a zone-folding and a tight-binding calculation. a) *ab initio* graphene electronic dispersion along the Γ*M* direction folded at the middle of the Brillouin zone; closed (open) symbols correspond to the first (second) half of the graphene Brillouin zone, i.e., $0 \leq k \leq \pi/\sqrt{3}a_0$ ($\pi/\sqrt{3}a_0 \leq k \leq 2\pi/\sqrt{3}a_0$), where $a_0 = 2.47\,\text{Å}$ is the lattice constant of graphene. b) *ab initio* calculation of a (10,0) nanotube. The dots mark the electronic bands with $m = 0, n$ quantum number, which in a zone-folding approximation should have the same dispersion as the graphene band structure shown in a). c) Tight-binding calculation of the (10,0) nanotube including only the π orbitals of graphene with $\gamma_0 = 2.7\,\text{eV}$. The dots indicate the bands with $m = 0, n$. The lattice constant $a = 4.27\,\text{Å}$ in a), b), and c).

higher energies, respectively. The energies of the π^* states in graphene in the (10,0) tube at the Γ point are downshifted by $\approx 1\,\text{eV}$ for the $m = n$ and by $\approx 4.4\,\text{eV}$ for the $m = 0$ band. While these bands are most strongly affected by the curvature of the tube, others are almost unchanged when comparing Fig. 5.7a) and b). In particular, one of the degenerate graphene σ^* bands at 8.14 eV in my calculation is almost at the same energy in the (10,0) nanotube and shows a similar *k* dependence. The tight-binding model is not able to reproduce the band structure of the tube above the Fermi level. The differences in energy at the Γ point, which is the critical point from which the singularities in the density of states originate, is vastly exaggerated when omitting the rehybridization (see also Section 5.3.).

To study the effect of curvature on the band structure of a nanotube more systematically I show in Fig. 5.8 the same calculations for a (6,6) armchair nanotube. The tube's k_z direction is now along the Γ*KM* line of graphene. When comparing the graphene dispersion to the non-degenerate bands of the (6,6) tube [indicated by the dots in Fig. 5.8b)] the overall agreement seems to be much better than for the zig-zag tube discussed above. In particular, the folded bands of graphene, see open symbols in Fig. 5.8a), are almost unaffected by the curvature. Below E_F even the accidental degeneracy of the π bands at the corner of the Brillouin

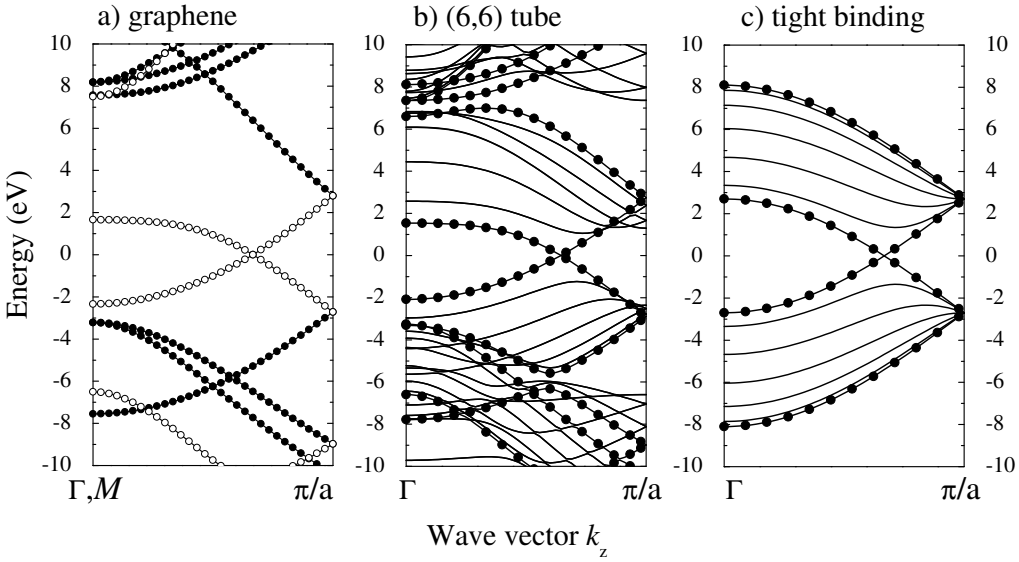

Figure 5.8: Band structure of a (6,6) isolated nanotube compared to a zone-folding and tight-binding approximation. a) Graphene *ab initio* calculation of the band structure along the Γ*KM* direction folded at $(\boldsymbol{k}_1 - \boldsymbol{k}_2)/2$. Closed (open) symbols correspond to the bands originating at the Γ (*M*) point of graphene. b) *Ab initio* calculation of an isolated (6,6) nanotube. The dots indicate the $m = 0, n$ bands, which correspond to the graphene dispersion shown in a). c) Tight-binding approximation of the same tube with $\gamma_0 = 2.7\,\text{eV}$. The lattice constant $a = 2.47\,\text{Å}$ in a), b), and c).

zone is reproduced by the *ab initio* calculations. Nevertheless, above the Fermi level the π^* conduction band at the Γ point is downshifted by 4.7 eV as in the zig-zag tube. Table 5.2 lists some selected electronic energies in the (10,0) and the (6,6) nanotube and compares them to the graphene values. The general trend as observed in Fig. 5.7 and 5.8 is reflected in the explicit values given in the Table, i.e., (i) the conduction bands of carbon nanotubes are well described in a zone-folding approximation, (ii) for the electronic bands originating from the Γ point of graphene the upshift of the σ^* and the corresponding downshift of the π^* states is similar for armchair and zig-zag tubes with the same radius, and (iii) the conduction bands derived from the graphene *M* point are strongly downshifted in the zig-zag tube, whereas they are close to graphene in the (6,6) nanotube.

In Fig. 5.9 I give an expanded view of the band structure in the energy range of the π^* and σ^* bands at the graphene Γ point; the *x* axis represent 4/10 of the (10,0) and (6,6) Brillouin zone. Full lines show the graphene band structure along the high-symmetry directions; the gray dots are the non-degenerate bands of the (10,0) (left) and the (6,6) (right) nanotube. The graphene bands are labeled by their irreducible representations at the Γ point and along the Γ*M* direction for the zig-zag tube and the Γ*K* direction for the armchair tube. In this picture the graphene dispersion was not folded to keep the figure as simple as possible. In the enlarged picture it is apparent that, e.g., the Γ_2^+ state and one of the bands forming the

Table 5.2: Selected electronic energies at the Γ and M point of graphene compared to the Γ point energies in nanotubes. In a zone-folding approximation the energy difference between graphene and a nanotube is expected to vanish. The twofold degeneracy of the σ^* conduction bands is lifted in carbon nanotubes. The calculated diameter of the nanotubes is given in the second column.

		conduction			valence			
		Γ		M	Γ		M	
	d(Å)	π(eV)	σ(eV)		π(eV)	π(eV)	σ(eV)	π(eV)
graphene		11.3	8.2		1.7	−7.5	−3.2	−2.3
(10,0)	7.8	7.0	10.3	7.7	0.6	−7.8	−3.2	−2.3
(6,6)	8.2	6.6	8.1	10.3	1.5	−7.8	−3.2	−2.1
(8,4)	8.4	6.8	10.3	8.1	1.6	−7.7	−3.2	−2.3
(9,3)	8.5	7.0	10.2	7.9	1.7	−7.8	−3.3	−2.1
(10,5)	10.4	7.2	10.5	8.1	1.6	−7.7	−3.2	−2.3
(19,0)	14.9	7.5	10.2	8.2	1.4	−7.6	−3.2	−2.4

degenerate Γ_6^- in graphene have similar energies and dispersion in graphene and in the tubes. In contrast, the Γ_4^+ band (π^*) and the second Γ_6^- state are shifted by the rehybridization. To understand this different behavior, let us consider the symmetry lowering by cutting a graphene sheet and rolling it up to a nanotube. By doing so I lose all rotations by angles other than 180° and all operations changing the graphene z coordinate like σ_h or the primed rotations. In achiral nanotubes I preserve reflections perpendicular to the x and y axis. This is a somehow local description of the symmetry of a curved sheet, since the point groups of nanotubes involve translational symmetry operations of graphene.[22] For the present purpose, however, this picture is sufficient. In the lower symmetry group Γ_6^- and Γ_4^+ belong to the same representation which is different from the original Γ_2^+ irreducible representation. A mixing and band repulsion can thus be expected for the two former bands. In the interior of the Brillouin zone T_1 and T_3 (along the ΓK direction) and Σ_2 and Σ_4 (ΓM) are correlated with the same representation. The behavior as expected by symmetry is nicely seen in Fig. 5.9.

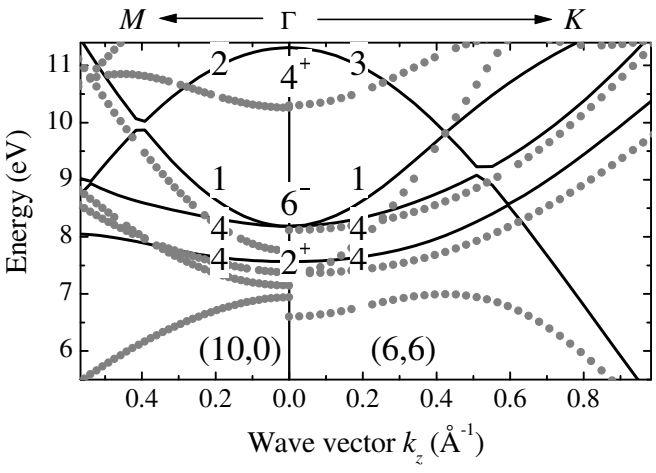

Figure 5.9: Electronic dispersion of graphene (full lines) around the Γ point in the energy range of the lowest lying conduction bands. The ΓM direction is displayed to the left together with the nondegenerate bands in a (10,0) nanotube (gray dots). To the right the ΓK electronic dispersion of graphene and the non-degenerate bands of a (6,6) armchair tube (gray dots) are shown. The irreducible representations of the graphene electronic bands are given in Slater's notation.[146]

At the Γ point the 2^+ state is pinned at its graphene energy, whereas a mixing and band repulsion is obvious for the 4^+ and the 6^- state. The mixing is only found for the Σ_4 and the T_1 band in the zig-zag and armchair nanotube, respectively, as predicted. In the (10,0) nanotube the symmetry analysis given so far is valid for all k_z and the π conduction band as a whole is expected to be downshifted. In armchair nanotubes, after passing the K point mixing is forbidden by symmetry even for the bent sheet for the bands within $\approx 10\,\mathrm{eV}$ of the π^* states. Their electronic energies corresponding to the graphene M point are thus more weakly affected by band repulsion as I found in the *ab initio* calculations.

5.2.2. Chiral nanotubes

In Table 5.2 I already included the electronic energies of the calculated (n_1, n_2) chiral nanotubes corresponding to the Γ and M point of graphene. Both high-symmetry points are always allowed states in carbon nanotubes. Therefore I can – as in achiral nanotubes – directly compare the graphene electronic energies to the *ab initio* calculations of the chiral nanotubes to estimate the effect of hybridization. As can be seen in Table 5.2 the curvature induced shift of the nondegenerate bands is of similar magnitude in chiral and achiral nanotubes of similar diameter. For the π^* band originating from the Γ point of graphene, the achiral tubes seem to indicate the two limiting cases with the strongest downshift in the (6,6) armchair and the weakest in the (10,0) zig-zag tube. However, neither of the two chiral tubes exhibits large differences to the zone-folding approximation for the bands derived from the M point of graphene. The (10,0) zig-zag tube is here clearly singled out compared to chiral or armchair tubes.

The full electronic dispersion for a (9,3) and an (8,4) nanotube is shown in Fig. 5.10a) and b), respectively. In the inset in Fig. 5.10b) the secondary gap of 20 meV can be seen induced in the (9,3) nanotube by curvature. The magnitude of the band gap is smaller than recently estimated by Kleiner and Eggert,[147] who considered the geometric effect of hybridization on the secondary gap. Using their relation I find a band gap on the order of 100 meV. The discrepancies might partly be due to the usual LDA problem of underestimating gap energies and partly to the band repulsion which was not considered by Kleiner and Eggert.[147]

The energies of the next highest valence and conduction bands at the Γ point are remarkable asymmetric with respect to the Fermi level. The asymmetry is particularly pronounced in the (9,3) nanotube, but visible in the (8,4) tube as well. Two reasons account for the different behavior below and above the Fermi level. First, the graphene electronic dispersion is slightly different for the valence and conduction bands. Second, the higher bands move toward the

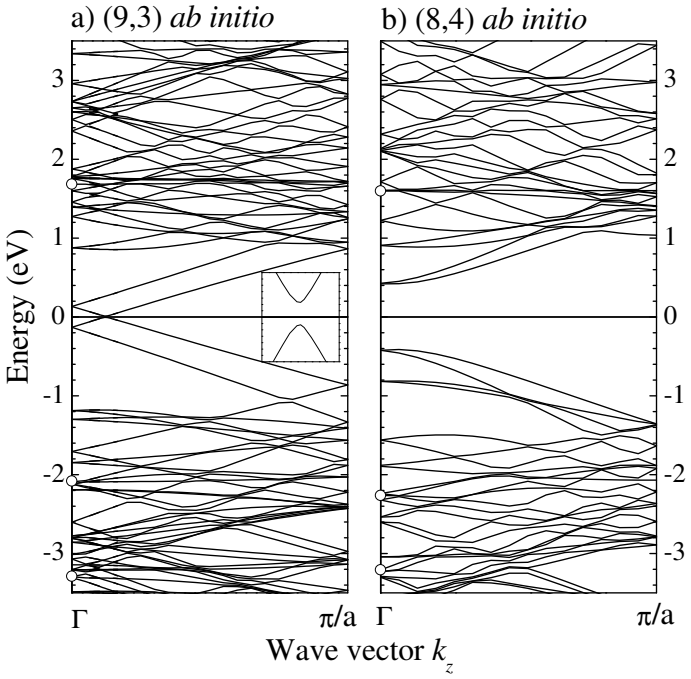

Figure 5.10: *Ab initio* band structure of two chiral nanotubes. a) (9,3) quasimetallic nanotube ($a = 15.44$ Å) The inset (vertical scale ± 35 meV) shows the secondary gap at the Fermi level evolving because of the curvature of the nanotube wall. b) (8,4) semiconducting nanotube ($a = 11.30$ Å). The open dots in a) and b) indicate the energy of the non-degenerate states at the Γ point, see Table 5.2

Fermi level because of the curvature. For example, in the (8,4) tube the third singularities below and above E_F are within zone-folding at -1.59 and 1.45 eV. In the *ab initio* calculation of the tube the valence energy is approximately the same as in zone-folding, whereas the conduction band is further lowered and has an energy of 1.22 eV in Fig. 5.10b). A very similar shift is observed for the first singularity in the (9,3) tube; again the valence band energies are the same, while I find a difference of 0.20 eV between the zone-folded and *ab initio* calculated conduction band. Note that these singularities are usually probed by optical experiments; they are responsible for the resonant Raman scattering in the red (metallic resonance) and the blue energy range.

5.2.3. Diameter dependence

Up to now, I considered only nanotubes with small diameters. In this section I discuss the band structure of a (19,0) nanotube which has a diameter more typical for real nanotube samples ($d = 14.9$ Å). I selected a zig-zag tube, because, as I showed in the last section, the hybridization effects are largest for these tubes. The (19,0) nanotube, in this sense, serves as a worst case scenario for judging how strongly curvature influences the band structure of real nanotubes.

Although the curvature of the (19,0) nanotube is considerably smaller than that of the (10,0) or any other nanotube discussed so far, I still find a downshift of the π^* band at the Γ point of 3.8 eV and an upshift of one of the σ^* states by 2 eV (see Table 5.2). These two values are not

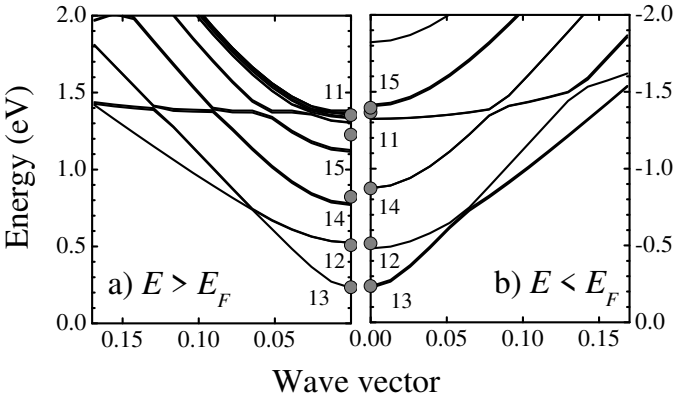

Figure 5.11: Band structure in the optical energy range of a (19,0) nanotube by first principles calculation. a) Conduction bands within 2 eV of the Fermi level. The labels indicate the m quantum numbers of the conduction bands; $m = 11$ refers to the second lowest band in energy in the group of bands at 1.34 eV (Γ point). b) Same as a) but for the valence bands. The gray dots show the zone-folding electronic energies at the Γ point.

so much different from the small diameter nanotubes as might be expected. As I discussed in Section 5.2.1. this can be understood by the lower symmetry in a curved sheet. The difference in energy between the zone-folding approximation and the *ab initio* calculation for the non-degenerate band originating from the M point of graphene, however, is much reduced in the (19,0) tube (0.3 eV) when compared to the (10,0) nanotube (1.1 eV).

In Fig. 5.11 I present the band structure within 2 eV around the Fermi level, i.e., in the optical energy range where many experiments have been performed. Figure 5.11a) shows the conduction bands labeled by their m quantum numbers; in part b) the valence bands are displayed [the y scale is negative in b)]. The gray dots indicate the position of the electronic states at the Γ point obtained within the zone-folding approximation from the *ab initio* calculation of graphene. Below the Fermi level zone-folding very nicely describes the first principles results. For the conduction bands with $m = 14$ and 15 clear deviations are seen. This is easily understood, since in a zig-zag tube the bands with $m \geq q/3$ have a $\boldsymbol{k}_\perp$ which is on the line between the K and the M point in graphene, see Eq. (5.1). The energy of the M point is most strongly changed by the hybridization in the (19,0) nanotube and, hence, the closer the confinement wave vector is to M the larger the expected energy shift. In the present example, $k_\perp \approx 0.2KM$ and $0.4KM$ for the band with $m = 14$ and 15, respectively. The bands with an m quantum number between 16 and 19 form the group of bands at 1.34 eV in Fig. 5.11a).

An interesting point arises when I fit the electronic energies E_m at the Γ point by the tight-binding approximation to test its validity. For zig-zag tubes at $k_z = 0$ the energies are given by[45]

$$|E_m| = \gamma_0 \left(1 + 2\cos m\pi/n\right). \tag{5.6}$$

The γ_0 I obtain increase monotonically from 2.4 to 2.6 eV between $m = 13$ and 11 (the $m = 15$ band shown in Fig. 5.11 has again a lower value). STM studies often concentrate on the lowest singularities in the density of states, while optical experiments are sensitive

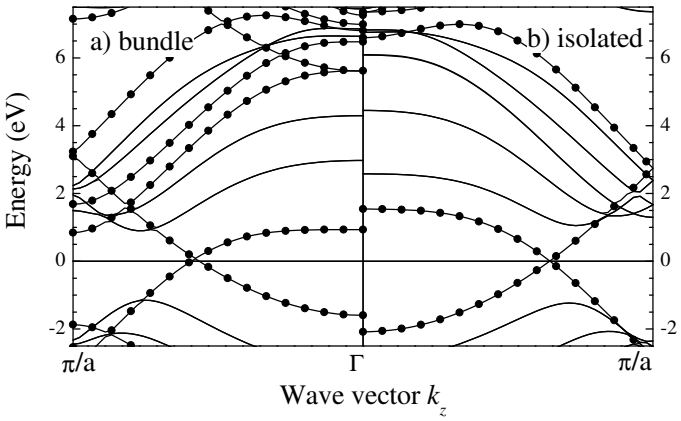

Figure 5.12: Dispersion along the k_z axis for a) a bundle of (6,6) armchair tubes and b) the isolated armchair tube. Nondegenerate bands are indicated by the closed dots. The Fermi level which is at $-5.79\,\mathrm{eV}$ in the bundle, but $-5.12\,\mathrm{eV}$ in the single tube was set to zero. Note that the crossing of the valence and conduction bands occurs slightly (70 meV) above the Fermi level.

to the bands higher in energy. This increase in γ_0 is probably one reason for the smaller carbon-carbon interaction energies found in STM compared to Raman experiments.[44, 148]

5.3. Bundled nanotubes

Bundling of the nanotubes to ropes induces further changes in the electronic dispersion along the tubes axis. The most prominent example is the opening of a pseudogap in armchair nanotubes.[149, 150] I also discuss the differences for the higher valence and conduction bands before turning to the dispersion perpendicular to the z axis.

5.3.1. Dispersion along k_z

In Fig. 5.12a) I show the band structure of a bundle of (6,6) armchair tubes and of the isolated tube in b). The non-degenerate states in both figures are indicated by small dots. When comparing bundled and isolated nanotubes a number of differences are apparent: (i) the first valence and conduction band cross slightly above the Fermi level (70 meV) in the bundles of tubes, (ii) a further shift of the valence bands is observed, which is most pronounced for the non-degenerate bands, and (iii) one of the doubly degenerate states in the isolated tubes splits in the bundle.

On first sight it might seem surprising that I do not obtain a secondary band gap in the nanotube bundles, but – as was pointed out by Delaney *et al.*[150, 151] – this is simply due to the high symmetry configuration I used for the bundles. I arranged the (6,6) tubes in a hexagonal lattice which fully preserves the D_{6h} symmetry of the hexagonal packing, i.e., half of the original mirror symmetries perpendicular to the z axis are also symmetry operations of the bundles (see Appendix I. for the arrangement of the bundled tubes in the calculations). The electronic wave functions can still be classified as even or odd with respect to these

reflections allowing a crossing of the two bands at high symmetry lines in the Brillouin zone.[150,151] Another example for such a crossing is seen at 7 eV roughly in the middle of the Brillouin zone in Fig. 5.12a). The π^* derived band which has odd parity under σ_v crosses with one of the σ^* bands; the latter is downshifted by the interactions between the tubes. The two newly obtained non-degenerate bands in the bundles of armchair tubes (Γ point energy 5.60 and 6.46 eV) originate from the doubly-degenerate bands with the quantum number $m = 3$ (6.10 eV). In the new point group they are correlated with the B_1 and B_2 representations (${}_kE_{A_n}$ and ${}_kE_{B_n}$ in the line group notation).[45] Likewise, m and $(6-m)$ now belong to the same representation, which opens up the small gaps at the zone boundary. The compatibility between the nanotube symmetry group and the hexagonal packing is, however, a special case, because D_{6h} is a subgroup of the (6,6) tube. In general, the symmetry is at least reduced to D_{2h} for achiral and D_2 for chiral tubes even in the highest symmetry configuration. These groups have only non-degenerate representations and hence the degeneracy will be lifted for all bands in a general tube, when it is bundled. An interesting question is how strongly the bundle band structure, in particular perpendicular to k_z, depends on the relative orientation of the tubes. The calculations by Delaney *et al.*[150,151] showed only a weak dependence of the density of states in armchair bundles on tube rotation for energies within 0.2 eV around the Fermi level. A systematic study of the band structure and its orientation dependence in bundles of different chirality might be the subject of a future work.

The bundling moves the Γ point energies of the lowest valence and conduction bands in the (6,6) nanotubes closer to the Fermi level. In contrast to isolated tubes, the bundling shifts the two bands by the same order of magnitude (-0.62 eV for the conduction and 0.48 eV for the valence band). In Section 5.2.3. I saw that the change in the M point energy is indicative for the Γ point energies of the other bands and the densities of electronic states. I therefore might expect a similar change in the electronic dispersion for other bundles as well. In Table 5.3 I summarize the energies at critical points in the Brillouin zone which I obtained by the different calculations. I included only the first three bands around the Fermi level within the tight-binding approximation using the π orbitals of graphene. The intertube coupling induces a shift of the valence and conduction band singularities, which might be as high as 0.25 eV in the (6,6) and (8,4) nanotube. The (10,0) nanotube is somewhat peculiar because of the strong splitting of its bands. Note that the valence and conduction band originating from the $m = 7$ band in the isolated tube are only separated by 0.2 eV in the bundle compared to 0.75 eV for the single tube. Moreover, the highest valence band is 0.02 eV above the Fermi level at the Γ point (see next section).

Table 5.3: Critical point energies around the Fermi level. The table compares results of the zone-folding approximation including only the π orbitals of graphene (π orbitals, $\gamma_0 = 2.7\,\mathrm{eV}$), zone-folding of the graphene band structure calculated with SIESTA (folding), the *ab initio* result of an isolated tube [*ai* (single)], and the *ab initio* calculation of bundles of tubes [*ai* (bundle)]. For the bundle the mean value for split bands was given; when the splitting was $> 0.1\,\mathrm{eV}$ I included the splitting in parenthesis. For each tube the rows are ordered by the energies of the tight-binding approximation for the graphene π orbitals.

tube	$\lvert m\rvert$	Electronic energies at critical points (eV)			
		π orbitals	folding	*ai* (single)	*ai* (bundle)
Conduction bands					
(6,6)	5	1.35	1.13	1.05	0.89
	6	2.34	1.58	1.34	1.27
(10,0)	7	0.47	0.43	0.38	0.43 (0.21)
	6	1.03	1.00	1.12	0.84 (0.14)
	8	1.67	1.28	0.80	0.47 (0.21)
(8,4)	19	0.45	0.42	0.43	0.40
	18	0.95	0.90	0.90	0.64
	20	1.70	1.45	1.22	0.96
Valence bands					
(6,6)	5	−1.35	−1.24	−1.23	−1.16
	6	−2.34	−2.06	−2.07	−2.13
(10,0)	7	−0.47	−0.44	−0.37	−0.35 (0.37)
	6	−1.03	−1.01	−0.87	−0.99 (0.45)
	8	−1.67	−1.49	−1.48	−1.87
(8,4)	19	−0.45	−0.42	−0.43	−0.38
	18	−0.95	−0.92	−0.92	−0.92
	20	−1.70	−1.59	−1.53	−1.77

Rao *et al.*[89] recently reported a parameterized calculation of isolated and bundled armchair nanotubes using the method of Kwon *et al.*[149] They observed differences of similar magnitude in the density of states in isolated and bundled tubes, but – in contrast to us – an increase in the separation of the valence and conduction band singularities. This discrepancy is partly due to my assumption that the points of vanishing slopes in the band structure reflect the density of states in the bundled tube (the van Hove singularities are broadened in the bundle). On the other hand, the band structures calculated by Kwon *et al.*[149] with the parameterized technique underestimate the differences between single tubes and bundles compared to *ab initio* calculations. Rao *et al.*[89] used the separation between the singularities in the valence and conduction bands to analyze the optical absorption in bundles of carbon nanotubes. For armchair nanotube bundles, however, this analysis includes indirect optical transitions, which are unlikely to occur (see the points of vanishing slopes in Fig. 5.12a).

A more detailed study should consider at least the joint density of states if not the optical transition matrix elements. STM measurements revealed no shift in the first singularity of the density of electronic states between an isolated armchair tube and the same nanotube on top of a bundle, while the second singularity below E_F is slightly at lower energies in the 'bundled' tubes.[148] Nevertheless, it would be interesting to repeat these measurements for small semiconducting zig-zag tubes, which I found to be much more sensitive to the intertube interaction.

5.3.2. Intratube dispersion

The interaction between nanotubes in a bundle does not only alter the k_z band structure, but causes a dispersion in the perpendicular plane as well. In graphite the intralayer dispersion for the π bands is $\approx 1\,$eV and below; the strongest dispersion is found for the σ^* states along the ΓA direction (3-4 eV),[133] see Fig. 5.2. The band structure of bulk C_{60} was investigated by Troullier and Martins,[132] who reported band widths around 0.5 eV.

I show in Fig. 5.13 the band structure of a bundle of (6,6) armchair tubes along several high-symmetry lines in the hexagonal Brillouin zone. The panel to the right shows the perpendicular dispersion at the Fermi wave vector along the z axis Δ_F. The secondary gap in the bundled tube is very nicely seen. I obtain the largest separation at the P point of the Brillouin zone $\Delta E = 1.2\,$eV. Note also the crossing of the two bands with $m = 3$ quantum numbers in the isolated tube (see the dotted lines in Fig. 5.12a and the discussion in the text) around

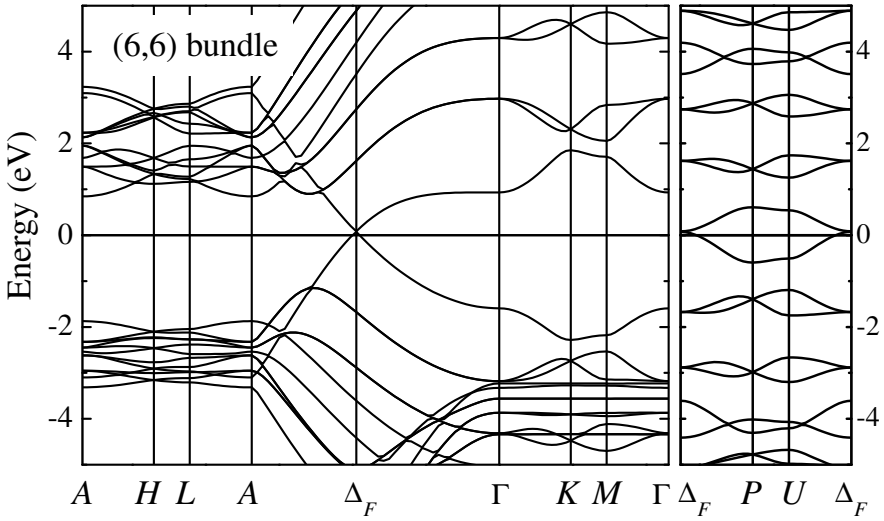

Figure 5.13: Band structure of a bundle of (6,6) nanotubes along several high-symmetry lines in the hexagonal Brillouin zone. The right panel shows the intratube dispersions at the Fermi wave vector $k_{zF} = 0.73\,\text{Å}^{-1}$ in this calculation.

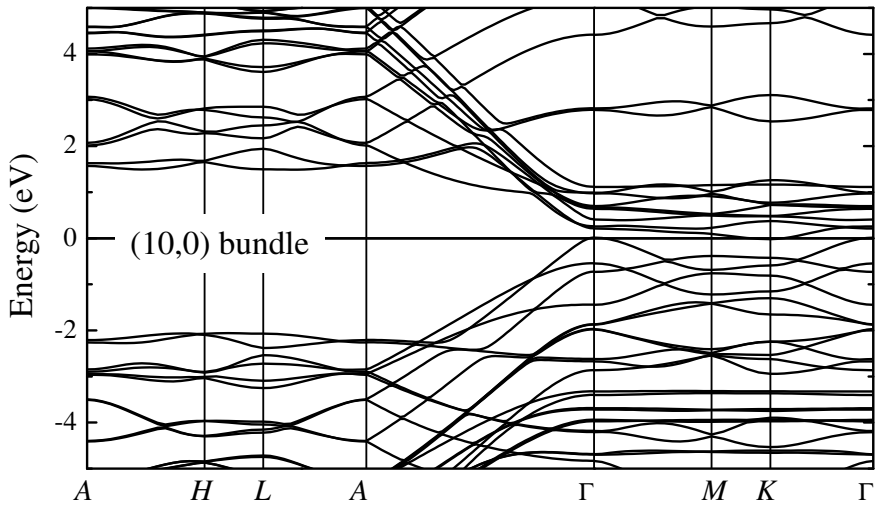

Figure 5.14: Band structure of a bundle of (10,0) nanotubes. The two valence bands next to the Fermi energy are strongly split by the tube intertube interaction. Note that the first conduction band is below the Fermi level at the K point of the hexagonal Brillouin zone.

± 4 eV. The band widths I obtained perpendicular to the z direction are typically between 400 and 600 meV, but might be as high as 900 meV for the two first valence bands at the ΓKM line. The perpendicular dispersion leads to a broadening of the density of states in bundled tubes. Similarly, the broad and unstructured features found in absorption experiments[88,144] on bundled nanotubes might already be expected from the band structure of a bundle composed of a single nanotube species with one important exception: The first optical transition E_{11} coming from the accidental singularities along the ΓA direction of the Brillouin zone falls into a gap of all other vertical excitations. Optical transitions at k points with $k_z = 0$ are forbidden in isolated armchair nanotubes and will be weak or absent in the bundled tubes as well;[45] all other transition energies are clearly different in energy from E_{11}. I can take the armchair tubes as representative for the metallic tubes with $\mathcal{R} = 3$, which refers to almost all metallic tubes for large enough diameters ($d \gtrapprox 1.2$ nm). Chiral tubes with $\mathcal{R} = 3$ have a band structure very similar to armchair tubes; in particular, they possess the same accidental critical point.[21,55] In Raman scattering experiments, the resonances for the first transition in metallic nanotubes are, therefore, expected to be much more pronounced than the semiconducting resonances, where a similar optical gap is not present (see below). This is in very good agreement with Raman experiments on bundled tubes.[41,43,44] Rafailov *et al.*[44] normalized their measurements to a reference crystal. Indeed, the scattering by metallic nanotubes is very weak outside a well defined resonance window (1.6-2.0 eV), whereas a comparatively strong signal from the semiconducting nanotubes is found even in the red energy range where they are not expected to be resonant.

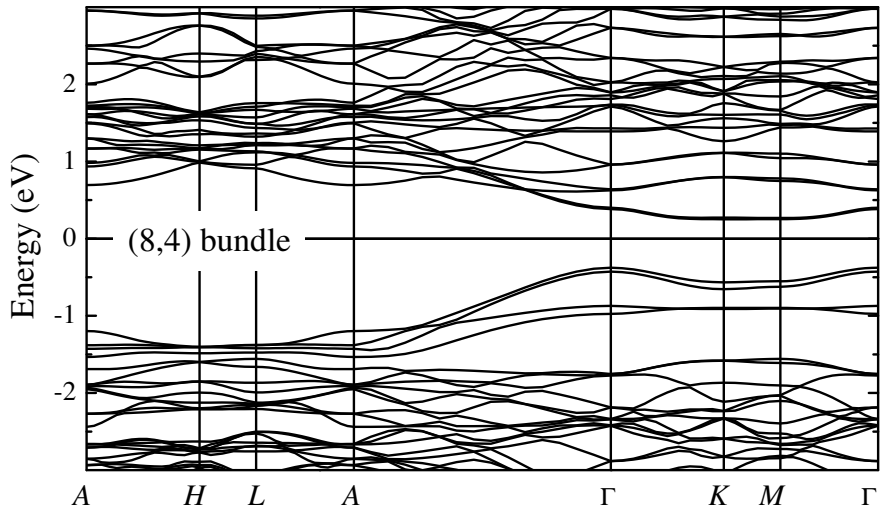

Figure 5.15: Band structure of a bundle of (8,4) chiral nanotubes. The x axis between the Γ and the A point was expanded by a factor of three.

In Fig. 5.14 I show the band structure of a bundle composed of (10,0) nanotubes. The dispersion of the electronic bands perpendicular to k_z is less than in armchair nanotubes; most of the bands have a width well below 400 meV. The large splitting of the first two valence states at the Γ point and of both conduction and valence bands at the A point of the Brillouin zone results in a stronger dispersion of the corresponding states perpendicular to k_z as well (0.4 - 0.9 eV). The most interesting point in Fig. 5.14 is, however, the dispersion of the lowest conduction and the highest valence band in the ΓKM plane. The conduction band – bending down when going away from the Γ point within the plane – crosses the Fermi level close to the K point of the Brillouin zone. Its minimum at K has an energy of -0.02 eV. The highest valence band has an hole pocket at the Γ point (0.02 eV). I thus find in my calculation the (10,0) nanotube bundle to be metallic. A reduction of the band gap by intratube interaction is observed in the (8,4) nanotube bundle as well (see Fig. 5.15). Again the lowest valence band bends down along the ΓKM line with a minimum at K (0.27 eV). The minimum is still above the Fermi level, because the energy at the Γ point in the (8,4) nanotube is considerably higher than in the (10,0) tube and the intratube dispersion narrower (0.13 eV instead of 0.23 eV). In general, the band gap of nanotubes scales as the inverse of the diameter. If the intratube dispersion is on the same order in larger diameter tubes, the spanning of the gap by the interaction between the tubes is expected to occur as well.

The dispersion I find in the chiral (8,4) nanotube bundle in Fig. 5.15 is again reduced when compared to the zig-zag tube bundle in Fig. 5.14. Only rarely I found a band width larger than 200 meV. I also stress that in the energy range corresponding to excitations in the visible the

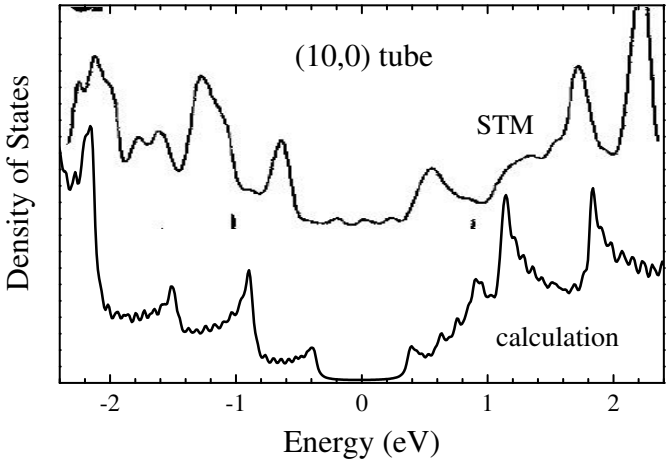

Figure 5.16: Density of states measured by scanning tunneling microscopy (top) and calculated with SIESTA. The calculations reproduce the main features of the experimental density of states, in particular, the relative heights of the peaks as is discussed in the text. The energy gap is underestimated by the LDA calculation. The STM data are from Ref. 129.

(8,4) bundles show a rich band structure in the *AHL* plane. This might considerably broaden the absorption bands as discussed above.

5.4. Comparison to experiments

In this section I compare my calculation to an STM and a Raman experiment. I show that indeed the discrepancies observed between STM measurement and the density of states above E_F within the tight-binding picture are due to the rehybridization as suggested by Odom *et al.*[129] A reliable energy for optical transitions cannot be obtained from the π orbitals tight-binding Hamiltonian.

5.4.1. Scanning tunneling microscopy

STM experiments provide the unique possibility of measuring the density of states on a nanotube of known chirality. Thus they allow a direct comparison between first principles calculation and experiments. A variety of STM measurements on atomically resolved single walled nanotubes have been reported.[127–129, 152, 153] Odom *et al.*[129] measured the density of states on a (10,0) nanotube, one of the tubes calculated in this work.

I compare the experimentally obtained density of states of a (10,0) nanotube to my calculation in Fig. 5.16. The shape and the relative height of the peaks are in very good agreement between experiment and theory. In particular, the low energy shoulder of the second peak above the Fermi level and the much lower height of the third peak below E_F are very nicely reproduced. The absolute energies of the peaks, on the other hand, are considerably smaller in the *ab initio* calculation than in the experimental spectrum. Li *et al.*[93] recently reported similar discrepancies between experiment and theory for very small nanotubes ($d = 4\,\text{Å}$).

Their LDA calculations underestimated the optical transition energies by 10-15 %. Note also that the relative energies of the σ and π valence bands in graphite are incorrectly predicted by *ab initio* methods (see Table 5.1 and Ref. 133). However, when comparing the absolute peak positions in the upper and lower trace in Fig. 5.16 the differences are too large to be attributable to the local density approximation. On the other hand, the calculations still show a very sharp onset of the singularities, whereas the experimental curve is much smoother. When I compare the onsets of the flanks rather than the maxima of the peaks the calculated energies are only 10-20 % too small, which is a typical value for an LDA calculation and was also found by Li *et al.*[93]

5.4.2. Raman scattering

Raman scattering is widely used to study the electronic structure of carbon nanotubes by resonant transitions. For bulk samples the approximation of Mintmire and White[34] in Eq. (5.4) was successfully used to model the absorption of an ensemble of tubes with a homogeneous chirality distribution.[43,44] The resonant enhancement of the radial breathing mode was also measured on a single tube using a variable excitation energy.[130] The width of the resonance window was reported to be $\approx 10\,\mathrm{meV}$, much smaller than found in tunneling experiments. The disadvantage of Raman scattering, however, is the unknown chirality of the scattering nanotube. Recently, attempts were made to determine not only the diameter, but also the chirality of a nanotube by Raman scattering.[16,154] To identify possible tubes resonant with the incoming or outgoing photons both groups used the tight-binding approximation of the graphene π orbitals with $\gamma_0 = 2.9\,\mathrm{eV}$ as found on nanotube bundles. Within this model the dependence of the electronic energies on chirality arises mainly from the trigonal shape of the energy contours around the graphene K point.[36,37] By comparing the intensities of the radial breathing modes coming from a number of different tubes they adjusted the dependence of the breathing mode on diameter until they found good agreement between the expected and observed intensities. The chirality assignment thus relied heavily on the assumed transition energies. The question arises whether this is indeed a reliable procedure to identify a particular (n_1, n_2) nanotube.

To study this question I selected the semiconducting (10,5) nanotube, which Jorio *et al.*[16] assigned on the basis of Raman data. I calculated the electronic density of states with the tight-binding approximation of the graphene π orbitals, zone-folding of a graphene sheet, and by a first principles calculation. The optical transition investigated in the Raman study corresponds to the $m = \pm 24$ quantum number in the (10,5) nanotube.[45] In Fig. 5.17 I compare the density of states obtained by the three models for this particular band. The energetic

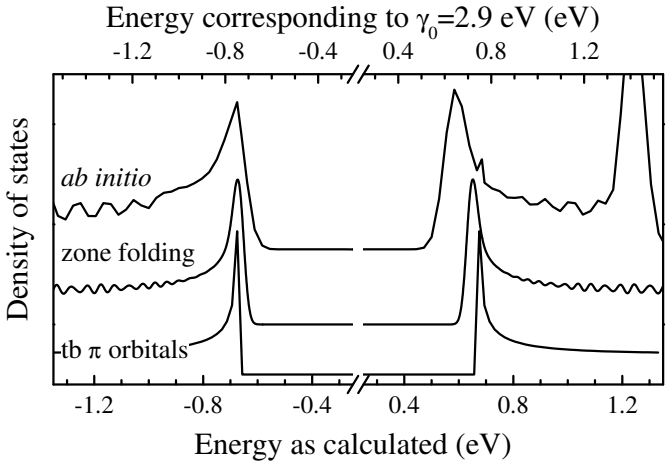

Figure 5.17: Density of states in a (10,5) nanotube for the band with quantum number $m = \pm 24$. From bottom to top I show the singularities obtained with the tight-binding approximation (π orbitals only), the zone-folding of the graphene bands structure, and an *ab initio* calculation. The bottom x scale is for energies obtained from the first principles calculations for a (10,5) nanotube and graphene; within the tight-binding calculation the overlap parameter was adjusted to yield the same energetic position for the singularity below E_F as in the first principles calculation ($\gamma_0 = 2.54\,\mathrm{eV}$). The top scale corresponds to $\gamma_0 = 2.9\,\mathrm{eV}$; it might be considered a correction for a too small band gap in the LDA approximation.

position of the valence band singularity within zone folding I found to be the same as in the full calculation of the (10,5) nanotube. I therefore adjusted the tight-binding approximation to yield the same energy ($\gamma_0 = 2.54\,\mathrm{eV}$). The upper scale corresponds to a tight-binding parameter $\gamma_0 = 2.9\,\mathrm{eV}$, which was found on bundles of nanotubes. Using the upper scale to directly compare my calculations to the work by Jorio *et al.*[16] I find a transition energy of 1.54 eV in the tight-binding approximation. This energy was within the resonance window in Ref. 16 between 1.48 and 1.68 eV. Already the zone-folding calculation shows a smaller separation of the valence and conduction band singularity. From the *ab initio* calculation of the (10,5) nanotube I obtain a transition energy 1.44 eV; clearly outside the resonant range. Note that the difference between the *ab initio* and tight-binding calculation is twice as much as the trigonal shape corrections (50 meV). The error made when using the tight-binding approach thus makes it impossible to use resonances for the assignment of chiralities to particular nanotubes.

5.5. Summary

The general features of the electronic band structure of carbon nanotubes can be described by zone-folding of the graphene bands. The confinement around the nanotube's circumference restricts the allowed k vectors to parallel lines in the graphene Brillouin zone. The zone-

folding picture provides an intuitive feeling for what is happening when graphene is cut and rolled up. On the other hand, this approximation is not suited for a precise study of the electronic properties of nanotubes. The rolling of the carbon sheet allows a mixing of the π and σ electronic wave function, which is forbidden in a flat sheet. The rehybridization is best studied by first principles methods as I did in this chapter for a series of nanotubes. Whereas the valence bands and the low energy conduction bands ($E < 1.0\,\mathrm{eV}$) are very well reproduced by a zone-folding approximation, deviations on the order of 200 meV were found for the conduction bands involved in optical transitions. Zig-zag nanotubes are particularly sensitive to hybridization effects; even in a (19,0) nanotube the energy band derived from the π conduction band at the graphene M point is downshifted by 0.3 eV.

Bundling of the tubes to nanoropes further shifts the Γ point energies towards the Fermi level. I found a shift on the order of 100 meV for both the valence and conduction bands compared to the isolated tubes. In the semiconducting bundles the intramolecular dispersion of the lowest conduction band is bending down when going away from the Γ point. In the chiral (8,4) tubes the band gap was thereby reduced by 20 % compared to the isolated case, whereas the (10,0) nanotube bundle turned out to be metallic. The electronic dispersion perpendicular to the tubes I found to range from $\approx 200\,\mathrm{meV}$ in chiral tubes to 1 eV in armchair nanotubes, which is expected to broaden the density of states as well as optical absorption bands in nanotube bundles.

Lastly, I investigated the validity of the tight-binding approximation of the graphene π orbitals by comparing its results to first principles calculations. In general, the agreement between the two calculations was found to be satisfactory. However, the simple tight-binding model is certainly not suited to predict electronic energies with an accuracy of 100 meV as assumed recently in Raman scattering experiments.

Chapter 6

Double Resonant Raman Scattering in Graphite and Nanotubes

One of the fundamental concepts in Raman scattering is that the observed frequency shift is independent of excitation energy. In 1981, however, Vidano *et al.*[18] reported that several Raman lines in graphite shifted linearly with excitation energy. The affected modes did not correspond to Γ point vibrations; the one receiving most attention in the following years was the so-called *D* mode with a frequency close to the *K* point LO phonon energy. The puzzle of the origin and the strange behavior of these lines was resolved only 20 years later when we showed it to be caused by double resonant Raman scattering.[19] Thinking back to carbon nanotubes we realized that the two strange aspects of the graphite *D* mode in fact applied to the entire Raman spectra of carbon nanotubes: Despite many attempts none of the experimentally observed Raman peaks of higher energy could be convincingly assigned to a Γ point vibration, and secondly, we had seen in an experiment the peculiar frequency shift with excitation energy as well. Hence I believe that we are now finally able to explain the entire Raman spectrum of single-walled nanotubes. As this work is still in progress I will concentrate in this chapter on graphite and the idea of double resonant Raman scattering.

In Section 6.1. I discuss the measurements on graphite, which established the peculiar features in its Raman spectrum. I then explain the mechanism for double resonant scattering on a textbook example and apply it to the graphite *D* mode in Section 6.2. In Section 6.3. and 6.4. I present measurements and first calculations for the *D* and the high-energy modes of carbon nanotubes.

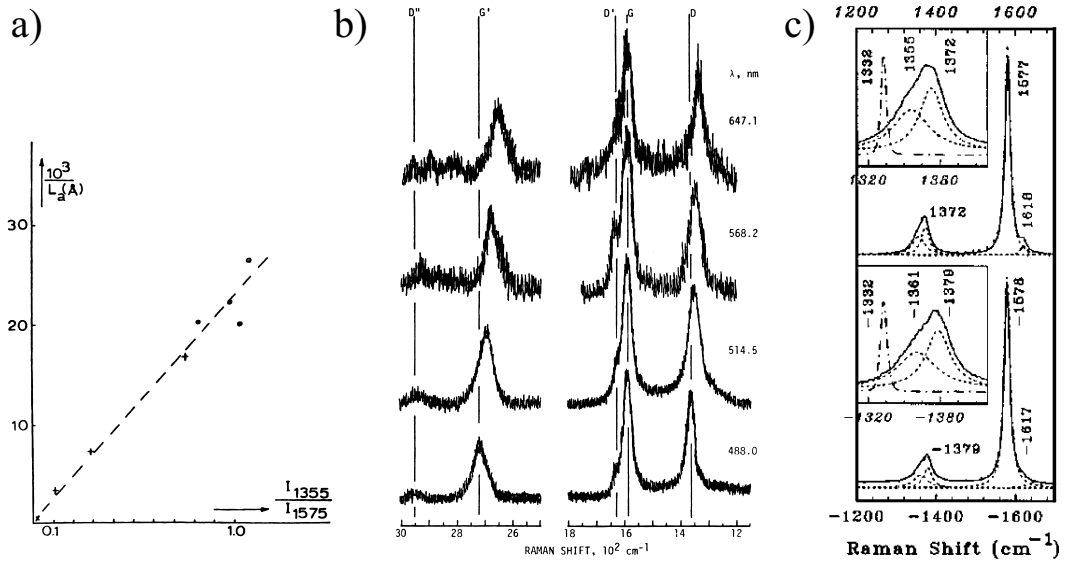

Figure 6.1: The key experiments on the D mode in graphite a) Linear relationship between the crystalline size of graphite and the intensity of the D band (labeled I_{1355}). The crystalline size was determined by x-ray spectroscopy; the D intensity was normalized to the intensity of the Γ point vibration (I_{1575}). From Tuinstra *et al.*[17] b) Graphite Raman spectra at different excitation wavelengths (given next to the curves). While the Γ mode (1582 cm^{-1}) is independent of excitation energy, the other peaks are shifting with increasing laser energy to higher frequencies. The D and D^* mode are labeled D and G' in the figure. From Vidano *et al.*[18] c) Stokes (upper panel) and anti-Stokes (lower) spectra of graphite. The D mode frequency differs by 7 cm^{-1} in Stokes and anti-Stokes scattering. From Tan *et al.*[155]

6.1. The D mode in graphite

Single crystals of graphite show only one Raman peak at 1575 cm^{-1} in the high energy region.[17] It originates from the high-energy E_{2g} Γ point vibration, where the two carbon atoms in the graphene unit cell vibrate out of phase within the layer plane. The second E_{2g} mode of graphite is at low frequency (44 cm^{-1}), a rigid displacement of the graphene sheets against each other. No other Γ point phonons belong to a Raman active representation. In polycrystalline material – even in highly oriented pyrolytic graphite – other peaks appear in the spectrum, which are induced by disorder and the finite crystal size. Most prominent are the D mode around 1350 cm^{-1} and the D^* mode at twice its frequency.* Figure 6.1 shows the three key experiments establishing the unusual properties of these modes. In the first report of the D mode Tuinstra *et al.*[17] showed that its intensity increases linearly with decreasing size of the scattering graphite crystals, see Fig. 6.1a). They proposed the mode to be associated with a high phonon density of states around the K point of the Brillouin zone, i.e., a classical example of a density of states feature seen in Raman scattering because

*The D^* mode is often also called G' in the literature, see, e.g., the figure by Vidano *et al.*[18] reproduced in Fig. 6.1b). I prefer the term D^* to emphasize that it is the overtone of the D peak.

of relaxed k conservation.[67] This obvious interpretation was only questioned ten years later when Vidano *et al.*[18] published Raman spectra on graphite excited with different lines of an Ar/Kr laser. Their spectra, which are reproduced in Fig. 6.1b), showed the D and D^* mode frequencies to increase with increasing excitation energy. They reported a shift of $56\,\mathrm{cm}^{-1}$ for 1 eV change in laser energy, similar values were published by many groups for a wide range of excitation energy.[156–159] No explanation was found for this frequency shift. An empirical "$k = q$ selection rule" that the wave vector of the resonantly excited electron is somehow transferred to the phonon gave agreement with the experimentally found shift, but lacked any physical grounding. Moreover, it failed to explain the last peculiarity in the disorder induced Raman spectrum, the difference in Stokes and anti-Stokes frequency. Tan *et al.*[155] found that the Stokes and anti-Stokes spectra of the D mode excited with the same laser wave length differed by $7\,\mathrm{cm}^{-1}$, see Fig. 6.1c), whereas the Γ mode frequencies agreed to within $1\,\mathrm{cm}^{-1}$ as expected in Raman scattering.

The first suggesting double resonances at the origin of the D peak in the graphite Raman spectrum were Sood *et al.*[160] They used the model of Martin and Falicov[69] for double resonance in parabolic bands. The model yields a square root dependence of the D mode frequency on excitation energy in contrast to the linear shift observed experimentally. To get a better overall agreement between theory and experiment they recently incorporated a third order Raman process involving two phonons and elastic scattering.[159] This process seems rather unlikely to result in a measurable intensity.

6.2. Double resonant scattering

The term resonant Raman scattering usually refers to incoming or outgoing resonances, i.e., the absorption or emission of the photon takes place between two real electronic states, see Chapter 3. Double resonant scattering means that additionally the excited or annihilated phonon makes a real transition. In a first order Raman process double resonances can only be achieved by tuning the energetic separation of two electronic states to match the phonon energy, e.g., by uniaxial stress, magnetic fields, or a proper choice of the thickness and constituent in semiconductor quantum wells.[84, 161, 162] In higher order Raman processes, however, double resonances are more easily realized and can occur for a wide range of excitation energies. The frequency of the doubly resonant phonon will dominate the Raman spectrum, which as I will show in the following naturally explains all peculiarities found in the graphite Raman spectrum.

6.2.1. Linear bands: An example

As an example for defect induced resonant Raman scattering in graphite I study a one-dimensional problem as depicted in Fig. 6.2.[19] An incoming photon resonantly excites an electron-hole pair ($i \to a$). The electron is then scattered across the k origin to another real state ($a \to b$). It is scattered back elastically by a defect conserving k in the process ($b \to c$). Finally, the electron-hole pair recombines ($c \to i$). The process described is one of the possible double resonances (e.g., other time ordering, outoing instead of incoming resonance, and hole scattering); additionally, singly or non-resonant transitions are possible as well, but with a much smaller cross section. The important point of the double resonance is that the transition $a \to b$ is real only for a unique combination of phonon energy $\hbar\omega_{\rm ph}$ and momentum q. The $(\omega_{\rm ph}, q)$ pair fulfilling the double resonant condition depends on the energy of the incoming photon as well as the phonon dispersion. For a higher electronic energy the incoming resonance occurs at larger k and a larger q is needed for the second resonant transition. If the phonon branch is dispersive the phonon energy is different.

After having explained the general idea of double resonances I calculate the Raman spectrum for the process shown in Fig. 6.2. The Raman cross section $K_{2f,10}$ is given by the usual expression[67,69]

$$K_{2f,10} = \sum_{a,b,c} \frac{M_f \mathcal{M}_{ba} \mathcal{M}_{cb} M_o}{(E_1 - E^e_{ai} - i\hbar\gamma)(E_1 - \hbar\omega_{\rm ph} - E^e_{bi} - i\hbar\gamma)(E_1 - \hbar\omega_{\rm ph} - E^e_{ci} - i\hbar\gamma)}, \quad (6.1)$$

where E^e_{ai} is the energy difference between the electronic state i and a (correspondingly for the other electronic states), E_1 and $E_2 = E_1 - \hbar\omega_{\rm ph}$ are the energies of the incoming and outgoing photon. $M_{o,f}$ are the (constant) transition matrix elements for the incoming and outgoing photon, $\mathcal{M}_{ba}$, $\mathcal{M}_{cb}$ represents the phonon or impurity which scatters the electron-hole pair from state a to b and from b to c, and γ, the broadening parameter, has been taken to be the same for all transitions. For linear bands with the Fermi velocities $v_1 < 0$ and $v_2 > 0$

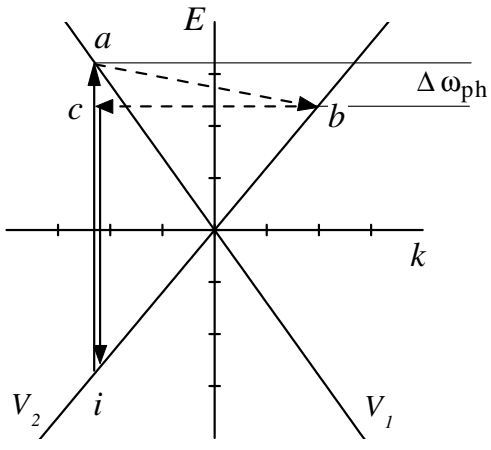

Figure 6.2: Schematic double resonance for electronic bands with linear dispersion. v_1 and v_2 are the Fermi velocities of the electronic bands. In the example, the first electronic transitions is real (first resonance) and the scattering of an electron by a phonon (second resonance). The elastic scattering in contrast ends in the virtual electronic state c. At most one phonon wave vector q and energy $\omega_{\rm ph}$ yields a second resonant transition across the origin of k.

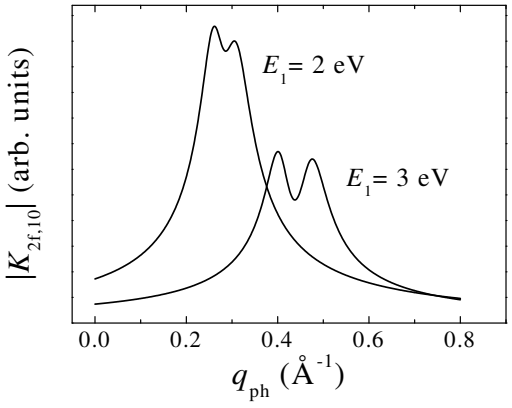

Figure 6.3: Raman matrix element of Eq. (6.4) as a function of the phonon momentum q for two incident photon energies E_1. The strong enhancement of the Raman cross section is caused by the double resonances. For the calculation I used the Fermi velocities $v_1 = -7\,\text{eV\AA}^{-1}$ and $v_2 = 6\,\text{eV\AA}^{-1}$ and a broadening parameter $\gamma = 0.2\,\text{eV}$. The phonon dispersion was taken to be linear varying from $1560\,\text{cm}^{-1}$ at $k = 0$ and $1270\,\text{cm}^{-1}$ at π/a.

(see Fig. 6.2) the differences in electronic energies are

$$E^e_{ai} = |k|(v_2 - v_1), \qquad E^e_{bi} \stackrel{k_i<0}{=} -qv_1 \text{ or } \stackrel{k_i>0}{=} qv_2, \text{ and} \qquad E_{ci} = |k|(v_2 - v_1). \tag{6.2}$$

The sum in Eq. (6.1) can be converted into an integral in one dimension. Inserting the energies in Eq. (6.2) into the expression for the Raman cross section I obtain[19,69]

$$K_{2f,10} = \frac{M_f \mathcal{M}_{ba} \mathcal{M}_{cb} M_o (2\kappa_2 - q)}{(v_2 - v_1)^3 (\kappa_2 - q\frac{v_2}{v_2 - v_1})(\kappa_2 + q\frac{v_2}{v_2 - v_1})} \int_0^\infty \frac{dk}{(\kappa_1 - k)(\kappa_2 - k)}, \tag{6.3}$$

with $\kappa_1 = (E_1 - i\hbar\gamma)/(v_2 - v_1)$ and $\kappa_2 = (E_1 - \hbar\omega_{ph} - i\hbar\gamma)/(v_2 - v_1)$. The integral is straightforwardly evaluated yielding

$$K_{2f,10} = \frac{M_f a \mathcal{M}_{ba} \mathcal{M}_{cb} M_o}{(\kappa_2 - q\frac{v_2}{v_2 - v_1})(\kappa_2 + q\frac{v_1}{v_2 - v_1})}. \tag{6.4}$$

Terms varying slowly with q were contracted into the factor

$$a = \ln(\kappa_2/\kappa_1)(2\kappa_2 - q)/[(v_2 - v_1)^2 \hbar\omega_{ph}].$$

The singularities in Eq. (6.4) occur at q where two of the denominators in the sum of Eq. (6.1) go to zero simultaneously. Physically, this means that we have a double resonance at

$$q = \frac{E_1 - \hbar\omega_{ph}}{v_2} \qquad \text{or} \qquad \frac{E_1 - \hbar\omega_{ph}}{-v_1}. \tag{6.5}$$

Both q are larger than the wave vector k_i at which the electron-hole pair was resonantly excited, i.e., the free carrier is scattered across $k = 0$. Looking at Fig. 6.2 it seems that another possibility for the second resonant transition exist with a q which is smaller than the electron-hole pair k vector (roughly at the point were the arrow indicating the backscattering by the impurity crosses the conduction band). These contributions, however, always interfere destructively when the summation in Eq. (6.1) is performed.[69]

The Raman cross section for double resonant scattering is much larger than for single resonances, which occur for all q, or non-resonant contributions. In Fig. 6.3 I plot the Raman

matrix element for two incoming photon energies E_1. I assumed a linear dependence of ω_{ph} on q, the Fermi velocities $v_1 = -7\,\mathrm{eV\AA}^{-1}$ and $v_2 = 6\,\mathrm{eV\AA}^{-1}$ I adapted from graphite. For each photon energy there are two maxima in Fig. 6.3. Note that the pronounced dip between the maxima is a consequence of the factor a in Eq. (6.4). a has its minimum – zero for $\gamma = 0$ – at $q = 2\kappa_2$, i.e., between the two doubly resonant q [Eq. (6.5)]. For different E_1 the maxima in $K_{2f,10}$ are at different phonon wave vector. Nevertheless, as long as the photon energy is large compared to the phonon energy the double resonances occur at wave vectors which are away from the Γ point. Within the present example q varies from 0.13 to 0.6 $\mathrm{\AA}^{-1}$ for photon energies between 1 and 4 eV as compared to $(1-4)\cdot 10^{-3}$ $\mathrm{\AA}^{-1}$ for non-defect induced scattering. Additionally, the doubly resonant q's are of similar order as the extension of the graphite Brillouin zone (1.5 $\mathrm{\AA}^{-1}$). Defect induced double resonant Raman scattering thus allows to study the phonon dispersion in the interior of the Brillouin zone – normally reserved for inelastic neutron or x-ray scattering.

6.2.2. Application to graphite

The example of the last section – linear bands crossing at the Fermi energy – resembles very much the electronic band structure of graphene and graphite as introduced in Chapter 5. We can thus expect qualitatively and even quantitatively a similar behavior as found in the textbook example. Before calculating the defect induced Raman spectra I take a closer look at the graphene Brillouin zone and the possible wave vectors for doubly resonant transitions.

Figure 6.4 shows the contour plot of the graphene π orbitals within the nearest neighbor approximation discussed in Section 5.1.2. Near the K point an electron (black circle) was resonantly excited to the conduction band by the incoming photon. A second resonant tran-

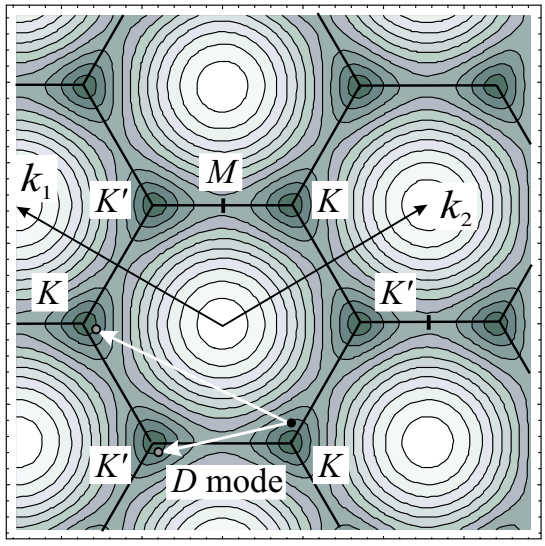

Figure 6.4: Double resonant scattering in graphite: The contour plot shows the electronic band structure of graphite in the nearest neighbor tight-binding approximation of the π orbitals. Scattering from the K to a K' point of the Brillouin zone (white arrow) yields a phonon wave vector which is close to ΓK and thus has the D mode frequency. Scattering between to K points gives a phonon wave vector around the Γ point (but still large compared to $k = 0$).

sition is obtained by scattering the electron to one of the K or K' points in the hexagonal Brillouin zone (white arrows and gray circles), because only there the electronic bands are close enough to the Fermi level. K and K' are connected by a vector pointing from Γ to K, see Fig. 6.4. Hence a phonon which scatters the electron from the neighborhood of K to K' has a phonon energy close to the K point frequency. In contrast scattering from K to the same or another K point in the Brillouin zone yields a phonon wave vector and energy close to the Γ point. In the following I will only consider the first double resonant transition. The second resonant transition results in the Raman peak slightly above the Γ point vibration which is seen in highly disordered graphite. This peak was observed, e.g., by Vidano *et al.*;[18] in Fig. 6.1b) it is labeled D'. The excitation energy dependence is much weaker for this peak than for the D mode, because of the flat phonon dispersion and the overbending in the vicinity of the Γ point.

To calculate the frequency and the excitation energy dependence of the graphite D mode I used the tight-binding nearest neighbor approximation with a carbon-carbon interaction energy $\gamma_0 = 3.03\,\mathrm{eV}$ and $s = 0.129$ [see Eq. (5.3) and (5.5) Section 5.1.2.]. To evaluate Eq. (6.1) for graphite the calculation was restricted to the irreducible domain of the graphene Brillouin zone, i.e., the triangle formed by the ΓM, MK, and $K\Gamma$ lines. Three simplifications were introduced to reduce the necessary computer power: Only the scattering from the K to the K' point of the Brillouin zone was considered as explained in the previous paragraph (the K and K' point coincide in the reduced zone scheme). As the phonon dispersion I used the LO optical branch of graphene, which I modeled by simple functions (linear and sin functions) such that they represent closely those obtained from force constants and *ab initio* calculations.[106,163,164] The Γ point frequency was $1580\,\mathrm{cm}^{-1}$, the ones at the M and K point 1480 and $1270\,\mathrm{cm}^{-1}$, respectively. The typical overbending of the optical branch to $1620\,\mathrm{cm}^{-1}$ was included as well.[96] Lastly, instead of performing the full summation in Eq. (6.1) I searched the Brillouin zone for incoming resonances and, when I found one at $\boldsymbol{k}^o$, summed

$$\sum_{\boldsymbol{k}^f} \left| \frac{1}{\{E_1 - [E_c(\boldsymbol{k}^o) - E_v(\boldsymbol{k}^f)] - \hbar\omega_{\mathrm{ph}}(\boldsymbol{k}^f - \boldsymbol{k}^o) - i\hbar\gamma\}\{\hbar\omega_{\mathrm{ph}}(\boldsymbol{k}^f - \boldsymbol{k}^o) - i\hbar\gamma\}} \right|^2 \quad (6.6)$$

over $\boldsymbol{k}^f$ in the irreducible Brillouin zone. The subscripts v and c refer to the valence and conduction band in the tight-binding approximation. Note that the singularities of Eq. (6.6) which cancel by destructive interference in the full summation need to be excluded explicitly from the calculation. The last approximation – fixed incoming resonances – must be treated with care when comparing the calculated results with experiments. First, it slightly shifts the calculated maximum of the Raman peak ($\approx 10\,\mathrm{cm}^{-1}$). Second, information on the relative intensities is lost completely, because "nearly resonant" electronic transitions are

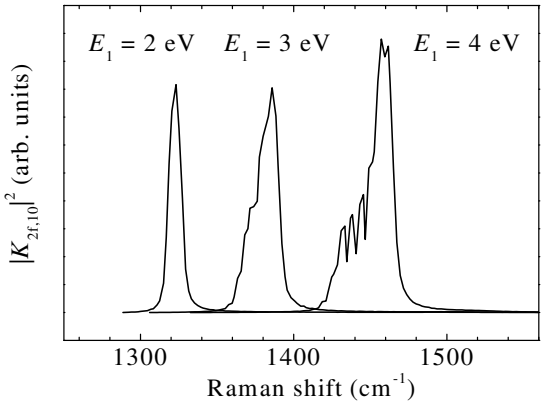

Figure 6.5: Calculated Stokes Raman spectrum of the *D* mode in graphite for three different excitation energies. The frequency shift with laser energy is clearly seen in the calculations. Note that the relative intensities calculated at different E_1 cannot be compared to each other (see text for details). A reciprocal life time $\gamma = 0.1\,\mathrm{eV}$ was used for the calculations.

not considered. For the *D* mode in nanotubes, a nice study of the dependence of the calculated Raman spectra on the mentioned approximations and the used parameters was done by Janina Maultzsch in her Diploma thesis.[165]

In Fig. 6.5 I show $|K_{2f,10}|^2$ as a function of the phonon frequency ω_{ph} for three different laser energies. Clearly the *D* mode Raman spectrum is obtained by considering double resonances in graphite. The peak shifts with increasing excitation energy to higher frequencies as found experimentally; also the spectral shape is nicely reproduced. The calculated peak width ($\approx 20\,\mathrm{cm}^{-1}$) is smaller than the experimental one ($\approx 40\,\mathrm{cm}^{-1}$), which is partly due to having fixed the incoming resonance in the calculations and partly to a too small reciprocal life time. In Fig. 6.6 I plotted the maxima of the calculated peaks as a function of excitation energy. Also shown in the Figure are experimental results for the *D* mode frequencies obtained by various groups. The agreement is found to be excellent, in particular, since all parameters were fixed during the calculation and no fitting to experimental data was performed. The calculated slope of the *D* mode's excitation energy dependence is $60\,\mathrm{cm}^{-1}/\mathrm{eV}$, slightly larger than the experimental values ranging from 44 to $56\,\mathrm{cm}^{-1}/\mathrm{eV}$.[18,156–158] The absolute frequency of the doubly resonant peak agrees excellently as well.

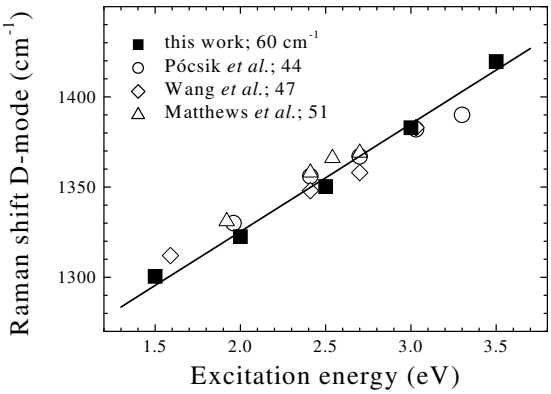

Figure 6.6: Measured and calculated frequency of the *D* band as a function of excitation energy. The filled squares are the frequencies calculated from the double resonant condition; the full line is a fit to the calculated data with a slope of $66\,\mathrm{cm}^{-1}/\mathrm{eV}$. Open symbols represent measurements by Pócsik *et al.*[156] (open circles), Wang *et al.*[157] (open diamonds), and Matthews *et al.*[158] (open triangles). The experimental slopes are given in the figure

When I discussed the experimental findings for the D band in graphite I mentioned three peculiarities of this mode: It appears only for disordered graphite and its intensity increases with the degree of disorder, the D mode frequency depends on excitation energy, and the Stokes and anti-Stokes frequencies are different. Obviously the first two characteristics are explained by defect-induced double-resonant Raman scattering. The difference in Stokes and anti-Stokes frequency also follows from the model. In the textbook example of double resonant scattering with two linear bands I depicted a Stokes process in Fig. 6.2. For anti-Stokes scattering – creation of a phonon – at the same incoming resonance a slightly larger phonon wave vector is required to meet the double resonance condition. Consequently, a larger phonon energy is expected for anti-Stokes scattering in graphite, since the phonon dispersion bends up when going away from the K point.[106,164] At a photon energy $E_1 = 2\,\mathrm{eV}$ I obtained a difference of $\approx 15\,\mathrm{cm}^{-1}$ in Stokes and anti-Stokes frequency compared to $7\,\mathrm{cm}^{-1}$ as found by Tan *et al.*[155]

The double resonant process also occurs for two phonons, i.e., instead of scattering the electron back by an impurity it is scattered back under the emission of a second phonon. This overtone of the D mode, the D^* band, is expected to have twice the frequency shift with varying excitation energy, which is indeed what is observed experimentally.[18] In contrast to the D mode the second order D^* mode is not defect induced and should also be found in the Raman spectra of graphite single crystals. Single crystal measurements are not available at present, but Nemanich and Solin[96] reported a strong D^* peak in highly-oriented pyrolytic graphite where the D mode is very weak. Moreover, the D^* band in their measurements was only half as large as the first order Γ point Raman signal. The large intensity of the second order signal as compared to first order Raman scattering independently confirms the interpretation of the D and D^* Raman peaks as due to double resonances.

6.3. The *D* mode in nanotubes

Scattering in the energy range of the D mode was reported in the very first papers on Raman scattering in nanotubes.[25,27] Similar phonon frequency shifts with excitation energy and differences in the Stokes and anti-Stokes spectra as in graphite were found in carbon nanotubes.[39,40,166,167] For some time it was thought that the D mode scattering came from graphite particles in the nanotubes samples, but measurements on isolated tubes proved it an intrinsic feature of carbon nanotubes. In Fig. 6.7 I reproduce the spectra measured by Düsberg *et al.*[15] on an individual single-walled nanotube residing on a glass substrate. Surprisingly, the Raman intensity of this single molecule is strong enough to be observed

experimentally. The spectrum shows the radial breathing mode, the high-energy modes, and – with similar intensity – the D mode of a single nanotube. The Raman spectra taken on isolated nanotubes are remarkably different in the D mode region. While some spectra show an intense D band as in Fig. 6.7, the mode is very weak or absent in other measurements.[15, 16, 154, 168] As I will show in the following these differences arise from the confined electronic bands in carbon nanotubes.[21]

The electronic structure of carbon nanotubes to first approximation was obtained from the one of graphene by cutting parallel lines out of the graphene Brillouin zone, see Chapter 5. The graphite double resonance condition is thereby modified such that all electronic and phononic states are restricted to the lines of allowed wave vectors of the particular tube. Rolling up the cut rectangle introduces m as quasi-conserved or $\tilde{m}$ as a fully conserved quantum number. This is equivalent to requiring that, additionally, defect scattering occurs only for bands of the same m and bands associated to m by the Umklapp rules (i.e., bands of the same $\tilde{m}$).* To obtain the D band systematically, points in the neighborhood of K and K' should, therefore, lie on the same or associated m lines. This seemingly complicated condition translates into a simple rule for the n_1 and n_2 indices of the tube if I consider symmetry, in particular, the symmetry-adapted tight-binding model of Section 2.5.2. instead of plain zone-folding. Before considering general tubes, however, I discuss the special case of armchair nanotubes.

Armchair tubes always fulfill the condition that the K and K' points of graphene are among their allowed states and belong the a line with the same $m = n$ quantum number (see Fig. 5.3 on page 89).[45] The π orbital tight-binding band structure of a (10,10) tubes is shown in the upper panel of Fig. 6.8. Resonant excitations in the visible energy range (1) occur close to the Fermi wave vector $k_F = 2\pi/3a$. The electron is scattered across the Γ point (2) to another

*Kürti *et al.*[169] calculated double resonances in nanotubes assuming that a change in m can be introduced by defect scattering, i.e., using only the boundary conditions of the cut graphene sheet. They gave, however, no justification for not treating m as a conserved quantum number.

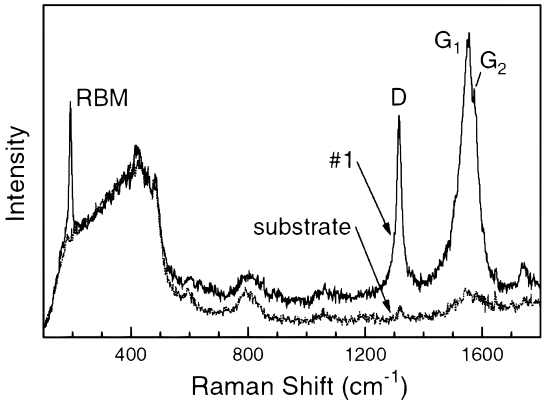

Figure 6.7: Raman spectrum of a single walled nanotube isolated on a substrate. The D mode appears with a similar intensity as the high-energy nanotube modes (labeled G_1 and G_2) and the radial breathing mode (RBM). The measurement shows that the D mode is an intrinsic feature of carbon nanotubes and does not originate from impurities like graphitic particles. From Ref. 15.

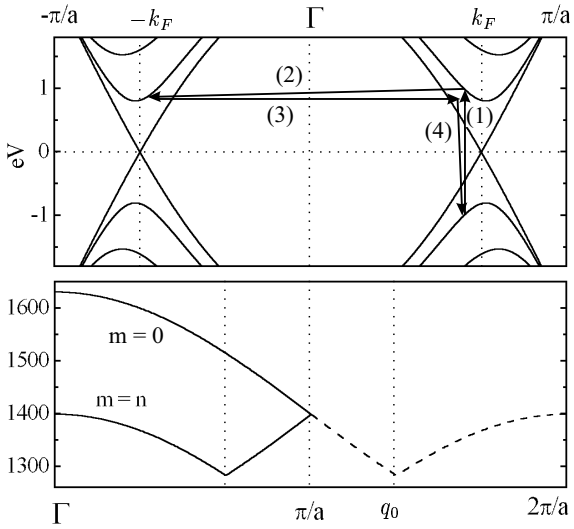

Figure 6.8: Double resonant scattering in a (10,10) armchair tube. In contrast to graphene the wave vectors are now confined to a single line. Upper panel: Close to the Fermi wave vector k_F an electron-hole pair is resonantly excited by the incoming photon (1). The electron is scattered to another real state with approximately opposite k (2). Step (3) and (4) show the backscattering by the impurity and the recombination. The two Fermi vectors correspond to the K and K' point of the graphene Brillouin zone. Lower panel: Model phonon dispersion of the (10,10) tube of the fully symmetric phonon mode ($m = 0, n$). The double resonance condition is fulfilled by phonons close to q_0.

real states followed by impurity induced backscattering (3) and recombination (4). The q vector required for the double resonance in step (2) is $|q| \approx 2k_F = 4\pi/3a =: q_0 = |k_F - G|$, i.e., approximately the same as electronic wave vector were the incoming transition took place. This is in fact to be expected, since in graphene both the electronic and phononic wave vector for doubly resonance D mode scattering corresponded to a ΓK vector. Similar k_z vectors are then also obtained for the tube by zone-folding. The lower panel of Fig. 6.8 displays the $m = 0$ and $m = n$ (dashed line) phonon dispersion in the extended zone scheme. The double resonant phonons around $q = 0$ indeed give frequencies in the range of the D mode.

To calculate the Raman spectrum I proceed as described for graphite in Section 6.2.2. The full expression for the Raman cross section in Eq. (6.1) was used in the numerical evaluation. The electronic dispersion was described by the symmetry adapted tight-binding Hamiltonian (see Section 2.5.2.) with $\gamma_0 = 2.9\,\text{eV}$; the phonon dispersion was obtained within zone-folding. As

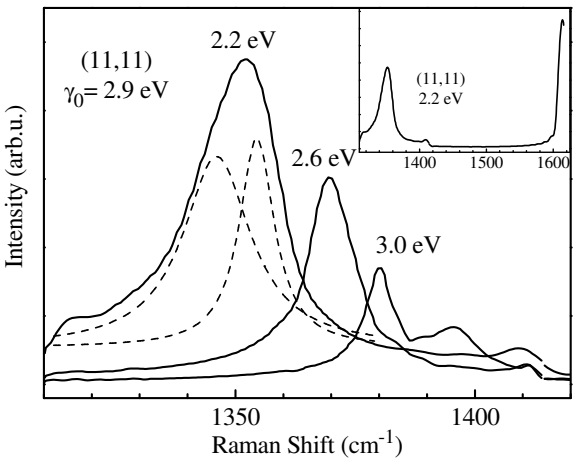

Figure 6.9: Calculated Raman spectra for an (11,11) tube at three different excitation energies E_1. In the frequency range of the D mode I obtain a double peak structure shifting with excitation energy. The two dashed lines show a fit to the calculated spectrum by two Lorentzians. Note the increasing intensity with decreasing E_1. The inset shows the complete first order spectrum resulting from the double resonance condition. The mode at $1600\,\text{cm}^{-1}$ is discussed in the next section.

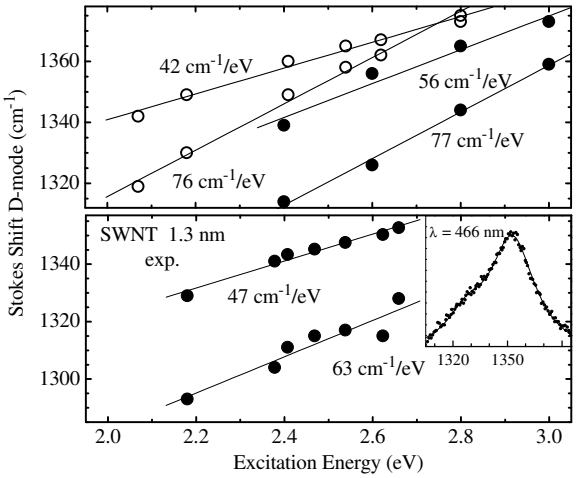

Figure 6.10: Calculated and measured frequency shift of the *D* mode in single walled carbon nanotubes. Upper panel: Calculated frequencies for a (10,10) (open symbols) and an (8,8) (closed symbols) nanotubes. In the (11,11) tube of Fig. 6.9 I obtained slopes of 35 and 65 cm^{-1}/eV. Lower panel: Measured *D* mode frequencies in a nanotube sample with a mean diameter $d = 1.3\,\mathrm{nm}$ as a function of laser energy. The inset shows the spectrum excited with $E_1 = 2.66\,\mathrm{eV}$; clearly the Raman spectrum shows the double peak structure with a main peak and a shoulder on the low frequency side.

a model phonon dispersion which fully reflects the hexagonal symmetry of graphene I took the tight-binding expression for the electronic bands in Eq. (5.3) (page 90), added a constant term $B = 1310\,\mathrm{cm}^{-1}$, and used a scaling parameter $A = 102\,\mathrm{cm}^{-1}$ (instead of γ_0). This electronic and phononic dispersion satisfactory describe graphene in the neighborhood of the *K* point, which is the part of the Brillouin zone I am currently focused on. The calculated Raman spectrum of an (11,11) tube I show in Fig. 6.9 for three excitation energies E_1. The *D* mode of nanotubes obviously has the same origin as in graphite and depends on E_1 as well.[21] Some interesting differences result from the one-dimensionality of the tubes, which were also found experimentally. The *D* mode consists of two peaks shifting with a different slope with laser energy. The double peak structure is due to (i) the slight shift of the electronic minima away from k_F, (ii) the asymmetry of the electronic and phononic dispersion around their minima as can be seen in Fig. 6.8, and (iii) different double resonant phonon wave vectors for incoming and outgoing electronic resonances. While all three points, in general, hold similarly for graphite, the double peak structure is smeared out by the 2D integration and becomes only visible at small laser energies.[156] In nanotubes – where the relevant part of the Brillouin zone is confined to a line – they are still visible after the integration. The second difference is the pronounced intensity increase in the calculated spectra for decreasing E_1. It reflects the high electronic density of states when approaching the minima and maxima of the confined subbands with the energy of the incoming or scattered light. Measurements of the absolute scattering efficiency of the *D* mode as a function of excitation energy were not performed so far, but it would be interesting to do so in the future. Nevertheless, in isolated tubes Pimenta *et al.*[168] reported the *D* mode to be in general stronger in intensity when excited in the red. I compare the calculated *D* mode frequency as a function of excitation energy to the experimental results in Fig. 6.10. The inset shows the Raman spectrum recorded with a laser wavelength $\lambda = 466\,\mathrm{nm}$ on bulk samples. The Raman mode

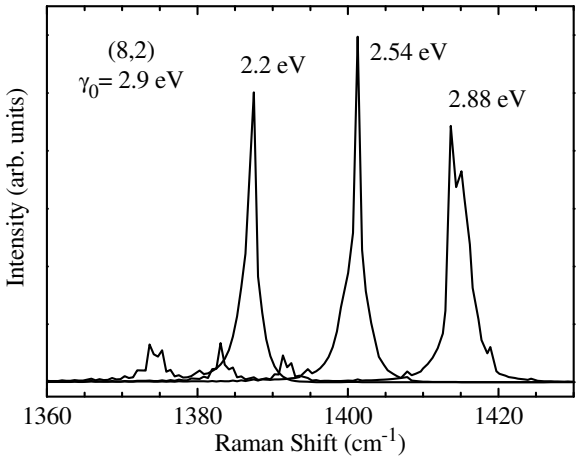

Figure 6.11: The *D* mode of a chiral (8,2) nanotube. The main peak shifts by 40 cm^{-1}/eV in this tube with a diameter of 0.72 nm (the smaller peak by 27 cm^{-1}/eV). In this $\mathcal{R}=3$ nanotube the *D* mode and its excitation energy dependence are systematically obtained for a wide range of laser energies.

consists of a main peak at 1353 cm^{-1} with a low-energy shoulder at 1328 cm^{-1} as I found in the calculations. The calculated slopes of the main *D* mode peak for the three armchair tubes range from 35 cm^{-1}/eV in the (11,11) tube to 56 cm^{-1} in the (8,8) tube. The experimental shift which was obtained on a bulk sample with a mean diameter $d=1.3$ nm is 47 cm^{-1}. In view of the homogeneous chirality distribution in the sample and the number of unknown parameters in the calculation the agreement is excellent. The other characteristics of the *D* mode, i.e., its D^* overtone and the difference in Stokes and anti-Stokes frequency, follow for armchair nanotubes in essentially the same way as in graphite.[21] I will not consider them here in any detail; instead I turn to general chiral tubes.

The important point for systematically obtaining a *D* mode in a wide range of excitation energies in nanotubes is that both the neighborhood of the *K* and the K' point is touched by a line of the same $\tilde{m}$ (all m connected by Umklapp processes). The *K* and K' point of graphene are connected by the U axis symmetry. Let us assume that the allowed state in a nanotube approaching closest the *K* point is given by the eigenstate $|\tilde{k},\tilde{m}\rangle$.[45] By the U operation this state is mapped to $|-\tilde{k},-\tilde{m}\rangle$. For the two $\tilde{m}$ to be the same, obviously, $\tilde{m}$ must be equal to zero or $q/2$, which is only fulfilled for tubes with $(n_1-n_2)/3n=$integer, the $\mathcal{R}=3$ nanotubes.[55] Zig-zag tubes never belong to this category and I do not expect a strong *D* mode for any excitation energy. In the Brillouin zone picture in Fig. 5.3b) (page 89) it is seen that following one allowed line near a graphene *K* point one will only arrive at another *K* but never at K'. Interestingly, tubes with $\mathcal{R}$ are always metallic and, moreover, they are those tubes where the crossing of the valence and conduction band is at $\tilde{k}_F \approx 2\pi/3a$ as in armchair tubes.[21,55] An example for double resonant scattering in an $\mathcal{R}=3$ tube is shown in Fig. 6.11. I find a double peak structure as in armchair nanotubes and a shift with excitation energy. The slope of the main peak 40 cm^{-1}/eV is lower than in armchair tubes, where the smallest diameter (8,8) tube has a shift of 56 cm^{-1}/eV. In zig-zag tubes and in chiral tubes with $\mathcal{R}=1$

an evaluation of the double resonant Raman cross section either yields no D mode at all or no systematic excitation energy dependence. A lower intensity, though, is usually found for phonon modes originating from the K and M points of graphene, because of the high density of states at these critical points. Nevertheless, a single tube spectrum as I showed in Fig. 6.7 with a strong D mode intensity can be interpreted as coming from a metallic nanotube (more precisely, from an $\mathcal{R} = 3$ tube). On the other hand, the $\mathcal{R} = 3$ selection rule requires that some tubes do not show D mode scattering at all, which could be confirmed by measurements on individual tubes. Such Raman spectra are still rare in the literature, in particular, in the high-energy range.[15,154,168] The spectra by Yu and Burns[154] indeed show on some tubes a D band intensity comparable to the measurements by Düsberg *et al.*,[15] whereas the mode is completely absent in other tubes. Pimenta *et al.*[168] also mention that "the D mode intensity appears to be random from one tube to another",[168] which supports our predictions. Another experiment – much easier to perform – are measurements of the absolute intensity of the D mode on bulk nanotube samples normalized to a reference crystal since the singularities in the optical absorption for metallic tubes are separated in energy from those of semiconducting nanotubes.[34,43,44]

One point I did not question up to now is that the D mode of a single nanotube is observable at all. The spectrum shown in Fig. 6.7 was taken on a single nanotube which was approximately 1.5 μm in length.[15] The finite length of the tube *per se* is thus not the mechanism relaxing k conservation in this experiment. Other possible sources are defects like pentagon-heptagon pairs or vacancies,[10,125,153] bending induced effects,[170] and a high optical absorption.[69] It is a little hard to judge how common defects are in carbon nanotubes since up to now most of the experimental work has concentrated on perfect tubes with only a few exceptions.[170–172] The optical penetration depths, on the other hand, is on the order of 10 nm. Optical absorption is treated slightly differently in the calculation of the Raman cross section, but leads to double resonances as well. The true mechanism for breaking k conservation still needs to be investigated. Nevertheless, the observation of the D mode on individual tubes confirms that double resonances are indeed involved in the Raman spectra of nanotubes. Other proposed explanations, e.g., a break-down of Raman selection rules, were not able to reproduce the subtle characteristics of the experimental spectra. Also other modes are expected to become Raman active for relaxed selection rules like the $m = q/2$ phonons originating from the M point of graphene in sharp contrast to the experimental observations.

The double resonance process I described in this section always required a scattering across the nanotubes Γ point to mimic the D mode double resonance in graphene. In Fig. 6.8, however, a second doubly resonant transition is easily identified, scattering across the conduction

band minimum with a comparatively small q. In fact, I already showed a Raman peak originating from this doubly resonant transition in the calculated spectrum of the (11,11) tube in Fig. 6.9. The inset of the figure showed the complete first order spectrum with a peak at $\approx 1600\,\mathrm{cm}^{-1}$, in the energy range of the high-energy nanotube modes. After realizing this second double resonance we started to think about the whole Raman spectrum in terms of double resonant scattering.[13]

6.4. The Raman spectrum of carbon nanotubes

In attempts to assign the high-energy Raman modes of single walled carbon nanotubes to Γ point vibrations two points have not been resolved so far: The peak of strongest intensity ($1595\,\mathrm{cm}^{-1}$) is above the frequency of the graphite Γ point vibration ($1582\,\mathrm{cm}^{-1}$). First explanations therefore assigned this peak to E_1 and E_2 phonon modes, which predicted them to be upshifted within zone-folding by $\approx 5\,\mathrm{cm}^{-1}$, but clearly violates the experimentally obtained selection rules, see Chapter 3. The peaks were then suggested to be LO and TO like vibrations split by the curvature of the graphene sheet. In chiral nanotubes, however, the eigenvectors are of mixed LO-TO character as I showed by pressure experiments and *ab initio* calculations. Moreover, the curvature of the graphene sheet was found to soften the force constants and is thus not able to explain the higher Raman frequency in the tubes.[40,106] The splitting of the high-energy Raman modes was also calculated to be much smaller ($5\,\mathrm{cm}^{-1}$) than the experimental difference of $20\,\mathrm{cm}^{-1}$ between the two most intense Raman peaks. The second difficulty in interpreting the Raman spectra was the intensity ratio of $2-4$ between the strongest and the second strongest peak. No suggestions were made for the origin of the different intensities except for the work by Saito *et al.*,[173] which started from the incorrect LO and TO eigenvectors for chiral nanotubes.

I propose that the high-energy mode originate from double resonant Raman scattering, which resolves the difficulties in the understanding of the modes. The scattering process giving rise to the high-energy modes is explicitly shown in Fig. 6.12a). The free carrier instead of being scattered across the Γ point to a state of approximately opposite wave vector [(2B), D mode] is scattered across the band extremum to another real state (2A). Since two optical modes belong to the fully symmetric representation and can thus scatter within the band I expect two phonon peaks two follow from this process. To calculate the Raman cross section for (2A) I used a model phonon dispersion for the LO and TO graphite optical modes, fitted to reproduce *ab initio* calculations.[13,106] The Γ point frequency was $1588\,\mathrm{cm}^{-1}$, the modes were degenerate at $k=0$. All other parameters were chosen as described for the D mode

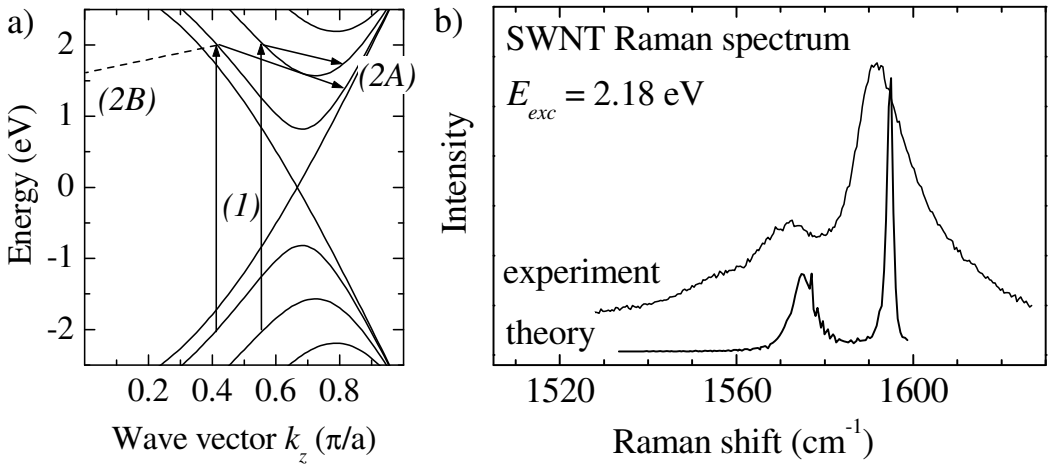

Figure 6.12: High-energy Raman spectra of single walled carbon nanotubes. a) Schematic double resonant scattering process. After the resonant absorption (1) the electron is scattered to another real electronic state. While scattering across the Γ point (2B) yields the *D* mode (dashed arrow), scattering across the conduction band minimum (2A) is the origin of the high-energy modes. For large enough laser energies two incoming resonances occur giving sligtly different doubly resonant wave vectors and frequencies. Backscattering and recombination are not shown for simplicity. b) Calculated and measured Raman spectrum for a (15,6) nanotube at an excitation energy $E_1 = 2.18\,\mathrm{eV}$ (only one incoming resonance). The two optical modes belonging to the fully symmetric representation at the Γ points give rise to two double resonantly scattered phonon peaks.

in graphite and nanotubes. The calculated spectrum for double resonant Raman scattering perfectly describes the experimental spectra in the high-energy region: I find the main peak above the Γ point frequency at $1597\,\mathrm{cm}^{-1}$ and a second, less intense peak at $1575\,\mathrm{cm}^{-1}$. The magnitude of the splitting as well as the absolute peak positions are in excellent agreement with experiments. The relative amplitude of the two peaks is also similar to the ratio found experimentally. The frequency shift compared to the Γ point frequency is due to the overbending of one of the phonon branches. The overbending and the flat dispersion in the vicinity also makes the $1597\,\mathrm{cm}^{-1}$ peak narrower and larger in height than the $1575\,\mathrm{cm}^{-1}$ peak coming from the stronger dispersive lower optical branch. For the (15,6) tube shown in Fig. 6.12b) and $E_1 = 2.18\,\mathrm{eV}$ only two almost degenerate incoming (or outgoing) electronic resonance are possible. In semiconducting nanotubes of similar diameter up to three incoming resonances contribute for this laser energy. Each electronic resonance also results in double resonant scattering as depicted schematically in Fig. 6.12a). Instead of only two up to six peaks are then calculated from the Raman cross section, although the processes where the electronic resonance occurs further away from the singularities in the electronic density of states are lower in intensity. For the weakly dispersive higher optical branch the three peaks are at similar frequency, whereas the lower energy peak develops small satellites

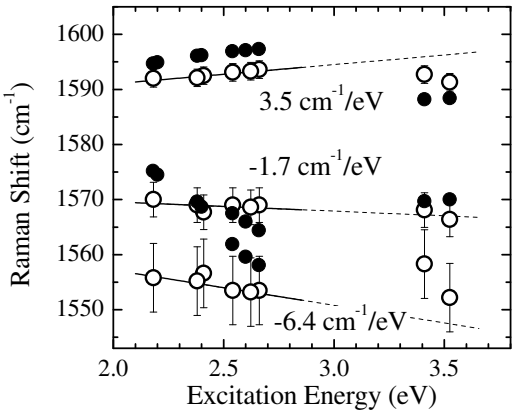

Figure 6.13: Excitation energy dependence of the high-energy modes in single walled nanotubes. The open symbols are experimental Raman frequencies excited with various Ar and Kr laser lines. The sample were bulk nanotubes with a mean diameter $d = 1.45\,\text{nm}$. The full lines are linear fits to the measured frequencies between 2.1 and 2.6 eV excitation. The broken lines show the extrapolation to the near UV energy range. The frequencies calculated for a (15,6) tube are shown by closed symbols.

at even lower frequency explaining the contributions below $1560\,\text{cm}^{-1}$ in the experimental spectra.

The main characteristic of double resonant scattering is the dependence of the Raman spectra on excitation energy. In contrast to the D mode, where the Raman frequency always increased with increasing laser energy, the high-energy modes should show an energy increase for the $1595\,\text{cm}^{-1}$ mode (overbending), but a decrease for the $1575\,\text{cm}^{-1}$ peak (downbending phonon dispersion). For excitation energies between 2.1 and 2.6 eV the $1595\,\text{cm}^{-1}$ peak frequency indeed increases with laser energy, whereas the two other modes have a negative slope, see Fig. 6.13. The shifts, however, are no longer linear when going to higher excitation in the UV energy range: All three modes come back to the positions they had around 2 eV. When we recorded the spectra almost two years ago I did not expect a frequency shift of the first order Raman modes nor did I understand this jumping above 3 eV. Curvature effects – the first obvious idea then – were not able to explain the effect consistently even if I assumed a much larger diameter distribution than the $\sigma = 0.1\,\text{nm}$ uncertainty present in the sample. Within the double resonant picture the shifting and jumping are a natural consequence of the model as the calculations for the (15,6) nanotube demonstrate in Fig. 6.13 (full dots). For increasing excitation energy the Raman peaks shift to higher or lower frequency according to the dispersion of the A_1 vibrations. At $\approx 3\,\text{eV}$ the laser approaches the next optical transition energy. The double resonant transition with dominant intensity then has a smaller q and, consequently, the observed frequencies are closer to the Γ point vibrations. The agreement between theory and experiment in Fig. 6.13 is surprisingly good for the $1595\,\text{cm}^{-1}$ peak even so the experiments were done on bundles and the calculations only for a single tube. This is again caused by the flat dispersion for the higher optical branch in contrast to the lower branch where the comparison is less satisfactory. Further calculations for different nanotubes most likely will resolve the remaining discrepancies. Additionally, the relative intensities for varying the excitation energy and the (n_1, n_2) indices and thus the electronic band structure

should be studied in the future. Since the intensity is further enlarged when the double resonance occurs for a high electronic density of states, the Raman spectra obtained on bulk samples reflect a convolution of these effects.

6.5. Summary

The Raman spectra of disordered graphite and carbon nanotubes share uncommon features, the most remarkably being their Raman frequencies depending on excitation energy. In graphite the *D* mode frequency dispersion was known for almost 20 years experimentally. In this chapter I showed that this Raman puzzle is resolved by defect induced double-resonant scattering. The double resonance condition picks out a unique combination of phonon frequency and wave vector at a given excitation energy, which dominates the experimental Raman spectrum. I calculated Stokes and anti-Stokes spectra for varying excitation energy and found excellent agreement with experiments. The *D* mode of carbon nanotubes has essentially the same origin, although the spectra are altered by the one-dimensionality of the tubes. In particular, only metallic tubes with $(n_1 - n_2)/3n =$integer are expected to show strong *D* mode scattering.

The observation of the *D* mode on isolated nanotubes with similar intensity as the other parts of the Raman spectrum lead me to the idea that the entire nanotube Raman spectrum is explained by double resonant scattering. I presented first calculations of the high-energy Raman spectrum based on this idea. For the first time, an attempt to model the high-energy Raman modes correctly predicted the double peak structure so well known from experiment. An intrinsic characteristic of double resonant scattering is the dependence of the Raman modes on excitation energy. Therefore, I performed measurements on bulk samples with a variety of excitation energies, which confirmed my theoretical predictions. The most intense Raman peak shifted to higher frequencies with increasing laser energy, because of the overbending of the higher optical A_1 phonon branch. In contrast the peaks originating from the lower phonon branch showed a negative slope as expected from the phonon dispersion.

Chapter 7

Summary

In this work I studied the vibrational and electronic properties of carbon nanotubes. My motivation was to explain the Raman spectra of this material, in particular, the group of broad high-energy modes around 1600 cm^{-1}. From the first reports on Raman scattering in nanotubes it was obvious that these modes are related to the graphite optical mode, which is at similar frequency. A first assignment as suggested by Rao *et al.*[27] explained the high-energy peaks as modes of different symmetry (A_1, E_1, and E_2) arising from the confinement around the nanotube's circumference. They also presented force constants calculations of achiral armchair tubes where they found the A_1 and E_2 high-energy phonon to have a circumferential and the E_1 mode an axial displacement. The model by Rao *at al.*[27] successfully predicted Raman active phonons in the frequency range of the high-energy modes, but soon it turned out that it was not able explain the shape and overall frequency range of the Raman spectrum. At first I thought that a refined approach, for example to include additional nanotubes, will lift the discrepancies between theory and experiment. During my work, however, I found that small corrections are not sufficient to understand the origin of the experimental spectra. We recently proposed an entirely different model of the Raman process in carbon nanotubes based on double resonant scattering.

My first difficulties with the then accepted interpretation of the Raman spectra arose from high-pressure Raman experiments. With an elastic continuum model I showed that the deformation of a nanotube under hydrostatic pressure is by a factor of 2 larger in the radial or circumferential than in the axial direction. A similar anisotropy is then expected for the pressure shifts of the Raman modes originating from axial and circumferential phonon eigenvectors. My prediction of a 15 % difference in pressure slopes was in sharp contrast with the experimental observations, where the logarithmic pressure derivatives of the high-energy Raman modes agreed to within 3 %. To learn more about phonon eigenvectors, in particular, about

the atomic displacement directions, I studied group theory and the symmetry properties of single-walled carbon nanotubes. I worked out a graphical group projector technique to find a symmetry adapted phonon eigenvector for a particular representation. In achiral armchair and zig-zag nanotubes the phonon eigenvectors are given by the nanotube symmetry alone. I found that a circumferential Raman active mode in an armchair tube corresponds to an axial mode in a zig-zag tube and *vice versa*. In chiral nanotubes, however, the displacement direction of the eigenvectors cannot be deduced from the nanotube symmetry. An arbitrary direction of the atomic displacement with respect to the nanotubes axis explains the apparent discrepancies between theory and experiment in the high-pressure Raman studies. The shear strain splitting introduced by the anisotropic elastic properties of carbon nanotubes washes out and only an average frequency shift is observed experimentally. This average frequency shift is given by the hydrostatic component of the strain tensor and the phonon deformation potentials. With the strain tensor I found from elasticity theory and the Grüneisen parameter of graphite I obtained a hydrostatic pressure slope of $3.9\,\mathrm{TPa}^{-1}$ in excellent agreement with the experimental value ($3.7\,\mathrm{TPa}^{-1}$). To finally prove my suggestion for the phonon eigenvectors in chiral nanotubes I calculated the eigenvectors of an (8,4) and a (9,3) nanotube with first principles methods. Indeed the atomic displacement pointed in arbitrary directions for the non-degenerate A and B phonon eigenvectors. Moreover, the displacement direction was varying for the degenerate E modes when going around the circumference of the tube. I called this unexpected behavior a wobbling of the eigenvector or the displacement direction and introduced the displacement ellipses to uniquely specify the eigenvectors in general chiral nanotubes. The mixed circumferential and axial character of the vibrations in chiral tubes thus nicely explains the high-pressure experiments, in particular, the observed uniform pressure slope of all Raman frequencies around $1600\,\mathrm{cm}^{-1}$.

Looking back to the original proposal by Rao *at al.*[27] for the interpretation of the nanotube Raman spectra the picture is now more complicated, since I have to take into account the chiral tubes and their vibrations explicitly. The basic idea – the Raman peaks originate from A and E symmetry phonons – may still be correct. My next step therefore was to determine the symmetry of the Raman scattered light and to decompose the spectrum into modes of different symmetry. On unoriented samples this can be done with the help of linearly and circularly polarized light to find the invariants of the Raman tensor. Experimentally, all Raman modes of single-walled nanotubes, i.e., from the low-energy radial breathing mode to the high-energy vibrations, showed exactly the same tensor invariants. Only totally symmetric A_1 phonons contribute to the Raman spectra. Moreover, the signal comes entirely from z polarized incoming and outgoing light. This observation immediately raises two questions: What is the origin of the different Raman peaks if only A_1 and not E_1 and E_2 phonons scatter?

What is the reason for the dominant *zz* contribution in the experiment? I started by pursuing the second question.

Raman scattering in carbon nanotubes was known to be strongly resonant throughout the visible energy range. Therefore, it was probably more important to consider the selection rules for the optical absorption than for the non-resonant Raman process. From the symmetry imposed selection rules in achiral nanotubes I found that z polarized transitions are always allowed in the visible between valence and conduction bands with the same m quantum number, whereas x or y polarized absorption was severely restricted in zig-zag tubes. In these tubes perpendicular polarized transitions below $\approx 4\,\mathrm{eV}$ were forbidden except for the combination of valence and conduction bands lying next to the Fermi level. The representations of the electronic states *per se* were, however, not sufficient to allow me to draw general conclusions for armchair or chiral nanotubes. Although by hand-waving arguments I expected the optical absorption to be low for perpendicularly polarized light in all nanotubes, the absolute transition matrix elements were necessary to fully judge on this question. By *ab initio* calculations of the dielectric function in chiral and achiral nanotubes I found the absorption strength to be by a factor of 4 smaller for x or y than for z polarized transitions in the visible energy range. Moreover, in contrast to the parallel polarization the perpendicular absorption spectrum was unstructured above $\approx 1.5\,\mathrm{eV}$ without the typical square root singularities expected for one-dimensional systems.

During my *ab initio* calculations of the optical properties in carbon nanotubes I realized a number of differences between the first-principles band structure and the one calculated from the tight-binding approximation of the graphene π orbitals, which I had been using before for simple band structure calculations. Since the tight-binding model is very popular for carbon nanotubes, e.g., for finding transition energies in absorption or Raman spectra or for the density of states in STM measurements, I started wondering how reliable the approximation was for the electronic energies in isolated and also bundled nanotubes. I calculated the electronic band structure for achiral and chiral nanotubes, both isolated and arranged in a hexagonal lattice. The curvature of the nanotube wall mixes the σ and π derived nanotube wave functions, which, in general, shifts the π electronic bands towards the Fermi level. The effect reduces with increasing diameter, but even for typical diameter tubes ($d = 1 - 1.5\,\mathrm{nm}$) I found the optical transitions energies to differ by $5 - 10\,\%$ between the zone-folding (neglecting curvature) and the *ab initio* result. Bundling of the tubes to ropes further reduces the band gap in semiconducting nanotubes and may even close the gap as I found for the (10,0) nanotube bundle. Additionally, the optical transition singularities are smeared out in the bundled tube because of the interaction between the tubes. Experiments performed on bulk samples can thus not simply be compared to an isolated tube theoretical

model. During my band structure studies I found the π orbital tight-binding approximation to yield an overall satisfactory description of the first principles band structure; the error in the absolute electronic energies, however, is as high as 20 % for tubes with diameters between 1 and 1.5 nm.

The band structure calculations in some sense were a side step from my original focus on the high-energy Raman spectra, although an understanding of the electronic dispersion is essential for the resonant Raman process. The second topic I was working on at this time – the disorder induced *D* mode in graphite – I first thought to be even further away, but there we finally found the key for the nanotube Raman spectra. Experimentally the frequency of the *D* mode was known to shift with the energy of the exciting laser by $50\,\mathrm{cm}^{-1}$/eV since the measurements by Vidano *et al.*[18] The origin of this peculiar behavior remained puzzling for almost two decades. As I showed in this work it is caused by a double-resonant Raman process, which selectively enhances a unique combination of phonon wave vector and frequency. The double resonantly enhanced wave vector and frequency depend on the energy of the incoming light and thus the Raman mode is dispersive with laser energy. The calculation of the matrix element yielded excellent agreement both in absolute frequencies of the *D* band as well as the rate of the frequency shift with laser energy ($60\,\mathrm{cm}^{-1}$/eV). Essentially the same process gives rise to the entire Raman spectrum of single-walled carbon nanotubes. Compared to the *D* mode, which is also present in nanotubes, the phonon wave vectors involved in the double resonant transitions of the high-energy modes are much smaller, but they are still large compared to the photon momentum. A calculation of the double resonant Raman cross section within a simple model showed that our suggestion correctly predicts the shape of the high-energy Raman spectrum. An intrinsic property of double resonant Raman scattering is the frequency change with laser excitation energy. I presented Raman measurements excited with a variety of laser energies, where the expected dependence was in excellent agreement with the theoretical expectations. In particular, the most intense high-energy Raman peak shifted to higher phonon frequencies with increasing laser energy, whereas for the other modes (in this frequency range) the frequency decreased. The different behavior follows from the overbending in the higher optical and the downbending dispersion in the lower optical phonon branch. Also a number of more subtle experimental findings like, e.g., the scattering symmetry or a difference in the Stokes and anti-Stokes spectra follow naturally from our new interpretation for the Raman spectra in carbon nanotubes. The interesting point in the double resonant process is that the involved phonon wave vectors are large compared to the Brillouin zone. The Raman spectra of nanotubes thus reflect the vibrational and electronic dispersion for a wide range of wave vectors. Both can be studied by varying excitation energies or selecting different tubes in a Raman experiment.

Appendix 1

Ab Initio Calculations with SIESTA

Ab initio or first principles methods calculate the physical properties of a material without any experimental input. Among them total energy calculations by density functional theory became extremely successful over the last decades in predicting and understanding solid state systems. This development is only partly due to the rapid increase in computer power, more important is the continuing progress in the theory itself, e.g., a better description of the exchange-correlation energy or the development of Order*N* algorithms.[174–176] In nanotube research first principles and also semi-empirical methods are particularly powerful, because the dependence of the nanotube's properties on chirality, diameter, or bundling can be addressed systematically.[106, 123–125, 131, 149, 151, 177] Experimentally, only STM experiments currently allow to study an individual tube of known chirality.[127, 128] All other methods either rely on bulk samples or are not able to determine the (n_1, n_2) structural indices precisely enough. When I started with SIESTA calculations of carbon nanotubes I was as an experimentalist frustrated by the lack of first principles information for chiral nanotubes. My major focus were therefore small diameter nanotubes, for which *ab initio* calculations of chiral tubes are possible on present day computers.

The SIESTA* project was started in 1995 by E. Artacho, P. Ordejón, D. Sánchez-Portal, and J. M. Soler with the goal to develop an *ab initio* code, where the computer time and memory requirements scale only linearly with the number of atoms. It is able to handle systems with more than 100 atoms in the unit cell on Pentium PC's and modest workstations. My

*SIESTA is an acronym for *Spanish Initiative for Electronic Simulations with Thousands of Atoms*. The current SIESTA version is 1.1. and its authors and developer are E. Artacho, J. Gale, A. García, J. Junquera, R. M. Martin, P. Ordejón, D. Sánchez-Portal, and J. M. Soler. The most recent descriptions of the code were done by Soler *et al.*[47] and Sánchez-Portal *et al.*;[46] older versions of the program and the implemented linear scaling methods are discussed in Ref. 178 and 179. For a detailed account on the numerical orbitals used as the basis functions see Artacho *et al.*[180] and Junquera *at al.*[181] Further information on SIESTA is available at http://www.uam.es/siesta.

results obtained with SIESTA on a variety of carbon nanotubes are scattered throughout this work (Chapter 3. to 5.) and I give in this appendix a brief introduction into the SIESTA method as well as an overview over my calculations. Section I.1. and I.1.1. introduce density functional theory and the SIESTA project. I proceed by describing the equilibrium structure of the calculated nanotubes in Section I.2.1. and comment on the pressure, phonon eigenvectors, electronic band structure, and optical calculations in Sections I.2.2. to I.2.4. I also present some additional, preliminary results, which should be interesting to further study in the future.

I.1. Density functional theory

The problem faced in an *ab initio* calculation of solids is the large number of interacting electrons and nuclei. The Born-Oppenheimer approximation – so fundamental that it is sometimes not explicitly mentioned – essentially treats the nuclei as classical particles producing an external potential in which the electrons move. But still, we need to find the ground state energy of the interacting electrons. A general theory of the interacting electron gas was developed by Hohenberg, Kohn, and Sham,[182,183] the density functional theory.[184–186] As the name says the central role in this formalism is played by the electron density, since Hohenberg and Kohn[182] proved that the ground-state energy of the electron gas $E_G[n]$ is a unique functional of the charge density $n(\boldsymbol{r})$

$$E_G[n] = F[n] + \int n(\boldsymbol{r}) V_{\mathrm{Ion}}(\boldsymbol{r}) d\,\boldsymbol{r}, \tag{I.1}$$

where V_{Ion} is the ionic potential and $F[n]$ includes the kinetic and interaction energies of the electrons. The minimum of E_G is the ground-state energy of the system and the density yielding the minimum is the correct ground state density. To find the minimum of $E_G[n]$ by a variational principle Sham and Kohn[183] first separated the functional $F[n]$ into the kinetic energy of the electrons, the averaged Coulomb energy (Hartree term), and the exchange and correlation energy involving the many-body effects. They then noted that the problem of finding the ground state density $n(\boldsymbol{r})$ of the interacting electrons can be replaced exactly by a set of single-particle equations. The Kohn-Sham equations can be formally interpreted as a Hamiltonian for a single non-interacting electron moving in the potential produced by the ions and all other electrons.

$$H_{\mathrm{LDA}}\Psi_i = \left[-\frac{\bar{h}}{2m}\nabla^2 + V_{\mathrm{Ion}}(\boldsymbol{r}) + V_H(\boldsymbol{r}) + V_{XC}\big(n(\boldsymbol{r})\big) \right] \Psi_i = \varepsilon_i \Psi_i, \tag{I.2}$$

where V_{Ion} is the Coulomb potential of the nuclei, V_H is the Hartree potential of the electrons

$$V_H(\boldsymbol{r}) = e^2 \int \frac{n(\boldsymbol{r}')}{|\boldsymbol{r} - \boldsymbol{r}'|} d\,\boldsymbol{r}, \tag{I.3}$$

and V_{XC} is the exchange-correlation potential which is formally given as the variational of the exchange-correlation energy with respect to the density. From the Ψ_i fulfilling Eq. (I.3) the ground state density is found $n(\boldsymbol{r}) = 2\sum_{i=1}^{N} |\Psi_i|$ and the total energy

$$E_G = 2\sum_{i=1}^{N} \varepsilon_i - \frac{e^2}{2} \int n(\boldsymbol{r}) d\,\boldsymbol{r} \int \frac{n(\boldsymbol{r}')}{|\boldsymbol{r}-\boldsymbol{r}'|} d\,\boldsymbol{r} - E_{XC}[n(\boldsymbol{r})] + \int n(\boldsymbol{r}) V_{XC}(n) d\,\boldsymbol{r}. \tag{I.4}$$

The electronic part of the effective potential in Eq. (I.3) depends on $n(\boldsymbol{r})$ and thus the wave functions Ψ_i. The Kohn-Sham equation must be solved self-consistently, i.e., the occupied electronic states must produce the potential which was used to construct the Hamiltonian.

Up to now, the treatment was exact, besides the Born-Oppenheimer approximation in the beginning. The exchange-correlation term in the Kohn-Sham equations, however, is not known. The most requently used approximation for E_{XC} (also the one I used) is the local density approximation (LDA) where the electron gas at each point $\boldsymbol{r}$ is regarded as homogeneous with the density $n(\boldsymbol{r})$

$$E_{XC}[n] = \int \varepsilon_{XC}^{\text{homo}}\big(n(\boldsymbol{r})\big) n(\boldsymbol{r}) d\,\boldsymbol{r}. \tag{I.5}$$

Several parameterizations exists for $\varepsilon_{XC}^{\text{homo}}$; I used the one due to Perdew and Zunger.[187] Although it might seem that we made much progress in solving the *ab initio* problem (we got rid of the many-body problem and have an approximation for the exchange energy), still the number of electronic states is infinite in a solid. The obvious solution is Bloch's theorem, which allows us to separate the wave functions Ψ_i into a wave like part and a cell periodic part. If, for example, I am only interested in the Γ point I can restrict the calculations to the electrons in the unit cell. In general, the total energy is now given by a sum of infinite k points, but usually it is sufficient to consider only a small number of points. To optimize the necessary numbers and the convergence of the total energy with respect to the k point a set of "special" points is selected. SIESTA uses the scheme proposed by Monkhorst and Pack[188] to find an optimized set.

An additional standard simplification is to replace the nuclei potentials and the core electrons by a pseudopotential for the valence electrons.[189–191] Since the core electrons are essentially unchanged in different environment, this is physically justified. Only the valence electrons are then included in the self-consistent calculation. The benefit is not only the smaller number of wave functions, but also that the rapidly varying part of the wave functions within the core is replaced by a smooth function (the valence and core wave functions are orthogonal, which produces nodes inside the core region).[189,190] *Ab initio* pseudopotentials are obtained by first solving the all-electron problem for the isolated atoms. An pseudopotential is then

constructed by imposing the following conditions on its pseudo-wave functions: The pseudo-wave must be equal to the all-electron wave function outside a cutoff radius r_c and yield the same charge inside the core as found by the all-electron calculation. If these conditions are met (and, of course, the potentials give the correct eigenvalues) the pseudopotentials are called "norm-conserving". A general pseudopotential depends on the angular-momentum quantum number l and the position $\boldsymbol{r}$. On the other hand, outside the core radius r_c all pseudopotentials of an atom must rapidly converge to the same value regardless of their angular momentum, since the electron away from the core feels only the attractive potential of the nucleus partly screened by the other electrons. It is possible to divide a pseudopotential into a local only r dependent part and a non-local angular momentum dependent part, which is non-vanishing only inside the core. An efficient way to do so are the Kleinmann-Bylander projectors.[192]

I.1.1. The SIESTA method

As already mentioned SIESTA is an *ab initio* code where the computer time and memory usage scales linearly with the number of atoms, also called Order$N$ or $\mathcal{O}(N)$ scaling. It is thus perfectly suited for systems with many atoms in the unit cell. Full linear scaling requires both the construction of the Hamiltonian and the minimization of the energy functional to be done in $\mathcal{O}(N)$ steps.[176] In my calculations I used only the former; the Hamiltonian was directly diagonalized to find the eigenvalues and eigenfunctions. The basic idea for linear scaling is that the properties at a given point $\boldsymbol{r}$ of a system are independent from another, sufficiently far away region.[193,194] To make use of this concept the basis functions are confined to finite space in SIESTA; outside they are exactly zero. Such functions – pseudo-atomic orbitals (PAO) – are obtained from the solution of the isolated pseudo atom, i.e., the atom constructed from the pseudopotentials.[180,181] The PAO's are confined by an infinite spherical potential. The confinement radii are controlled by the energy gain of the wave function due to the localization; this energy shift is one of the parameters entering the calculation.[180,181] The exact choice of the basis is flexible in SIESTA. Multiple functions may be used to represent an pseudoatomic orbital, which is called a multiple-ζ basis. Additionally, polarization orbitals can be added to give more angular freedom to the valence electrons.[180,181] The second point for using locality in the Kohn-Sham equations is to eliminate any long-range potentials in the LDA Hamiltonian.[46,47] With the Kleinmann-Bylander form of the pseudopotentials the Hamiltonian in Eq. (I.3) is given by

$$H = -\frac{\bar{h}}{2m}\nabla^2 + \sum_I V_I^{\text{local}}(\boldsymbol{r}) + \sum_I V_I^{\text{nl}} + V_H(\boldsymbol{r}) + V_{XC}(\boldsymbol{r}). \tag{I.6}$$

To avoid the long range ionic potential V_I^{local} is screened by the charge of the valence electrons in their atomic configuration, i.e., the collective charge produced by the wave functions of the isolated pseudoatoms. Since the resulting neutral atom potential V_I^{na} (zero outside the atom) partly contains the Coulomb interaction, the Hartree term is reduced by the same amount. The modified δV_H is obtained from the charge density $\delta n(\boldsymbol{r}) = n(\boldsymbol{r}) - n^{\text{na}}(\boldsymbol{r})$, i.e., the difference between the self consistent charge density including, in particular, the changes introduced by the solid environment, and the charge density produced by the isolated or chemically inert atoms. Thus the final Hamiltonian SIESTA works with is[46,47]

$$H = -\frac{\bar{h}}{2m}\nabla^2 + \sum_I V_I^{\text{na}}(\boldsymbol{r}) + \sum_I V_I^{\text{nl}} + \delta V_H(\boldsymbol{r}) + V_{XC}(\boldsymbol{r}). \tag{I.7}$$

The first three terms, the kinetic energy, the non-local part of the pseudopotentials, and the neutral atom potential, are independent of the charge density $n(\boldsymbol{r})$. The matrix elements of the kinetic energy and the nonlocal part of the pseudopotential are calculated in reciprocal space at the beginning of the self-consistent cycle and stored in tables.[46,47,195] The remaining terms are evaluated on a real space grid. The short ranged and charge independent neutral atom potential V_I^{na} like the first two terms needs to be found only once and is stored for reference during the self-consistent cycles. The electron density is directly calculated from the wave functions on the real space grid and V_{XC} and δV_H are found (the latter by solving Poisson's equation). The matrix elements of V_I^{na}, V_{XC}, and δV_H are computed by direct integration on the grid. Note that all matrix elements are zero for distant enough atoms, since the wave functions are zero beyond the cutoff radius. As a consequence the integration can be performed in $\mathcal{O}(N)$ operations.[46,47,176,195]

Once the Hamiltonian is obtained it is diagonalized (cube-scaling) and the next charge density and Hamiltonian is found. SIESTA also includes linear scaling algorithm for minimizing the total energy functional, which I did not use. Setting up a new Hamiltonian and finding its eigenvalues and eigenfunctions is repeated until the relative differences between the old and the new charge density are below a specific cutoff value (usually on the order of 10^{-4}). For the converged density matrix, finally, the total energy is calculated – the explicit formula is given in Ref. 46 and 47 – and the forces and stresses are found from the derivatives of the total energy with respect to the atomic positions.[47,196,197] SIESTA also routinely provides other information, e.g., the Hamiltonian eigenvalues or the population of the orbitals, and additional calculations can be specified in the input file like a force constant calculation or a relaxation of the atomic positions (see next section).

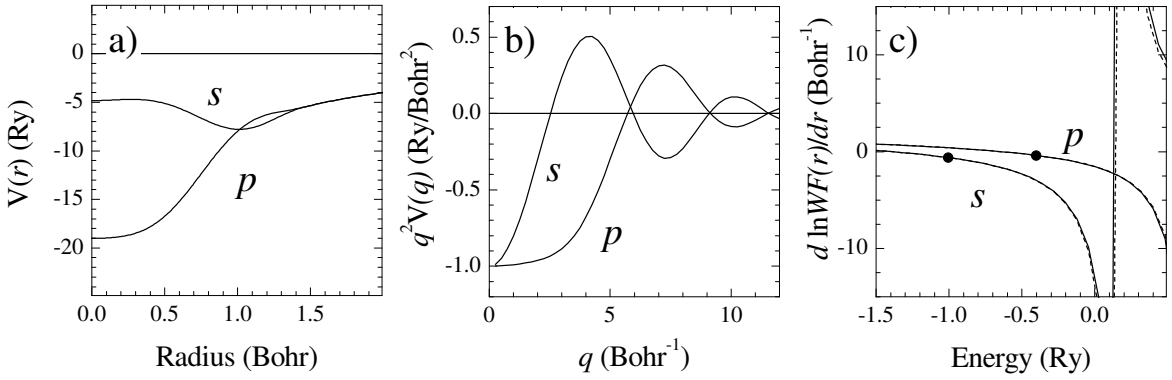

Figure I.1: Carbon pseudopotentials. a) Pseudopotentials for the *s* and *p* orbital of carbon. The cutoff radius $r_c = 1.50\,\text{Bohr}$ for both orbitals. b) Fourier space representation of the two pseudopotentials. A rapid decrease with increasing q as seen in the figure is required for a low real space grid cutoff (mesh cutoff). c) Logarithmic derivative of the all-electron (full lines) and the pseudo wave function (broken lines). The two dots mark the eigenvalues of the *s* and *p* orbital. The agreement between the all-electron and the pseudo wave function is indicative for the transferability of a pseudopotential.

I.2. SIESTA calculations of carbon nanotubes

The *ab initio* calculations require a number of input parameters which are specified by the user. Besides obviously necessary things like the atomic species or positions I mentioned in the previous sections some parameters – k points, atomic basis, pseudopotential cutoff radii, real space grid, etc. – which control the quality of a calculation. All these parameters must be sufficiently large (or small) to get valid results. The optimal values depend on the systems and the problem under study; they are found by comparing the total energies calculated with different parameter sets. When the total energy is converged for all parameters the real calculations can be performed. In the following I first describe the equilibrium structure I found for the different nanotubes. I then comment on the force constants, pressure, and band structure calculations, which I presented in Chapter 3. to 5.

I.2.1. Equilibrium structure

When I started the *ab initio* calculations of nanotubes SIESTA had already been applied to a number of carbon systems including nanotubes.[106,198–200] Thus for many of the necessary parameters converged values were known quite accurately and represent a standard choice for SIESTA calculations in this system. In Fig. I.1 I show the pseudopotentials for the *s* and *p* orbital of carbon. They were generated according to the scheme proposed by Troullier and Martin[191] with Perdew and Zunger's[187] parameterization of the local density approximation and a cutoff radius of $r_c = 1.50\,\text{Bohr}$. Figure I.1a) shows the pseudopotential in real space,

while b) is the reciprocal space representation. A rapid decrease of the amplitude in b) with increasing q guarantees a good convergence of the *ab initio* calculation with respect to the cutoff of the real space grid. The indicator for the transferability of the pseudopotentials, i.e., that it is able to closely reproduce all-electron calculations for other environments, is the logarithmic derivative of the pseudo wave function, see Fig. I.1c).[191] The agreement is very good around the eigenenergy. Further testing of a pseudopotential is done by comparing all-electron and pseudopotential calculations for different excited atomic configurations.[191]

I calculated a number of chiral and achiral nanotubes; most profoundly I studied a (6,6) armchair, a (10,0) zig-zag, an (8,4) chiral, and partly also a (9,3) chiral nanotube. In Chapter 5. I also presented band structure calculations for a (19,0) zig-zag tube with a larger diameter and a (10,5) nanotube for comparison to Raman experiments. The starting configuration for the atomic positions in the various tubes I found from the idealized cylindrical geometry as given in Eq. (2.9). The valence electrons were described by a double-ζ basis set plus an additional polarizing orbital with cutoff radii of 5.12 and 6.25 Bohr for the s and the p orbital, respectively.[180,181] These cutoff radii correspond to a PAO energy shift of 50 meV by the localization. The quality or fineness of the real space grid for the integrations is controlled by the so-called mesh cutoff. It is defined as the highest plane-wave energy, which can be reproduced by the grid spacing. The mesh cutoff I used varied between 240 and 300 Ry depending on the specific nanotube and problem under study. For all other parameters (except the k sampling, which I give below) I took the default values; they can be found in the SIESTA Users guide together with a description of the input and output data format.*

For isolated nanotubes I placed the cylindrical nanotube into an orthonormal unit cell. In the plane perpendicular to the z axis I chose a square length such that the tube-tube distance was around $5-7$ Å. To verify that the intertube coupling produced by the periodic boundary conditions was sufficiently small I compared the total energy calculated with a k point sampling including the Γ point of this unit cell with one shifted in the k_x direction. The absolute differences were below 10 meV, on the order of $10^{-6}-10^{-7}$ compared to the total energy, which was generally the range were I considered the calculations converged. The k sampling along the z direction varied from tube to tube. For the (6,6) armchair tube I used 30 special k points (the highest value) since armchair tubes both have the shortest periodicity along z and are metallic. In zig-zag tubes – (10,0) and (19,0) – I found 10 k_z points sufficient, while for the chiral (8,4), (9,3), and (10,5) nanotubes only the Γ point was included because of their larger translational periodicity. For comparison, in particular, in the band structure study, I also calculated graphite and graphene with a k point sampling of $10\times10\times5$ and

*The Users Guide is available at http://www.uam.es/siesta/

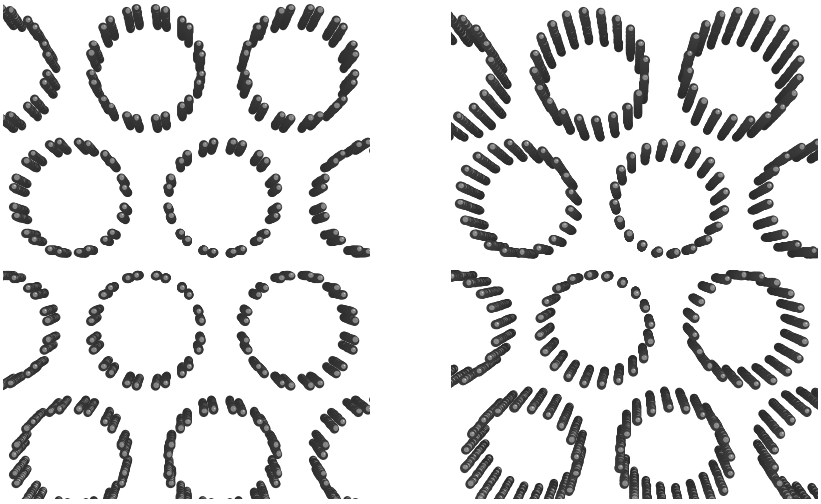

Figure I.2: Achiral nanotube bundles calculated with SIESTA. Left: Armchair (6,6) bundle which was arranged with the highest possible symmetry with respect to z rotation. Note the vertical and diagonal mirror planes in the figure. Right: Zig-zag (10,0) bundle with the lowest symmetry packing. In particular the bundle has no mirror planes besides the horizontal plane which is always present in achiral bundles. There seems to be a diagonal mirror plane in in the picture, but inspection of the atomic positions shows that this is not the case.

$40 \times 40 \times 1$, respectively. After obtaining converged input parameters for the SIESTA calculations I relaxed the atomic positions of the nanotubes by a conjugate gradient minimization until the forces on the atoms were below 0.04 eV/Å. The z axis translational periodicity I determined for the three most profoundly studied tubes, the (6,6), the (10,0), and the (8,4), by hand, i.e., performing total energy calculations for different unit cell vectors along z and finding the minimum of a cubic fit to the energy *versus* unit length curve. For the other tubes I did a conjugate gradient minimization with a variable unit cell, which was terminated when both the atomic forces and the stress tensor components were converged (< 0.04 eV/Å and < 0.02 GPa).

The four small diameter nanotubes [(6,6), (10,0), (8,4), and (9,3)] I then placed into an hexagonal unit cell to perform bundle calculations. The bundle unit cell fully preserves the horizontal mirror plane in the achiral tubes. Additionally, the tubes might be rotated around their z axis to yield arrangements of particular high or low symmetry. In Fig. I.2 I show a top view of the (6,6) (left) and the (10,0) (right) nanotube bundle. The (6,6) bundle has the highest possible symmetry configuration (D_{6h}); the vertical mirror planes are nicely seen in the figure. In contrast the (10,0) bundle is maximally disordered (C_{2h}); it does not have vertical mirror planes or horizontal rotation axes. An example for a chiral bundle is given in Fig. I.3 by the (8,4) nanotubes. The left side again shows the top view were the order of the principal rotation axes is reduced from C_{56} for the isolated tube to C_2 in the bundle. The right

(n_1,n_2)	$2q$	r (Å)	r_c (Å)	a (Å)	a_c (Å)	b (Å)	Θ (°)	$(C_q^w\|\frac{an}{q})$
(6,6)	24	4.11	4.07	2.466	2.461	11.36	30	$(C_{12}\|\frac{a}{2})$
(8,4)	112	4.18	4.14	11.30	11.28	11.43	19.1	$(C_{56}^{9}\|\frac{a}{14})$
(9,3)	156	4.27	4.24	15.44	15.39	11.49	13.9	$(C_{78}^{19}\|\frac{a}{26})$
(10,0)	40	3.92	3.92	4.27	4.263	11.00	0	$(C_{20}\|\frac{a}{2})$
(10,5)	140	5.20	5.18	11.29	11.28	–	19.1	$(C_{70}^{9}\|\frac{a}{14})$
(19,0)	76	7.45	7.44	4.27	4.263	–	0	$(C_{38}\|\frac{a}{2})$

Table I.1: Radius r, translational period a, bundle lattice constant b obtained in the *ab initio* calculations. The expected radius r_c and translational period a_c of an ideal cylindrical tube are given for comparison. Θ is the chiral angle and $2q$ the number of carbon atoms in the unit cell; the screw axis is denoted in the last column.

side of Fig.I.3 is a side view of the (8,4) bundle and points out the horizontal U axis, which is preserved by the packing. The nanotube bundles were again relaxed by a conjugate gradient minimization (forces $< 0.04\,\text{eV/Å}$ and stresses $< 0.02\,\text{GPa}$) to finally yield the equilibrium structure in the bundled nanotubes. For the (6,6) nanotube bundle the k point sampling was increased to $2\times2\times30$; for the other bundles the same sampling as for the isolated tubes was used.*

Table I.1 lists the equilibrium structure of the six nanotubes under investigation. The radius r and the translational period a are compared to the radius r_c and the periodicity a_c for an ideal cylinder, see Table 2.1 on page 17. The agreement between the expected and calculated

*Later on I found in the band structure calculations the (10,0) bundle to be in fact metallic, see Chapter 5. I therefore recalculated the bundle with a finer k grid $10\times10\times30$ whereby the forces on the atoms increased to $< 0.07\,\text{eV/Å}$. The relaxation of the (10,0) bundle thus probably suffers from an incomplete set of k points. In particular, in the high-pressure calculations the (10,0) showed a larger scattering of the structural parameters with pressure.

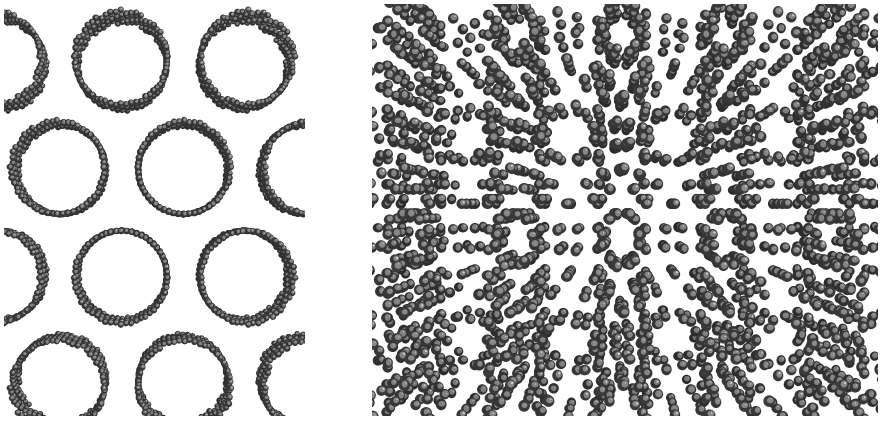

Figure I.3: Chiral (8,4) nanotube bundle calculated with SIESTA. Left: Top view of the bundle, which only has a two-fold principal rotation axis. Right: Side view of the (8,4) bundle for two translational periodicities along z. Nicely seen is the U horizontal rotation axis pointing to the reader.

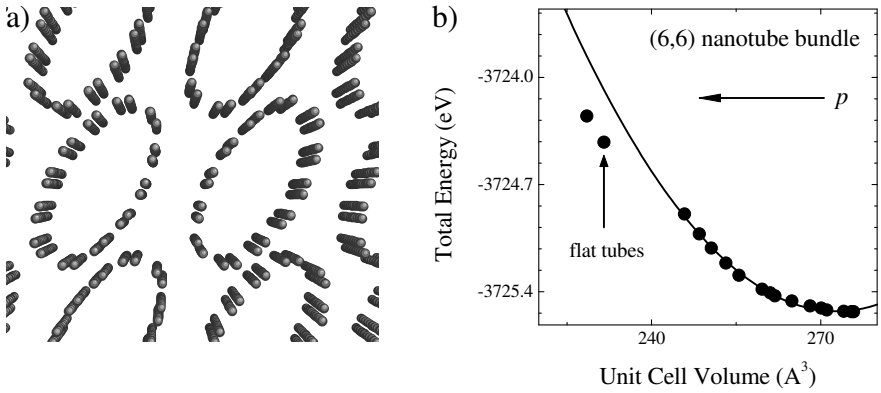

Figure I.4: Flattening of the (6,6) tubes in a nanotube bundle at high pressure. a) Relaxed structure at 9.5 GPa. This structure might be preferred at high pressures, because the empty volume inside the tubes is largely reduced when compared to the circular cross section, but it requires a strong bending of the nanotube's wall. b) Total energy *versus* volume under increasing pressure. The full line is a cubic fit to the low pressure points with a unit cell volume above 240 Å^3. The two points calculated for the flattened tubes (9.5 and 10 GPa) have a smaller total energy than expected from the extrapolation of the low pressure curve.

values is excellent, in particular, in view of the fact that true experimental values are not available for carbon nanotubes. The carbon-carbon distance I obtained for graphite (1.242 Å) is in very good agreement with experiment (1.421 Å). In graphite the equilibrium interplane distance I found as 3.3 Å compared to 3.41 Å experimentally. In the tube bundles the wall-to-wall distance is systematically a little lower $\approx$ 3.1 Å, see Table I.1.

I.2.2. Pressure calculations

The pressure calculations I did by relaxing the unit cell structure and the atomic positions under the constraint of a hydrostatic stress tensor. They were done for the (6,6), the (8,4), and the (10,0) nanotube bundles between zero and $\approx$ 10 GPa by a conjugate gradient minimization. I tolerated atomic forces below 0.04 eV/Å and stress tensor components within 10 % at low pressure points (0.02 GPa tolerance at 0.25 GPa) and around 5 % at higher pressure (0.45 at 8 GPa). Particular attention I paid to the off-diagonal stress components, which I required to be below 0.03 GPa even for the highest pressure points. When comparing my *ab initio* calculations to experiment and the continuum mechanical model in Chapter 4. I was interested in the volume deformation of the single tubes within the bundle. Since the interwall distance changes strongest under pressure, the total volume of the unit cell is not suitable for the comparison. I obtained the volume of the single tubes by assuming them to be cylindrical, i.e., $V_{\text{tube}} = \pi\, r(p)^2\, a(p)^2$. The translational periodicity a is given by the relaxation; for the radius r of the tubes I used the mean distance to the tube center of all the atoms in the unit cell. All three nanotubes were slightly hexagonally distorted within

the bundle. The deviations of the radii from their mean value increased from $< 1\%$ at zero pressure to $\approx 5\%$ at high pressure, which is still sufficiently small to neglect it in the volume determination.

An interesting point I did not mention in Chapter 4. is a sudden flattening of the tubes I obtained at 9.5 GPa in the armchair bundle. Figure I.4 shows the relaxed (6,6) structure at 9.5 GPa. This flattening might be related to the widely discussed phase transition under pressure, which was sometimes claimed to be found experimentally around 2 GPa and sometimes above 10 GPa.[98,102,201] In part b) of Fig. I.4 I present the total energy of the (6,6) bundle as a function of the unit cell volume (or pressure). It is clearly seen that the 9.5 GPa point and the even higher at 10 GPa have a smaller total energy than the extrapolation of the low pressure curve. A more detailed study, i.e., under decreasing pressure for the flat structure to complete the total energy curves, will be done in the future. Nevertheless, I did not find such a behavior in the (8,4) tube up to now, where my highest calculated pressure was 11 GPa.

I.2.3. Phonon calculations

Two approaches for calculating the vibrational properties by *ab initio* methods are currently widely used in the literature. In the frozen-phonon approximation the phonon frequency is found from the difference in total energy for the undistorted structure and a structure where the atoms were displaced according to a particular phonon eigenvector, see, e.g., Kürti *et al.*[202] for an application to carbon nanotubes. For this method, however, the phonon eigenvector must be known *a priori*. I therefore used the finite difference approach which directly calculates the force constants matrix from first principles.[106,178,203] In this method a single atom is displaced successively in the x, y, and z direction and the forces on all atoms in the unit cell are calculated from the Hellmann-Feynman theorem.[196] To account for anharmonic effects a negative and a positive displacement is done for all three direction (the force constants are averaged for positive and negative displacement), which means a total of 6 self-consistent cycles per atom. Then the next atom is displaced until the force constant matrix is complete. A full calculation according to this scheme was only possible for the (6,6) nanotube with 24 atoms in the unit cell where it took 9 days running on 4 nodes of a Linux cluster. For the other tubes I calculated only the forces for two displaced atoms which were connected by the U rotational axis. I generated the other forces with the screw axis symmetry, see Chapter 2. Since I was only interested in the Γ point vibrations the fractional translations do not change the force constants. The angle between two atoms I found from their positions and then simply used the vector transformation properties under rotation as given, e.g., in Eq. (2.28) on page 38 for the screw and rotation axes. The force constant

matrix is read by the Vibra package, which is part of SIESTA. The dynamical matrix is set up and diagonalized yielding all phonon frequencies and eigenvectors.[57, 106, 203]

In Section 2.2. I showed that all nanotubes are single orbit systems. In general, it would therefore be sufficient to calculate the forces only for one displaced atom. Including the U axis symmetry in the force constants transformation I obtained the whole force constant matrix by the same approach. I decided not to use the U axis in chiral tubes or the horizontal mirror plane in achiral tubes to have a measure for the accuracy of my calculations. As I discussed in Section 4.4. these additional symmetry operations were very well reproduced by the *ab initio* calculations. To further verify the symmetry based approach I also did a full calculation – displacing all the atoms – for the (6,6) nanotube and used different sets of atoms for the (10,0), the (8,4), and the (9,3) nanotube. The agreement in phonon frequency was excellent, within $3\,\mathrm{cm}^{-1}$ in the achiral and $15\,\mathrm{cm}^{-1}$ in the chiral tubes for the high-energy modes and the radial breathing mode. The eigenvectors were not affected in a fundamental manner during the test calculations.

I.2.4. Band structure and optical absorption calculations

The electronic energies of the k points used in the total energy calculations are routinely included in the SIESTA output. A band structure or an optical absorption calculation, however, usually requires more special k points than the total energy calculation *per se*. Additional points may be specified in the input file, which are only used to find the eigenvalues for the band structure and the eigenvectors for the optical matrix elements from the self-consistent, converged Hamiltonian.

In the band structure calculations I included $10-30$ k points along the z axis for the isolated (8,4), (9,3), and (10,5) nanotube, 45 for the isolated (10,0) and (19,0) zig-zag tubes, and 60 for the isolated (6,6) armchair tube. The different numbers reflect the different length of the nanotube unit cell. For example, the same absolute sampling for a zig-zag and an armchair tube requires $\sqrt{3}$ less k points in the former. In the perpendicular direction I included a total of 45 points for the ΓM, MK, and $K\Gamma$ triangle ($k_z = 0$), the same number at $k_z = \pi/a$ (AL, LH, and HA), and at the Fermi wave vector $k_z = k_F$ ($\Delta_F U$, UP, and $P\Delta_F$). Note that the Brillouin zones of graphite and bundled carbon nanotubes are the same. The highly dispersive direction in nanotubes is, however, the ΓA direction in contrast to the mostly in-plane electronic dispersion in graphite. In my calculations I always treated the (10,0) nanotube and the (10,0) bundle as semiconducting as expected from the nanotubes indices (10 is not a multiple of 3). In the first principles bundle band structure calculations, however, I found

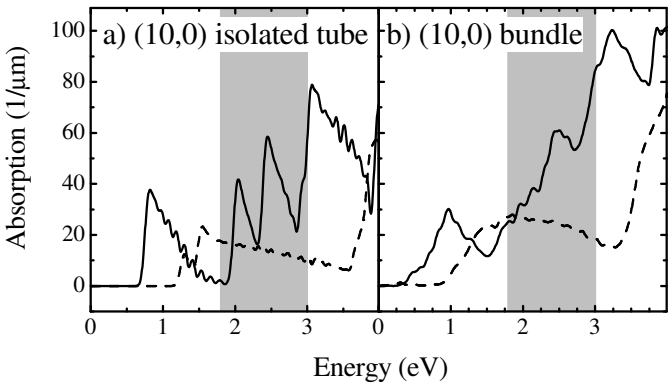

Figure I.5: Effect of bundling on the optical absorption spectra of an (10,0) nanotube. a) Absorption of the isolated nanotube, compare Fig. 3.9 on page 60 b) absorption spectrum of the (10,0) nanotube bundle. The lower singularities in the spectrum shift to smaller energies and broaden strongly. In particular, in the visible energy range (gray area) the singularities are completely smeared out by the bundling.

this tube to be metallic because of its intertube dispersion, see Chapter 5. In a recalculation of the (10,0) bundle with a finer $10 \times 10 \times 30$ k grid I obtained differences in the total energy and the forces (900 meV corresponding to 10^{-4} of the total energy and 0.03 eV/Å), but the band structure was exactly the same except for a shift in the Fermi energy by 20 meV.

In the description of the equilibrium structure I discussed the arrangement of the tubes within a bundle. It would be interesting to study how strongly the electronic band structure is affected by the exact arrangement. For example, a higher symmetry configuration for the (10,0) bundle is obtained by a small rotation of the tubes in Fig. I.2 or the bundle unit cell could be doubled to include two tubes and the vertical mirror symmetry be broken by a small shift of one of the tubes along the z axis. A first principles calculation of a bundle composed of two tubes of different chirality is rather difficult, because most combinations are incommensurable or have a very large translational periodicity, e.g., none of the combinations of the (6,6), (10,0), (8,4), and (9,3) nanotubes have a finite unit cell along the z axis.

The output of an optical calculation with SIESTA is the imaginary part of the dielectric function ε_2; the real part ε_1 is obtained by a Kramers-Kronig transformation. ε_1 and ε_2 yield all the optical properties of a material like the absorption, the reflectivity, or the electron energy loss spectra.[57] I calculated ε_2 between 0 and 8 eV with a Lorentzian broadening of 50 meV per energy point. The small linewidth was necessary to reproduce the square root singularities in the absorption spectrum. It required a particularly fine k sampling for convergence. The dielectric function in isolated (6,6) tubes was found from 240 special points along z, 120 in the (10,0), and 50 in the (8,4) nanotube.

In the discussion of the bundle band structure in Chapter 5. I mentioned that I expect the optical absorption singularities to broaden in the bundle because of the electronic dispersion perpendicular to k_z. In Fig. I.5b) I present preliminary results for the absorption spectrum in a (10,0) bundle. Figure I.5a) shows again the isolated tube spectrum of Fig. 3.9. The bundling of the tubes shifts the singularities below 3 eV to smaller energy, a trend I already

found from the band structure calculations. Moreover, the singularities are smeared out, in particular, in the visible energy range, as I expected. Further calculations will reveal whether this is a general finding in nanotube bundles that was responsible for the broad and unstructured features in the experimental absorption and reflection spectra.[88, 144]

Appendix 2

Raman Intensities on Unoriented Systems

The appendix shows how to obtain the Raman intensities for any polarization on randomly oriented systems. I demonstrated the basic approach in Chapter 3., where I calculated the matrix element for a particular Raman tensor and configuration and then averaged over Euler's angles. To generalize the result I use the transformation properties of the Raman tensor, i.e., any tensor of rank two. The transformations of tensors under rotation are best described by irreducible spherical tensors, which is a decomposition with respect to the rotation group. Moreover, irreducible spherical tensors $T_m^{(j)}$ have sharp j and m quantum numbers; under rotation they transform according to[59,80,81]

$$T_m^{(j)} = \sum_p T_p^{(j)} D_{pm}^{(j)}(\psi,\theta,\varphi), \tag{II.1}$$

where $D^{(j)}$ is the matrix representation of the rotation group (rotation matrices). The decomposition of a tensor with rank k into irreducible tensors of rank $0,1,\ldots,k$ is done with the help of the Clebsch-Gordan coefficients. The procedure is described in a number of textbooks.[59,80,81] A normalized set of irreducible tensors for the Raman tensor $\Re = T^{(0)} + T^{(1)} + T^{(2)}$ is[70]

$$T_0^{(0)} = -\tfrac{1}{3}(\alpha_{xx}+\alpha_{yy}+\alpha_{zz}) \qquad T_{\pm1}^{(1)} = \tfrac{1}{2}[(\alpha_{zx}-\alpha_{xz}) \pm (\alpha_{zy}-\alpha_{yz})] \tag{II.2}$$

$$T_0^{(1)} = \tfrac{i}{\sqrt{2}}(\alpha_{xy}-\alpha_{yx}) \qquad T_{\pm2}^{(2)} = \tfrac{1}{2}[(\alpha_{xx}-\alpha_{yy}) \pm i(\alpha_{xy}+\alpha_{yx})] \tag{II.3}$$

$$T_{\pm1}^{(2)} = \mp\tfrac{1}{2}[(\alpha_{zx}+\alpha_{xz}) \pm (\alpha_{zy}+\alpha_{yz})] \qquad T_0^{(2)} = \tfrac{1}{\sqrt{6}}(2\alpha_{zz}-\alpha_{xx}-\alpha_{yy}). \tag{II.4}$$

To obtain the intensity I_{IS} in a fixed scattering configuration (e_I, e_S) I calculate the matrix element with the help of the Wigner-Eckart theorem for a fixed configuration and then use

J	0	1	2
$\sum_p [T_p^{(J)}]^2$	$3\bar{\alpha}^2$	$\frac{2}{3}\gamma_{as}^2$	$\frac{2}{3}\gamma_s^2$

Table II.1: Reduced matrix elements in terms of the Raman tensor invariants. For $\bar{\alpha}$, γ_{as}^2, and γ_s^2 see Chapter 3.

Eq. (II.1) to average over the randomly oriented molecules.[70,80,81,204]

$$I_{IS} \propto |e_I \Re e_S|^2 = \int_\Omega |\sum_J e_I T^{(J)} e_S|^2 d\omega = \int_\Omega \Big\{ \sum_{J,M} \langle J_i m_i | T_M^{(J)} | J_s m_s \rangle \Big\}^2 d\omega \tag{II.5}$$

$$= \int_\Omega \Big\{ \sum_{J,M} \langle (-1)^{J_i+J+m_s} (J_i J_s - m_i m_s | J - M) T_M^{(J)} \rangle \Big\}^2 d\omega \tag{II.6}$$

where $(J_i J_s - m_i m_s | J - M)$ are the Clebsch-Gordan coefficients; using Eq. (II.1) and the selection rule $M = m_i - m_s$ I find

$$= \int_\Omega \Big\{ \sum_J (J_i J_s - m_i m_s | J [m_s - m_i]) \langle \sum_p T_p^{(J)} D^{(J)}_{p(m_s - m_i)} \rangle \Big\}^2 d\omega. \tag{II.7}$$

The rotation matrices are orthonormal

$$\int_\Omega {D^{(j_1)}_{k_1\mu_1}}^* D^{(j_2)}_{k_2\mu_2} d\omega = \frac{\Omega}{\sqrt{2j_1+1}} \delta_{j_1 j_2} \delta_{k_1 k_2} \delta_{\mu_1 \mu_2}. \tag{II.8}$$

I can therefore treat the contributions from irreducible tensors of different rank J separately. With the orthonormality of the rotation matrices Eq. (II.7) reduces to

$$I_{IS}^J \propto (J_i J_s - m_i m_s | J [m_s - m_i])^2 \cdot \frac{1}{2J+1} \cdot \sum_p [T_p^{(J)}]^2. \tag{II.9}$$

The sum over p is independent on the angular momentum quantum numbers m. It has to be calculated only once for every J under consideration. Note that in deriving Eq. (II.9) I implicitly assumed that e_I and e_S have only one sharp angular momentum quantum number and are not a coherent superposition as, e.g., $e_X = \frac{1}{2}(e_{1-1} + e_{11})$. The extension to this case is straightforward. Care must be taken when summing over p by using the orthogonality of the rotation matrices of Eq. (II.8), since the mixed elements in the squared sum are not necessarily canceled. However, this is only dangerous when $m_s - m_i$ are the same for the two coherent contributions as for $(e_X e_X)$ configuration. In all other cases the result for the coherent is the same as for the incoherent superposition. This can be verified by writing out Eq. (II.5).

The next step in finding I_{IS} is to calculate $\sum_p [T_p^{(J)}]^2$ for $J = 0, 1, 2$ with the irreducible tensors in Eq. (II.4). The results are summarized in Table II.1 in terms of the traditional invariants used in Raman scattering (see Chapter 3. page 50 and Ref. 82). Finally, I use the values for

IS	$\parallel$	$\perp$	$\circlearrowleft\circlearrowleft$	$\circlearrowleft\circlearrowright$
$45\,I_{IS}$	$45\bar{\alpha}^2+4\,\gamma_s^2$	$5\,\gamma_{as}^2+3\,\gamma_s^2$	$6\,\gamma_s^2$	$45\bar{\alpha}^2+5\,\gamma_{as}^2+\gamma_s^2$

Table II.2: Intensities in the four backscattering configurations on three dimensionally unoriented crystals. The intensities in arbitrary configuration can be found in the papers by Chiu.[70,204,205]

the Clebsch-Gordan coefficients in Ref. 80 and Eq. (II.9) to obtain the Raman intensities for a desired scattering configuration. For example, for $I_{ZZ}=I_{\parallel}$ I find ($J_i=J_s=1; m_i=m_s=0$)

$$I_{ZZ}=\sum_{J=0}^{2} I_{ZZ}^{J} \propto \frac{1}{3}\cdot 1\cdot 3\bar{\alpha}^2+0\cdot\frac{1}{3}\cdot\frac{2}{3}\,\gamma_{as}^2+\frac{2}{3}\cdot\frac{1}{5}\cdot\frac{2}{3}\,\gamma_s^2=\frac{45\bar{\alpha}^2+4\,\gamma_s^2}{45}.$$

This is the same result as I obtained in Eq. (3.4) on page 49 by a direct integration over Euler's angles. Nevertheless, in the derivation presented in this Appendix I did not use any special form of the Raman tensor as in Chapter 3. The intensities I_{IS} for the other scattering configurations on unoriented crystals are given in Table II.2 for Raman backscattering.

Bibliography

[1] S. Iijima, "Helical microtubules of graphitic carbon", Nature **354**, 56 (1991).

[2] S. Iijima and T. Ichihasi, "Single-shell carbon nanotubes of 1-nm diameter", Nature **363**, 603 (1993).

[3] D. S. Bethune, C. H. Kiang, M. S. deVries, G. Gorman, R. Savoy, J. Vazques, and R. Beyers, "Cobalt-catalyzed growth of carbon nanotubes with single-atomic-layer", Nature **363**, 605 (1993).

[4] J. M. Kim *et al.*, "Carbon nanotube emitter techniques for field emitter displays", in *Electronic Properties of Novel Materials-Progress in Molecular Nanostructures*, edited by H. Kuzmany, J. Fink, M. Mehring, and S. Roth, IWEPS Kirchberg (2001), p. xxxx.

[5] R. H. Baughman, C. Cui, A. Zakhidov, Z. Iqbal, J. N. Barisci, *et al.*, "Carbon nanotube actuators", Science **284**, 1340 (1999).

[6] M. Hirscher, M. Becher, M. Haluska, U. Dettlaff-Weglikowska, A. Quintel, *et al.*, "Hydrogen storage in sonicated carbon materials", Appl. Phys. A: Mater. Sci. Process. **72**, 129 (2001).

[7] A. C. Dillon, K. M. Jones, T. A. Bekkedahl, C. H. Kiang, D. S. Bethune, and M. J. Heben, "Storage of hydrogen in single-walled carbon nanotubes", Nature **386**, 377 (1997).

[8] F. Léonard and J. Tersoff, "Novel length scales in nanotube devices", Phys. Rev. Lett. **83**, 5174 (1999).

[9] S. J. Tans, A. Verschueren, and C. Dekker, "Room-temperature transistor based on a single carbon nanotube", Nature (London) **393**, 6680 (1998).

[10] V. H. Crespi, M. L. Cohen, and A. Rubio, "In situ band gap engineering of carbon nanotubes", Phys. Rev. Lett. **79**, 2093 (1997).

[11] C. Thomsen, S. Reich, H. Jantoljak, I. Loa, K. Syassen, *et al.*, "Raman spectroscopy on single and multi-walled nanotubes under pressure", Appl. Phys. A **69**, 309 (1999).

[12] S. Reich, C. Thomsen, and P. Ordejón, "Eigenvectors of chiral nanotubes", Phys. Rev. B **64**, 195416 (2001).

[13] J. Maultzsch, S. Reich, and C. Thomsen, "Raman scattering in carbon nanotubes revisited", Phys. Rev. Lett. (submitted (10/2001)).

[14] S. Reich, C. Thomsen, and P. Ordejón, "Structural and vibrational properties of single walled nanotubes under hydrostatic pressure", in *Electronic Properties of Novel Materials-Progress in Molecular Nanostructures*, edited by H. Kuzmany, J. Fink, M. Mehring, and S. Roth, AIP 591 (2001), p. 388.

[15] G. S. Duesberg, I. Loa, M. Burghard, K. Syassen, and S. Roth, "Polarized Raman spectroscopy of individual single-wall carbon nanotubes", Phys. Rev. Lett. **85**, 5436 (2000).

[16] A. Jorio, R. Saito, J. H. Hafner, C. M. Lieber, M. Hunter, *et al.*, "Structural (n,m) determination of isolated single-wall carbon nanotubes by resonant Raman scattering", Phys. Rev. Lett. **86**, 1118 (2001).

[17] F. Tuinstra and J. L. Koenig, "Raman spectrum of graphite", J. Chem. Phys. **53**, 1126 (1970).

[18] R. P. Vidano, D. B. Fischbach, L. J. Willis, and T. M. Loehr, "Observation of Raman band shifting with excitation wavelength for carbons and graphites", Solid State Commun. **39**, 341 (1981).

[19] C. Thomsen and S. Reich, "Double-resonant Raman scattering in graphite", Phys. Rev. Lett. **85**, 5214 (2000).

[20] C. Thomsen, S. Reich, and J. Maultzsch, "The dependence on excitation energy of the D-mode in graphite and carbon nanotubes", in *Electronic Properties of Novel Materials-Progress in Molecular Nanostructures*, edited by H. Kuzmany, J. Fink, M. Mehring, and S. Roth, AIP 591 (2001), p. 376.

[21] J. Maultzsch, S. Reich, and C. Thomsen, "Chirality selective Raman scattering of the D-mode in carbon nanotubes", Phys. Rev. B **64**, 121407(R) (2001).

[22] M. Damnjanović, I. Milošević, T. Vuković, and R. Sredanović, "Full symmetry, optical activity, and potentials of single-wall and multiwall nanotubes", Phys. Rev. B **60**, 2728 (1999).

[23] C. Journet and P. Bernier, "Production of carbon nanotubes", Appl. Phys. A: Mater. Sci. Process. **67**, 1 (1998).

[24] L. Henrard, A. Loiseau, C. Journet, and P. Bernier, "Study of the symmetry of single-wall nanotubes by electron diffraction", Eur. Phys. B **13**, 661 (2000).

[25] H. Hiura, T. W. Ebbesen, K. Tanigaki, and H. Takahashi, "Raman studies of carbon nanotubes", Chem. Phys. Lett. **202**, 509 (1993).

[26] J. M. Holden, P. Zhou, X. X. Bi, P. C. Eklund, S. Bandow, *et al.*, "Raman scattering from nanoscale carbons generated in a cobalt-catalyzed carbon plasma", Chem. Phys. Lett. **220**, 186 (1994).

[27] A. M. Rao, E. Richter, S. Bandow, B. Chase, P. C. Eklund, *et al.*, "Diameter-selective Raman scattering from vibrational modes in carbon nanotubes", Science **275**, 187 (1997).

[28] S. Bandow, S. Asaka, Y. Saito, A. M. Rao, L. Grigorian, E. Richter, and P. C. Eklund, "Effect of the growth temperature on the diameter distribution and chirality of single-wall carbon nanotubes", Phys. Rev. Lett. **80**, 3779 (1998).

[29] U. D. Venkateswaran, A. M. Rao, E. Richter, M. Menon, A. Rinzler, R. E. Smalley, and P. C. Eklund, "Probing the single-wall carbon nanotube bundle: A Raman scattering study under high pressure", Phys. Rev. B **59**, 10 928 (1999).

[30] C. Thomsen, S. Reich, A. R. Goñi, H. Jantoljak, P. Rafailov, *et al.*, "Intramolecular interaction in carbon nanotube ropes", phys. stat. sol. (b) **215**, 435 (1999).

[31] M. Milnera, J. Kürti, M. Hulman, and H. Kuzmany, "Periodic resonance excitation and intertube interaction from quasicontinuous distributed helicities in single-wall carbon nanotubes", Phys. Rev. Lett. **84**, 1324 (2000).

[32] L. Henrard, E. Hernandez, P. Bernier, and A. Rubio, "Van der Waals interaction in nanotube bundles: Consequences on vibrational modes", Phys. Rev. B **60**, R8521 (1999).

[33] D. Kahn and J. P. Lu, "Vibrational modes of carbon nanotubes and nanoropes", Phys. Rev. B **60**, 6535 (1999).

[34] J. W. Mintmire and C. T. White, "Universal density of states for carbon nanotubes", Phys. Rev. Lett. **81**, 2506 (1998).

[35] C. T. White and J. W. Mintmire, "Density of states reflects diameter in nanotubes", Nature (London) **394**, 29 (1998).

[36] S. Reich and C. Thomsen, "Chirality dependence of the density-of-states singularities in carbon nanotubes", Phys. Rev. B **62**, 4273 (2000).

[37] R. Saito, G. Dresselhaus, and M. S. Dresselhaus, "Trigonal warping effect of carbon nanotubes", Phys. Rev. B **61**, 2981 (2000).

[38] S. Lebedkin, P. Schweiss, B. Renker, S. Malik, F. H. Hennrich, *et al.*, "Single-wall carbon nanotubes with diameters up to 6 nm made by laser vaporization", in *Electronic Properties of Novel Materials-Progress in Molecular Nanostructures*, edited by H. Kuzmany, J. Fink, M. Mehring, and S. Roth, IWEPS Kirchberg (2001), p. xxxx.

[39] J. Kastner, T. Pichler, H. Kuzmany, S. Curran, W. Blaus, *et al.*, "Resonance Raman and infrared-spectroscopy of carbon nanotubes", Chem. Phys. Lett. **221**, 53 (1994).

[40] C. Thomsen, "Second-order Raman spectra of single and multi-walled carbon nanotubes", Phys. Rev. B **61**, 4542 (2000).

[41] A. Kasuya, Y. Sasaki, Y. Saito, K. Tohji, and Y. Nishina, "Evidence for size-dependent discrete dispersions in single-wall nanotubes", Phys. Rev. Lett. **78**, 4434 (1997).

[42] A. Kasuya, M. Sugano, T. Maeda, Y. Saito, K. Tohji, *et al.*, "Resonant Raman scattering and the zone-folded electronic structure in single-wall nanotubes", Phys. Rev. B **57**, 4999 (1998).

[43] M. A. Pimenta, A. Marucci, S. A. Empedocles, M. G. Bawendi, E. B. Hanlon, *et al.*, "Raman modes of metallic carbon nanotubes", Phys. Rev. B **58**, R16 016 (1998).

[44] P. M. Rafailov, H. Jantoljak, and C. Thomsen, "Electronic transitions in single-walled carbon nanotubes: A resonance Raman study", Phys. Rev. B **61**, 16 179 (2000).

[45] M. Damnjanović, T. Vuković, and I. Milošević, "Modified group projectors: Tight binding method", J. Phys. A: Math. Gen. **33**, 6561 (2000).

[46] D. Sanchez-Portal, P. Ordejón, E. Artacho, and J. M. Soler, "Density-functional method for very large systems with LCAO basis sets", Int. J. Quantum Chem. **65**, 453 (1997).

[47] J. M. Soler, E. Artacho, J. D. Gale, A. García, J. Junquera, P. Ordejón, and D. Sánchez-Portal, "The SIESTA method for *ab initio* order-*N* materials simulation", J. Phys: Cond. Mat. (2001), submitted, cond-mat/0111138.

[48] I. Božović, M. Vujičić, and F. Herbut, "Irreducible representations of the symmetry groups of polymer molecules I", J. Phys. A **11**, 2133 (1978).

[49] I. Božović and M. Vujičić, "Irreducible representations of the symmetry groups of polymer molecules II", J. Phys. A **14**, 777 (1981).

[50] M. Damnjanović, "Standard components of polar and axial vectors for quasi one-dimensional systems", Phys. Lett. A **94**, 337 (1983).

[51] M. Damnjanović, I. Božović, and N. Božović, "Selection rules for polymers and quasi one-dimensional crystals: II. Kronecker product for the line groups isogonal to D_n", J. Phys. A: Math. Gen. **17**, 747 (1984).

[52] N. Božović, I. Božović, and M. Damnjanović, "Selection rules for polymers and quasi one-dimensional crystals: IV. Kronecker product for the line groups isogonal to D_{nh}", J. Phys. A: Math. Gen. **18**, 923 (1985).

[53] R. Saito, G. Dresselhaus, and M. S. Dresselhaus, *Physical Properties of Carbon Nanotubes* (Imperial, London, 1998).

[54] I. Božović, N. Božović, and M. Damnjanović, "Optical dichroism in nanotubes", Phys. Rev. B **62**, 6971 (2000).

[55] M. Damnjanović, T. Vuković, and I. Milošević, "Fermi level quantum numbers and secondary gap of conducting carbon nanotubes", Solid State Commun. **116**, 265 (2000), Table 1 in the reference contains a small error: For chiral tubes and the $\tilde{k}$ quantum numbers $\tilde{k}_F = 2q\pi/3na$ for $\mathcal{R} = 3$ tubes and $\tilde{k}_F = 0$ for $\mathcal{R} = 1$ nanotubes.

[56] T. Inui, Y. Tanabe, and Y. Onodera, *Group Theory and its Application in Physics* (Springer Verlag, Berlin Heidelberg New York, 1996).

[57] P. Y. Yu and M. Cardona, *Fundamentals of Semiconductors* (Springer-Verlag, Berlin, 1996).

[58] E. B. Wilson, J. C. Decius, and P. C. Cross, *Molecular Vibrations* (Dover, New York, 1980).

[59] G. Burns, *Introduction to group theory with applications* (Academic, New York, 1977).

[60] D. L. Rousseau, R. P. Bauman, and S. P. S. Porto, "Normal mode determination in crystals", J. Raman Spectroscopy **10**, 253 (1981).

[61] W. G. Fateley, N. T. McDevitt, and F. F. Bentley, "Infrared and Raman selection rules for lattice vibrations: The correlation method", Appl. Spec. **25**, 155 (1971).

[62] I. Milošević and M. Damnjanović, "Normal vibrations and Jahn-Teller effect for polymers and quasi-one-dimensional systems", Phys. Rev. B **47**, 7805 (1993).

[63] P. R. Wallace, "The band theory of graphite", Phys. Rev. **71**, 622 (1947).

[64] J. W. Mintmire, D. H. Robertson, and C. T. White, "Properties of fullerene nanotubules", J. Phys. Chem. Solids **54**, 1835 (1993).

[65] C. T. White, D. H. Robertson, and J. W. Mintmire, "Helical and rotational symmetries of nanoscale graphitic tubules", Phys. Rev. B **47**, 5485 (1993).

[66] M. Damnjanović and I. Milošević, "Modified group-projector technique: subgroups and generators", J. Phys. A: Math. Gen. **27**, 4859 (1994).

[67] M. Cardona, "Resonance phenomena", in *Light Scattering in Solids II*, edited by M. Cardona and G. Güntherodt (Springer, Berlin, 1982), vol. 50 of *Topics in Applied Physics*, p. 19.

[68] A. Pinczuk and E. Burstein, "Fundamentals of inelastic light scattering in semiconductors and insulators", in *Light Scattering in Solids I* (Springer Verlag, Berlin, 1983), vol. 8 of *Top. Appl. Phys.*, p. 23, 2 edn.

[69] R. M. Martin and L. M. Falicov, "Resonant Raman scattering", in *Light Scattering in Solids I: Introductory Concepts*, edited by M. Cardona (Springer-Verlag, Berlin Heidelberg New York, 1983), vol. 8 of *Topics in Applied Physics*, p. 79, 2 edn.

[70] Y.-N. Chiu, "General orientation dependence of Rayleigh and Raman scattering by linear molecules in arbitrary electronic states", J. Opt. Soc. Am. **60**, 607 (1970).

[71] C. Kane-Maguire and J. A. Koningstein, "On the vibroelectric Raman effect", J. Chem. Phys. **59**, 1899 (1973).

[72] H. Sun, Z. Tang, J. Chen, and G.Li, "Polarized Raman spectra of single-wall carbon nanotubes mono-dispersed in channels of $AlPO_4$-5 single crystals", Solid State Commun. **109**, 365 (1999).

[73] H. H. Gommans, J. W. Alldredge, H. Tashiro, J. Park, J. Magnuson, and A. G. Rinzler, "Fibers of aligned single-walled carbon nanotubes: Polarized Raman spectroscopy", J. Appl. Phys. **88**, 2509 (2000).

[74] A. M. Rao, A. Jorio, M. A. Pimenta, M. S. S. Dantas, R. Saito, G. Dresselhaus, and M. S. Dresselhaus, "Polarized Raman study of aligned multiwalled carbon nanotubes", Phys. Rev. Lett. **84**, 1820 (2000).

[75] A. Jorio, G. Dresselhaus, M. S. Dresselhaus, M. Souza, M. S. S. Dantas, *et al.*, "Polarized Raman study of single-wall semiconducting carbon nanotubes", Phys. Rev. Lett. **85**, 2617 (2000).

[76] S. Reich, C. Thomsen, G. S. Duesberg, and S. Roth, "Intensities of the Raman active modes in single and multiwall nanotubes", Phys. Rev. B **63**, R041401 (2001).

[77] S. Reich and C. Thomsen, "Tensor invariants in resonant Raman scattering on carbon nanotubes", in *Proc. 25th ICPS, Osaka*, edited by N. Miura and T. Ando (Springer, Berlin, 2001), p. 1649.

[78] M. Tinkham, *Group theory and quantum mechanics* (McGraw-Hill, New York, 1964).

[79] J. E. Rosenthal and G. M. Murphy, "Group theory and the vibrations of polyatomic molecules", Pev. Mod. Phys. **8**, 317 (1936).

[80] V. Heine, *Group Theory in Quantum Mechanics: An Introduction to its present usage* (Pergamon, Oxford, 1977).

[81] D. M. Brink and G. R. Satchler, *Angular Momentum* (Oxford, New York, 1993), 3 edn.

[82] J. Nestor and T. G. Spiro, "Circularly polarized Raman spectroscopy: Direct determination of antisymmetric scattering in the resonance Raman spectrum of ferrocytrochrome *c*", J. of Raman Spectroscopy **1**, 539 (1973).

[83] J. Maultzsch, S. Reich, A. R. Goñi, and C. Thomsen, "Resonant Raman scattering in GaAs induced by an embedded InAs monolayer", Phys. Rev. B **63**, 033306 (2000).

[84] A. Alexandrou, M. Cardona, and K. Ploog, "Doubly and triply resonant Raman scattering by LO phonons in GaAs/AlAs superlattices", Phys. Rev. B **38**, R2196 (1988).

[85] S. Reich and C. Thomsen, "Comment on 'Polarized Raman study of aligned multiwalled carbon nanotubes"', Phys. Rev. Lett. **85**, 3544 (2000).

[86] A. M. Rao, A. Jorio, M. A. Pimenta, M. S. S. Dantas, R. Saito, G. Dresselhaus, and M. S. Dresselhaus, "Rao *et al.* reply", Phys. Rev. Lett. **85**, 3545 (2000).

[87] C. Thomsen, S. Reich, P. M. Rafailov, and H. Jantoljak, "Symmetry of the high-energy modes in carbon nanotubes", phys. stat. sol. (b) **214**, R15 (1999).

[88] J. Hwang, H. H. Gommans, A. Ugawa, H. Tashiro, R. Haggenmueller, *et al.*, "Polarized spectroscopy of aligned single-wall carbon nanotubes", Phys. Rev. B **62**, R13 310 (2000).

[89] A. M. Rao, J. Chen, E. Richter, U. Schlecht, P. C. Eklund, *et al.*, "Effect of van der Waals interactions on the Raman modes in single walled carbon nanotubes", Phys. Rev. Lett. **86**, 3895 (2001).

[90] A. G. Rinzler, private communication.

[91] H. Ajiki and T. Ando, "Carbon nanotubes: Optical absorption in Aharonov-Bohm flux", Jpn. J. Appl. Phys. **Suppl. 34-1**, 107 (1994).

[92] S. Tasaki, K. Maekawa, and T. Yamabe, "π -band contribution to the optical properties of carbon nanotubes: Effects of chirality", Phys. Rev. B **57**, 9301 (1998).

[93] Z. M. Li, Z. K. Tang, H. J. Liu, N. Wang, C. T. Chan, *et al.*, "Polarized absorption spectra of single-walled 4 Å carbon nanotubes aligned in channels of an $AlPO_4$-5 single crystal", Phys. Rev. Lett. **87**, 127401 (2001).

[94] R. Ahuja, S. Auluck, J. M. Wills, M. Alouani, B. Johansson, and O. Eriksson, "Optical properties of graphite from first-principles calculations", Phys. Rev. B **55**, 4999 (1997).

[95] L. G. Johson and G. Dresselhaus, "Optical properties of graphite", Phys. Rev. B **7**, 2275 (1973).

[96] R. J. Nemanich and S. A. Solin, "First- and second-order Raman scattering from finite-size crystals of graphite", Phys. Rev. B **20**, 392 (1979).

[97] P. V. Teredesai, A. Sood, D. Muthu, R. Sen, A. Govindaraj, and C. Rao, "Pressure-induced reversible transformation in single-wall carbon nanotube bundles studied by Raman spectroscopy", Chem. Phys. Lett. **319**, 296 (2000).

[98] M. J. Peters, L. E. McNeila, J. P. Lu, and D. Kahn, "Structural phase transition in carbon nanotube bundles under pressure", Phys. Rev. B **61**, 5939 (2000).

[99] S. Reich, H. Jantoljak, and C. Thomsen, "Shear strain in carbon nanotubes under hydrostatic pressure", Phys. Rev. B **61**, R13 389 (2000).

[100] P. V. Teredesai, A. K. Sood, S. Sharma, S. Karmakar, S. K. Sikka, A. Govindaraj, and C. N. R. Rao, "Pressure effects on single wall carbon nanotube bundles", phys. stat. sol. (b) **223**, 479 (2001).

[101] U. D. Venkateswaran, E. A. Brandsen, U. Schlecht, A. M. Rao, E. Richter, *et al.*, "High pressure studies of the Raman-active phonons in carbon nanotubes", phys. stat. sol. (b) **223**, 225 (2001).

[102] J. Tang, L.-C. Qin, T. Sasaki, M. Yudasaka, A. Matsushita, and S. Iijima, "Compressibility and polygonization of single-walled carbon nanotubes under hydrostatic pressure", Phys. Rev. Lett. **85**, 1887 (2000).

[103] J. F. Nye, *Physical properties of crystals* (Oxford, Oxford, London, 1979).

[104] V. G. Hadjiev, M. N. Iliev, S. Arepalli, P. Nikolaev, and B. S. Files, "Raman scattering test of single-wall carbon nanotube composites", Appl. Phys. Lett. **78**, 3193 (2001).

[105] M. M. J. Treacy, T. W. Ebbesen, and J. M. Gibson, "Exceptionally high Young's modulus observed for individual carbon nanotubes", Nature (London) **381**, 678 (1996).

[106] D. Sánchez-Portal, E. Artacho, J. M. Soler, A. Rubio, and P. Ordejón, "*Ab initio* structural, elastic, and vibrational properties of carbon nanotubes", Phys. Rev. B **59**, 12678 (1999).

[107] E. Hernández, C. Goze, P. Bernier, and A. Rubio, "Elastic properties of C and $B_xC_yN_z$ composite nanotubes", Phys. Rev. Lett. **80**, 4502 (1998).

[108] J. Lu, "Elastic properties of carbon nanotubes and nanoropes", Phys. Rev. Lett. **79**, 1297 (1997).

[109] J. P. Lu, "Elastic properties of single and multilayered nanotubes", J. Phys. Chem. Sol. **58**, 1649 (1997).

[110] L. D. Landau and J. M. Lifschitz, *Lehrbuch der Theoretischen Physik, Bd. VII* (Akademie Verlag, Berlin, 1991).

[111] W. L. Smirnow, *Lehrgang der höheren Mathematik*, vol. 4 (Deutscher Verlag der Wissenschaften, Berlin, 1961), 2 edn., in particular §94, p. 242.

[112] J. Bernard and A. Zunger, "Is there an elastic anomaly for a (001) monolayer of InAs embedded in GaAs?", Appl. Phys. Lett. **65**, 165 (1994).

[113] M. Hanfland, H. Beister, and K. Syassen, "Graphite under pressure: Equation of state and first-order Raman modes", Phys. Rev. B **39**, 12 598 (1989).

[114] F. Cerdeira, C. J. Buchenauer, F. H. Pollack, and M. Cardona, "Stress-induced shifts of first-order Raman frequencies of diamond- and zincblende-type semiconductors", Phys. Rev. B **5**, 580 (1972).

[115] E. Anastassakis, "Morphic effects in lattice dynamics", in *Dynamical Properties of Solids*, edited by G. Horton and A. Maradudin (North-Holland, Amsterdam, 1980), vol. 4, p. 157.

[116] P. Wickboldt, E. Anastassakis, R. Sauer, and M. Cardona, "Raman phonon piezospectroscopy in GaAs: Infrared measurements", Phys. Rev. B **35**, 1362 (1987).

[117] F. Pollack, "Effects of homogeneous strain on the electronic and vibrational levels in semiconductors", in *Strained-Layer Superlattices: Physics*, edited by T. Pearsall (Academic, New York, 1990), vol. 32 of *Semiconductors and Semimetals*, p. 19.

[118] E. Anastassakis, "Angular dispersion of optical phonon frequencies in strained cubic crystals", J. Appl. Phys. **81**, 3046 (1997).

[119] E. Anastassakis, "Selection rules of Raman scattering by optical phonons in strained cubic crystals", J. Appl. Phys. **82**, 1582 (1997).

[120] C. Thomsen, S. Reich, and P. Ordejón, "*Ab initio* determination of the phonon deformation potentials of graphene", Phys. Rev. B (in print 2002).

[121] M. H. Grimsditch, E. Anastassakis, and M. Cardona, "Effect of uniaxial stress on the zone-center optical phonon of diamond", Phys. Rev. B **18**, 901 (1978).

[122] K. Bradley, S.-H. Jhi, P. G. Collins, J. Hone, M. L. Cohen, S. G. Louie, and A. Zettl, "Is the intrinsic thermoelectric power of carbon nanotubes positive?", Phys. Rev. Lett. **85**, 4361 (2000).

[123] H. J. Choi, J. Ihm, S. G. Louie, and M. L. Cohen, "Defects, quasibound states, and quantum conductance in metallic carbon nanotubes", Phys. Rev. Lett. **84**, 2917 (2000).

[124] M. S. Fuhrer, J. Nygard, L. Shih, M. Forero, Y.-G. Yoon, *et al.*, "Crossed nanotube junctions", Science **288**, 494 (2000).

[125] M. Terrones, H. Terrones, F. Banhart, J.-C. Charlier, and P. M. Ajayan, "Coalescence of single-walled carbon nanotubes", Science **288**, 1226 (2000).

[126] O. Dubay and G. Kresse, "Accurate density functional calculations of phonons in carbon nanotubes", in *Electronic Properties of Novel Materials-Progress in Molecular Nanostructures*, edited by H. Kuzmany, J. Fink, M. Mehring, and S. Roth, IWEPS Kirchberg (2001), p. xxxx.

[127] J. W. G. Wildöer, L. C. Venema, A. G. Rinzler, R. E. Smalley, and C. Dekker, "Electronic structure of atomically resolved carbon nanotubes", Nature **391**, 59 (1998).

[128] T. W. Odom, J. L. Huang, P. Kim, and C. M. Lieber, "Atomic structure and electronic properties of single-walled carbon nanotubes", Nature **391**, 62 (1998).

[129] T. W. Odom, J.-L. Huang, P. Kim, and C. M. Lieber, "Structure and electronic properties of carbon nanotubes", J. Phys. Chem. B **104**, 2794 (2000).

[130] A. Jorio, A. G. S. Filho, G. Dresselhaus, M. S. Dresselhaus, R. Saito, *et al.*, "Joint density of electronic states for one isolated single-wall carbon nanotube studied by resonant Raman scattering", Phys. Rev. B **63**, 245416 (2001).

[131] X. Blase, L. X. Benedict, E. L. Shirley, and S. G. Louie, "Hybridization effects and metallicity in small radius carbon nanotubes", Phys. Rev. Lett. **72**, 1878 (1994).

[132] N. Troullier and J. L. Martins, "Structural and electronic properties of C_{60}", Phys. Rev. B **46**, 1754 (1992).

[133] M. C. Schabel and J. L. Martins, "Energetics of interplanar binding in graphite", Phys. Rev. B **46**, 7185 (1992).

[134] S. Reich, C. Thomsen, and P. Ordejón, "Electronic band structures of isolated and bundled carbon nanotubes", Phys. Rev. B (09/2001 submitted).

[135] J. W. McClure, "Band structure of graphite and de Haas-van Alphen effect", Phys. Rev. **108**, 612 (1957).

[136] E. R. Taft and H. R. Philipp, "Optical properties of graphite", Phys. Rev. **138**, 197 (1965).

[137] A. Zunger, "Self-consistent LCAO calculation of the electronic properties of graphite. I. The regular graphite lattice", Phys. Rev. B **17**, 626 (1978).

[138] N. A. W. Holzwarth, S. G. Louie, and S. Rabii, "X-ray from factors and the electronic structure of graphite", Phys. Rev. B **26**, 5382 (1982).

[139] T. Fauster, F. J. Himpsel, J. E. Fischer, and E. W. Plummer, "Three-dimensional energy band in graphite and Li-intercalated graphite", Phys. Rev. Lett. **51**, 430 (1983).

[140] T. Takahashi, H. Tokailin, and T. Sagawa, "Angle-resolved ultraviolet photoelectron spectroscopy of the unoccupied band structure of graphite", Phys. Rev. B **32**, 8317 (1985).

[141] W. Schülke, U. Bonse, H. Nagasawa, A. Kaprolat, and A. Berthold, "Interband transitions and core excitation in highly oriented pyrolytic graphite studied by inelastic synchrotron x-ray scattering: Band-structure information", Phys. Rev. B **38**, 2112 (1988).

[142] J.-C. Charlier, X. Gonze, and J.-P. Michenaud, "First-principles study of the electronic properties of graphite", Phys. Rev. B **43**, 4579 (1991).

[143] R. F. Willis, B. Feuerbacher, and B. Fitton, "Graphite conduction band states from secondary electron emission spectra", Phys. Lett. A **34**, 231 (1971).

[144] O. Jost, A. A. Gorbunov, W. Pompe, T. Pichler, R. Friedlein, *et al.*, "Diameter grouping in bulk samples of single-walled carbon nanotubes from optical absorption spectroscopy", Appl. Phys. Lett. **75**, 2217 (1999).

[145] J. Mintmire and C. T. White, "First-principles band structures of armchair nanotubes", Appl. Phys. A **67**, 65 (1998).

[146] J. C. Slater, *Quantum Theory of Molecules and Solids*, vol. 2 (McGraw-Hill, New York, 1965).

[147] A. Kleiner and S. Eggert, "Curvature, hybridization, and STM images of carbon nanotubes", Phys. Rev. B **64**, 113402 (2001).

[148] M. Ouyang, J.-L. Huang, C. L. Cheung, and C. M. Lieber, "Energy gaps in 'metallic' single-walled carbon nanotubes", Science **292**, 702 (2001).

[149] Y.-K. Kwon, S. Saito, and D. Tománek, "Effect of intertube coupling on the electronic structure of carbon nanotube ropes", Phys. Rev. B **58**, R13 314 (1998).

[150] P. Delaney, H. J. Choi, J. Ihm, S. G. Louie, and M. L. Cohen, "Broken symmetry and pseudogaps in ropes of carbon nanotubes", Phys. Rev. B **60**, 7899 (1999).

[151] P. Delaney, H. J. Choi, J. Ihm, S. G. Louie, and M. L. Cohen, "Broken symmetry and pseudogaps in ropes of carbon nanotubes", Nature (London) **391**, 466 (1998).

[152] P. Kim, T. W. Odom, J.-L. Huang, and C. M. Lieber, "Electronic density of states of atomically resolved single-walled carbon nanotubes: Van Hove singularities and end states", Phys. Rev. Lett. **82**, 1225 (1999).

[153] L. C. Venema, J. W. Janssen, M. R. Buitelaar, J. W. G. Wildöer, S. G. Lemay, L. P. Kouwenhoven, and C. Dekker, "Spatially resolved scanning tunneling spectroscopy on single-walled carbon nanotubes", Phys. Rev. B **62**, 5238 (2000).

[154] Z. Yu and L. E. Brus, "(n,m) structural assignments and chirality dependence in single-wall carbon nanotube Raman scattering", J. Phys. Chem. B **105**, 6831 (2001).

[155] P.-H. Tan, Y.-M. Deng, and Q. Zhao, "Temperature-dependent Raman spectra and anomalous Raman phenomenon of highly oriented pyrolytic graphite", Phys. Rev. B **58**, 5435 (1998).

[156] I. Pócsik, M. Hundhausen, M. Koos, and L. Ley, "Origin of the D peak in the Raman spectrum of microcrystalline graphite", J. Non-Cryst. Sol. **227-230B**, 1083 (1998).

[157] Y. Wang, D. C. Alsmeyer, and R. L. McCreery, "Raman spectroscopy of carbon materials: Structural basis of observed spectra", Chem. Mater. **2**, 557 (1990).

[158] M. J. Matthews, M. A. Pimenta, G. Dresselhaus, M. S. Dresselhaus, and M. Endo, "Origin of dispersive effects of the Raman *D* band in carbon materials", Phys. Rev. B **59**, R6585 (1999).

[159] A. K. Sood, R. Gupta, and S. A. Asher, "Origin of the unusual dependence of Raman *D* band on excitation wavelength in graphite-like materials", J. Appl. Phys. **90**, 4494 (2001).

[160] A. K. Sood, R. Gupta, C. H. Munro, and S. A. Asher, "Resonance Raman scattering from graphite: Novel consequences", in *Proceedings of the XVI International Conference on Raman Spectroscopy*, edited by A. M. Heyns (Wiley-VCH, Berlin, 1998), p. 62.

[161] F. Cerdeira, E. Anastassakis, W. Kauschke, and M. Cardona, "Stress-induced doubly resonant Raman scattering in GaAs", Phys. Rev. Lett. **57**, 3209 (1986).

[162] S. I. Gubarev, T. Ruf, and M. Cardona, "Doubly resonant Raman scattering in the semimagnetic semiconductor $Cd_{0.95}Mn_{0.05}Te$", Phys. Rev. B **43**, 1551 (1991).

[163] R. A. Jishi and G. Dresselhaus, "Lattice-dynamical model for graphite", Phys. Rev. B **26**, 4514 (1982).

[164] G. Kresse, J. Furthmüller, and J. Hafner, "*Ab initio* force constant approach to phonon dispersion relations of diamond and graphite", Europhys. Lett. **32**, 729 (1995).

[165] J. Maultzsch, "Resonant Raman scattering in carbon nanotubes", Diploma Thesis, Technische Universität Berlin, June 2001.

[166] S. D. M. Brown, P. Corio, A. Marucci, M. S. Dresselhaus, M. A. Pimenta, and K. Kneipp, "Anti-stokes Raman spectra of single-walled carbon nanotubes", Phys. Rev. B **61**, R5137 (2000).

[167] A. Grüneis, M. Hulman, C. Kramberger, T. Pichler, H. Peterlik, *et al.*, "Oscillatory behaviour of Raman modes in SWNT", in *Electronic Properties of Novel Materials-Progress in Molecular Nanostructures*, edited by H. Kuzmany, J. Fink, M. Mehring, and S. Roth, IWEPS Kirchberg (2001), p. xxxx.

[168] M. A. Pimenta, A. Jorio, S. D. M. Brown, A. G. S. Filho, G. Dresselhaus, *et al.*, "Diameter dependence of the Raman *D*-band in isolated single-wall carbon nanotubes", Phys. Rev. B **64**, 041401(R) (2001).

[169] J. Kürti, V. Zólyomi, A. Grüneis, and H. Kuzmany, "Disorder-induced triple resonant Raman phenomena in single wall carbon nanotubes", Phys. Rev. B (2001), submitted.

[170] D. Tekleab, D. L. Carroll, G. G. Samsonidze, and B. I. Yakobson, "Strain-induced electronic property heterogeneity of a carbon nanotube", Phys. Rev. B **64**, 035419 (2001).

[171] M. Bockrath, W. Liang, D. Bozovic, J. H. Hafner, C. M. Lieber, M. Tinkham, and H. Park, "Resonant electron scattering by defects in single-walled carbon nanotubes", Science **291**, 283 (2001).

[172] P. G. Collins, A. Zettl, H. Bando, A. Thess, and R. E. Smalley, "Nanotube nanodevice", Science **278**, 100 (1997).

[173] R. Saito, A. Jorio, J. H. Hafner, C. M. Lieber, M. Hunter, *et al.*, "Chirality-dependent *G*-band Raman intensity of carbon nanotubes", Phys. Rev. B **64**, 085312 (2001).

[174] J. P. Perdew, K. Burke, and M. Ernzerhof, "Generalized gradient approximation made simple", Phys. Rev. Lett. **77**, 3865 (1996).

[175] R. Car and M. Parrinello, "Unified approach for molecular dynamics and density-functional theory", Phys. Rev. Lett. **55**, 2471 (1985).

[176] P. Ordejón, "Order-*N* tight-binding methods for electronic-structure and molecular dynamics", Comput. Mater. Sci. **12**, 157 (1998).

[177] M. Verissimo-Alves, R. B. Capaz, B. Koiller, E. Artacho, and H. Chacham, "Polarons in carbon nanotubes", Phys. Rev. Lett. **86**, 3372 (2001).

[178] P. Ordejón, E. Artacho, and J. M. Soler, "Self-consistent order-*N* density-functional calculations for very large systems", Phys. Rev. B **53**, R10 441 (1996).

[179] P. Ordejón, D. A. Drabold, R. M. Martin, and M. P. Grumbach, "Linear system-size scaling methods for electronic-structure calculations", Phys. Rev. B **51**, 1456 (1995), and references therein.

[180] E. Artacho, D. Sánchez-Portal, P. Ordejón, A. García, and J. Soler, "Linear-scaling ab-initio calcluations for large and complex systems", phys. stat. sol. (b) **215**, 809 (1999).

[181] J. Junquera, O. Paz, D. Sánchez-Portal, and E. Artacho, "Numerical atomic orbitals for linear scaling", Phys. Rev. B **64**, 235111 (2001).

[182] P. Hohenberg and W. Kohn, "Inhomogeneous electron gas", Phys. Rev. **136**, B864 (1964).

[183] L. J. Sham and W. Kohn, "One-particle properties of an inhomogeneous interacting electron gas", Phys. Rev. **145**, 561 (1966).

[184] M. C. Payne, M. P. Teter, D. C. Allan, T. A. Arias, and J. D. Joannopoulos, "Iterative minimization techniques for *ab initio* total-energy calculations: Molecular dynamics and conjugate gradients", Rev. Mod. Phys. **64**, 1045 (1992).

[185] R. M. Martin, "*Ab initio* total energy methods in semiconductor physics", Festkörperprobleme (Advances in Solid State Physics) **25**, 3 (1985).

[186] J. Callaway and N. H. March, "Density functional methods: Theory and application", in *Solid State Physics*, edited by H. Ehrenreich and D. Turnbull (Academic, New York, 1984), vol. 38, p. 136.

[187] J. P. Perdew and A. Zunger, "Self-interaction correction to density-functional approximations for many-electron systems", Phys. Rev. B **23**, 5048 (1981).

[188] H. J. Monkhorst and J. D. Pack, "Special points for Brillouin-zone integrations", Phys. Rev. B **13**, 5188 (1976).

[189] J. C. Phillips and L. Kleinman, "New method for calculating wave functions in crystals and molecules", Phys. Rev. **116**, 287 (1959).

[190] D. R. Hamann, M. Schlüter, and C. Chiang, "Norm-conserving pseudopotentials", Phys. Rev. Lett. **43**, 1494 (1979).

[191] N. Troullier and J. L. Martins, "Efficient pseudopotentials for plane-wave calculations", Phys. Rev. B **43**, 1993 (1991).

[192] L. Kleinman and D. M. Bylander, "Efficacious form for model pseudopotentials", Phys. Rev. Lett. **48**, 1425 (1982).

[193] V. Heine, "Electronic structure from the point of view of the local atomic environment", in *Solid State Physics: Advances in Research and Applications*, edited by F. Seitz, C. Turnbull, and H. Ehrenreich (Academic, New York, 1980), vol. 35.

[194] W. Kohn, "Density functional and density matrix method scaling linearly with the number of atoms", Phys. Rev. Lett. **76**, 3168 (1996).

[195] O. F. Sankey and D. J. Niklewski, "*Ab initio* multicenter tight-binding model for molecular-dynamics simulations and other applications in covalent systems", Phys. Rev. B **40**, 3979 (1989).

[196] R. P. Feynman, "Forces in molecules", Phys. Rev. **56**, 340 (1939).

[197] O. H. Nielsen and R. M. Martin, "First-principles calculation of stress", Phys. Rev. Lett. **50**, 697 (1983).

[198] A. Rubio, D. Sánchez-Portal, E. Artacho, P. Ordejón, and J. M. Soler, "Electronic states in a finite carbon nanotube: A one-dimensional quantum box", Phys. Rev. Lett. **82**, 3520 (1999).

[199] E. Burgos, E. Halac, R. Weht, H. Bonadeo, E. Artacho, and P. Ordejón, "New superhard phases for three-dimensional C_{60}-based fullerites", Phys. Rev. Lett. **85**, 2328 (2000).

[200] J. I. Pascual, J. Gomez-Herrero, A. M. Baro, D. Sanchez-Portal, E. Artacho, P. Ordejon, and J. M. Soler, "Seeing molecular orbitals", Chem. Phys. Lett. **321**, 78 (2000).

[201] S. M. Sharma, S. Karmakar, S. K. Sikka, P. V. Teredesai, A. K. Sood, A. Govindaraj, and C. N. R. Rao, "Pressure-induced phase transformation and structural resilience of single-wall carbon nanotube bundles", Phys. Rev. B **63**, 205417 (2001).

[202] J. Kürti, G. Kresse, and H. Kuzmany, "First-principles calculations of the radial breathing mode of single-wall carbon nanotubes", Phys. Rev. B **58**, 8869 (1998).

[203] W. Frank, C. Elsässer, and M. Fähnle, "*Ab initio* force-constant method for phonon dispersions in alkali metals", Phys. Rev. Lett. **74**, 1791 (1995).

[204] Y.-N. Chiu, "Theory of a novel odd-parity Raman scattering mechanism: Depolarization ratios and reversal coefficients for random molecular systems", J. Chem. Phys. **52**, 3641 (1970).

[205] Y.-N. Chiu, "Rotational structure of a novel Raman effect in quantized symmetric- and spherical-top molecules", J. Chem. Phys. **52**, 4950 (1970).

Acknowledgments

Many people contributed to this work over the last three years. Especially I would like to thank...

... my thesis advisor Christian Thomsen. He convinced me that it would be interesting to work for "two or three months" on nanotubes before coming back to my research on semiconductors. Taking his advice was a decision I have never regretted. Many thanks for all the joint work on group and elasticity theory, Raman scattering, in particular, the double resonant version, and hexagon drawing. Also for teaching me the ins and outs of publishing, proposal writing, and composing emails to unknown people (on the phone calls I am still working).

... my second advisor Pablo Ordejón for teaching me Density Functional Theory and SIESTA. I very much enjoyed the possibility to look at my problems from a different point of view and to find answers to questions which I could not study experimentally. I was always impressed by his patience, his interest in experimental work and in the problems I wanted to pursue. Thanks also for the extensions of SIESTA (not to mention vibrator), bug searching, and, last but not least, the nice time in Barcelona and Oviedo.

... Peter Zimmermann for being the chairman of my thesis committee.

... Milan Damnjanović and the group in Belgrade. Although I was already convinced on the power of group theory and symmetry, I did not have the slightest idea what really can be done by the method. The six hours tutorial on modified group projectors gave me a little insight, even more so, since it was accompanied by enlightening demonstrations why a rotation by 2π is different from one by 4π. Thank you very much for the nice week in Serbia and the long discussions on many topics.

... Janina Maultzsch for working together on nanotubes for more than a year. Without her many parts of this thesis would not have been finished, in particular, the double resonant Raman scattering in the tubes. I really enjoyed discussing the length of various vectors, *S* and *D* modes, and "first squaring and then summing" or not, besides just talking, travelling, and – from time to time – some chocolate. Many thanks also for proof reading this manuscript and the encouraging comments.

... María Machón for joining the SIESTA team. It was really nice to suddenly have somebody doing SIESTA as well and helped me a lot to stay focused on the calculations in a group working mostly experimentally. I am sorry that the G-topic was so much trouble, but – extra für Dich – I prepared some of the future work proposals in the SIESTA chapter; take a look at them.

... Marianne Heinold, Sabine Morgner, Heiner Perls, and Bernd Schöler for all their support. Sabine Morgner I would like to thank once again for the help in preparing the lecture last year. Bernd Schöler and Heiner Perls were always there when I was looking for help with the labs or some new equipment (wenn auch die Höllenmaschine ihre Versprechen nicht gehalten hat). Heiner Perls's excellent web page of our group I appreciated whenever I was in Barcelona and was looking for one of our publications. Norbert Lindner took care of the laptop on which this work was written, thanks for that besides other things.

... the other authors of SIESTA, Daniel Sánchez-Portal, Emilio Artacho, and José Soler, for guiding my first steps with the program and Javier Junquera for the very first input file.

... the research groups in Berlin and Barcelona for all the support, discussions, and the nice time I had. Special thanks to the frequent corridor visitors and the most frequent corridor visitor and to my two roommates.

and

... my family.